Maximization of Power Generation From Thermoelectric Generators Operating Under Constant Heat Flux

Marcos Compadre Torrecilla

BSc, MSc

Submitted in fulfillment of the requirements for the Degree of Philosophy Doctorate (Ph.D.)

School of Engineering

University of Glasgow

March, 2019

Abstract

Thermoelectric generators (TEGs) are used to convert thermal energy into electricity. TEGs present an emissions-free source of power and, despite the low efficiency they offer, with typical values of 5%, they can be used to harvest waste-heat energy in different type of applications. The high robustness presented by TEGs allows their use in low-maintenance applications.

TEGs can operate under two different conditions: constant temperature gradient or constant input heat flux. When a TEG operates under constant temperature gradient, the input heat flux varies with the electrical operating conditions of the TEG devices. Under these conditions the TEG is modeled by a constant voltage source with a constant resistance in series with the voltage source. When operated under constant heat flux, the temperature gradient of the TEG changes with the electrical operating conditions of the device. In this situation of constant heat flux, both the equivalent voltage source and the resistance in series with it change their values with the electrical operating point.

The location of the Maximum Power Point, or MPP, of the TEG is different in both operating conditions. In constant temperature gradient the MPP is located at half of the instantaneous open-circuit voltage of the TEG, whereas under constant heat flux the MPP is located at an electrical point higher than half of the instantaneous open-circuit voltage. DC/DC converters are mainly used to operate TEGs at the MPP and Maximum Power Point Tracking (MPPT) techniques are used to operate the TEG at the MPP. Due to the difference in the location of the MPP between constant temperature gradient and constant input heat flux, the MPPT techniques will be different between these two operating conditions.

This thesis focuses in the study of the location and MPPT techniques for TEGs operated under constant heat flux. A computational model of the TEG for its operation under constant heat flux is first developed. The model of the TEG is then interfaced with the model of a boost, or step-up, converter, which implements a new MPPT algorithm to operate the TEG at the true MPP. The output energy of the power converter is used to charge a lithium-ion (Li-Ion) battery.

The complete model of the TEG system is then used to compare the new algorithm proposed in this thesis against two state-of-the-art algorithms: the Fractional Open-Circuit method and the Perturb and Observe method. The comparison is made under three different input heat flux profiles: constant heat flux, ramp-varying heat flux and step-changing heat flux.

The last chapter of this thesis presents a hardware implementation of the TEG system and the MPPT power converter. Experimental results are presented for the new and the two state-of-the-art algorithms and a comparison between the three algorithms are presented for the three different input heat flux profiles described previously.

The TEG model and the MPPT algorithm presented in this work can be applied to any TEG applications where the TEG operates under constant heat flux.

Dedicada a mis abuelos

(to my grandparents)

Table of Contents

List of Tables

List of Figures

Acknowledgments

First of all I would like to thank Prof. Andrew Knox for guiding me throughout these years as my supervisor.

I would also like to thank Clyde Space for supporting me in doing this PhD.

Big thanks to Dr. Jonathan Siviter, Dr. Paul Mullen and Dr. Elena Anamaria Man for all the support, and the knowledge they have shared with me, during these years. I would also like to thank them, and Dr. Francesco Mirando, for the great experiences shared during all the conference trips.

I would not be able to thank enough for the technical and personal support from my great friend Andrea Montecucco (Dr. Andrea Montecucco, but I would like to leave the formalities aside). Without you I would not have been able to complete this journey. *Grazie mille caro mio!*

I want to also thank my friend and mentor Alan Weinberg for all the knowledge he has always shared with me and all the fun we always have together doing circuit design.

Many thanks to all my family for always supporting me.

Also, *grazie* Roberta for always being there for me.

"I declare that, except where explicit reference is made to the contribution of others, this thesis is the result of my own work and has not been submitted for any other degree at the University of Glasgow or any other institution."

Signature: _____

Printed name: _____

List of Acronyms

1-D	One-dimensional
ADC	Analog-to-Digital Converter
AUV	Autonomous Underwater Vehicle
BM	Bisection Method
BOL	Beginning of Life
BOM	Beginning of Mission
CCM	Continuous Conduction Mode
COTS	Commercial off-the-shelf
DAC	Digital-to-Analog Converter
DCM	Discontinuous Conduction Mode
DC/DC	Direct-Current to Direct-Current (Converter)
DSP	Digital Signal Processor
EMI	Electro-Magnetic Interference
EoC	End of Charge
FOC	Fractional Open-Circuit
FOV	Fractional Open-Circuit Voltage
FPGA	Field-Programmable Gate Array
GPHS	General Purpose Heat Source
INC	Incremental Conductance
IoT	Internet of Things
LCD	Liquid Crystal Display
Li-Ion	Lithium Ion
MPP	Maximum Power Point
MPPT	Maximum Power Point Tracking

MQF	Manufacture Quality Factor
MRFM	Modified Regula Falsi Method
NRM	Newton Raphson Method
PCB	Printed Circuit Board
P_{el}	Electric Power
PFM	Pulse Frequency Modulation
P_{th}	Thermal Power
PV	Photovoltaic
PWM	Pulse Width Modulation
P&O	Perturb and Observe
RAM	Random Access Memory
RFM	Regula Falsi Method
RTG	Radioisotope Thermoelectric Generator
SM	Secant Method
SMPS	Switched Mode Power Supply
SoC	State of Charge
TE	Thermoelectric
TEC	Thermoelectric Cooler
TEG	Thermoelectric Generator
THP	Thermoelectric Heat Pump
W_{el}	Watt (electrical)
W_{th}	Watt (thermal)
Z	Figure of merit
ZCS	Zero Current Switching
ZT	Dimensionless figure of merit

Chapter 1 Introduction

Thermoelectric devices are semiconductor-based components that can be used to convert heat into electricity and *vice versa*. They are made of *p*- and *n*-type semiconductor pellets connected electrically in series and thermally in parallel. Such pellets are usually sandwiched between two electrically insulating plates that function as the mechanical interface between the semiconductor pellets and the heat sink or the heat source, as well as with the substrate for the electrical interconnects. When used to convert heat energy into electrical energy the devices are referred to as thermoelectric generators, or TEGs, and exploit the so-called *Seebeck* effect. In this case the TEGs are coupled to a heat source, on one side, and a heat sink on the other side so that a temperature gradient is generated across the device in response to a flow of thermal energy. The temperature gradient produces a flux of free charges inside the semiconductor pellets and an electrical potential is developed across the TEG terminals; and a current will flow through the pellets when the circuit is closed with an electric load. Conversely, when thermoelectric devices are used to transfer heat from one side of the device to the other side they are referred to as thermoelectric heat pumps (THPs) or thermoelectric coolers (TECs), and exploit the so-called *Peltier* effect. The process of pumping heat using the Peltier effect is also referred to as *Peltier cooling*. When used as thermoelectric heat pumps, a current is forced through the device and the charges in motion absorb heat on one side of the device and reject heat on the other side thus generating heat transport from one side to the other side. In both cases there is a polarity match between the direction of heat flow and the voltage across the device. This thesis focuses primarily on the use of thermoelectric devices as TEGs used to generate electrical energy.

Different materials have different properties for different temperature gradients and not all the materials behave equally under the same temperature range. The thermoelectric figure of merit *ZT* is a parameter that defines the efficiency of thermoelectric materials, and depends on the temperature gradient across the device. Ideally, a high performance thermoelectric material will present a high value of *ZT* over a wide temperature range.

Some electrical properties, like the equivalent internal electrical resistance, or the thermal resistance of the TEG, can be adjusted by modifying the geometrical dimensions of the thermoelectric pellets. Part of the on-going wider research by the thermoelectric devices community focuses on the development of materials with higher values of the figure of merit as well as applying changes at a macroscopic level, like sizing the thermoelectric pellets, in order to improve the thermoelectric efficiency of TEGs.

The semiconductor structure and the lack of moving parts make TEGs robust, long-lived devices that require very little maintenance and can be used in diverse and harsh environments. For instance, they are used in Radioisotope Thermoelectric Generators (RTGs) in deep-space missions and exploration missions of the Martian surface, where the TEGs are interfaced with a radioactive heat source and have to operate under the harsh conditions found in the space environment. They are also used to convert waste heat in industrial and automotive applications, where the TEG is placed under large temperature gradients with the hot side reaching temperatures of 400-500 ^{o}C. In medical applications TEGs are used to harvest human body heat and power low-power consumption sensors that are placed under the skin.

Selecting the appropriate semiconductor material over a given operating temperature range is not the only consideration for optimizing the amount of electrical power a TEG can produce in a given application. For any given temperature gradient or value of input heat flux there is a maximum value of power generation in the power-voltage (or power-current) characteristic curve. In order to maximize the amount of power the TEG can deliver, the TEG must operate at that point, also known as Maximum Power Point, or MPP. There are many methods to operate the TEG at the MPP, the most common being the use of a SMPS to control the operating point of the TEG. When a battery is used to store the energy produced by the TEG, the output voltage of the SMPS is fixed, and the input voltage (or the TEG current) can be changed by adjusting the control variable of the SMPS; that is, the *duty-cycle*. Note that the load must be capable of absorbing all the power produced by the TEG for operation at the MPP to be maintained. Most of the Maximum Power Point Tracking, MPPT, techniques that have been developed to date for TEGs are optimized for applications where the TEG operates under a constant temperature gradient. These techniques, however, are not optimized for applications where the TEG operates under a constant heat flux, where the thermal transient response of the TEG influences the accuracy of an MPPT algorithm to operate the TEG at the true MPP. Indeed, most of the research done to date contemplates TEGs operated under a constant

temperature gradient ΔT. In most practical applications, however, the TEG operates under a constant heat flux, and the temperature gradient across the TEG depends on the thermal resistance of the different TEG system elements as well as on the operating point of the TEG itself. This is because, even for electrical power generation, the current flowing through the TEG induces a corresponding Peltier effect that pumps heat from the hot to the cold side. This Peltier effect is considered as parasitic in power generation applications and it changes (reduces) the temperature gradient across the TEG. This thesis presents the development an MPPT algorithm that is able to operate the TEG at the true MPP when operating under constant heat flux conditions.

TEGs are commonly modeled by a Thevenin equivalent circuit involving a voltage source with a resistor in series with it. The voltage source represents the value of open-circuit voltage whereas the resistor in series models the equivalent internal resistance of the semiconductor pellets and the interconnection elements within the TEG. The circuit represents an accurate model for TEGs that operate under constant temperature gradient ΔT, situation in which the value of the equivalent circuit elements are fixed for a given value of ΔT. For constant heat flux applications, this simplified model is no longer valid due to various factors including the variations of ΔT with the operating point of the TEG, differences between *p*- and *n*-type materials, and their respective temperature-dependent non-linearity. Hence a more elaborate model is required. An accurate TEG model is essential for the development of thermoelectric applications since computer simulations have demonstrable limitations compared with experimental data obtained with real hardware.

This thesis presents a novel model of a TEG for operation under constant heat flux conditions that can be easily interfaced with the model of a SMPS for the development of MPPT techniques, but it is not limited to only these applications. The model of the TEG replicates, with a good degree of accuracy, the thermal transient response of the TEG. This is important because the electrical and thermal response time constants can be up to twelve orders of magnitude (10^{12}) different. The model is developed in Matlab/Simulink, and it is interfaced with the model of a *boost* converter that is used to charge a 28 V battery, while controlling the operating point of the TEG. The model includes a script that implements a novel MPPT technique that is optimized for applications where the TEG operates under constant heat flux. The new algorithm proposed in this thesis has been tested in the complete thermoelectric system and the results have been validated against two state-of-the-art and well established MPPT algorithms: the Fractional Open Circuit Voltage, or

FOV, algorithm and the Perturb & Observed, or P&O, algorithm. The two state-of-the-art algorithms have also been tested using the same simulation model. The complete thermoelectric system has been implemented in hardware using a TEG test jig, described in Chapter 3, and a PCB that contains a boost converter and a microcontroller that implements the MPPT algorithm. The results obtained with the three algorithms, along with the test data, are presented in this work.

1.1 Thesis structure

This section presents a brief description of the structure of this thesis.

- Chapter 1 (this section) is the introduction of the thesis.

- Chapter 2 describes the work performed to date, in thermoelectric power generation for waste heat recovery applications, found in the literature. A description of thermoelectric parameters, materials, applications and MPPT methods are described in this chapter and discussed in context.

- Chapter 3 presents the theory that describes the thermoelectric phenomena and the underlying physics. The mechanical structure of a TEG is presented and the relationships between thermal and electrical energy, at microscopic level in the semiconductor pellets, is explained. The three main thermoelectric effects (Seebeck, Peltier and Thomson) are explained, along with the Kelvin relationships. The thermoelectric model, based on the Seebeck voltage and the internal resistance of the TEG, is developed. The one-dimensional heat conduction equation is developed, which is the basis of the model presented in Chapter 4. The figure of merit (ZT) and the thermoelectric efficiency are also defined. Considerations when handling TEGs are given at the end of this Chapter.

- Chapter 4 presents the main differences between the operation under constant temperature gradient and constant input heat flux. First, the characteristic curves for a TEG operated under constant ΔT, obtained from the equations presented in Chapter 3, are presented; and the concept of variable and unlimited heat flux is explained. Then, the operation under constant finite heat flux is explained and the characteristic curves are obtained both theoretically, through Matlab simulations,

and experimentally, using a TEG in a test jig built for that purpose. The building blocks and the operation of the TEG test jig are described in this chapter. The analytical solution of the MPP of a TEG operated under constant heat flux is analysed as well. The last part of the chapter is dedicated to the dynamic transient response of the TEG, with characteristic curves showing such transient response.

- Chapter 5 examines the model of the TEG system. First, the model of the TEG device is developed. The model implements the transient response observed experimentally in Chapter 4. The model of the power converter is then developed. Starting from the steady-state equations of the converter, the average model is developed using the small-signal average model of the boost converter. The model of the TEG is connected to the model of the boost converter and an MPPT script, containing the new proposed MPPT algorithm, controls the converter. The performance of the new algorithm is tested against two state-of-the-art algorithms: FOV and P&O. The algorithms are tested against different input heat flux profiles. The results and improvements obtained with the new algorithm are presented at the end of this chapter.

- Chapter 6 shows the experimental results of the new algorithm. The MPPT algorithm is tested using the same test jig used in Chapter 4. The design of the hardware is presented and the behaviour of the MPPT algorithm is shown. The performance of the new MPPT algorithm is compared against the performance of FOV and P&O. The results are presented and compared against the results obtained with the simulation model.

- Chapter 7 reports the contents of the thesis and presents the conclusions obtained from the work and results presented in this study. Consideration of future work is also presented.

1.2 Original contribution

A list of the original contributions that have been originated from the work presented in this thesis is presented below.

- A study of the transient response of TEGs operated under constant heat flux, explaining the transitions between constant ΔT and constant heat flux characteristic curves.

- A method to model the transient response of the TEG through theoretical calculations.

- A fast model that simulates the steady-state and dynamic behaviour of the TEG.

- An MPPT method with a superior performance over the two most used state-of-the-art MPPT algorithms: Fractional Open-Circuit Voltage and Perturb & Observe methods.

- A method of measuring the open-circuit voltage of the TEG, without disconnecting the TEG from the power converter, through the use of a number of dedicated pairs of pellets.

- A mechanism to detect variations in the input heat flux by monitoring the open-circuit voltage of the TEG.

- A method to calculate a non-derivative adaptive step based on the instantaneous open-circuit voltage of the TEG.

1.3 List of publications

Part of the work presented in this thesis has been published and presented in the references listed below.

1.3.1 Journal papers

[J1] **M. Compadre Torrecilla**, A. Montecucco, J. Siviter, A. Strain, A.R Knox, "Transient response of a thermoelectric generator to load steps under constant heat flux", *Applied Energy*, vol. 212, pp. 293-303, Feb. 2018.

[J2] **M. Compadre**, A. Montecucco, J. Siviter, A.R Knox, A. Strain, "Novel TEG model and MPPT algorithm for thermoelectric generators operated under constant heat flux", *Applied Energy.* **Paper under review**.

1.3.2 Conference papers

[C1] **M. Compadre Torrecilla**, A. H. Weinberg, P. Hutton, C. Clark, "Multi-output power converter, operated from a regulated input bus, for the Sireus rate sensor", 11th *European Space Power Conference 2016,* Thessaloniki, Greece 2017, DOI: 10.1051/e3sconf/20171614001.

1.3.3 Conference proceedings

[CP1] **M. Compadre**, A. Montecucco, J. Siviter, P. Mullen, A. Ashraf A. Strain, A.R Knox, "Maximum power generation in a system using two TEGs in a cascade configuration", *International Conference in Thermoelectrics, Dresden, 2015*.

[CP2] **M. Compadre**, A. Montecucco, J. Siviter, A.R Knox, "Maximum Power Point Tracking on a TEG operated under constant heat conditions", *International Conference in Thermoelectrics, Caen, 2018*.

1.3.4 Conference posters

[P1] **M. Compadre**, A. Montecucco, A.R Knox, A. Strain "Experimental investigation of the behaviour of an MPPT algorithm for TEG systems operated under constant heat conditions ", *European Conference in Thermoelectrics, Lisbon, 2016*.

[P2] **M. Compadre**, A. Montecucco, A.R Knox, A. Strain, "Maximum Power Point Tracking on a TEG operated under constant heat conditions", *European Conference in Thermoelectrics, Padova, 2017*.

1.3.5 Other papers

The papers listed below are not directly related to the work presented in this thesis but are the result of research and collaborations with Clyde Space Ltd. and other research institutions.

[O1] A. Garrigos, D. Marroqui, J.M. Blanes, R. Gutierrez, **M. Compadre**, C. Clark, "An analog maximum power point tracking for photovoltaic systems: applications for nanospacecrafts", *19th European conference on power electronics and applications, EPE'17-ECCE,* Warsaw, Poland, September 2017, IEEE EPE Conference Proceedings.

[O2] A. Garrigos, D. Marroqui, J.M. Blanes, R. Gutierrez, **M. Compadre**, C. Clark, M. Macdonald "Investigation into the potential use of integrated switching regulators for low-voltage, low-power photovoltaic conversion in space applications", *41st IEEE industrial electronics conference, IECON,* Yokohama, Japan, November 2015.

[O3] A. Garrigos, D. Marroqui, J.M. Blanes, R. Gutierrez, **M. Compadre**, "Seguidor de máxima potencia global analógico para sistemas fotovoltaicos: aplicación a nanosatélites", *Seminario anual de automática, electrónia industrial e instrumentación, SAAEI 2017,* Valencia, Spain, Julio 2017, proceedings SAAEI 17. ISBN 978-84-606-8573-9

[O4] J. Borrell, D. Marroqui, A. Garrigos, J.M. Blanes, R. Gutierrez, **M. Compadre**, "Estudio del LT4357 como diodo ideal en el Sequential Switching Shunt

Regulator (S3R)", *Seminario anual de automática, electrónia industrial e instrumentación, SAAEI 2017,* Valencia, Spain, Julio 2017, proceedings SAAEI 17. ISBN 978-84-606-8573-9

1.3.6 Books

[B1] **M. Compadre**, A. Garrigos, A. Strain. *Chapter 9 – Power Systems, Nanosatellites*. Wiley, 2019. **Currently under edition. Publication planned for 2019**.

Chapter 2 Literature Review – State of the Art

2.1 Brief history

In 1821 Thomas Johann Seebeck, an Estonian-born German scientist, discovered the operating principle of a TEG, when he observed that a circuit made of two dissimilar materials with the junctions at different temperatures would deflect a compass magnet. Seebeck discovered that this circuit produced a voltage difference and that current would flow when closed with a resistive element. Seebeck called this effect *thermomagnetism*. The term *thermoelectricity* was coined by the Danish physicist Hans Christian Ørsted. Thirteen years later, in 1834, the French watchmaker and part time physicist Jean Charles Athanase Peltier found that passing current through a circuit made with two dissimilar materials would produce heating or cooling at the junction. These two effects are known as the *Seebeck* and *Peltier* effects, and are the basis of thermoelectric generation and cooling, respectively.

In 1854, twenty years after the discovery of the *Peltier* effect, William Thomson, also known as Lord Kelvin, a Scots-Irish physicist and engineer, found that the *Seebeck* and *Peltier* effects are related to each other. He found that any thermoelectric material could be used for both power generation, when the material operates under a temperature gradient, and pumping heat when a current is applied to it.

a) b) c)

Figure 2–1 a) Thomas Johann Seebeck b) Jean Charles Athanase Peltier c) William Thomson (Lord Kelvin)

Seebeck performed his first experiment using a metal bar but he then found that some materials, which today are known as semiconductors, exhibited better performance to generate thermoelectricity. The relationship between the voltage generated by a thermoelectric material and the temperature difference across it is known as the *Seebeck coefficient.*

The first TEG was built in 1823 as a result of a collaboration between Ørsted and Joseph Fourier, and it used bismuth and antimony thermocouples [1].

In 1909, the German physicist and engineer Edmund Altenkirch expressed that the efficiency of a TEG depends on the Seebeck coefficient and the thermal and electrical conductivities of the material. It is considered the first reference to the thermoelectric *Figure of Merit* [2], [3] although it was the Russian scientist Abram F. Ioffe who, between 1949 and 1956, used the *Z* parameter to define the efficiency of thermoelectric devices, as described in Equation. (**2-1**).

$$Z = \alpha^2 \cdot \frac{\sigma}{\kappa} \tag{2-1}$$

Where *Z* is the figure of merit, α is the Seebeck coefficient, and σ and κ are the electrical and thermal conductivities, respectively. As it can be seen from Equation (**2-1**), a good thermoelectric material presents a high Seebeck coefficient and electrical conductivity and a low thermal conductivity.

In 1993 Hicks and Dresselhaus presented experimental results showing that quantum well structures could significantly modify and improve the thermoelectric figure of merit of certain materials [4], see Figure 2–3. After these findings were published, further improvements in the figure of merit of bulk thermoelectric materials were made which is reflected in the rapid evolution of thermoelectric materials during the last 20 years.

2.2 Thermoelectric materials and their figure of merit

A high performance thermoelectric material is one that offers the large figure of merit over a wide temperature range. It is also important to find materials that offer good mechanical characteristics in order to be able to use them in thermoelectric modules. There, however, is a limit in the maximum value of the figure of merit. A TEG is a heat engine and thus subject to the *Carnot* efficiency limit.

Metals were used in the first thermoelectric experiments performed by T.J. Seebeck [5] and, although they present a very good electrical conductivity, the low Seebeck coefficient and the high thermal conductivity they present prevent them from being good thermoelectric materials.

From 1950 semiconductors were investigated for their use as thermoelectric materials due to the possibility of optimizing the three parameters involved in the figure of merit by adjusting the carrier concentration and the type of dopants. Special interest in these materials resurged in 1960s when the United States Navy required a silent source of electrical power for submarine propulsion. During these years the properties of Bi_2Te_3, *PbTe* and *SiGe* alloy were investigated [2]. Since the parameters involved in the figure of merit are, generally, strongly dependent on temperature, a specific semiconductor compound is optimized only around a specific temperature range. Another important parameter is the melting point of a specific material as it is necessary to operate at high temperatures in order to achieve high thermoelectric conversion efficiencies [6]. This last requirement is not only imposed to the thermoelectric material used but also to the other materials used in the application, like the pellet interconnection tabs, solder and TE interface plates.

Bulk *Si* has a very high thermal conductivity, which translates into a very poor *ZT*. However, it has been demonstrated that the thermal conductivity can be reduced via nano-

structuring. Also, the main thermoelectric parameters can be modified changing both the dopant concentration and the dopant species [7].

Bismuth Telluride, Bi_2Te_3, has been used for many years for power generation and power cooling at low temperatures and it is probably the most commonly used material for thermoelectric applications. Most cooling applications are required to operate at around room temperatures making this material an optimum candidate for these applications. This material presents good thermoelectric properties for power generation at temperatures up to about 400 *K*, although they are routinely used up to 620 *K*. Even though the peak performance is reached at temperatures below 400 *K*, the power generated still increases with temperature. Bulk Bi_2Te_3 alloys like the *p*-type $Bi_xSb_{2-x}Te_3$ and *n*-type $Bi_2Te_{1-x}Se_x$ have *ZT* values around 1 [8] although nanostructured bismuth telluride based materials have shown *ZT* values higher than 1. To put the performance in context, a 40 *mm* x 40 *mm* Bi_2Te_3 TEG can generate 15 W_{el} of electrical power (10 kW_{el}/m^2). A solar cell of the same physical size will generate about 0.3 W_{el} (about 180 W/m^2); 50 times greater energy output per unit area, albeit with a higher heat flux.

Group-IV tellurides, like *PbTe*, *GeTe* or *SnTe* as well as alloys like $AgSbTe_2$, are used in mid-temperature range applications, between 400 *K* and 900 *K*, approximately, and have shown values of $ZT > 1$ for both *n* and *p*-type materials [9].

Zinc antimony, Zn_4Sb_3, has been reported as one of the most efficient thermoelectric materials with a relatively high *ZT* in the range of 450 *K* to 670 *K*, with a reported value of $ZT = 1.3$ at 670 *K* [9].

Silicon-Germanium, *SiGe*, and alloys are used in high temperature applications (> 900 *K*), like in the case of RTGs, both for *n* and *p*-type materials. They present good mechanical properties although the *ZT* is relatively low, below 1, due to the high thermal conductivity of the structure of the *p*-type material [9], [10], see Figure 2–2.

Polymer-based (conductive polymers) TEGs are non-toxic flexible plastic materials that are easily manufactured and are mainly used for both implantable and wearable medical applications. Some polymer-based materials have reported a *ZT* value of 0.42 [2].

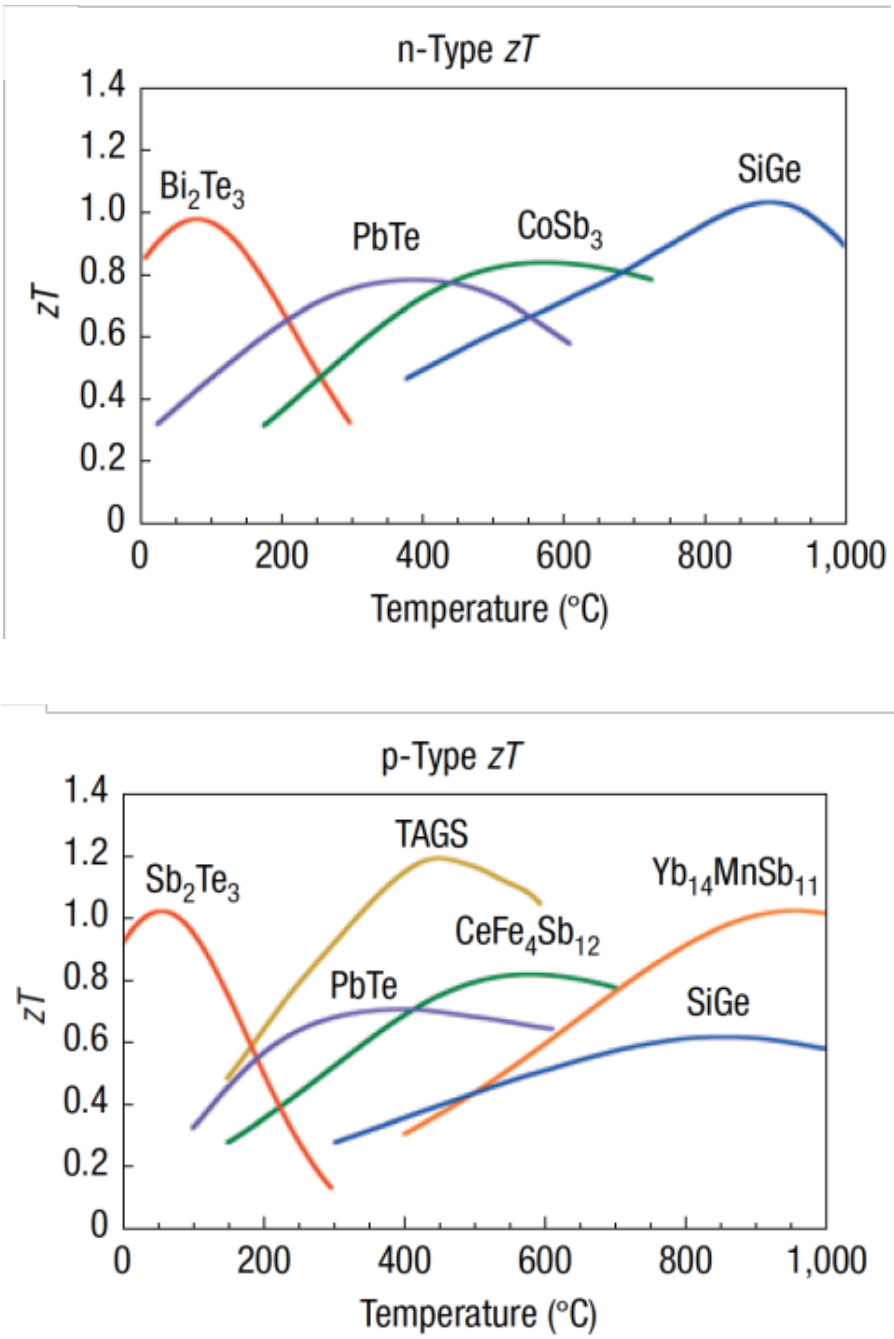

Figure 2–2 *ZT* for some *n* and *p*-type materials. Credit: Snyder G.J., Toberer E.S., Complex thermoelectric materials. Nature Materials, vol. 7, 105-114 (2008).

Figure 2–3 shows the progress in reported *ZT* values of bulk materials over time. Values of *ZT* for bulk materials are quite limited as shown in Figure 2–3, where it can be seen that the maximum value of *ZT* is around 1.

High *ZT*-materials have been discovered although high efficiency has only been proven in laboratory experiments. High *ZT* materials have been developed through nanostructure techniques and these materials are prohibitively expensive for commercial applications

[11]. The reported progression of high *ZT*-materials is shown in Figure 2–4 [12], with values of *ZT* of 2.7, approximately, being the state-of-the-art as of 2010.

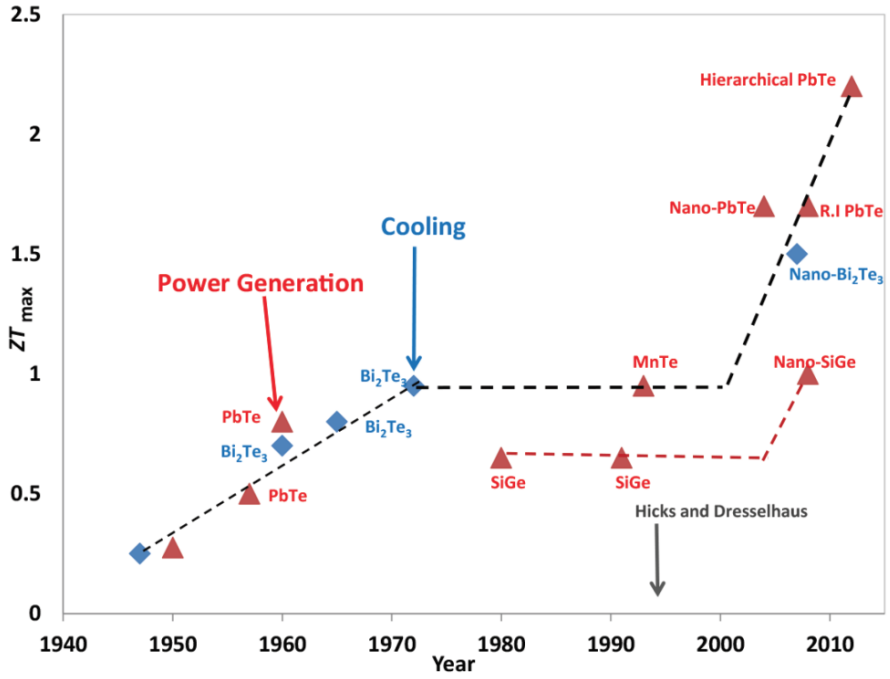

Figure 2–3 Progress in reported *ZT* values, of bulk materials, over time. Credit: Reprinted from Macmillan Publisher Ltd, Nature Technology.

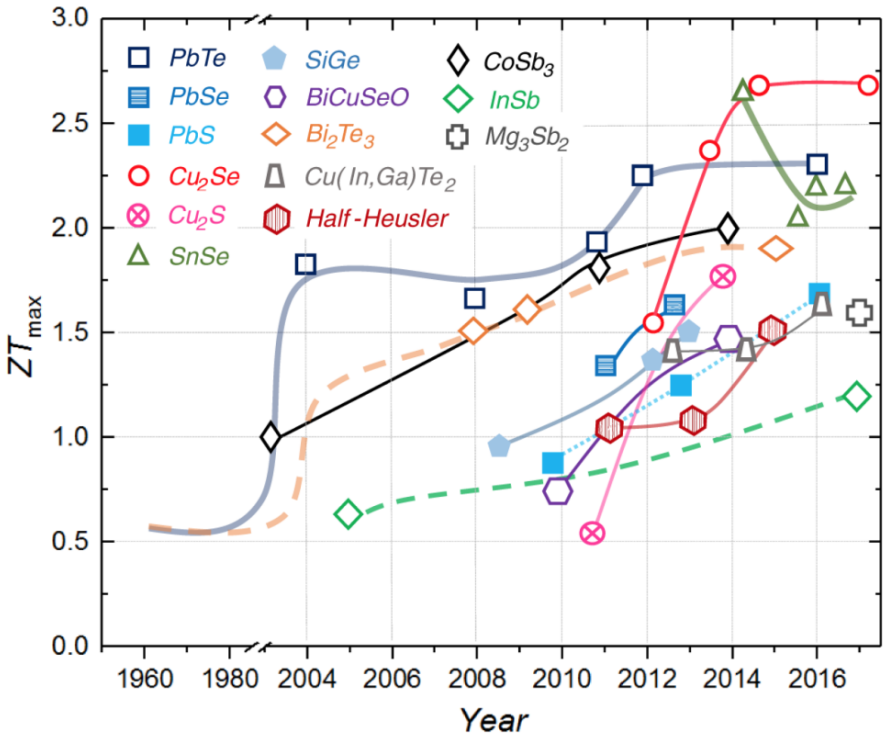

Figure 2–4 Progress in reported high *ZT*-materials over time. Credit: J. He, T.M. Tritt, Science 357 eaak9997 (2017). DOI:10.1126/science.aak9997

As shown in Figure 2–2 the various existing thermoelectric materials exhibit distinct properties and, therefore, behave differently under diverse operating conditions. Such differences in the material performance are manifested with the exhibition of the peak value of *ZT* at different temperature gradients. An important requirement on the *p* and *n*-type materials is that both must exhibit their peak value of *ZT* at the same, or very similar, temperature gradient [13].

Bismuth tellurides/selenides are optimized for low temperature applications (lower than 250 ^{o}C). Organic materials are also used in applications with a temperature lower than 130 ^{o}C [14].

Chalcogenides materials, group to which Bi_2Te_3, Bi_2Se_3, *PbTe* and *TAGS*, amongst others, skutterudites, silicides and half-Heuslers show the best performance in low and mid temperature range applications (between 250 ^{o}C and 650 ^{o}C). Chalcogenides materials contain one or more chalcogen elements such as *S*, *Se* or *Te*. Tellurium is a costly material due to its scarcity so it is often substituted by *Se*. Skutterudites are compounds that are made combining a transition metal and pnictide elements, such as *P*, *Sb* and *As*. Skutterudites are represented by MX_3, where *M* is the transition metal and *X* the pnictide element [15]. Silicides are low cost materials that contain silicon. Despite silicon not being a good thermoelectric material, it is possible to improve its thermoelectric performance alloying it with a small amount of other components, like germanium [13]. Skutterudites and silicides are low cost materials that are optimized for mid temperature ranges [11]. Half-Heusler materials are intermetallic compounds with a simple cubic structure and TAGS are *Te-Ag-Ge-Sb* alloys.

Oxide materials are relatively low-cost materials that are optimized for high temperature applications [13]. They are also used for thin film thermoelectric devices.

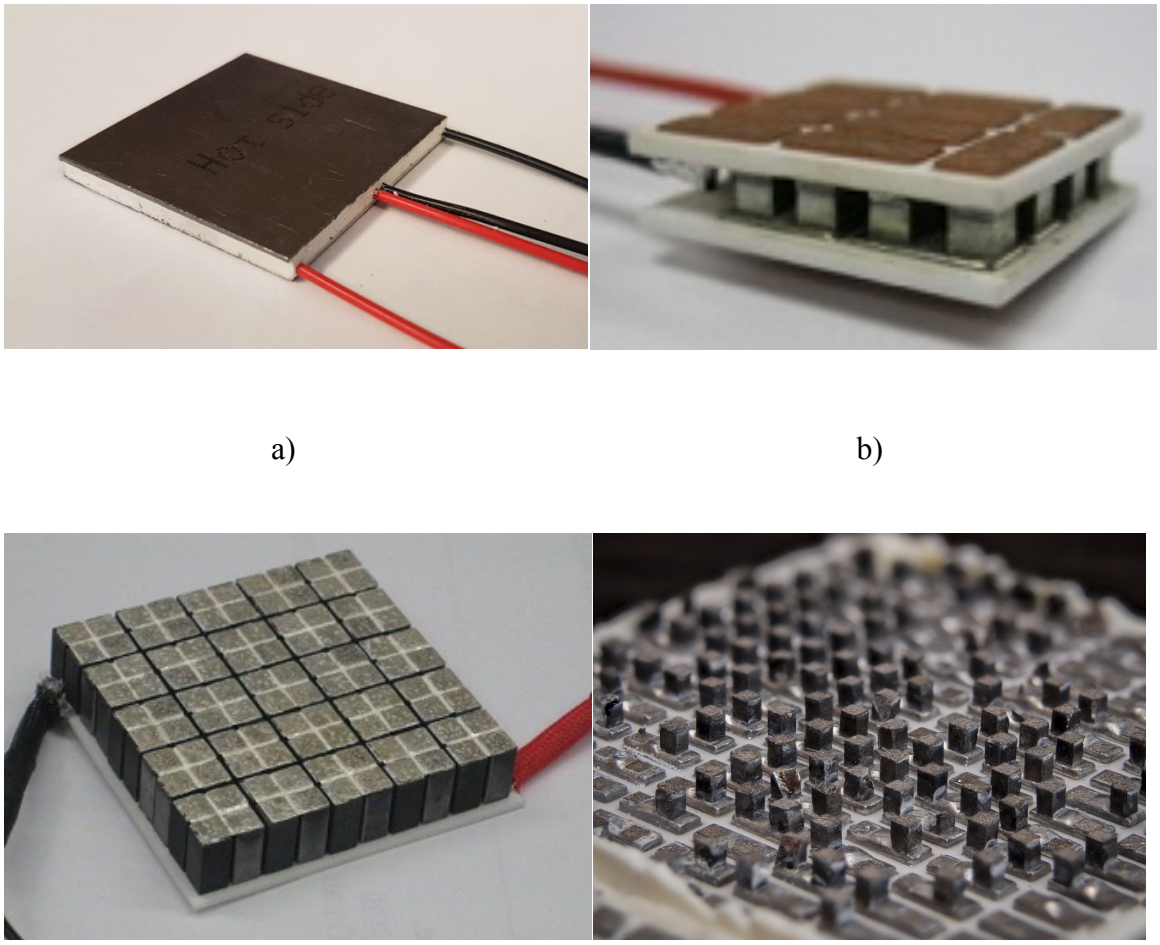

a) b)

c) d)

Figure 2–5 - Different TEG modules a) Bismuth-Telluride module with integrated open-circuit voltage sensing terminals. Credit: Thermoelectric Conversion Systems b) TAGS module. Credit: TECTEG MFR c) Oxide module. Credit: TECTEG MFR d) Internal arrangement of thermoelectric pellets inside a TEG module.

2.3 Thermoelectric applications

Thermoelectric materials present relatively low efficiency and high cost per electrical Watt, W_{el}, when compared with other technologies, like photovoltaic. This is one of the reasons why the use of thermoelectric technology has been limited to mainly the military and aerospace industry, where cost and efficiency are not always the main drivers and alternative sources of energy are sometimes required. Thermoelectric devices do however present many advantages as power sources. The lack of moving parts makes them robust, reliable as well as silent and vibration free. They are also a source of emissions-free power that requires very little maintenance.

2.3.1 Space applications

Solar cells represent the main source of power in satellite applications and, for most missions, solar power represents the most effective source of power. The main deficiency of solar power is that the specific power, measured in Watts per kilogram, decreases at a rate of $1/R^2$ being R the distance from the sun. RTGs (radioisotope thermoelectric generators) use radioisotopic power, which employs radioactive decay to produce heat that is transferred to thermoelectric modules [16]. RTGs are mainly used in interplanetary and deep space missions, where the deficiency of solar power makes PV fall behind thermoelectric technology. The schematic diagram of an RTG is shown in Figure 2–6 [17].

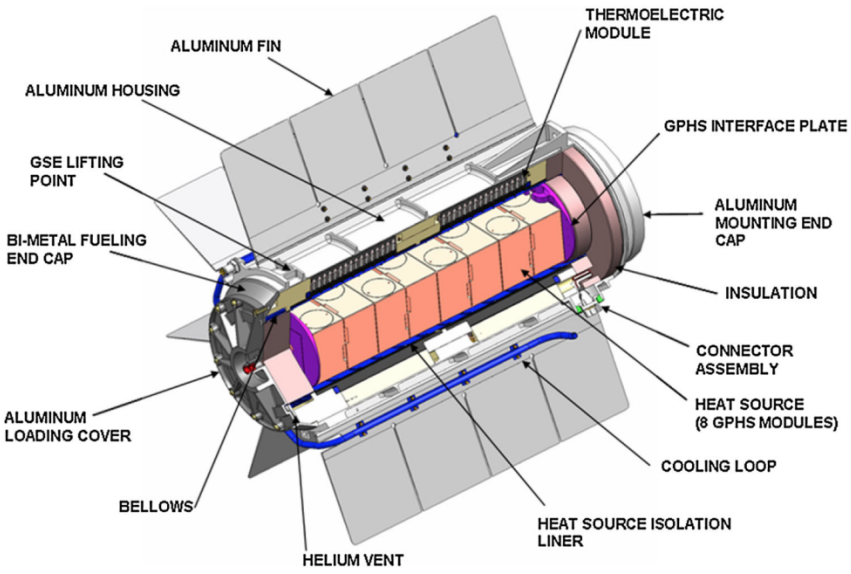

Figure 2–6 Schematic diagram of an RTG. (Reproduced with permission of [17]**, Copyright 2015, Springer US.**

In 1961 the US Navy deployed the Transit-4 satellite, the first satellite that used an RTG, the SNAP-3B, which was designed to operate for a period of over 5 years. It used Plutonium-238 as radioactive material and 27 spring-loaded pairs of thermoelectric elements connected in series. The thermoelectric elements were made of *PbTe* and operated at 336 *K* and 783 *K* at the cold and hot junctions, respectively. The system weighed 2.1 *kg* and offered an overall conversion efficiency between 5 *%* and 6 *%* [16].

In 1977 the two *Voyager-1* and *Voyager-2* spacecraft were launched to conduct studies of the satellites, magnetospheres and interplanetary medium of Jupiter and Saturn. To power these two satellites the Multi-Hundred Watt Radioisotope Thermoelectric Generator

(MHW-RTG) was used, with an average mass of 37.69 *kg* [18]. The heat source contained 24 pressed plutonium oxide fuel spheres and the conversion to electric power was performed using 312 *SiGe* thermoelectric couples. The cold and hot junction temperatures were 573 *K* and 1273 *K*, respectively. The RTG was capable of generating 158 W_{el} at the beginning of the mission (BOM). The *Voyager* missions were successfully completed by the end of 1989, although NASA designed the *Voyager Interstellar Mission* (VIM), a mission that would increase the mission lifetime of the *Voyager-2* spacecraft due to the healthy operation of the scientific instruments. The RTG has the capability to continue generating adequate power until 2020 [19].

RTGs have also been used to power missions to Mars. In 1975 the *Viking-1* and *Viking-2* were launched, with the lander craft landing on the surface of Mars about a year later; and it was powered from two SNAP-19 RTGs. These RTGs used plutonium-238 to provide the heat and 6 modules with 15 thermoelectric couples on each module. The couples were made of TAGS-85 for the *p*-type legs and TEGS-2N with a thin layer of *PbTe* (on the hot side) for the *n*-type legs. Each RTG provided a minimum of 35 W_{el} throughout the 90 days mission [16]. The *Viking-1* operated for 6 years until the lander was shut down, and the *Viking-2* operated for 4 years, until the relay link was lost.

In June 2003 *Aerojet Rocketdyne*[1] and *Teledyne Energy Systems*[2] collaborated in the development of the multi-mission RTG (MMRTG), which would be first used in the *Curiosity* mission to Mars. The design was based on the SNAP-19, also developed by Teledyne Energy Systems. The general-purpose heat source (GPHS) used in the SNAP-19 RTG is also used in the MMRTG (plutonium-238). It was originally designed to generate 100 W_{el} at beginning of life (BOL) and a specific power of around 2.8 W_{el}/kg. The first flight on board the Curiosity was capable of producing, at BOL, 120 W_{el}. One year after it was launched, and before it began to descend towards the surface of Mars, in 2012, the MMRTG was capable of generating 107 W_{el}. The power generation by the MMRTG throughout the mission can be seen in Figure 2–7 a). The fluctuations in power are due to the changes in electric loading of the generator whereas the overall decline of the average power is due to the degradation of the Pu-238 and performance of the TE material and interfaces [17].

[1] www.rocket.com

[2] www.teledynees.com

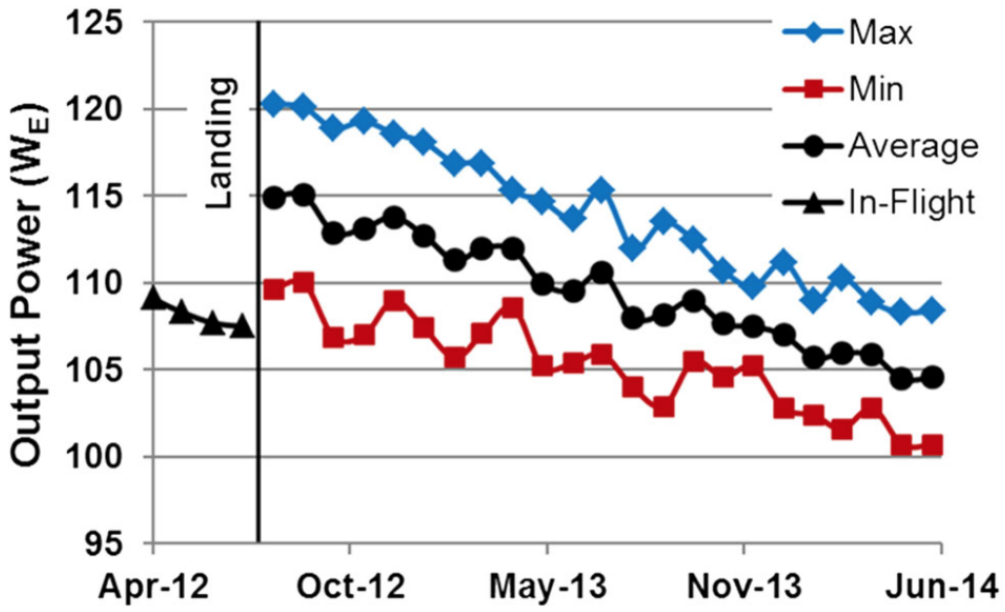

a)

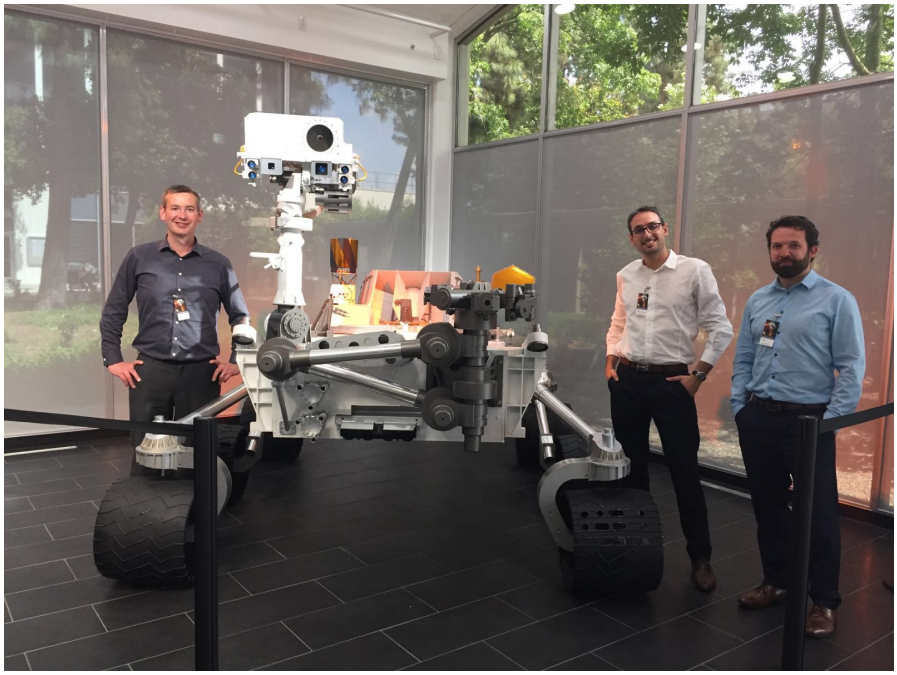

b)

Figure 2–7 a) Power generated by *Curiosity* from launch until June 2014. Credit: Holgate T.C., Bennett R., Hammel T., Caillat T., Keyser S., Sievers B. Increasing the efficiency of the Multi-mission Radioisotope Thermoelectric Generator. *Journal of electronic materials*, Vol. 44, No. 6, 2015. b) Author of this thesis (center) with the model of *Curiosity* at the NASA Jet Propulsion Laboratory in California (2016)

2.3.2 Automotive applications

Combustion engines present efficiencies that are, typically, below 30 % due to the losses across the entire vehicle system. Around 40 % of the combustion energy is dissipated as waste heat [10] in the exhaust, and a large amount of research has been done to convert this rejected energy into electricity.

In a typical TEG system for automotive applications, the TE elements are coupled to the exhaust of the car through a heat exchanger, which serves as the hot side. The TE elements are coupled to the cold side using also a heat exchanger and the cold side block can be refrigerated using air coolers, water or the engine coolant.

Chuang and Chau [20] uses a TEG system that harvests power from the heat conveyed by the exhaust gas. The power converter topology is a *Cúk* converter that it is used to charge a battery. The choice of this topology lies on the continuous input and output current, which reduces the disturbances to the TEG and the battery. The MPPT control is based on Perturb & Observe.

Champier [14] presents different research results on TEG applications. In 2011 a TEG prototype was mounted on the exhaust of a BMW X6. The prototype was water-cooled and produced about 600 W_{el} at a speed of about 125 *km/h*, which is translated into a fuel gain of about 1.2 %[3].

Brignone and Ziggiotti [21] presented in 2012 a study explaining the improvements that can be achieved by using TEGs in automobiles. With TEGs having a *ZT* of 1-1.2 it is possible to get an overall system efficiency of 4-5 %, which translates into the generation of 400-500 W_{el} with small-medium gasoline engines driven in motorway conditions. Under these conditions a reduction of about 6-7 *g/km* of CO_2 can be achieved.

In 2013 Tatarinov *et al.* [22] presented the results of a simulated model of a compact car indicating fuel savings of about 5 % for electrical power outputs of 409 W_{el}. The same year Kumar *et al.* [23] presented a model for automotive waste heat recovery systems. They showed that the electrical generated power is a strong function of the flow rate and inlet exhaust temperature. A second work presented by the same authors [24] presents an

[3]No attempt was made to use this power on the vehicle due to the very low voltage and very high current produced by the TEG array

evaluation of different parameters, like the geometry of the heat exchanger and the TEG module configuration, on the TEG performance.

Liu *et al*. [25] present a TEG system using four Bi_2Te_3 modules. The output power of the system was measured at revolution rates between 2700 and 3200 *rpm*. The highest output power of a single module occurs at 3200 *rpm* with an output power equal to 183.24 W_{el} and an average temperature difference of 235 ^oC. The maximum output power of the four TEG system was equal to 390 W_{el} with an average temperature difference of 133 ^oC.

Kütt and Lehtonen [26] stated in 2015 that the highest efficiency number presented to date for simulations of TEG systems reached over 5 *%*, and that TEG systems have reported maximum efficiency numbers of 5 *%*.

Brito *et al*. [27] showed in 2015, in an application for waste heat in exhaust systems, that the use of heat pipes has significant advantages as it passively helps providing constant operating temperatures.

In 2018 Huang *et al.* [28] presented an improved design for a concentric cylindrical TEG system that uses heat pipes to improve the heat transfer in the radial direction. The novel approach of this design is that it is the cooling water that flows inside the TEG system, as opposed to the exhaust gas. The temperature difference across the TEGs is optimum for Bi_2Te_3 modules, which are used in the proposed system. The results presented in this article show an increase of 86.2 *K* across the TEGs, which translates into an increase of output power of 25 W_{el}, with respect to the gas-inside design.

Similar to the work presented by Kumar *et al*., Wang et al. [29] presented a TEG model where the exhaust gas of a vehicle is used for the heat source. The work presented includes impact of different parameters like the temperature and mass flow rate of both the exhaust gas and the cooling fluid, the convection heat transfer coefficient, the pellets dimension and the ratio of the load to the internal resistance of the TEG. The generated power and efficiency of the TEG are plotted against different values of the different parameters described before. Trade-offs are then made. Many other studies found in the literature are devoted to improvements of the heat exchangers, modeling the gas flow within the exhaust, the dimension of the thermoelectric pellets and the geometry of the overall system, amongst others [30]–[33].

2.3.3 Stove applications

The electricity grid does not reach all the populated areas in many countries, leaving certain areas in different countries without access to the electricity provided by the grid. Houses in those areas have to find electricity using alternative sources. Photovoltaic technology is the most popular source of off-the-grid electricity but in some areas, where the number of hours of sunlight is scarce, this technology might not be the most suitable solution. In other cases, waste heat produced by fossil sources can be harvested to produce electricity. There are several factors that influence the cost of off-grid energy production such as the initial capital costs of the system, maintenance and fuel costs. Thermoelectric devices do not require fossil fuels to produce electricity. Instead, household waste heat can be used for energy production.

In 1996 Killander and Bass [34] presented an application of TEG systems to supply electricity in rural areas in northern Sweden. The system used a TEG system on a stove-top. The system was capable of producing up to 10 W_{el} using two 75x75 *mm* TEGs, although the electrical efficiency of the system was very poor as the system used a heat-sink cooled using a 2.2 W_{el} fan.

Min and Rowe [35] presented a "symbiotic" application where a TEG is used to generate electricity from the heating process of a fluid. The TEG is connected between the outlet and inlet of the fluid heater. Part of the heat energy contained within the hot fluid, coming out of the hot liquid outlet, is converted into electricity by the TEG. The energy leaving the cold side of the TEG is returned into the cold water at the heater inlet, rather than being lost in the environment.

In 2005 Rida *et al.* [36] presented a design of a stove based TEG system cooled by convection using a heat-sink. The output power using two TEGs is around 8 W_{el}, which is comparable to the work presented in [34] without the need of a fan.

Favarel *et al.*[37] presented a design of a TEG system for a stove application using eight 56 *x* 56 mm^2 Bi_2Te_3 TEGs. The TEGs were cooled using domestic water stored in a water tank so that it was pre-heated thus reducing the amount of energy required by the domestic heating system. The TEGs are driven with a ΔT of around 150 *K* and they produce around 28 W_{el}. The system uses a fan to extract the gases out of the heating system, which consumes 15 W_{el}. The power output is 0.11 W_{el}/cm^2.

In 2010 Rinalde *et al*. [38] proposed a thermoelectric generator system for electrification of rural areas. The thermoelectric devices are coupled to a firewood stove to harvest energy from the residual heat thrown away. This work presents the importance of the thermal contact resistance with the generated output power, and proposes the use of springs to provide constant and almost uniform pressure.

In 2011 Champier *et al*. [39] presented a study to produce electricity in a wood stove. A single TEG is able to produce up to 9.5 W_{el} when it is operated at the MPP using a switching regulator. The output power is used to charge a 6.7 V nominal voltage battery.

Later in 2015, Montecucco *et al*. [40], [41] developed a similar TEG system to the one presented in [37] for a solid-fuel stove. Four 40x40 mm^2 Bi_2Te_3 TEGs were used with each one individually cooled with a water-cooled block. The water blocks also used domestic water that was stored in an insulated water tank. The system produced a peak power of 42 W_{el} with a ΔT across the TEGs of around 250 K, with an average power production of 27 W_{el}. This is equivalent to 0.42 W_{el}/cm^2, which shows an improvement with respect the work presented in [37]. The thermal-to-electrical efficiency was calculated to be between 4 % and 5 % transferring around 582 W_{th} to the water tank. The pump used to re-circulate the water from the tank to the water blocks, and back to the water tank, consumed 8 W_{el}.

Codecasa *et al*. [42] presented a TEG system that is coupled onto a self-standing natural combustion gas stove. The purpose is to feed a fan convector to improve heating efficiency from 85 % to 91 % as well as powering the safety and control devices. The system comprised two TEGs connected in series working with a ΔT of 104 K. The system produced 2.75 W_{el}, with an estimated heat power across the TEG of approximately 60 W_{th}, which was enough to power the fan, consuming 1 W_{el}, leaving 1.6 W_{el} to power other functions.

Shaughnessy et al. [43] used TEGs on cooking stoves in a rural community in Malawi. The users of the cooking stoves were able to charge their mobile phones, lights and radios. The power generated was in excess compared to the required electric power, which represents a daily average of 3 Wh.

2.3.4 Low power applications

Technological advances have given rise to the development of low power consumption devices and small TEGs can provide enough energy to power these devices, even when operated at low temperature gradients. In some applications, such as animal tracking sensors, access to the battery can be very difficult. In other specific applications, *e.g.*, implantable medical sensors, battery replacement, or even the use of a battery, might not be an option. The typical power consumption of implantable medical sensors is in the order of micro-watts and small wearable TEGs are capable of producing enough energy to power them using human body heat. The main problem when dealing with such low power outputs is that the voltage delivered by the TEG is usually in the order of few tens of millivolts, presenting a technological challenge to the development of electronic circuits that can operate with such low input voltages. Low voltage start-up conditions and relatively high efficiencies are required for power harvesting with such low output power sources.

Damaschke [44] presented in 1997 a self-starting DC/DC converter, for low-grade exhaust heat energy, to power instrumentation electronics. The temperature difference in this application can be as low as 20 K and Bi_2Te_3 TEGs were used, which were capable of producing an open-circuit voltage of around 300 mV. The converter was designed to produce a 5 V regulated output voltage and it could supply up to 131 mW_{el} to the output load, presenting an efficiency of 76 %.

In 2010 Carlson *et al*. [45] presented the design of a power converter to be implemented in a 0.13 μm CMOS technology integrated circuit. It operated with an input voltage range between 20 mV to 250 mV to supply a 10 μW_{el} load at 1 V regulated output. The power converter consumed 1.6 μW_{el} of quiescent power at 20 mV input voltage, being capable of delivering up to 25 μW_{el} presenting an efficiency of 46 %. The performance of the power converter increases at 100 mV input power, with a quiescent power of only 1.1 μW_{el}, power delivery of up to 175 μW_{el} and an efficiency of 75 %.

In 2011 Ramadass *et al*. [46] developed a battery-less body-heat energy harvester for thermoelectric devices implemented in a 0.35 μm CMOS technology integrated circuit. The system used the mechanical body vibrations to produce energy for the start-up circuit. The circuit was capable to start-up with input voltage as low as 35 mV, but once started could operate with 25 mV at the input, and used a capacitor to store the energy produced by the

TEG. The output was regulated to 1.8 V by an additional step-down power converter. The reported end-to-end efficiency of the converter was 58 %.

In 2012 Jong-Pil *et al*. [47] presented their work on a micro-watt energy harvester capable of self-starting with an input voltage of 40 mV. The start-up condition is achieved using a resonant transformer that produces a resonant peak voltage higher than the TEG input voltage. The resonant waveform is then rectified and the voltage is used to start-up the power converter. The converter produces a 2 V regulated output presenting a maximum efficiency of 61 % achieved with an input voltage of 300 mV.

Shuttleworth and Simpson [48] present the design of a step-up converter for a 60-400 mV thermoelectric energy harvesting source. The peak efficiency of the converter is 72 % and the highest load matching error occurs at an open-circuit voltage of 400 mV, which lowers the generated input power by 0.56 %.

2.3.5 Other TEG applications

Buckle et al. [49] presented a model and simulation results for a TEG system to be integrated into an autonomous underwater vehicle (AUV). The systems implements a heat store that is insulated from the rest of the AUV body and the TEG is placed between the heat store block and the water, without using any heat exchanger. The TEG system generates electrical energy from the thermal gradient generated between the heat store block and the temperature of the water. The results presented show an energy production of almost 4500 J per day, assuming 20 dives per day, when the energy storage mass is equal to 250 kg and the system uses 25 TEGs, and almost 45000 J with 500 TEGs.

Ebling *et al*. [50] presented an application to recover heat, that would otherwise be lost in the environment, from a steel plant. The forged parts produced in the plant can reach temperature as high as 1300 ^oC, which are then cooled to room temperature. Using 50 bismuth telluride TEGs the system is capable of absorbing up to 4.8 kW_{th} of radiated heat power and generate 388 W_{el} into the power grid.

Aranguren *et al*. [51] proposed an application where 48 TEGs, covering an area of 0.25 m^2, have been used to generate power from the heat released by an exhaust combustion chamber. The system was capable of producing up to 21.56 W_{el} of net power, which is

equivalent to an approximate power density of 100 W_{el}/m^2, with an input heat power of 150 kW_{th}. The maximum temperature of the exhaust gas in this application is equal to 800 ^oC.

Merotto *et al*. [52] present an application where TEGs are used to generate energy in a catalytic combustor for portable power generation. The proposed device is capable of producing 9.86 W_{el} with an efficiency of 2.85 %.

Min and Yatim [53] presented a thermal resistor based on the Peltier effect. This work states that the relationship between the heat flux and the temperature difference, in a thermoelectric module, can be controlled by an external resistor connected to the output of the device.

2.3.6 Optimization of thermoelectric modules

Most research on thermoelectric materials is focused on finding materials with a higher figure of merit. For power generation, materials with a higher Seebeck coefficient and lower thermal conductivity are desired to increase the output voltage of thermoelectric modules. Lower internal resistance can be achieved if the electrical conductivity of a given material is increased. Most of these improvements are done at microscopic level by changing the internal structure of the thermoelectric materials.

In any case, there are also improvements in efficiency and power generation capability at macroscopic level. These changes involve appropriate sizing of the thermoelectric pellets. The length and area of the pellets have an important influence on the thermal and electrical properties of the device. The pellets packing factor, defined as the ratio of surface area of thermoelectric material over the total area of the device, also has an influence on the performance of the thermoelectric module.

Rezania *et al*. [54] studied the influence of changing the ratio between the area of the *n*-type pellet to the area of the *p*-type pellet, for a fixed pellet length of 2 *mm* and a total fixed area of the two pellets equal to 8 mm^2. It is shown how the temperature across the *n*-type pellet is lower than on the *p*-type because of the higher thermal conductivity of *n*-type materials. It states that, although the Seebeck coefficient increases slightly with the footprint ratio, the voltage generation is largely dominated by the temperature difference across the pellets. For that reason, increasing the footprint ratio of the *n*-type pellet over the *p*-type one will decrease the overall voltage generation due to the lower temperature

gradient. Under these circumstances the power generation also decreases. Also, the lower the ratio the lower the thermal conductivity and, therefore, the output voltage increases due to a higher temperature gradient across the pellets. Decreasing too much the ratio produces an increase of the electrical resistance, which translates into a lower power generation. The results presented in [54] show that the maximum power generation occurs at a ratio lower than 1 ($A_N/A_P < 1$) due to the lower electrical resistance and higher thermal conductivity of the *n*-type material under consideration.

Montecucco *et al*. [55] developed a simulation tool for thermoelectric generators operating under constant heat flux as well as for geometrical optimization of the devices. Firstly, a simulation is performed varying the number of pellets and the clearance between them. It is shown that the same performance can be obtained for different combinations of the two parameters. Montecucco suggests that high power can be obtained with large pellets if there is enough clearance between the pellets, which is required to decrease the thermal conductivity of the device. By doing so, TEGs with low voltage and high currents are obtained, although they are not very interesting for power electronics conditioning circuits. On the other hand, it is shown that longer pellets help reducing the thermal conductivity of the device although the internal resistance increases, decreasing the output current capability. Secondly, a simulation is performed varying the height of the pellets and the fill factor, where it is shown that the maximum performance can be obtained, again, for different combinations of the two varying parameters. From an economic point of view, the minimum thermoelectric volume is achieved with short pellets and low fill factor while the maximum volume corresponds to long pellets and high fill factor. The difference in volume is an order of magnitude but the performance of the modules is very similar.

Rowe and Min [56] present a realistic estimate of the conversion efficiency of a thermoelectric module that is based on the power output and its relationship with the contact properties. They show that the conversion efficiency is improved by operating at higher temperature differences and/or increasing the length of the pellets. However, the maximum power output will decrease if a longer pellet is used. This result is in agreement with that presented in [55]. Based on this analysis the “manufacture quality factor” (MQF) is obtained, which is based on the selection of contact materials, the formation of electrical junctions and thermal contact layers. In other words, given a fixed geometry of the pellets used in the device, a given thermoelectric material and a given temperature regime, the performance of the device will depend on the quality of the manufacturing process. The MQF gives an idea of the quality of the manufacturing process for TEGs made of the same

thermoelectric material and having the same geometry. Rowe and Min state that TEG systems are economically viable when the mean time before failure of the system is in the order of ten years. In this scenario, the MQF is a good indicator for the appropriate selection of a given manufacturer for the TEGs.

2.4 Maximum power generation

The operating point of a TEG is not only dictated by the temperature gradient across the TEG but also by the current and voltage at the device terminals. For each value of temperature difference ΔT across the device a unique voltage-current behaviour is associated to it. This unique relationship corresponds to a parabolic power function as shown in Equation (**2-2**). Figure 2–8 a) shows the voltage and power curves of a GM250-127-14-10 thermoelectric module, from European Thermodynamics Ltd, for three different values of ΔT: 100 ^{o}C, 150^{o}C and 200 ^{o}C. The characteristic parabolic power response a thermoelectric device presents, for each value of ΔT, a single point where the output power is at its maximum. This point corresponds to the maxima of the power curve. Photovoltaic cells present a logarithmic current-voltage response as shown in Figure 2–8 b) (red curve) and a power-voltage response (blue curve) that also presents a maxima which corresponds to the maximum power output of the PV cell. This point is known as the maximum power point, or MPP.

In power generation applications it is important to operate at the maximum power point so that the maximum power available by the source is extracted at any given moment of time. This principle applies to both TEGs and solar cells.

$$P_{TEG} = V^2 \cdot \frac{R_L}{(R_{INT} + R_L)^2} = \alpha^2 \cdot \Delta T^2 \cdot \frac{R_L}{(R_{INT} + R_L)^2} \quad (2\text{-}2)$$

Where R_L is the load resistance and R_{INT} the internal resistance of the TEG

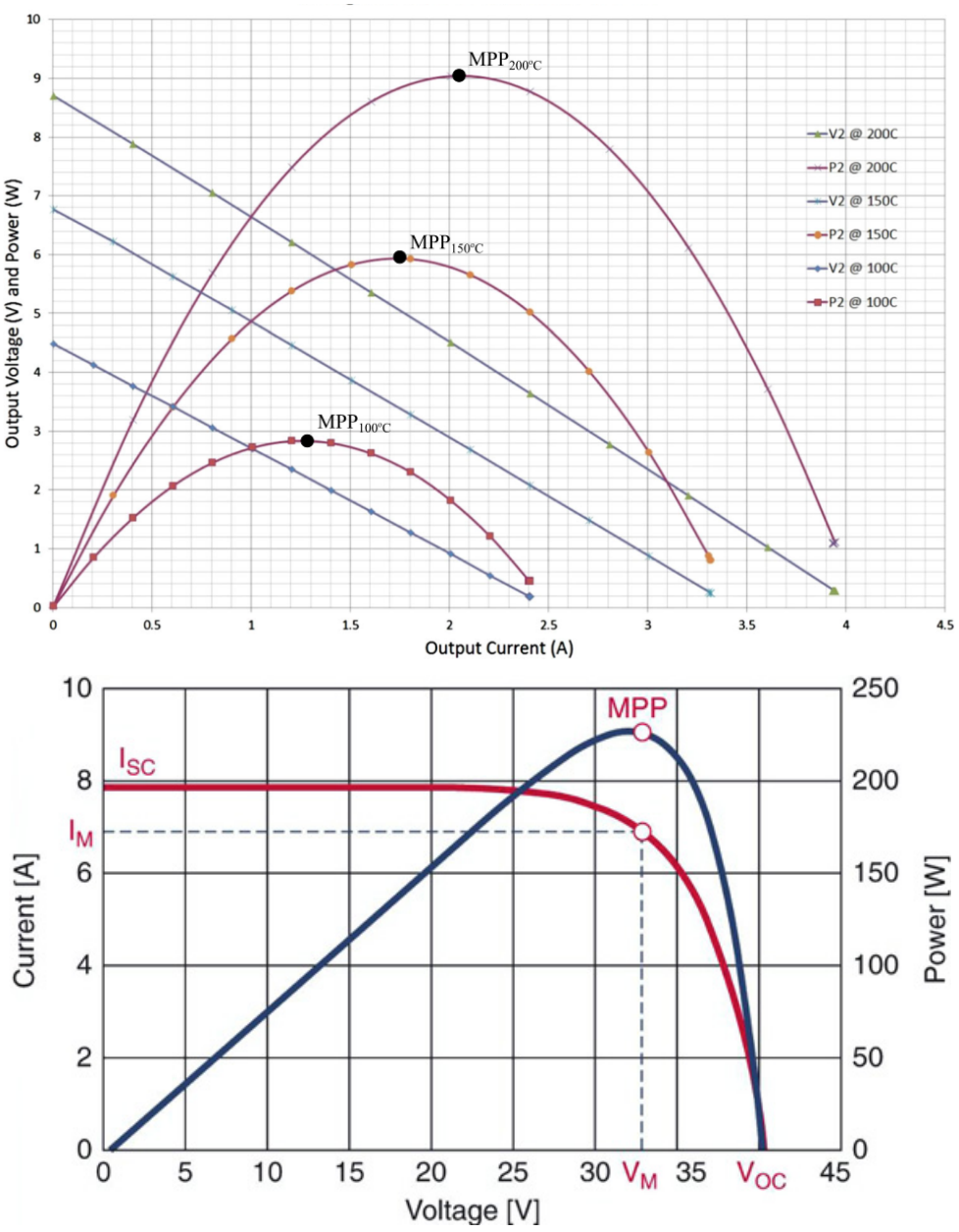

Figure 2–8 Voltage and power versus current a) GM250-127-14-10[4] thermoelectric module. Credit: O. Maganga, N. Phillip, K.J. Burnham, A. Montecucco, J. Siviter, A. Knox and K. Simpson. Hardware implementation of Maximum Power Point Tracking for Thermoelectric Generators. Journal of Electronic Materials. DOI: 10.1007/s11664-014-3046-0. 2014. b) Current-Voltage (red trace) and Power-Voltage (blue trace) characteristic curves of a photovoltaic cell

When a TEG is operated under a constant temperature gradient ΔT, the MPP is reached when the load impedance matches the internal impedance of the TEG, as dictated by the *maximum power transfer theorem*; that is, $R_L = R_{INT}$ [57], [58]. As a result of this theorem, and in order to operate at the MPP, the load connected to the output has to be equal in

[4] European Thermodynamics Ltd.

value to the internal resistance of the TEG. When operated under this condition, the voltage observed at the output terminals of the TEG will be equal to half of the open circuit voltage, as dictated by *Ohm* and second *Kirchoff* laws. Indeed, it can be observed in Figure 2–8 a) that the MPP lies in the middle of the power curve, where the output voltage is half of the open-circuit voltage, and the output current is half of the short-circuit current.

The power generated when the TEG operates at the MPP, or P_{MPP}, is dictated by Equation (**2-3**).

$$P_{TEG,MPP} = V^2 \cdot \frac{R_L}{(R_{INT} + R_L)^2} = \frac{\alpha^2 \cdot \Delta T^2}{4 \cdot R_{INT}} \tag{2-3}$$

On the other hand, the maximum efficiency is defined as the ratio between the output electrical power to the thermal input power to the TEG system. Under these conditions of constant temperature gradient, the point of maximum power generation is different from the point of maximum efficiency [59], [60]. From the thermal model point of view, Stevens [61] found that the MPP is found when the value of the equivalent thermal resistance of the TEG equals the value of the thermal resistances between the TEG and the hot source and heat-sink.

When the TEG operates under constant heat flux, the MPP is found when the load resistor is somewhat higher than the internal resistance of the TEG [62].

2.4.1 Maximum power point tracking techniques

The most efficient mechanism to generate power from a TEG, while being able to change its operating point so that it operates at the MPP, is the use of a DC/DC converter. With a DC/DC power converter it is possible to implement a control loop that controls the input voltage, the input current, or both. If the TEG is connected to the input of the power converter, the controlled variables become the TEG output voltage and TEG output current and the operating point can be controlled. This is a very common method used for battery charge regulators because, with the battery connected to the output, output voltage control is not required.

There are several power converter topologies being the most famous the buck [63] (or step-down converter), the boost [64] (or step-up converter), the SEPIC [65] (Single Ended Primary Inductor Converter) and the buck-boost converter [66]. The buck converter is used when the input voltage is higher than the output voltage and the boost converter when the input voltage is lower than output voltage. The SEPIC and buck-boost are topologies that are used whenever the input voltage is higher or lower than the output voltage.

There are different MPPT techniques used with TEGs, which are inherited from PV applications. The most famous techniques are *Perturb and Observe* (P&O), *Incremental Conductance* (INC) and *Fractional Open Circuit Voltage* (FOV).

P&O and INC are known as *hill climbing algorithms* because the operating point moves up and down the power curve around the MPP. In FOV, as the names indicates, the operating point is selected to be a fraction of the open-circuit voltage. A brief explanation of these methods can be found in [67], [68].

A similar method to FOV was presented by Garrigós *et al*. [69] whereby instead of measuring the open-circuit voltage in order to set the operating point, the current-voltage curve of the PV array was periodically scanned and the operating point was selected based on the peak power measured during the scanning process. The advantage of this method is that the inaccuracy inherent to the FOV method, due to variations in solar array characteristics, is overcome by the measurement of the instantaneous peak power. Another advantage of this method is that it can be implemented using only analog circuitry, which presents an advantage for high-reliability applications.

In P&O, the operating point of the TEG is perturbed to produce changes in the output power. If, as a consequence of the perturbation, the output power increases, the TEG is perturbed once again in the same direction. If, on the other hand, the output power decreases, then the TEG is perturbed in the opposite direction. This process is repeated until the MPP is found. At that point, the operating point of the TEG will oscillate around the MPP and the operation of the TEG and the power converter is considered to be in steady-state conditions. During these oscillations, the operating point moves away from the true MPP with a consequent decrease in power generation. In order to minimize the decrease in power generation the perturbation step size must be kept small.

Apart from the oscillations around the MPP, another disadvantage of P&O is the slow speed to find the MPP. This is particularly important in applications undergoing fast changes in input power. In order to increase the speed of P&O the step size must increase; which, on the other hand, increases the oscillations around the MPP.

These two problems are solved using INC. INC uses the relationship $dI/dV = -I/V$ to detect when the MPP has been reached and stop the perturbations. If the operating point lies to the left of the MPP, then $dI/dV > I/V$, and, if to the right, then $dI/dV < I/V$. INC can also respond faster than P&O to rapid changes in input power but it is somewhat more complex than P&O.

In order to perform these two types of MPPT methods, a processing unit is required, like a microcontroller, a DSP or an FPGA, and the algorithm is programmed in it. Analogue-to-Digital conversion is required to digitize the measured variables, usually voltage and current, so that they can be processed by the algorithm. In this sense, the circuitry required to perform P&O and INC becomes rather complex but it offers the flexibility of having a processor in the control circuit. Another advantage of these techniques is the high level of accuracy they provide in the control at the MPP.

FOV, on the other hand, presents a very simple method of performing MPPT. It exploits the fact that, when a TEG operates under constant ΔT, the MPP is found when the voltage at the terminals of the device is equal to half of the open-circuit voltage. This relationship holds for any value of ΔT across the device. The circuitry required to perform FOV is very simple and it can be implemented in analogue circuitry without the use of complex digital integrated circuits or processing units. The main disadvantage of this method is that, in order to measure the open-circuit voltage of the TEG it is necessary to disconnect it from the load. During the disconnection time, the TEG does not provide power to the load, which has an effect reducing the overall efficiency of the system. When this method is used under temperature changing conditions across the TEG, the accuracy will depend on the frequency at which the open-circuit voltage is sampled. The accuracy of FOV increases with the frequency at which the open-circuit voltage is sampled. However, as stated previously, the more frequent the open-circuit voltage is sampled, the lower the overall efficiency.

2.4.2 Maximum power point tracking in TEG applications

The most simple power conversion technique for battery charge applications, shown by Huang *et al.* [70], is the direct connection between the power source and the battery. The main disadvantage of this technique is that the operating point of the TEG is dictated by the battery voltage, and it varies with battery state of charge (SoC). [70] shows this technique using a TEG and defines it as *near MPPT* operation (nMPPO). The main advantage of using this technique is that a power converter is not required and the conversion efficiency is very high, taking into consideration the losses of the interconnections between the TEG and the battery and the power dissipated by the diode connected at the output of the TEG and required to avoid reverse current from the battery to the TEG. Huang *et al.* compare this technique with a conventional digitally implemented P&O using a SEPIC converter for a TEG power range between 3.2 W_{el} and 6.3 W_{el}. In this particular work, the low MPPT efficiency of the nMPPT is compensated by the high efficiency power transfer achieved by direct connection to the battery. Conventional P&O provides an overall efficiency in the range of 61.9 % to 80 %, taking into consideration the power losses of the SEPIC whereas the conversion efficiency of the nMPPT technique is in the range of 82.2 % to 89.3 %. A similar work was done by Kinsella *et al*. [71] but the nMPPT method is compared to both P&O and FOV, also using a SEPIC converter. This work provides a wider analysis than [70] and the MPPT methods are compared for different temperature gradients. It is shown that for temperatures above 120 ^oC, the impedance of the battery approaches the impedance of the TEG and the TEG operates very close to the theoretical MPP. Under these conditions, the connection of a power converter to the TEG would not provide any benefit and it would decrease the overall efficiency due to the converter losses. Below 120 ^oC, there is a considerable mismatch between the TEG and battery impedance and the overall efficiency is improved even when the power converter presents an efficiency of 85 %. In this study, the power delivered by the P&O and FOV algorithms are almost equal.

Many applications are intended for providing power to loads that require a regulated voltage. In those cases more than one converter is required, one to regulate the TEG at the MPP and a second one to regulate the output voltage. Kim *et al.* [72] used a power stage comprised of two cascaded converters. This is a common architecture that allows the control of both input and output voltages. The input converter controls the TEG at the MPP and the output converter is used to regulate the output voltage. A first circuit uses a boost converter to control the TEG voltage and a buck to regulate the output voltage. A second

circuit shows an equivalent topology where the TEG voltage is controlled using a SEPIC converter. The use of a SEPIC allows the control of a TEG voltage that is either higher or lower than the intermediate voltage. The main results showing the performance of the circuit are presented for the boost-buck case. The output voltage is controlled using linear PWM, which provides accurate voltage control whereas the TEG voltage uses a simple hysteretic control [73] using a single comparator. The main disadvantage of hysteretic control is that it produces variable frequency PWM, which produces wide spectrum EMI. The MPPT technique used is FOV, regulating the TEG voltage to half of the instantaneous open-circuit voltage. A circuit using three MOSFETs and two sample and hold capacitors is used to capture the target voltage that is used in the input voltage control circuit. The sampling frequency of the open-circuit voltage is 2.4 *Hz* with a sampling duration of 1 μs so that the short sampling time minimizes the loss of power generation during the sampling period. The results show that the TEG operates between 98 % and 100 % of the true MPP, around 116.4 W_{el}, even under sudden load changes using simple analog circuitry.

D. Schwartz [74] presented a simplified version of the circuit shown in [72] and it only uses the input power stage. The power stage is a SEPIC converter and it is controlled using linear PWM control, which produces fixed frequency PWM. The MPPT technique is also FOV, regulating the TEG voltage to half of the instantaneous open-circuit voltage. The sampling frequency is 2.5 *Hz* with a sampling time of 100 μs, which is equivalent to a loss of generated power almost a hundred times higher than in [72]. In any case, the relatively small sampling time translates into a loss of power generation of only 0.025 %. The maximum power generated by the input TEG is 2.3 W_{el} with a maximum voltage of 2.8 *V*. The converter is tested with two different loads of 5 Ω and 20 Ω, and it is shown how the input voltage control is almost independent of the output load.

Rae-Young and Jih-Sheng [75] present another boost-cascaded-buck converter for power generation in vehicle applications. The converters are implemented as three-phases interleaved converters, which helps to reduce the current ripple and provide current sharing between the phases. The application is developed to charge the vehicle battery and implements a two-loop control to switch between MPPT and battery end-of-charge (EoC) mode. The input voltage range is 0 to 25 V, depending on the temperature difference, and the converter needs to regulate the output voltage between 12.3 *V* and 16.5 *V*. The MPPT method used is a modified P&O, implemented using a DSP, that reduces the step size when the operating point approaches the MPP, which is an improvement with respect to normal P&O.

An application using a super-buck converter [76] is presented by Sun *et al.* in [77], which is designed for spacecraft applications. A super-buck converter is similar to the normal buck with the advantage of producing continuous current at both the input and the output of the converter. The MPPT control is implemented using a technique presented by [78] which is based on INC but it only requires analog components, providing higher reliability for space environments. The main components for the sampling and hold circuit are two comparators, a flip-flop and an integrator. The main disadvantage of this MPPT method is that the operating point of the TEG oscillates around two points and the true MPP is never reached. The prototype built is capable of processing 1 kW_{el} of power and is connected to a simulated TEG operating under constant temperature difference, which might differ from real space applications where the TEG operates under constant heat flux. The TEG voltage ripple when the circuit operates around the MPP is around 4 V when the MPP voltage is around 60 V.

Junling *et al*. [79] present a variable step size P&O implemented in a DSP using an interleaved boost converter as the main power stage. The power converter supplies power to charge a battery and it transitions between MPPT to constant battery voltage mode when the battery voltage reaches the EoC voltage. This work presents the difference in power generation between different connections of 32 TEGs. The more TEGs in parallel the lower the power output because the overall internal resistance decreases and there is a higher influence of the interconnection wires whereby there is more power being dissipated along those wires. Also, the higher the number of TEGs connected in parallel the higher the influence of mismatch between the different TEGs. A very important conclusion of the work presented in [79] is that the effect of the parasitic Peltier can deceive the decision of the P&O algorithm, providing steps in the wrong direction that contribute to an overall reduction in power generation.

Liu *et al*. [80] present a novel MPPT algorithm that combines FOV and P&O. The aim is to drive an array of TEGs at the MPP reducing the time it takes the TEG to reach an operating point close to the MPP at start-up, under variable temperature conditions. The first operating point is set to be 50 % of the instantaneous open-circuit voltage, and then a fixed step P&O MPPT control is applied. The experimental results show that the initial tracking speed of the algorithm is superior compared to a conventional fixed step P&O. The fixed step P&O, and the fact that FOV is only performed at start-up, translates into a slow algorithm under fast changing temperature conditions that occur after the power converter has started-up.

Carstens and Gühmann [81] propose a buck-boost converter for battery charge in vehicle applications. The buck-boost converter uses a capacitor between the buck and the boost stage that acts as an energy buffer between the two stages. The boost is connected to the input and controls the TEG at the MPP. The buck is connected to the output battery and acts as a link between the TEG and the battery bus of the system. The MPPT technique used is based on hill-climbing techniques, similar to P&O, with an adaptive step size that depends on the difference between the sampled power and the value sampled during the previous iteration. The algorithm produces three different step sizes depending on three different conditions, which minimizes the oscillations around the MPP while increases the speed of the tracking speed when the operating point is far from the MPP.

Some thermoelectric applications involve TEGs that are operated under very low temperature gradients, or they simply produce very little power. This is the case of energy harvesters used in wireless sensor networks or bio-medical applications, amongst other applications. Lowering the power consumption of the control electronics of the power converter or starting-up the converter with only few tens of millivolts are some of the challenges in this type of applications.

Complex algorithms require more computational power, which has an impact on the power consumption of the control circuit. In thermoelectric harvesting applications the power delivered by the TEG can be in the range of milliwatts, or even microwatts, and it is very important to minimize the complexity of the MPPT algorithm in order to maximize power generation. A similar issue is presented by the sensors required to monitor voltage, current and power, variables that are required in the decision making process of the algorithm. Power consumption of the control circuit increases with the number of sensors utilized, and some research has been done to reduce the number of sensors required. Bond and Park [82] developed a duty-cycle based MPPT scheme with power estimation based on duty-cycle measurements to estimate the power delivered by the TEG. The MPPT technique is a common P&O with the interesting peculiarity that the changes in power and current are measured by monitoring changes in the ON time of the converter. Nakayama and Koizumi [83] designed a boost converter that also uses the duty-cycle and the output voltage to calculate the input open circuit voltage, similar to [45] and [46]. The equation used in this work takes into consideration the voltage drop across the output diode as well as the equivalent series resistance of the different components. The MPP is then calculated as half of the instantaneous open-circuit voltage. In this case the converter operates in CCM. Win et al. [84] also developed another buck-boost converter with an MPPT circuit that

consumes only 250 μA, and it is based on impedance matching. The system does not require any sensor and the MPP is calculated by setting the duty-cycle based on the current measurement when the converter operates in DCM.

Ramadass and Chandrakasan [46] presented a power converter control design for low power applications that is capable to start-up with input voltages as low as 35 mV. The circuit is designed to harvest power from human-body heat and uses a boost that is employed to produce a voltage, from the TEG, that is high enough to drive the control electronics. The boost is controlled by a mechanically activated switch that can change state with body vibrations. A second boost is used to operate the TEG at the MPP. A very interesting MPPT technique is used, where theoretical operation at the MPP is achieved if the switching frequency is $f_S=R_T/(8L)$, where f_S is the switching frequency, R_T the internal resistance of the TEG and L the value of the boost inductor. This technique assumes that the MPP is found when the TEG voltage is half of the instantaneous open-circuit voltage. A buck converter, connected to an energy storage capacitor, is used to provide a regulated output. The overall measured efficiency, from end to end (TEG to regulated output) is 58 %.

Paraskevas and Koutroulis [85] produced a low power consumption MPPT control that is based on INC and used off-the-shelf components (COTS). The algorithm solves the issue of oscillations around the MPP, typical of a P&O, while reducing the control complexity of the classic INC. It is based on the assumption that the TEG has a fixed value of internal resistance, which is only applicable to situations where the TEG operates under constant temperature gradient. The controller does not need to compute the dI_{TEG}/dV_{TEG} and the condition $I_{TEG}/V_{TEG} = 1/R_{INT}$ is evaluated instead. The loss of power generation due to the loss of accuracy attributed to variations of R_{INT} with temperature is lower than the power consumption that a more complex INC algorithm would produce.

Yamada *et al.* [86] present the design of a boost converter that matches the load resistance to the TEG internal resistance, using only a single current sensor and operating in DCM. The method assumes a fixed internal resistance of the TEG, which is only true for a fixed temperature gradient. The MPPT method employed is capable to estimate the MPPT from a single current sensor without disrupting the operation of the power converter.

Solid-state power switches require a minimum turn-on voltage, which is usually below the output voltage delivered by the TEG. This presents a challenge for low voltage

applications as the converter needs to start-up before higher voltages can be generated to drive the control circuit, *i.e.* using step-up topologies. Damaschke [44] designed a converter that solves the problem of starting up at low voltages by using a start-up circuit for the main boost converter that uses a self-resonant circuit using a normally on switch so that the converter can start-up autonomously. The circuit does not operate at the MPP; however, it provides a regulated output designed for low power sensors with an overall efficiency of 76 % for an output power of 131 mW_{el}. Similar to [44] Jong-Pil *et al*. [47] designed a converter based on a single-ended converter and uses a self resonant transformer to be able to start-up when the input voltage reaches 40 mV. The MPPT method is based on FOV regulating the TEG voltage to half of the instantaneous open-circuit voltage, however, the TEG is not detached from the converter and the voltage is sampled, every 20 *ms*, during the off time of the converter.

Ahmed and Mukhopadhyay [87] solved the issue of start-up using a current based analog oscillator that is capable of producing very high duty cycles. The circuit is designed to be implemented in an integrated circuit and, although it does not implement MPPT, it is capable of producing a regulated output voltage in the range of 0.66 V to 3.3 V with a standby current consumption of only 3.5 μA, providing a maximum efficiency of 82 %. The system is capable of harvesting power from voltages as low as 12 mV. Hidaka *et al*. [88] propose a boost converter that uses a start-up circuit that allows the converter to start-up with an input voltage of less than 500 mV. Once the converter starts the start-up circuit is disconnected, decreasing the overall power consumption of the converter, and the control circuit is driven from the output. The MPPT algorithm is based on P&O, which allows for a reported tracking accuracy of almost 100 %.

Carlson *et al*. [45] designed a boost converter that was capable of starting up with an input voltage of 600 mV being able to operate with an input voltage as low as 20 mV. The efficiency is increased by operating the converter in DCM so that the inductor current does not become negative. It also adjusts the switching frequency to turn the high side switch off when the current crosses zero amperes thus allowing for zero current switching (ZCS). The MPPT control is digitally implemented performing FOV and regulates the TEG voltage to half of the instantaneous open-circuit voltage. The open-circuit voltage is inferred by measuring the output voltage and the duty-cycle; and, by doing so, the TEG does not need to be disconnected from the power converter and power generation is not disrupted.

Jungmoon and Chulwoo [89] present a design for low power applications, where the start-up problem is tackled by using the battery voltage. The converter topology is a boost that operates with variable frequency and ZCS, and the MPPT is FOV regulating to half of the open-circuit voltage. The open-circuit voltage is sampled by disconnecting the TEG from the converter, although the sampling time is only 4 μs with a sensing interval of 340 μs thus minimizing the loss of power generation. The main converter, along with the control, presents an efficiency of 72.2 %.

There are cases where, rather than dealing with a single TEG, the TEG system comprises several TEG units and some other aspects, like temperature mismatch between TEGs or higher internal impedances, influence the maximum power capability of the TEG system.

As the number of TEGs connected in series increases, the output impedance of the TEG also increases. The internal resistance of a single TEG changes with temperature, so large changes in internal resistance will be expected when several TEGs are connected in series. Carreon-Bautista *et al.* [90] developed a boost converter for multi-TEG arrays, where the problem lies in dealing with relatively high output impedance. It operates in DCM under pulse frequency modulation (PFM) to minimize power consumption and maximize efficiency for light loads. It performs impedance matching, for a large range of internal resistances, so that the MPP is found by operating at half of the instantaneous open-circuit voltage. The efficiency achieved is 61.15 % at 140 mV input voltage delivering an output power of 359 μW_{el}.

Temperature mismatch between different TEGs is a phenomenon that occurs when several TEGs are coupled to a heat source without a homogeneous temperature distribution across it. This is the case, for instance, of TEG arrays coupled to the exhaust of a vehicle, where the temperature gradient across the different TEGs decreases as the exhaust gas approaches the output. Qiu *et al.* [91] presents a complex arrangement where several buck-boost converters are connected to the different TEGs in a cascaded distributed arrangement. The distributed system is compared to a centralized one, showing an increase of the generated output power between 0.45 % and 1.78 % when the input power varies between 100 W_{el} and 190 W_{el}, approximately. Although the conversion efficiency of the centralized one is higher, the input and output power generated, under the same conditions, by the distributed system is higher.

An interesting analysis of power processing architectures to optimize power generation under mismatched conditions is presented by Petucco *et al*. [92]. The analysis is performed between three different power processing topologies: *series configuration*, for TEGs connected in series; *module-integrated configuration*, where each TEG is connected to an individual power converter and *differential power processing configuration*, where the differential current between two series-connected TEGs is processed to make it equal to $I_{SC}/2$. The loss of available power of each configuration is characterized using the mismatch between the TEG short-circuit current and internal resistance as input variables. The conclusion is that the series configuration of TEG modules represents the most simple, hardware-saving and efficient configuration of all three even for large mismatches between TEG modules. The other two architectures require high-efficiency power converters in order to match the performance of the series configuration. These results confirm the results previously presented by Montecucco *et al*. in [93].

Wu *et al*. [94] perform a similar evaluation of different power processing topologies. They also agree that the series configuration, referred to as the centralized topology, represents the most simple, cost effective and efficient topology for low levels of mismatch. They propose a centralized-distributed hybrid topology where most of the power is processed by the centralized architecture and only the mismatched energy is processed by the distributed stages. This concept is very similar to the differential power processing configuration presented in [92]. The proposed topology offers high MPPT and conversion efficiency, simultaneously.

2.4.3 Maximum Power Point Tracking in photovoltaic applications

Most of the MPPT techniques developed for TEG applications are inherited from PV applications and it is important to take a close look at the developments and improvements made on MPPT algorithms for PV. Some of these improvements could be applied to already existing MPPT techniques for thermoelectric applications, leading to potentially more accurate MPPT algorithms that optimize the output power generated by the TEG. Speed response to input power changes, and variable step sizes are desirable behaviours that lead to faster and more accurate MPPT algorithms. Piegari *et al*. [95] analyze the most suitable perturbation step to optimize MPPT performance and suggest a design criterion to select the parameters of the MPPT controller. The step is calculated from an estimated

maximum power point voltage, $V_{M,est}$, the measured voltage, V, and a minimum voltage step, ΔV_{min}, to ensure the algorithm tracks the MPP in the vicinity of the true MPP. The drawback of this method is that requires the characterization of the PV panel and, since the characteristics change over time, a periodical characterization is required. Ahmed and Salam [96] propose an improved P&O algorithm that is based in adaptive-step P&O. Adaptive-step algorithms change the step size in such a way that they can move the operating point faster when it is far away from the MPP and decrease the step size to increase the tracking accuracy in the vicinity of the MPP. The proposed method climbs the power-voltage curve until it reaches the MPP. When it starts to oscillate around the MPP, the step size is reduced until it reaches a minimum value. Once the minimum step size is reached, the normalized change in output power, $\Delta P/P$, is kept below a certain threshold limit. By setting different thresholds, the algorithm is capable of recognizing whether the change in power generation is due to a change in operating point by the algorithm, or a gradual or fast change in irradiance. The perturbation size is then calculated accordingly in order to combine fast tracking and high accuracy.

Other important aspect to take into consideration in real digitally implemented MPPT applications, are the limitations imposed by different factors like the numerical stability and discretization and quantization errors. These have been discussed more extensively in the literature that treats photovoltaic applications. Chun and Kwasinski [97] discuss these aspects as well as explaining other less common MPPT techniques, like *Newton Raphson* (NRM), *Secant* (SM), *Bisection* (BM), *Regula Falsi* (RFM) and *Modified Regula Falsi* (MRFM) methods. These are root-finding methods very similar to P&O or INC although some of these methods, like NRM, require calculations of second derivatives of power with respect to voltage, which, in some cases and depending on the type of application, imply a computational complexity that might not justify the benefits they offer. A comparison between digitally implemented P&O and INC is compared against SM, BSM, RFM and MRFM.

In the case of PV applications, rapid changes of irradiance produce rapid changes in the input power to the PV arrays. Under these rapid variations, the MPPT algorithm must correctly track the MPP in order to avoid loss of available energy. Also, the MPPT algorithm must be able to discern between voltage and current changes produced by external irradiance variations from those produced by changes in the operation conditions produced by the MPPT algorithm itself. Increasing the sampling frequency of the MPPT algorithm could, in some cases, increase the tracking speed thus reacting quicker to

external irradiance changes. On the other hand, overshoots and undershoots, inherent to the dynamics of the power converter, can be captured by the sampling and hold circuit producing false measurements that could deceive the MPPT algorithm. Femia *et al*. [98] show the condition for the MPPT algorithm not to be deceived when the irradiance and the operating point of the PV array change at the same time. Femia states that if the power variation due to the change of operating point is higher than the power variation due to illumination, then the MPPT algorithm does not get confused, otherwise it does. Femia also gives an expression for the minimum duty-cycle variations in order for the algorithm not to get confused. Another work by Femia *et al*. [99] treats the influence of the dynamic response of a boost converter on the MPPT algorithm. The dynamics of the duty-cycle to input transfer function $G_{vd}(S)$, makes the system oscillate in a damped manner when the duty-cycle changes. Steady-state conditions must be reached in order to sample the correct steady state value; otherwise de MPPT algorithm could be deceived. Femia discusses the choice of the sampling time in order to allow, after each duty cycle variation, the system to reach a steady state condition before the next perturbation occurs.

2.5 Thermoelectric generator models

A computer-based model simulates the physical behaviour of the device using the equations that represent the underlying physics that drive the TEG. The importance of having an accurate model of a TEG resides in the need to create tools that aid the development of thermoelectric applications saving time, cost and resources. An accurate model allows the user to develop a specific application without the need to build an entire test setup, a task that, in some cases, is rather complex. The more accurate the model is the higher the chances that the final application will produce, in real world, the expected results. Having an accurate model helps the user saving time in different phases during the development of the application. A more accurate model means, in most cases, a more complex one that will require more computational and time resources. TEG models are usually implemented using different tools, like Spice or Matlab/Simulink.

In power processing applications the TEG model is sometimes connected to the model of a power conversion stage that represents the power converter the TEG interfaces to. An accurate and detailed simulation that comprises the model of a switched mode power supply (SMPS) requires simulation step times that are an order of magnitude lower than the switching frequency of the power converter. The time constant of a TEG, dictated in

some cases by the thermal time constants of the overall system, are several orders of magnitude higher than the step size required by the power conversion stage. In these cases, the model of the power converter will render the overall TEG system model very slow, and several hours of simulation might be required to simulate few minutes of the system behaviour. It is therefore very important to trade-off model accuracy against simulation time, and in this case, a less accurate model of the power converter can considerably reduce the overall simulation time. In some other cases and when the TEG model is treated independently, the relatively large thermal time constants of the system might allow for longer simulation step times. These trade-offs must be evaluated and will depend on the type of intended application.

A very simple model of the TEG was used by Chen *et al*. [100] where the TEG was modeled as a constant voltage source with a resistor in series, the values of which were obtained experimentally. The TEG was operated at three different voltages on the hot and cold plates, respectively, and the V-I curves of the TEG were obtained under the three different temperature gradients. From these curves, the values of voltage and resistance of the voltage source, representing the open-circuit voltage, and the series resistance, representing the internal resistance of the TEG, were obtained. The model presented by Chen is only valid for applications where the TEG operates under constant temperature gradient, and it represents the simplest model of a TEG.

Tatarinov *et al*. [22] developed a more accurate model where the electrical, thermal and material-dependent behaviours were modeled. The electrical model is based on the equivalent circuit of the TEG when it operates under constant ΔT, equivalent to the approach shown in [100]. The thermal behaviour is modeled based on the heat flow 1-D equation, which represents the power balance across the TEG. The material-dependent behaviour is based on the efficiency of the TEG which, in turn, depend on intrinsic values specific to each TEG like the figure of merit, Seebeck coefficient, thermal and electrical conductivities as well as the temperatures across the device. The model was validated through experimental results that matched, to a certain degree, the behaviour obtained by the simulated model.

Lineykin and Ben-Yaakov [101] had developed, prior to [100] and [22], a Spice compatible model for thermoelectric coolers and generators, where all non-electrical processes are emulated by electrical analogies. The model is based on the heat-flow 1-D equation and the voltage source with series resistance model. It presents a method to

calculate the parameters of the model from the manufacturer's datasheet. A very similar circuit model approach was also presented by Dziurdzia [102].

Montecucco and Knox [103] present a more accurate and comprehensive Simulink-Matlab based model, where the overall system architecture is included. The thermal blocks are modeled and the input power transfer to the hot thermal mass is calculated using well-known laws of heat conduction and convection. Montecucco models the temperature dependencies of the open-circuit voltage and the internal resistance using linear functions, as well as including the appropriate scaling factors depending on the number of TEGs connected in series and in parallel. The Peltier effect is calculated from the current passing through the TEG and the results are fed-back to the thermal block. The model is validated using an experimental test rig showing a very good correlation between the model and the real behaviour.

2.6 Conclusions

This chapter shows the developments in thermoelectric materials and thermoelectric applications. Since the discovery of the thermoelectric phenomenon by Thomas J. Seebeck, one of the main objectives is to develop thermoelectric materials with a better figure of merit, which offer better thermoelectric performance. The maximum value of *ZT* reported for bulk materials is 2, whereas nanostructured materials have shown values of *ZT* higher than 2.

Several applications are shown where thermoelectric devices are used as a source of energy; *i.e*. TEG. From house-heating stoves to RTGs in interplanetary missions, thermoelectric devices are used to convert heat into electricity. Notwithstanding the low efficiency of thermoelectric generators, they are used to obtain green energy from waste heat and used as the main source of energy whenever other energy sources are not available.

MPPT techniques are employed, along with power converters, to extract the maximum available energy from a TEG. This chapter covers the most important MPPT techniques used in TEG applications that have been used in different applications, from low to medium power. Improvements in MPPT techniques for PV applications are also reviewed as they can serve as the basis for improvements in TEG applications.

Different TEG models have been presented and the importance of an accurate model for a successful development of a TEG application has been highlighted.

This chapter shows that there are several degrees of improvement in TEG applications, from improvements in the nanostructure of a given material, proper arrangement of TEGs along a heat source, better heat-sink performance and more accurate and faster MPPT techniques. Some of these factors are limited by physical constraints, like the size and weight of a heat-sink or the maximum efficiency of a thermoelectric material, which is limited by the Carnot efficiency.

Most of the MPPT techniques have been optimized for applications where the TEG operates under constant temperature gradient. In most real applications, however, the TEG operates under a constant heat flux, which utilizes a limited heat power source. This

highlights the need of a more accurate MPPT algorithm that takes into consideration the mode of operation of the TEG.

Chapter 3 Theory of thermoelectric devices

3.1 Thermoelectric modules

Thermoelectric modules are made of small semiconductor elements often called *legs* or *pellets*. A pair of pellets, or thermoelectric pair (TE pair), consists of a pellet of *p*-type material and another of *n*-type material. The two pellets are connected electrically in series so that the same current flows through both of them. The connection between the two pellets is made using a conductive interconnector that establishes the electrical connection between the pellets. The interconnector connects to the pellets using electrical contacts on each side of each pellet. In order to prevent the electrical contact from diffusing into the pellets, which could change the properties of the semiconductor material, a diffusion barrier is used between the pellet and the contact. An electrically insulating plate is used to isolate the interconnector from the external elements that are used to couple the heat sources or heat sinks to the thermoelectric pair. An adhesion layer is added between the interconnector and the insulating plate to mechanically bond the two elements [8]. A thermoelectric pair is shown in Figure 3–1 a). Figure 3–1 b) shows a photo of a commercial TEG.

In a thermoelectric material, and due to the doping of the different *p* and *n*-type materials, there are free holes and electrons that carry both charge and heat [9]. When a TE pair operates under a temperature gradient ΔT, both types of charges move in the same direction as the heat flow, creating a flux of electrons in the *n*-type material and holes in the *p*-type material, Figure 3–2 a). Due to the geometrical arrangement and the series connection of the thermoelectric pair, when the circuit formed by the thermoelectric couple is closed by a resistive element (or any other material that allows for a current to flow) an electric current flows in both materials in the same direction, and an electrical potential is developed across the load connected to the TE pair.

Conversely, when an electrical potential is applied across the TE pair a current will flow through it. The current direction is such that both electrons and holes in the *n*- and *p*-type legs, respectively, will flow in the same direction and the heat transport is also produced in the same direction, Figure 3–2 b).

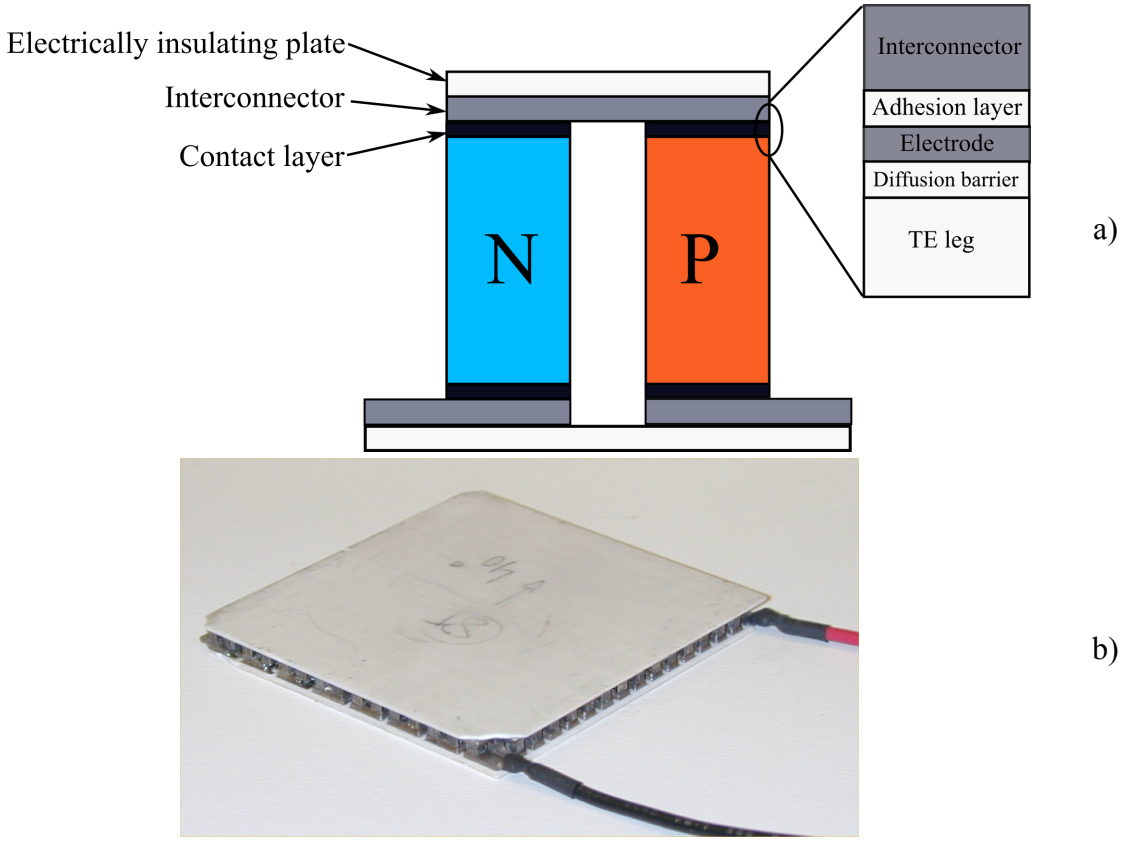

Figure 3–1 – a) Schematic diagram of a thermoelectric pair b) Commercial TEG

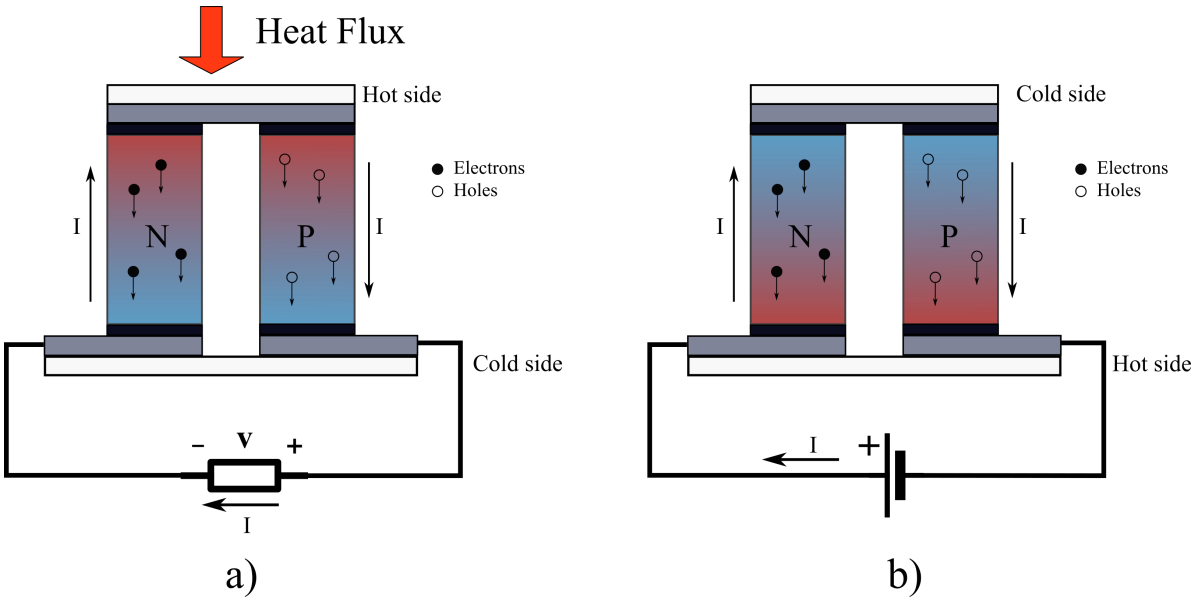

Figure 3–2 - Heat and charge transport in a thermoelectric pair a) power generation b) Peltier cooling

A thermoelectric module is made of several pairs of pellets that are connected electrically in series and thermally in parallel. By doing so, all the pellets carry the same current (the module current) and operate under the same thermal gradient ΔT.

Figure 3–3 shows a 3-D cut-away view of a TEG with the heat flux and current directions indicated by the arrows. The voltage difference across the TE module is the sum of the voltages of each individual TE leg, with typical voltages per TE pair of 350 $\mu V/K$ in Bismuth Telluride (Bi_2Te_3). Each TEG contains hundreds of TE pairs, being typical values 127, 254 or 449 [104].

A schematic drawing of the electrical and thermal arrangement of the TE pairs within the TEG is shown in Figure 3–4 where the electrical connection in series and thermal arrangement in parallel of TE pairs is shown.

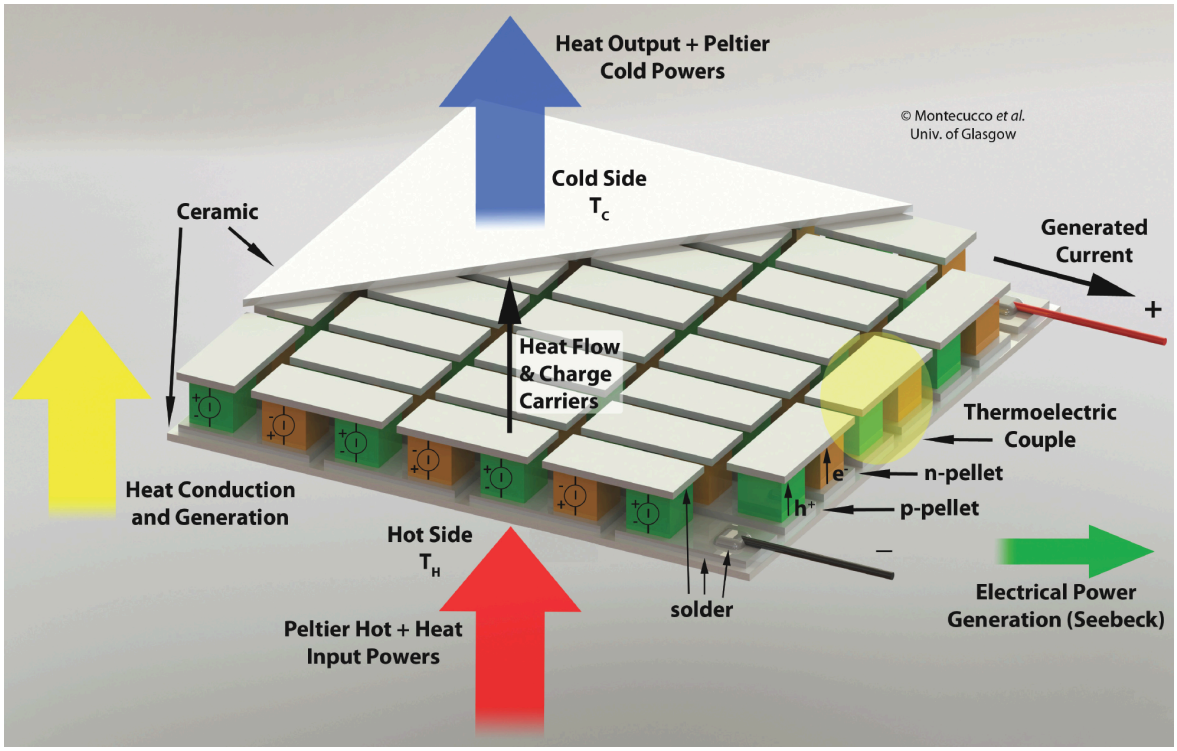

Figure 3–3 - 3D view of a thermoelectric module. Credit: Andrea Montecucco, PhD Thesis "Efficiently Maximising Power Generation from Thermoelectric Modules", University of Glasgow.

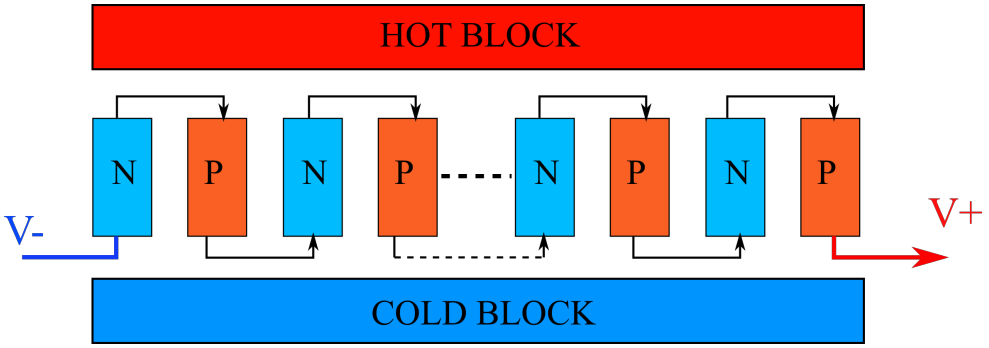

Figure 3–4 - Electrical and thermal arrangement of TE pairs within a TEG

3.2 Considerations when handling thermoelectric generators

In spite of being robust devices without moving parts, there are few aspects that must be taken into consideration in order to preserve the integrity of the device.

The maximum temperature on the hot side is a limiting factor of the TEG and precautions should be taken so that the maximum temperature of the solder employed in the interconnection tabs as well as the maximum temperature of the diffusion layer between the copper contacts (see Figure 3–1) is not exceeded. The temperature of the hot side must be evenly distributed across the ceramic plate so that hot spots do not appear as these could produce localized damage. Heat spreaders must be used to avoid any hot spots [104], [105]. Low temperatures below zero degrees Celsius can be applied on the cold side of the TEG so long as particles of water are not present in the TEG structure, as these could freeze, producing permanent damage to the TEG [104].

In order to minimize the thermal resistance between the heat source and the TEG thermal conductive paste or graphite is used to exclude air at the interface. A flat and smooth (ideally polished) surface on both the interface of the heat source and the ceramic plate of the TEG helps to minimize the thermal resistance on the hot side. Also, the clamping force used on the TEG against the heat source must be maximized to increase the heat transfer. There is, however, a limitation on the maximum clamping force to avoid damage to the ceramic plates and, ultimately, to the pellets. 1 *MPa* is widely accepted as a suitable pressure to use in most applications.

In certain applications where mechanical vibrations exist, as it is the case in space applications, a suitable TEG capable of withstanding the required vibration levels must be used.

3.3 Thermal and electrical conductivities

The thermal and electrical conductivities are two parameters that play an important role in the efficiency of a thermoelectric material. The thermal conductivity establishes how easily heat will flow across the TEG thus allowing heat being transferred from the hot to the cold side of the TEG. The higher the thermal conductivity of a TEG the lower the temperature difference across the hot and cold plates (this is only true when the heat flux is limited). The electrical conductivity of the thermoelectric material establishes how easily current will flow through the TEG when a load is connected across its electrical terminals.

The thermal conductivities of the *p* and *n*-type materials, κ_p and κ_n respectively, are measured in [$W/m{\cdot}K$]. From the thermal conductivities of the *p* and *n*-type materials and using Equation (**3-1**) the overall TEG thermal conductance is calculated. In Equation (**3-1**) N is the number of TE pairs in the TEG, A_p and A_n are the areas of the *p* and *n*-type TE pellets, respectively, and L_p and L_n the length of the *p* and *n*-type TE pellets, respectively. The thermal conductance of the TEG has units of [W/K] and has been denoted as K_{OC} as it indicates the conductance when the current through the TEG is equal to zero. The reason for this convention is that the thermal conductance increases with the TEG current. The thermal resistance, θ_{OC}, is the inverse of K_{OC} as shown in Equation (**3-2**).

$$\kappa_{OC} = N \cdot \left(\kappa_p \cdot \frac{A_p}{L_p} + \kappa_n \cdot \frac{A_n}{L_n} \right) \tag{3-1}$$

$$\theta_{OC} = \frac{1}{K_{OC}} \tag{3-2}$$

The electrical conductivity of the *p* and *n*-type materials, denoted as σ_p and σ_n respectively, are measured in [S/m] (Siemens per meter). The internal resistance of a TEG is calculated using Equation (**3-3**) for which it is required to know the electrical resistivity, ρ, of the *p* and *n*-type materials. The units of ρ are [$\Omega{\cdot}m$]. The electrical resistivity is the reciprocal of

the electrical conductivity, as shown in Equation (**3-4**). The parameters N, A_p, A_n, L_p and L_n are defined in the same manner they were for Equation (**3-1**).

$$R_{int} = N \cdot \left(\rho_p \cdot \frac{L_p}{A_p} + \rho_n \cdot \frac{L_n}{A_n} \right) \tag{3-3}$$

$$\rho = \frac{1}{\sigma} \tag{3-4}$$

The internal resistance, R_{INT}, shown in Equation (**3-3**) is an approximation, as this expression does not take into consideration the resistance of the interconnections between the TE pellets, $R_{CONTACTS}$. The approximation of Equation (**3-3**) is only valid when $R_{CONTACTS}$ is negligible compared to R_{INT}. This is the case with TE pellets with relatively small cross-sectional area and relatively long length. Whenever these assumptions do not hold true, the internal resistance should be changed to $R_{INT} + R_{CONTACTS}$ [104].

The thermal and electrical resistance of the TEG is adjusted by adjusting the size (changing either the cross-sectional area, length, or both) of the TE couples as well as the TE material used. In order to achieve the best thermoelectric performance of the module it is desirable to produce a module with the highest thermal and the lowest electrical resistances. For a given temperature gradient across the TEG, a high thermal resistance reduces the thermal flux across the device. On the other hand, a low electrical resistance translates into lower *Joule* conduction losses, for a given output current.

By simple inspection of Equations (**3-1**) and (**3-3**) it can be observed that when increasing the ratio L_x/A_x, with x indicating the p or n-type material, both thermal and electrical resistances are increased. On the other hand, when the ratio L_x/A_x is decreased, both thermal and electrical resistances are decreased. It is therefore not possible to increase the thermal resistance and decrease the electrical resistance by just changing the length and cross-section of the TE pellets for a given material composition.

For a TEG of a fixed area, the voltage of the TEG will increase by increasing the number of TE couples. This can be achieved reducing the cross-section of the TE couples in order to integrate more within the given TEG area. By doing so, however, the electrical resistance of the device will increase, and the power losses inside the TEG will also

increase. If, on the other hand, it is desirable to increase the output current of the TEG, TE couples with larger cross-section will be required so that the *Joule* conduction losses are minimized. In this case, a smaller number of TE couples will fit in a TEG of a certain area, thus reducing the maximum output voltage the TEG will generate.

The use of taller TE couples will usually produce a TEG with a higher thermal resistance, thus reducing the thermal flux across the TEG when it operates under constant temperature gradient. In this situation the electrical resistance will also increase thus increasing the *Joule* conduction losses.

3.4 The Seebeck effect

As explained in Section 3.1, charge carriers can be set in motion by the flow of heat. Whenever an electrical conductor is placed between two different temperatures, the conductor transfers thermal energy from the warmer side to the colder one, and charge carriers are moved in the same direction. The charges will transport both heat and electrical charge from the hot to the cold side.

The Seebeck effect describes the phenomenon whereby a voltage is produced in a circuit of two dissimilar materials when the two junctions are maintained at different temperatures [6], [57], [106]. The voltage generated is described in Equation (**3-5**), where ΔT is the temperature gradient across the two dissimilar materials and ΔV the voltage developed.

$$\Delta V = \alpha \cdot \Delta T \tag{3-5}$$

The coefficient α is referred to as the Seebeck coefficient and is defined as in Equation (**3-6**), and it has units of [V/K].

$$\alpha = \left.\frac{\Delta V}{\Delta T}\right|_{\Delta T \to 0} \tag{3-6}$$

The Seebeck coefficient, α, is a relative quantity that is associated with the properties of the two materials (material "*a*" and '*b*'). For this reason, it is sometimes referred to as α_{ab}, see Equation (**3-7**).

$$\Delta V = \int_{T_C}^{T_H} (\alpha_a - \alpha_b) dT = \int_{T_C}^{T_H} \alpha_{ab} dT \tag{3-7}$$

3.5 The Peltier effect

The Peltier effect states that if a direct current is passed through a circuit of dissimilar materials, one junction will be heated and the other will be cooled. It is the complement of the Seebeck effect and it is also reversible in that, if the direction of the current flow is reversed, the junction that was formerly heated will be cooled and the formerly cooled junction will be heated. The Peltier effect is described in Equation (**3-8**), where $\dot{Q}$ is the heat generated across junctions *a* and *b*, Π_{ab} is the Peltier coefficient across junctions *a* and *b* and *I* is the current flowing through the junctions [57], [106].

$$\dot{Q} = \Pi_{ab} \cdot I \tag{3-8}$$

The Peltier coefficient is a strong function of temperature and is defined in Equation (**3-9**).

$$\Pi_{ab} = \left. \frac{\dot{Q}}{I} \right|_{\Delta T \to 0} \tag{3-9}$$

The Peltier heating (or cooling) can be interpreted as happening due to the change in the average energy (kinetic energy) of a charge when it crosses a junction.

3.6 The Thomson effect

The Seebeck and Peltier effects only occur in a system that consists of, at least, two different materials. For a single material, the absorption (or dissipation) of heat can occur

when the material is subjected to a temperature difference and electric current, simultaneously, as depicted in Figure 3–5 [106]. In most applications the Thomson effect is not of primary importance although it should be considered in detailed calculations [57].

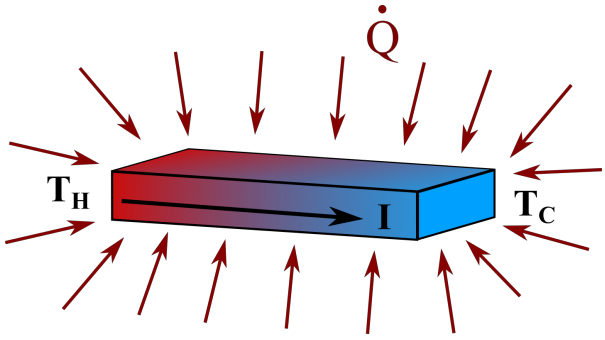

Figure 3–5 - Heat absorption by a material subjected to a temperature difference and a current flowing through it

The Thomson coefficient, τ, is defined in Equation (**3-10**) where $\dot{Q}$ is the heat transfer rate, in *Watts*, absorbed by the conductor when the current flows towards the cold side.

$$\tau = \frac{1}{I} \cdot \frac{d\dot{Q}}{dT} \Rightarrow \dot{Q} = \tau \cdot I \cdot \Delta T \tag{3-10}$$

3.7 The Kelvin relationships

The three thermoelectric coefficients are not independent of each other, but are related by the Kelvin relationships [106]. The three effects and the phenomenological constants that describe them (α, Π and τ) are related through an energy balance which states that the electrical power generated, as a result of a temperature difference, equals the heat dissipated:

Power Generated (Seebeck): $\Delta V \cdot I = \alpha_{ab} \cdot \Delta T \cdot I$ (3-11)

Heat generated (Peltier): $\dot{Q} = \Pi_{ab} \cdot \mathrm{I}$ (3-12)

$$\text{Thomson: } \dot{Q} = \tau_a \cdot \Delta T \cdot \mathrm{I} - \tau_b \cdot \Delta T \cdot \mathrm{I} = \tau_{ab} \cdot \Delta T \cdot \mathrm{I} \tag{3-13}$$

Equations (**3-11**)-(**3-13**) can be written in differential form as in Equations (**3-14**) and (**3-15**).

$$\int_{T_C}^{T_H} \alpha_{ab} \cdot I \cdot dT = \Pi_{ab} \cdot \mathrm{I} + \int_{T_C}^{T_H} (\tau_a - \tau_b) \cdot \mathrm{I} \cdot dT \tag{3-14}$$

$$\alpha_{ab} = \frac{d\Pi_{ab}}{dT} + (\tau_a - \tau_b) \tag{3-15}$$

The Peltier and Seebeck coefficients are related to each other by the following relationship:

$$\Pi_{ab} = \alpha_{ab} \cdot T_j \tag{3-16}$$

Where T_j is the temperature of the junction. From Equation (**3-12**) and Equation (**3-16**) the following relationship is obtained:

$$\dot{Q} = \alpha_{ab} \cdot T_j \cdot I \tag{3-17}$$

The Thomson coefficient is related to the Seebeck coefficient by the following relationship [106]:

$$\frac{d\alpha_a}{dT} = \frac{\tau_a}{T_{AVG}} \qquad \frac{d\alpha_b}{dT} = \frac{\tau_b}{T_{AVG}} \qquad \Rightarrow \frac{d\alpha_{ab}}{dT} = \frac{\tau_{ab}}{T_{AVG}} \tag{3-18}$$

Where T_{AVG} is the average temperature $(T_H+T_C)/2$.

3.8 Figure of merit

The figure of merit of a thermoelectric device is a parameter that indicates the performance of a given thermoelectric material [1], and it is related to the efficiency of a given thermoelectric device. In fact, the figure of merit is a parameter that limits the conversion efficiency of thermoelectric devices [106]. It is shown in Equation (**3-19**), in [K^{-1}], where α is the Seebeck coefficient, ρ is the electrical resistivity of the material and κ the thermal conductivity.

$$Z = \frac{\alpha^2}{\rho \cdot \kappa} \tag{3-19}$$

The figure of merit is a parameter that varies with temperature. It is therefore desirable to find materials with large figures of merit in the temperature range for a given application. The optimization of the figure of merit involves the control of three parameters: the Seebeck coefficient, the electrical resistivity and the thermal conductivity and each of these parameters is a function of the density of charge carriers in the material. The thermal conductivity increases with the concentration of charge carriers whilst the Seebeck coefficient and the electrical resistivity decrease. However, the effect of the charge carrier concentration on thermal conductivity is minor because the increase of electronic thermal transport is relatively small when compared to that associated with phonon (lattice wave) motion, which is independent of electron density [107].

Since the internal electrical resistance of a thermoelectric material, R_{int}, is related to the electrical resistivity by the relationship $R_{int}=\rho L/A$, it is possible to re-write Equation (**3-19**) as in Equation (**3-20**).

$$Z = \frac{L}{R_{int} \cdot A} \cdot \frac{\alpha^2}{\kappa} \tag{3-20}$$

A more convenient parameter to evaluate the efficiency of a thermoelectric material is the dimensionless figure of merit. The dimensionless figure of merit is defined as Equation (**3-20**) multiplied by the average temperature T_{AVG}.

$$ZT_{AVG} = \frac{L}{R_{int} \cdot A} \cdot \frac{\alpha^2}{\kappa} \cdot \frac{T_H + T_C}{2} \tag{3-21}$$

3.9 Equivalent electrical model of a thermoelectric generator

The open-circuit voltage generated by a TEG, arising from a temperature gradient across the TEG plates, ΔT, and dictated by the Seebeck effect, is defined by Equation (**3-5**). On the other hand, the TEG presents an internal resistance that is defined by Equation (**3-3**). The internal impedance of a TEG usually varies with temperature, but it can be approximated as being constant for a given temperature range. The internal resistance of the TEG will cause the voltage to drop across the TEG terminals when current flows through the device, as well as internal Joule effect losses, so it can be modeled as a resistor in series with the open-circuit voltage of the TEG.

Having a voltage source, representing the voltage generated by the Seebeck effect, and a resistor in series, representing the internal resistance of the TEG, it is possible to obtain the Thevenin [108] equivalent circuit for the TEG. This equivalent circuit is shown in Figure 3–6 where V_{OC} represents the Seebeck voltage, R_{INT} the internal resistance of the TEG and R_{LOAD} the load resistance connected to the terminals of the TEG.

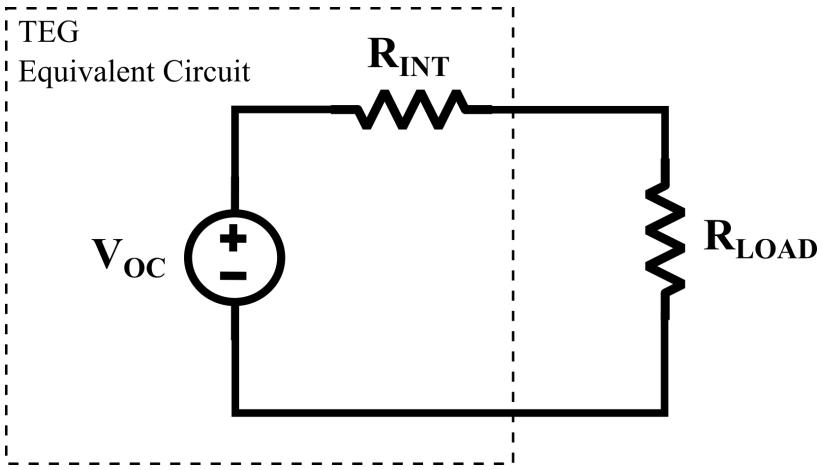

Figure 3–6 - Equivalent circuit of a TEG

The voltage and power across the load resistor R_{LOAD} can be calculated using Equations (**3-22**) and (**3-23**), respectively.

$$V_{LOAD} = V_{OC} - R_{INT} \cdot I_{LOAD} \tag{3-22}$$

$$P_{LOAD} = V_{OC} \cdot I_{LOAD} - R_{INT} \cdot {I_{LOAD}}^2 \tag{3-23}$$

The maximum electrical power transferred to the load is found through the derivative of the load power with respect to the load current, and equating the result to zero, as stated by the *maximum power transfer theorem* [108]:

$$\frac{dP_{LOAD}}{dI_{LOAD}} = V_{OC} - 2 \cdot R_{INT} \cdot I_{LOAD} = 0$$

$$I_{LOAD}|_{MPP} = \frac{V_{OC}}{2 \cdot R_{INT}} \tag{3-24}$$

$$V_{LOAD}|_{MPP} = \frac{V_{OC}}{2}$$

Where the subscript MPP refers to the evaluation of the parameters at the maximum power point. The conditions stated by Equation (**3-24**) are fulfilled when $R_{LOAD} = R_{INT}$. Under these conditions, the maximum power transferred to the load can be calculated using Equation (**3-25**).

$$P_{LOAD}|_{MPP} = \frac{{V_{OC}}^2}{4 \cdot R_{INT}} \tag{3-25}$$

The power and voltage, versus current, curves of the TEG, operating under a constant ΔT, are shown in Figure 3–7. These curves assume an open-circuit voltage equal to 12 V and an internal resistance equal to 2.5 Ω. Under these conditions, the short-circuit current is equal to I_{SC} = 12 V/2.5 Ω = 4.8 A so the maximum power point is found when the load current and voltage are 2.4 A and 6 V, respectively. The maximum load power, calculated using Equation (**3-25**), is 14.4 W_{el}.

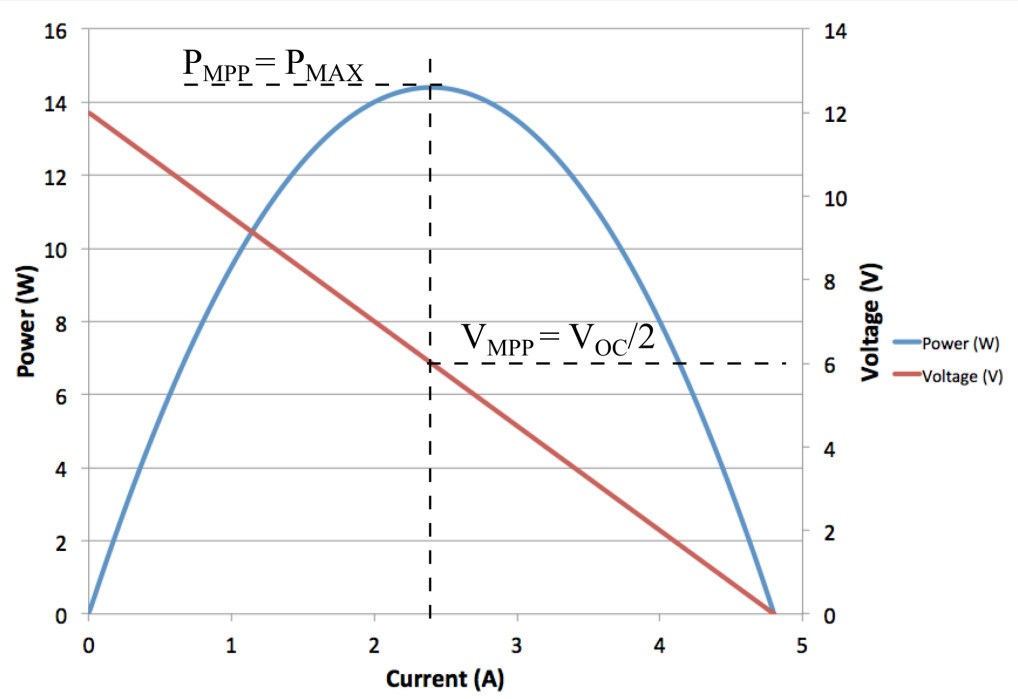

Figure 3–7 - TEG power and voltage curves against output current

3.10 Thermal conduction and Fourier's law

Thermal conduction is the transfer of internal energy by microscopic diffusion and collisions of particles within a body due to a temperature gradient. The heat flux density is defined as the heat transfer rate in the *x* direction per unit area perpendicular to the direction of transfer, and it is proportional to the temperature gradient, *dT/dx*, in this direction. For the one-dimensional plane wall shown in Figure 3–8, having a temperature distribution *T(x)*, the rate equation, also known as *Fourier's law*, is [109]:

$$\dot{Q}'' = -\kappa \frac{dT}{dx} \tag{3-26}$$

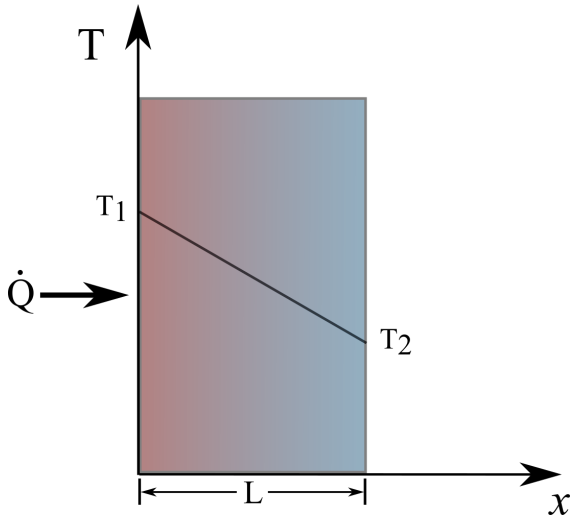

Figure 3–8 - One-dimensional heat transfer by conduction

where κ is the thermal conductivity [$W/m{\cdot}K$]. Heat is conducted from the hot to the cold side: it is therefore conducted in the direction of decreasing temperature and hence the negative sign. Fourier's law is phenomenological and Equation (**3-26**) is based on experimental evidence. The heat flux, or heat transfer rate, has units of [W/m^2]. Taking into consideration that $\dot{Q}"=d\dot{Q}/dS$; being $df(x)/dS$ the derivative of $f(x)$ with respect to the surface:

$$\dot{Q} = -\kappa \oint \frac{dT}{dx} dS = -= -\kappa \oint \nabla T \, dS \tag{3-27}$$

Following Equation (**3-27**) the heat rate is defined as the heat flux multiplied by the cross-sectional area of the element it flows through:

$$\dot{Q} = -\kappa \cdot A \frac{dT}{dx} \tag{3-28}$$

3.11 One-dimensional (1-D) heat conduction equation for solids with internal energy generation

When a TEG is coupled to a heat source there is a heat flux entering the hot side and a heat flux leaving the cold side. The difference between the two fluxes represents the power

generated and dissipated in the TEG. The power generated represents the electrical energy produced by the TEG while the dissipated power represents the conduction, or Joule effect, losses across the internal resistance.

It is possible to derive the expressions for the heat fluxes entering and leaving the hot and cold sides, respectively, by solving the one-dimensional heat conduction equation with internal power generation [101], [110], Equation (**3-29**), for each one of said heat fluxes.

$$\frac{d^2T}{dx^2} + \frac{\dot{q}}{\kappa} = 0 \tag{3-29}$$

Where $\dot{q}$ represents the internally generated heat per unit volume [W/m^3]. The generic solution to Equation (**3-29**) is shown in Equation (**3-30**) to which boundary conditions have to be applied in order to find a solution. The boundary conditions are shown in Figure 3–9.

$$\frac{d^2T}{dx^2} = -\frac{\dot{q}}{\kappa}$$

$$\frac{dT}{dx} = -\frac{\dot{q}}{\kappa}x + A \tag{3-30}$$

$$T(x) = -\frac{1}{2}\cdot\frac{\dot{q}}{\kappa}x^2 + Ax + B$$

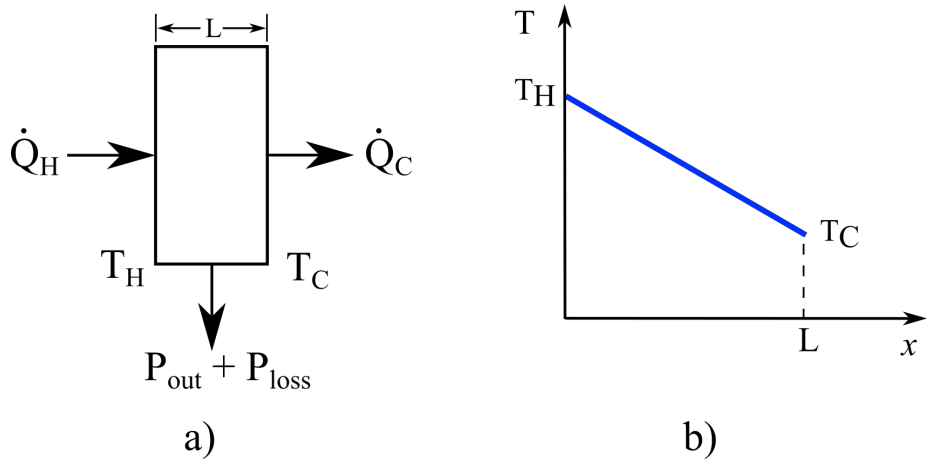

Figure 3–9 - a) Balance of powers b) Boundary conditions for the hot side

Applying the boundary conditions to Equation (**3-30**):

$$T(0) = T_H \Longrightarrow B = T_H$$

$$T(L) = T_C \Longrightarrow T_C = -\frac{1}{2}\cdot\frac{\dot{q}}{\kappa}\cdot L^2 + A\cdot L + T_H$$

$$\Longrightarrow A\cdot L = T_C - T_H + \frac{1}{2}\cdot\frac{\dot{q}}{\kappa}\cdot L^2 \tag{3-31}$$

$$\Longrightarrow A = \frac{T_C - T_H + \frac{1}{2}\cdot\frac{\dot{q}}{\kappa}\cdot L^2}{L}$$

The solution is found in Equation (**3-32**):

$$T(x) = -\frac{1}{2}\cdot\frac{\dot{q}}{\kappa}\cdot x^2 + \frac{T_C - T_H}{L}\cdot x + \frac{1}{2}\cdot\dot{q}\cdot\frac{L}{\kappa}\cdot x + T_H \tag{3-32}$$

Equation (**3-32**) can be combined with Fourier's law, but it is required to calculate *dT(x)/dx*:

$$\frac{dT(x)}{dx} = -\frac{\dot{q}}{\kappa}\cdot x + \frac{T_C - T_H}{L} + \frac{1}{2}\cdot\dot{q}\cdot\frac{L}{\kappa} \tag{3-33}$$

Equation (**3-33**) can be combined with Equation (**3-28**):

$$\dot{Q_h} = -\kappa\cdot A\frac{dT}{dx} = \kappa\cdot A\cdot\frac{\dot{q}}{\kappa}\cdot x - \kappa\cdot A\cdot\frac{T_C - T_H}{L} - \kappa\cdot A\cdot\frac{1}{2}\cdot\dot{q}\cdot\frac{L}{\kappa} \tag{3-34}$$

To solve for the hot side, $x = 0$:

$$\dot{Q_h} = \kappa\cdot A\cdot\frac{T_H - T_C}{L} - \frac{1}{2}\cdot\dot{q}\cdot A\cdot L \tag{3-35}$$

$\dot{q}$ is defined as the internally generated heat per unit volume, so the total internally generated heat, due to Joule effect, can be expressed as:

$$\dot{q}|_{TOTAL} = \dot{q} \cdot A \cdot L = R_{INT} \cdot I^2 \tag{3-36}$$

Combining Equations (**3-35**) and (**3-36**):

$$\dot{Q_h} = \kappa \cdot A \cdot \frac{\Delta T}{L} - \frac{1}{2} \cdot R_{INT} \cdot I^2 \tag{3-37}$$

When current flows through the TEG there is heat absorbed on the hot side. From Equation (**3-17**) of the Kelvin relationships the heat absorbed on the hot junction is defined as $\dot{Q}_H = \alpha_{ab} \cdot T_H \cdot I$. This term has to be added to Equation (**3-37**) to account for all the heat flux entering the hot side.

$$\dot{Q_h} = \kappa \cdot A \cdot \frac{\Delta T}{L} - \frac{1}{2} \cdot R_{INT} \cdot I^2 + \alpha_{ab} \cdot T_H \cdot I \tag{3-38}$$

The same calculations can be performed for the cold side of the TEG. In order to apply the boundary conditions, it has to be taken into consideration that, in this instance, the cold side becomes the origin (see Figure 3–10).

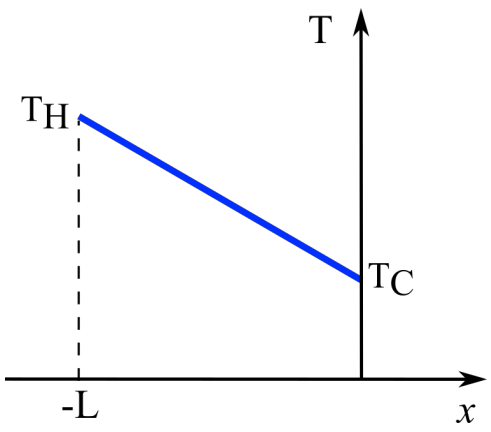

Figure 3–10 - Boundary conditions when solving for the cold side of the TEG

Applying the boundary conditions shown in Figure 3–10 to Equation (**3-30**):

$$T(0) = T_C \Longrightarrow B = T_C$$

$$T(-L) = T_H \Longrightarrow T_H = -\frac{1}{2}\cdot\frac{\dot{q}}{\kappa}\cdot L^2 - A\cdot L + T_C$$

$$\Longrightarrow A\cdot L = -(T_H - T_C) - \frac{1}{2}\cdot\frac{\dot{q}}{\kappa}\cdot L^2 \tag{3-39}$$

$$\Longrightarrow A = -\frac{(T_H - T_C)}{L} - \frac{1}{2}\cdot\frac{\dot{q}}{\kappa}\cdot L$$

Taking the derivative *dT(x)/dx* and applying Fourier's law, Equation (**3-40**) is obtained:

$$\dot{Q}_c = \kappa\cdot A\cdot\frac{\Delta T}{L} - \frac{1}{2}\cdot\dot{q}|_{TOTAL} = \kappa\cdot A\cdot\frac{\Delta T}{L} + \frac{1}{2}\cdot R_{INT}\cdot I^2 \tag{3-40}$$

Adding the Peltier term, corresponding to the heat absorbed on the cold side, $\dot{Q}_C = \alpha_{ab}\cdot T_C\cdot I$:

$$\dot{Q}_c = \kappa\cdot A\cdot\frac{\Delta T}{L} + \frac{1}{2}\cdot R_{INT}\cdot I^2 + \alpha_{ab}\cdot T_C\cdot I \tag{3-41}$$

Having solved the heat equations for the hot and cold sides, leading to Equations (**3-38**) and (**3-41**), respectively; and given the power balance shown in Figure 3–9 a), the difference between $\dot{Q_H}$ and $\dot{Q_C}$ represent the electrical power generated minus the internal power losses:

$$\dot{Q}_h - \dot{Q}_c = \alpha_{ab}\cdot I\cdot(T_H - T_C) - R_{INT}\cdot I^2 = \alpha_{ab}\cdot I\cdot\Delta T - R_{INT}\cdot I^2 \tag{3-42}$$

Where:

$\alpha_{ab} \cdot I \cdot \Delta T$: represents the electrical power generated due to the Seebeck effect.

$R_{INT} \cdot I^2$: represents the power dissipated in the internal resistance of the TEG due to the Joule effect.

The positive sign of the Seebeck effect term indicates that the power is generated, P_{out} in Figure 3–9 a), whereas the negative sign of the Joule effect term indicates that the power is dissipated, P_{loss} in Figure 3–9 a).

3.12 Conversion efficiency of a thermoelectric generator

Section 3.11 shows that the heat flux (or heat power) absorbed by the TEG on the hot side is converted into electricity exploiting the Seebeck effect. As with any other physical process, there is a conversion efficiency associated to the conversion from heat to electricity. The conversion efficiency of a TEG can be defined as the ratio of the output electric power to the heat flux absorbed at the hot junction.

$$\eta_{TEG} = \frac{Output\ electric\ Power\ (P_{out})}{Heat\ flux\ absorbed\ at\ the\ hot\ junction\ (\dot{Q_H})} \tag{3-43}$$

The power delivered to the load is found solving the circuit of Figure 3–6:

$$P_{out} = \frac{\alpha_{ab} \cdot \Delta T}{R_{LOAD} + R_{INT}} \cdot \alpha_{ab} \cdot \Delta T \frac{R_{LOAD}}{R_{LOAD} + R_{INT}} = \\ = (\alpha_{ab} \cdot \Delta T)^2 \cdot \frac{1}{R_{INT}} \cdot \frac{s}{(1+s)^2} \tag{3-44}$$

Where $s = R_{LOAD}/R_{INT}$. The heat absorbed by the hot junction corresponds to Equation (**3-38**) and the conversion efficiency becomes:

$$\eta_{TEG} = \frac{{\alpha_{ab}}^2 \cdot \Delta T^2 \cdot \frac{1}{R_{INT}} \cdot \frac{s}{(1+s)^2}}{\kappa \cdot A \cdot \frac{\Delta T}{L} - \frac{1}{2} \cdot R_{INT} \cdot I^2 + \alpha_{ab} \cdot T_H \cdot I}$$

$$= \frac{{\alpha_{ab}}^2 \cdot \Delta T^2 \cdot s}{(1+s)^2 \cdot \kappa \cdot A \cdot R_{INT} \cdot \frac{\Delta T}{L} - \frac{1}{2} {R_{INT}}^2 I^2 \cdot (1+s)^2 + \alpha_{ab} \cdot T_H \cdot I \cdot (1+s)^2} \tag{3-45}$$

$$= \frac{\Delta T^2 \cdot s}{(1+s)^2 \cdot \frac{1}{Z} \Delta T - \frac{1}{2} {R_{INT}}^2 I^2 \cdot (1+s)^2 \cdot \frac{1}{{\alpha_{ab}}^2} + \frac{1}{\alpha_{ab}} T_H I R_{INT} (1+s)^2}$$

$$= \frac{\Delta T}{T_H} \cdot \frac{s}{\frac{(1+s)^2}{Z \cdot T_H} - \frac{\Delta T}{2 \cdot T_H} + (1+s)}$$

$$\eta_{TEG} = \frac{T_H - T_C}{T_H} \cdot \frac{s}{\left(1 + \frac{R_{LOAD}}{R_{INT}}\right) - \frac{T_H - T_C}{2 \cdot T_H} + \frac{\left(1 + {R_{LOAD}}/{R_{INT}}\right)^2}{Z \cdot T_H}} \tag{3-46}$$

With Z being the figure of merit as defined in Equation (**3-20**). The maximum efficiency is calculated by deriving Equation (**3-45**) with respect to "s" and equating the result to zero:

$$\frac{d\eta_{TEG}}{ds} = 0 \implies 2 \cdot Z \cdot T_H - Z \cdot \Delta T - 2 \cdot s^2 + 2 = 0 \tag{3-47}$$

$$s = \sqrt{Z T_{AVG} + 1}$$

Leading to the maximum conversion efficiency stated in Equation (**3-48**).

$$\eta_{TEG} = \frac{T_H - T_C}{T_H} \cdot \frac{\sqrt{ZT_{AVG} + 1}}{1 + \sqrt{ZT_{AVG} + 1} - \frac{T_H - T_C}{2T_H} + \frac{\left(1 + \sqrt{ZT_{AVG} + 1}\right)^2}{ZT_H}} \tag{3-48}$$

A simplified version of Equation (**3-48**), shown in Equation (**3-49**), is used throughout most of the literature related to thermoelectric devices.

$$\eta_{TEG} = \frac{T_H - T_C}{T_H} \cdot \frac{\sqrt{ZT_{AVG} + 1} - 1}{\sqrt{ZT_{AVG} + 1} - \frac{T_C}{T_H}} \tag{3-49}$$

Chapter 4 TEGs operated under constant heat flux and the true MPP

TEGs can be characterised under two different regimes: constant temperature gradient (constant ΔT; infinite available heat flux), or constant (finite) heat flux. A TEG operating under constant heat flux represents the mode of operation that corresponds to most heat waste harvesting applications. However, manufacturers generally provide performance data obtained under constant ΔT operation. In this chapter the main differences between the two different regimes are discussed highlighting the impact on the location of the MPP. Theoretical and experimental characterizations of TEGs operating under constant heat flux are presented.

The thermal capacitance of the different elements in the TEG system introduces a thermal delay that affects the transient response of the TEG. This transient, or dynamic, response of the TEG is a characteristic behaviour that only affects TEGs operating under constant heat flux. Such dynamic response is also presented in this chapter and experimental characterizations are performed for a TEG operated under different values of heat flux.

4.1 TEGs operated under constant temperature gradient

4.1.1 TEG parameters

The electrical model of a TEG operated under constant temperature gradient has already been presented in Section 3.9. This electrical equivalent model of the TEG is built using a constant voltage source with a resistor connected in series, R_{INT}, and it is presented again in Figure 4–1. The voltage source is equivalent to the TEG output voltage in open-circuit conditions. This voltage is developed as a consequence of the Seebeck effect, and depends on the temperature gradient ΔT across the TEG interface plates (see Equation (**3**-**5**)). The

open-circuit voltage of the TEG will therefore depend on a) the Seebeck coefficient of the TE pellets, which depend on the type of material; b) on the number of TE couples connected in series and c) the temperature difference between both interface plates. In reality the TEG's *p*- and *n*-type Seebeck coefficients ($\mu V/K$) vary non-linearly with the absolute temperature also, but this second order effect is not considered here.

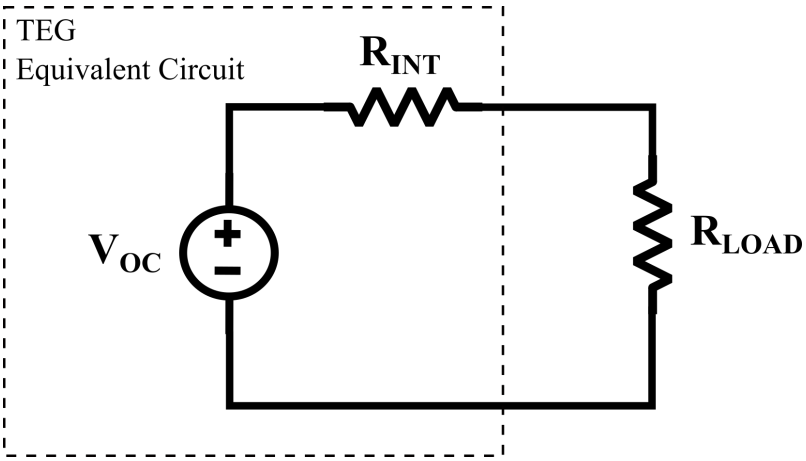

Figure 4–1 - Equivalent circuit of a TEG operated under constant ΔT

R_{INT} represents the internal resistance of the TEG, and its value depends on the resistance of all the TE pellets connected in series as well as the resistance of the interconnection tabs and the solder used to connect the TE pellets to the tabs. A theoretical calculation of R_{INT} might not lead to the correct value as it might not be straightforward to measure the equivalent length and area of the interconnection tabs and the solder used on each junction. Instead, a practical approach to obtain the equivalent internal resistance of a TEG is usually the preferred option. One simple method to measure R_{INT} consists of connecting the TEG to an electronic load, as in Figure 4–2, and measure the output voltage V_{OUT} at two different output current levels. The equivalent internal resistance can then be calculated as:

$$R_{INT} = \frac{\Delta V}{\Delta I} = \frac{V_{OUT,1} - V_{OUT,2}}{I_{LOAD,2} - I_{LOAD,1}} \tag{4-1}$$

Where $V_{OUT,1}$ can be the open-circuit voltage with $I_{LOAD,1}$ equal to zero.

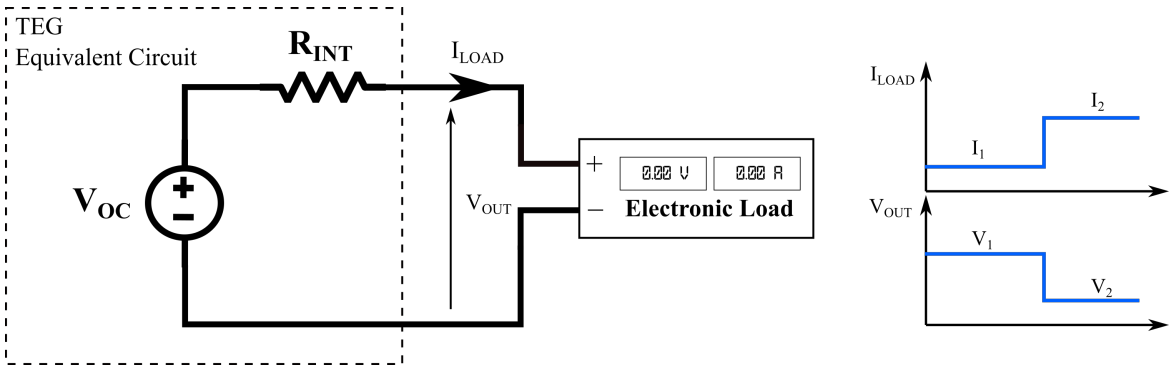

Figure 4–2 - Experimental setup to measure the equivalent series resistance of a TEG

The internal resistance and the Seebeck coefficient of a TEG are parameters that change with temperature and can be approximated by second order polynomial equations. Future references to the Seebeck coefficient α_{ab} will be made as just α, for simplicity. The temperature-dependent equations for the Seebeck coefficient and the equivalent internal resistance can be written as in Equations (**4-2**) and (**4-3**), respectively, with "*a, b, c, d, e* and *f*" being real coefficients.

$$\alpha(\Delta T) = a\Delta T^2 + b\Delta T + c \tag{4-2}$$

$$R_{INT}(\Delta T) = d\Delta T^2 + e\Delta T + f \tag{4-3}$$

The coefficients for Equations (**4-2**) and (**4-3**) can be calculated experimentally using the same test setup as in Figure 4–2. The Seebeck coefficient can be measured leaving the TEG in open-circuit (or zero current draw from the electronic load) and measuring the output voltage for different values of ΔT. In order to calculate the real coefficients of the internal resistance, the method used in Figure 4–2 has to be performed for different values of ΔT. Once the curves for $\alpha(\Delta T)$ and $R_{INT}(\Delta T)$ are obtained, the real coefficients can be obtained applying curve fitting methods. Table 4-1 shows the parameters $\alpha(\Delta T)$ and $R_{INT}(\Delta T)$ for two different TEGs, the monTE™ TEG device from Thermoelectric Conversion Systems[5] and the GM250-241-10-12™ of European Thermodynamics[6]. These parameters have been obtained by performing electrical measurements following the methodology presented herein.

[5] www.teconversion.com

[6] www.europeanthermodynamics.com

TEG Module	Seebeck coefficient	Internal resistance $R_{INT}(\Delta T)$
monTE™	0.0517	$-6\cdot10^{-6}\cdot\Delta T^2+0.0068\cdot\Delta T+1.6033$
GM250-241-10-	$-3\cdot10^{-6}\cdot\Delta T^2+0.098\cdot\Delta T$	$-2\cdot10^{-5}\cdot\Delta T^2+0.0231\cdot\Delta T+5.9357$

Table 4-1 - Second order polynomial representation of $\alpha(\Delta T)$ and $R_{INT}(\Delta T)$ for the monTE™ and GM250-241-10-12™

4.1.2 Characteristic curves of a TEG operated under constant temperature gradient

The output voltage and power of a TEG can be obtained experimentally with the test setup shown in Figure 4–2 measuring the output voltage and current for different values of load current. These measurements will provide the power and voltage curves of the TEG plotted against load current; and can be performed at different values of ΔT so that the output power and voltage characteristics can be examined at different temperature gradients. The measurements are performed with fixed cold side temperature, T_C, equal to 25 ^oC. On the other hand, these curves can be calculated using Equations (**3-22**) and (**3-23**) if the parameters $\alpha(\Delta T)$ and $R_{INT}(\Delta T)$ are known. For instance, using the parameters of the monTE™ defined in Table 4-1 the output power and voltage curves are obtained for values of ΔT equal to 50 ^oC, 100 ^oC, 150 ^oC, 200 ^oC and 250 ^oC. All the calculated values of output power and voltage required to plot the characteristic curves of the TEG are gathered in Table 4-2. The characteristic curves obtained from the calculated values are plotted in Figure 4–3 a), while Figure 4–3 b) shows the same curves obtained performing experimental measurements on the actual device. The curves of Figure 4–3 b) have been taken from the manufacturer's datasheet.

The accuracy of the calculated curves, once the parameters $\alpha(\Delta T)$ and $R_{INT}(\Delta T)$ have been accurately obtained, is observed by simple comparison of Figure 4–3 a) and b). The power curves show a single maximum value, defined by Equation (**3-25**), which corresponds to $V_{OC}/2$ and $I_{SC}/2$, with V_{OC} and I_{SC} being the instantaneous open-circuit voltage and short-circuit current, respectively, see Figure 3–7. This maximum point is commonly known as the Maximum Power Point, or MPP, and represents the maximum power the TEG can deliver for a given temperature gradient.

$\Delta T = 50^{o}C$			$\Delta T = 100^{o}C$			$\Delta T = 150^{o}C$		
I_{LOAD}	V_{OUT}	P_{OUT}	I_{LOAD}	V_{OUT}	P_{OUT}	I_{LOAD}	V_{OUT}	P_{OUT}
0.0 *A*	2.59 *V*	0.00 W_{el}	0.0 *A*	5.17 *V*	0.00 W_{el}	0.0 *A*	7.76 *V*	0.00 W_{el}
0.2 *A*	2.2 *V*	0.44 W_{el}	0.3 *A*	4.50 *V*	1.35 W_{el}	0.4 *A*	6.76 *V*	2.70 W_{el}
0.4 *A*	1.81 *V*	0.73 W_{el}	0.6 *A*	3.84 *V*	2.30 W_{el}	0.8 *A*	5.76 *V*	4.61 W_{el}
0.6 *A*	1.43 *V*	0.86 W_{el}	0.9 *A*	3.17 *V*	2.85 W_{el}	1.2 *A*	4.77 *V*	5.72 W_{el}
0.8 *A*	1.04 *V*	0.84 W_{el}	1.2 *A*	2.50 *V*	3.00 W_{el}	1.6 *A*	3.77 *V*	6.04 W_{el}
1.0 *A*	0.66 *V*	0.66 W_{el}	1.5 *A*	1.84 *V*	2.75 W_{el}	2.0 *A*	2.78 *V*	5.56 W_{el}
1.2 *A*	0.27 *V*	0.33 W_{el}	1.8 *A*	1.17 *V*	2.10 W_{el}	2.4 *A*	1.78 *V*	4.28 W_{el}
1.3 *A*	0.00 *V*	0.00 W_{el}	2.1 *A*	0.50 *V*	1.05 W_{el}	2.8 *A*	0.79 *V*	2.21 W_{el}
-	-	-	2.3 *A*	0.01 *V*	0.03 W_{el}	3.1 *A*	0.02 *V*	0.05 W_{el}

$\Delta T = 200^{o}C$			$\Delta T = 300^{o}C$		
I_{LOAD}	V_{OUT}	P_{OUT}	I_{LOAD}	V_{OUT}	P_{OUT}
0.0 *A*	10.34 *V*	0.00 W_{el}	0.0 *A*	15.51 *V*	0.00 W_{el}
0.5 *A*	8.98 *V*	4.49 W_{el}	0.7 *A*	13.34 *V*	9.34 W_{el}
1.0 *A*	7.62 *V*	7.62 W_{el}	1.4 *A*	11.17 *V*	15.63 W_{el}
1.5 *A*	6.26 *V*	9.38 W_{el}	2.1 *A*	8.99 *V*	18.89 W_{el}
2.0 *A*	4.89 *V*	9.79 W_{el}	2.8 *A*	6.82 *V*	19.10 W_{el}
2.5 *A*	3.53 *V*	8.83 W_{el}	3.5 *A*	4.65 *V*	16.27 W_{el}
3.0 *A*	2.17 *V*	6.51 W_{el}	4.2 *A*	2.48 *V*	10.40 W_{el}
3.5 *A*	0.81 *V*	2.83 W_{el}	4.9 *A*	0.30 *V*	1.49 W_{el}
3.8 *A*	0.02 *V*	0.07 W_{el}	5.0 *A*	0.03 *V*	0.12 W_{el}

Table 4-2 - Calculated values of output power and voltage, at different values of load current and for different temperature gradients

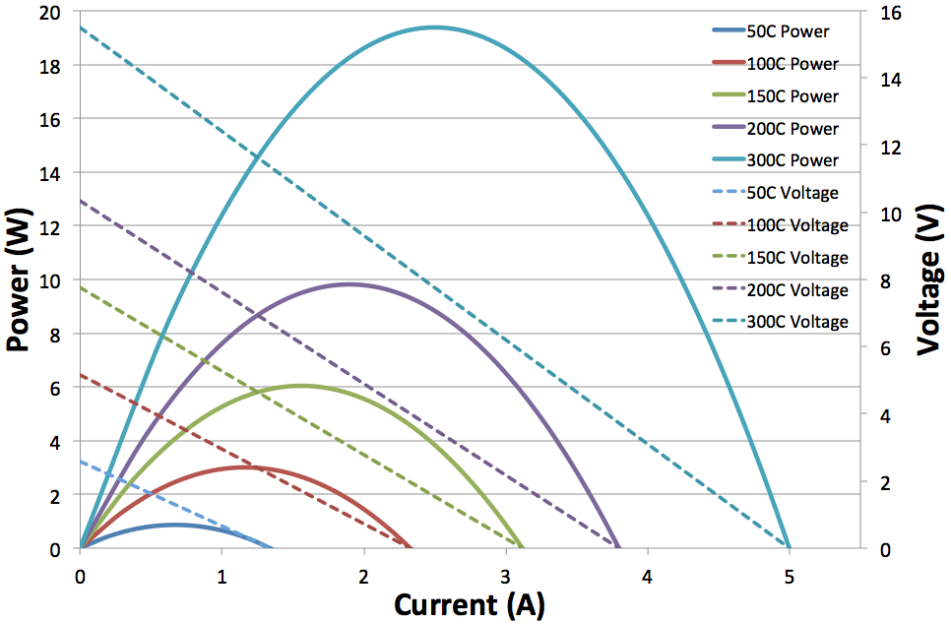

a)

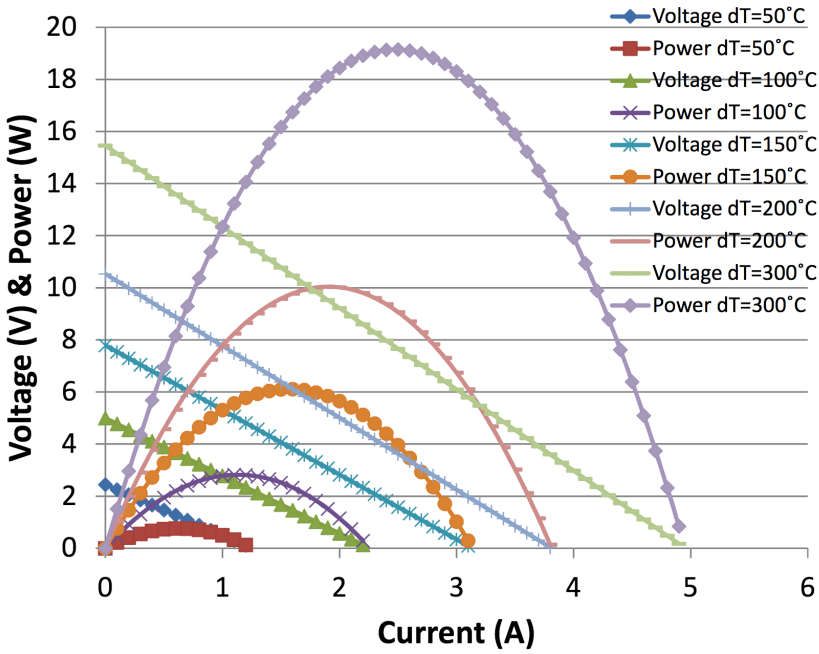

b)

Figure 4–3 - Power and voltage curves for the monTE™ obtained a) by calculation and b) performing experimental measurements (credit: Thermoelectric Conversion Systems, monTE™ datasheet).

4.1.3 Variable and unlimited heat flux conditions

The power and voltage curves, plotted against output current, for a TEG operated under constant ΔT have been presented and discussed in Section 4.1.2. The Peltier effect was introduced in Chapter 3 using Equation (**3-8**), and introduced in Equations (**3-38**) and (**3-40**) to account for the additional heat absorbed at the hot and cold sides of the TEG,

respectively, due to the current flowing through the TEG. The additional heat power absorbed at the hot side, due to the current flowing through the TEG is equal to $\dot{Q}_h = \alpha_{ab} \cdot T_H \cdot I$, with I being the TEG current. This additional power absorbed at the hot side can be expressed by the effect of the modulation of the effective thermal conductance of the TEG, K_{eff}, due to the current flowing through it. On that basis, the effective thermal conductance of the TEG can be expressed as:

$$K_{eff} = \frac{Q_h}{\Delta T} = \frac{Q_h}{T_H - T_C} \tag{4-4}$$

From the one-dimensional heat conduction equation, Equation (**3-38**) and, and neglecting the Thomson effect, the relationship between K_{eff} and the current through the TEG is found. This relationship is shown in Equation (**4-6**), with K_{TEG} being the thermal conductance of the TEG when zero current flows through it; *i.e.* open-circuit conditions.

$$Q_h = \frac{kA\Delta T}{L} + \alpha T_H I - \frac{1}{2} R_{int} I^2 \tag{4-5}$$

$$\begin{aligned} K_{eff} = \frac{Q_h}{\Delta T} &= \frac{\frac{kA\Delta T}{L} + \alpha T_H I - \frac{1}{2} R_{int} I^2}{\Delta T} = \frac{kA}{L} + \frac{\alpha T_H I}{\Delta T} - \frac{R_{int} I^2}{2\Delta T} \\ &= K_{TEG} + I \cdot \frac{V_{OUT} + \alpha(T_H + T_C)}{2\Delta T} \end{aligned} \tag{4-6}$$

The effective thermal conductance of the TEG is equal to the thermal conductance in open-circuit conditions, K_{TEG}, plus another factor proportional to the output current. When the output current increases, the effective thermal conductance increases too, hence the thermal resistance of the TEG decreases. When the thermal resistance of the TEG decreases, the temperature gradient across the TEG will decrease unless additional heat is introduced in the system. The opposite occurs when the output current decreases. Under these conditions, the effective thermal conductance decreases and the thermal resistance of

the TEG increases. With a higher thermal resistance, the temperature gradient across the TEG will increase, unless the external heat flux is decreased[7].

Indeed, when a test is performed under true constant temperature gradient a control loop is implemented in the heating system so that the heat flux is varied in order to maintain a constant ΔT across the TEG under variable load current. The effect of the thermal control loop is that the heat flux will increase or decrease until the ΔT reaches the target value. This situation defines the concept of variable and unlimited heat flux.

The efficiency of a TEG was discussed in Section 3.12, and the condition for maximum efficiency was shown in Equation (**3-47**), re-written in Equation (**4-7**). The maximum efficiency is achieved when $(R_{LOAD} / R_{INT}) > 1$, which means that the maximum efficiency is not found at the MPP, which corresponds to $(R_{LOAD} / R_{INT}) = 1$ (or $V_{OUT} = V_{MPP} = V_{OC}/2$), but at a voltage that is higher than V_{MPP}.

$$s = \frac{R_{LOAD}}{R_{INT}} = \sqrt{ZT_{AVG} + 1} \tag{4-7}$$

By taking a close look at the power curve of the TEG, Figure 4–3, it can be seen that the curve is very steep at the extremes, around $V_{OUT} = 0V$ and $I_{LOAD} = 0A$. The power curve, however, is quite flat around the MPP, where $dP/dV = 0$, which means that large variations of V_{OUT} will produce small variations in the output power, a situation that is graphically described in Figure 4–4. Also, working at output voltages that are higher than V_{MPP} require less heat flux from the thermal source. Based on these observations, one can say that the loss in electrical output power, when operating at a voltage $V_{MAX.EFF}$ that is somewhat higher than V_{MPP}, is lower than the extra heat flux that would be required to move the operating point from $V_{MAX.EF}$ to V_{MPP}. It is therefore more efficient to operate to the right of the MPP in the power-voltage characteristic curve (left of the power-current curve) than operating to the left (or to the right in the case of the power-current curve). It is very important to note that it is the thermal efficiency that increases when operating at $V_{MAX.EFF}$ and not the electric power. The point of maximum electric power generation remains at V_{MPP} (but the absolute value of the MPP may change).

[7] Note that a change in temperature gradient has a square-law effect on the MPP, since the output power is proportional to V^2.

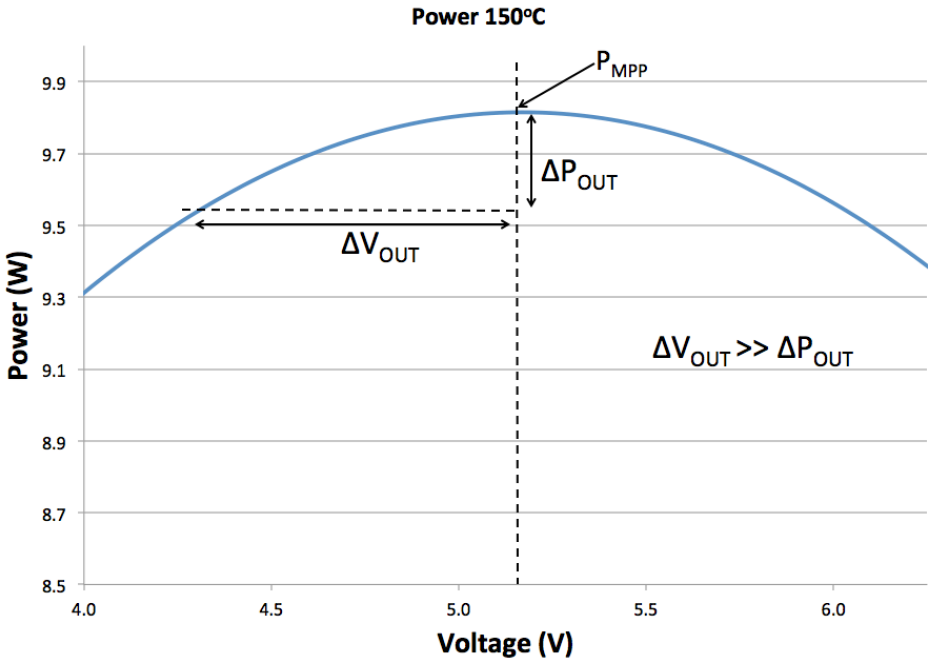

Figure 4–4 - Close view of the power-voltage characteristic curve of the TEG around the MPP

4.2 TEG operated under constant heat flux

4.2.1 Constant and limited heat flux conditions

The concept of variable and unlimited heat flux was explained Section 4.1.3. It represents the working regime for TEGs that operate under constant ΔT and variable heat flux.

In most applications, however, there is a limited amount of heat flux available from the heat source. For instance, in a combustion stove, the amount of heat power will depend on, and will be limited by, the energy produced by the internal combustion process. In a vehicle exhaust system, the heat flux will depend on the temperature of the exhaust gases travelling inside the pipe, the mass flow rate of these gases and the external temperature. Most heat waste applications produce a certain amount of heat that can be harvested and converted into electricity. However, the amount of heat generated is not increased or decreased in order to modify the temperature gradient across the TEG. This situation explains the concept of limited heat.

The concept of constant heat refers to the case in which the amount of limited heat flux across the TEG is fixed and does not vary with time. Most waste heat power sources will

vary the amount of heat power produced with time, and the magnitude of heat power will depend on the regime of the system (amount of combustible material in the case of the combustion stove or the engine speed in the case of the vehicle exhaust system). It is possible, however, to consider the amount of heat produced by a system as constant for limited periods of time. Also, the operation of a TEG under constant heat flux is very useful to highlight the main differences between operation under constant ΔT and constant heat flux (unlimited versus limited heat flux).

Based on Equations (**4-4**)-(**4-6**), the equivalent thermal conductance will increase or decrease when the output current increases or decreases respectively. Based on the assumption of constant and limited heat flux conditions there will be an increase or decrease of the temperature gradient across the TEG when the output current decreases or increases, respectively.

Another important difference between the operations under constant ΔT and constant heat flux is the operating point under which the TEG reaches maximum thermal efficiency. The efficiency of the TEG was defined in Equation (**3-43**), and re-written in Equation (**4-8**).

$$\eta_{TEG} = \frac{Output\ electric\ Power\ (P_{out})}{Heat\ flux\ absorbed\ at\ the\ hot\ junction\ (\dot{Q_H})} \tag{4-8}$$

Under constant heat flux conditions the denominator of Equation (**4-8**) is fixed and does not change with output current or, in a more general term, the operating point of the TEG. The maximum efficiency will be achieved when the output electric power, the numerator of the equation, is at its maximum; that is, at the MPP. In other words, when the TEG operates under constant heat flux, the point of maximum efficiency is the same as the MPP.

4.2.2 Theoretical characteristic curves of a TEG operated under constant heat flux

The characteristic curves of the TEG operated under constant heat flux are obtained using Equations (**3-5**), (**3-22**), (**3-23**), (**4-2**), (**4-3**) and (**4-5**), rearranged appropriately in Equations (**4-9**):

$$\alpha(\Delta T) = a\Delta T^2 + b\Delta T + c$$

$$R_{INT}(\Delta T) = d\Delta T^2 + e\Delta T + f$$

$$\Delta T = \frac{Q_h + \frac{1}{2}R_{int}I^2 - \alpha I T_C}{K_{TEG} + \alpha I} \tag{4-9}$$

$$V_{LOAD} = V_{OC} - R_{INT} \cdot I_{LOAD}$$

$$V_{OC} = \alpha \cdot \Delta T$$

$$P_{LOAD} = V_{OC} \cdot I_{LOAD} - R_{INT} \cdot {I_{LOAD}}^2$$

With the previous equations it is possible to find out the value of the electrical parameters and the temperature gradient across the TEG. The independent variable in the previous set of equations is the TEG output current, *I*. Parameters α and R_{INT} are temperature dependent parameters. Since the temperature gradient across the TEG changes when the operating point of the TEG is also changed, parameters α and R_{INT} will also change. In order to find out steady-state values an iterative loop is implemented for each operating point. In the first iteration of this iterative loop the temperature gradient ΔT is calculated and the new values of V_{LOAD}, V_{OC} and P_{LOAD} are calculated as well. During the second iteration, the values of α and R_{INT} are re-calculated with the new value of ΔT (from the previous iteration) and new values of ΔT, V_{LOAD}, V_{OC} and P_{LOAD} are re-calculated once again. With this iterative loop the temperature dependent parameters α, $R_{INT,}$ V_{LOAD}, V_{OC} and P_{LOAD} converge to their steady-state values for each value of output current. The flow chart of the iterative loop is shown in Figure 4–5 and it is applied in *Matlab*[8]. Ten iterations have proven to be sufficient to achieve good convergence to the steady-state values.

[8] www.mathworks.com

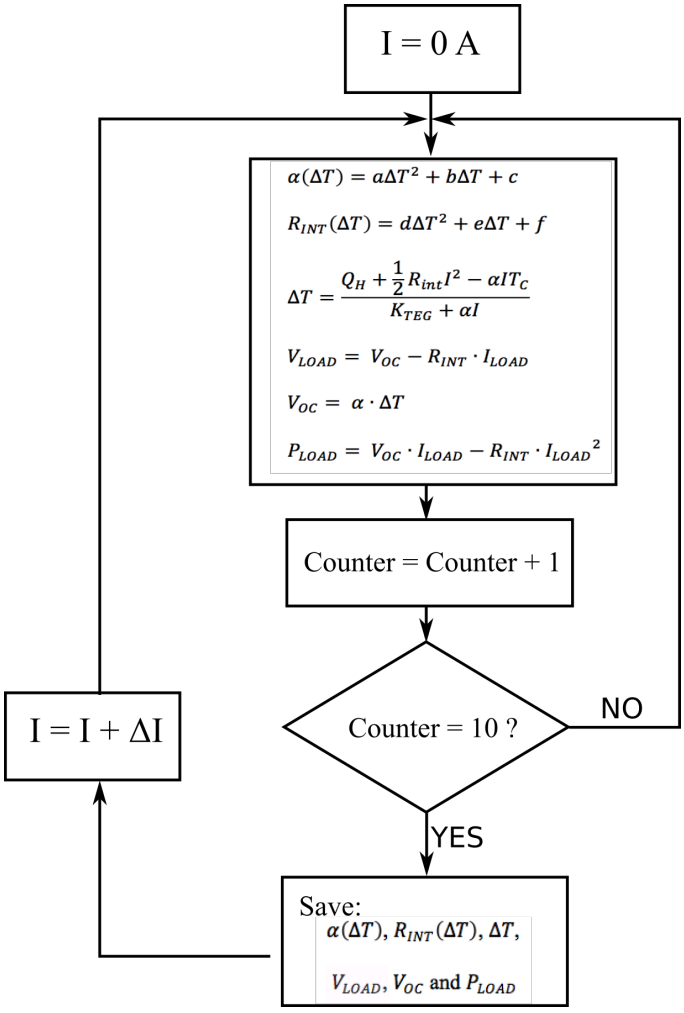

Figure 4–5 - Flow chart of the iterative loop to converge to steady-state values

Six different simulations have been performed for different values of input heat flux: 75 W_{th}, 100 W_{th}, 150 W_{th}, 200 W_{th}, 250 W_{th} and 300 W_{th}. The simulated TEG is the monTE™, and the parameters used are the same as in Section 4.1.2. The value of the thermal conductance is taken from the manufacturer's datasheet and has a value of $K = 1.03\ ^oC/W$. The cold side temperature is assumed to be 25 ^oC which is equal to 298.15 K. *Matlab* simulations are shown in the figures below, where the output electric power, TEG temperature gradient, output voltage and beta factor, have been plotted against output TEG output current. The beta factor is a new parameter that is defined as the ratio of the load output voltage to the instantaneous open-circuit voltage of the TEG, (see Equation (**4-10**)).

$$\beta\ (beta\ factor) = \frac{Load\ Voltage}{Instantaneous\ open-circuit\ voltage} = \frac{V_{LOAD}}{V_{OC}} \qquad (4\text{-}10)$$

Table 4-3 shows steady-state values of for different operating points, from open-circuit to short-circuit, of the TEG with an input heat flux of 75 W_{th}. Figure 4–6 shows the characteristic curves of output power and ΔT, Figure 4–7 shows the characteristic curves of output power and load voltage, and Figure 4–8 shows the characteristic curve of output power and β; all for $Q_h = 75\ W_{th}$.

$Q_h = 75\ W_{th}$				
Power (W)	**V_{TEG} (V)**	**I_{TEG} (A)**	**V_{OC} (V)**	**β**
0.000	3.994	0.0	3.994	1.000
0.676	3.378	0.2	3.792	0.891
1.112	2.780	0.4	3.599	0.772
1.319	2.198	0.6	3.413	0.644
1.305	1.631	0.8	3.236	0.504
1.080	1.080	1.0	3.065	0.352
0.651	0.543	1.2	2.902	0.187
0.027	0.019	1.4	2.745	0.007

Table 4-3 - Steady-state parameters for $Q_h = 75\ W_{th}$

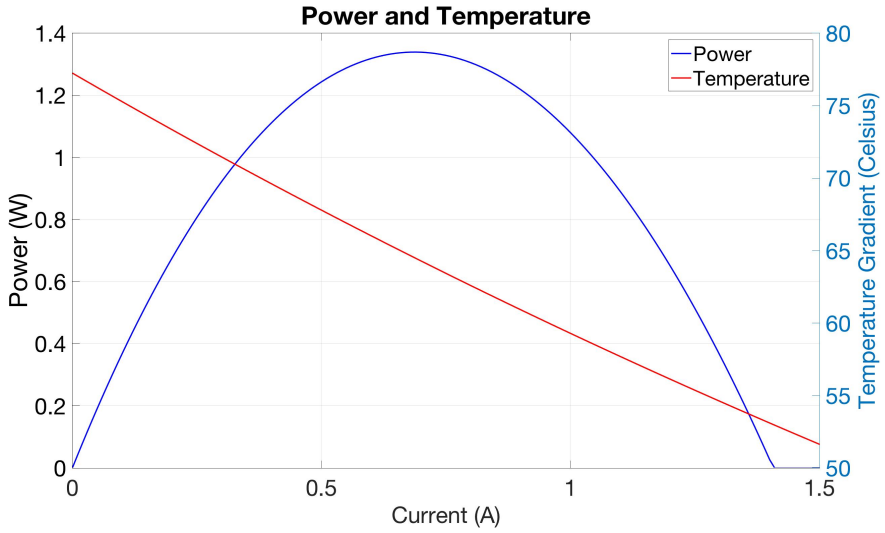

Figure 4–6 - Power and ΔT against TEG current for $Q_h = 75\ W_{th}$

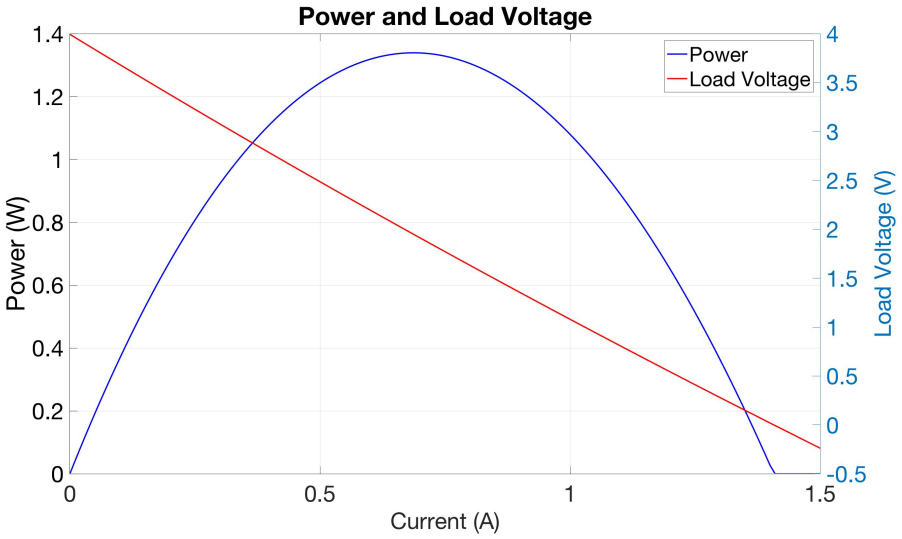

Figure 4–7 - Power and load voltage against TEG current for Q_h = 75 W_{th}

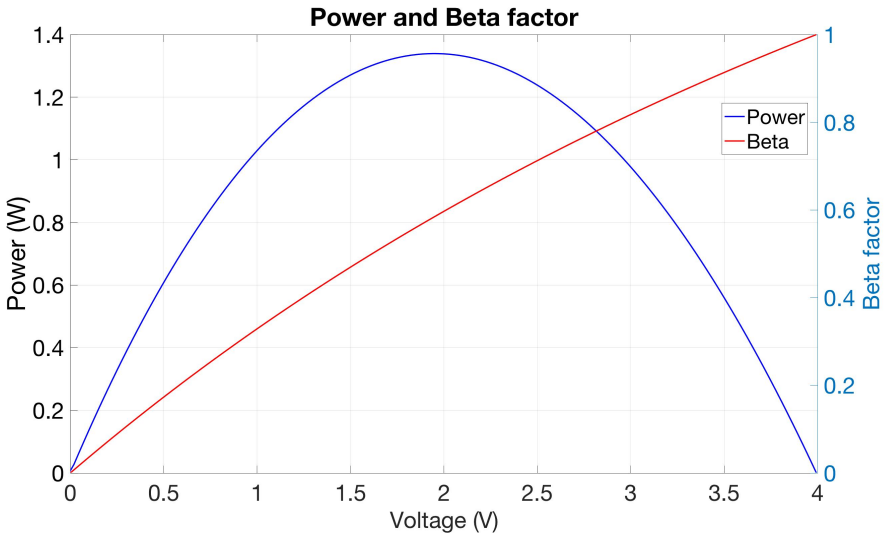

Figure 4–8 - Power and beta factor against load voltage for Q_h = 75 W_{th}

The steady-state curves, and steady-state values, for Q_h equal to 75 W_{th}, 100 W_{th}, 150 W_{th}, 200 W_{th}, 250 W_{th} and 300 W_{th} are presented in Appendix A.

By simple inspection of the previous figures, and the figures presented in Appendix A, three main conclusions can be drawn. Firstly, the power curve has a very similar shape to the power curves for constant ΔT obtained in Section 4.1.2. The power curve also contains a single point at which the generated output power presents a maximum value, the MPP. Secondly, the temperature gradient curve is not linear and, therefore, in accordance with Equation (**3-5**), the voltage curve is also non-linear. The third observation is that the MPP does not correspond to a point at which the beta factor is equal to 0.5 or, in other words, it

does not correspond to $V_{LOAD} = V_{OC}/2$. This last point highlights the main difference of the location of the MPP, with respect to the load current, between TEGs operated under constant ΔT and TEGs operated under constant heat flux.

Table 4-4 shows the simulated values of load voltage, instantaneous open-circuit voltage, maximum power and TEG current for the monTE™ for the values of heat flux presented in the previous figures.

	$Q_h=75W_{th}$	$Q_h=100W_{th}$	$Q_h=150W_{th}$	$Q_h=200W_{th}$	$Q_h=250W_{th}$	$Q_h=300W_{th}$
β_{MPP}	0.589	0.575	0.572	0.571	0.568	0.574
P_{MPP}	1.339	2.249	4.577	7.474	10.859	14.693
$V_{LOAD,MPP}$	1.969	2.555	3.814	5.084	6.314	7.653
$V_{OC,MPP}$	3.341	4.441	6.671	8.900	11.108	13.332
I_{MPP}	0.680	0.880	1.200	1.470	1.720	1.920

Table 4-4 - Electrical parameters of the monTE™ at the maximum power point. Values are given in SI units.

The value of the beta factor at the MPP is around 0.57 and it is not fixed but varies with the input heat flux.

4.2.3 Test fixture for testing TEGs under constant heat flux

In order to obtain the experimental characteristic curves using a TEG, a test jig capable of generating a constant heat flux has to be used. Such a test fixture is described in [111], [112] and it is represented in Figure 4–9.

The system uses a water-cooled heat-sink block placed at the top of the fixture and it is used as the cold side temperature reference of the TEG. The heat sink is made of aluminium, with a thermal conductivity equal to $\kappa_{Al} = 205\ W/m{\cdot}K$, and has a size of 40 *mm* x 40 *mm* x 25 *mm*. The temperature of the water is controlled and kept constant using a chiller that keeps the heat sink temperature at approximately 25 ^{o}C. This is done using a control loop on the heat pump that adjusts the coolant temperature in order to maintain it constant. One *K*-type thermocouple is placed in the heat sink, next to the TEG surface, and it is used to measure the temperature on the cold plate of the TEG.

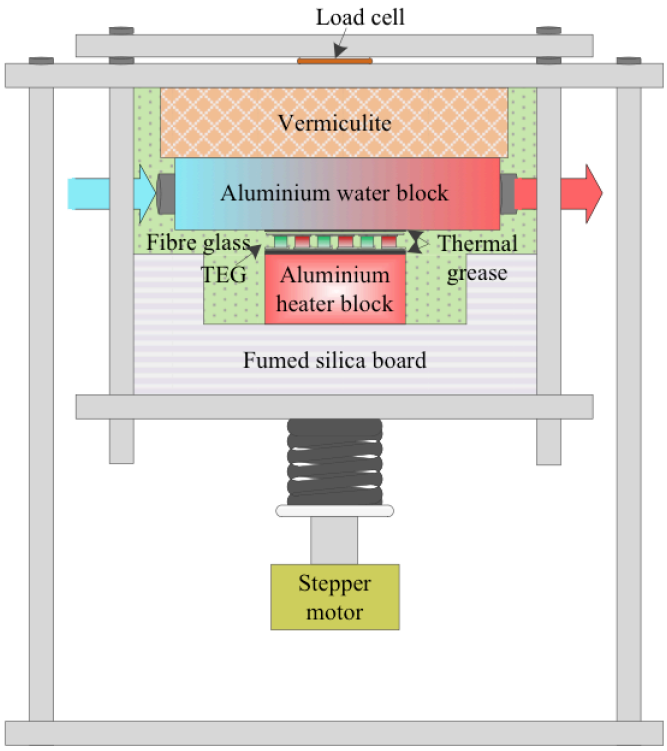

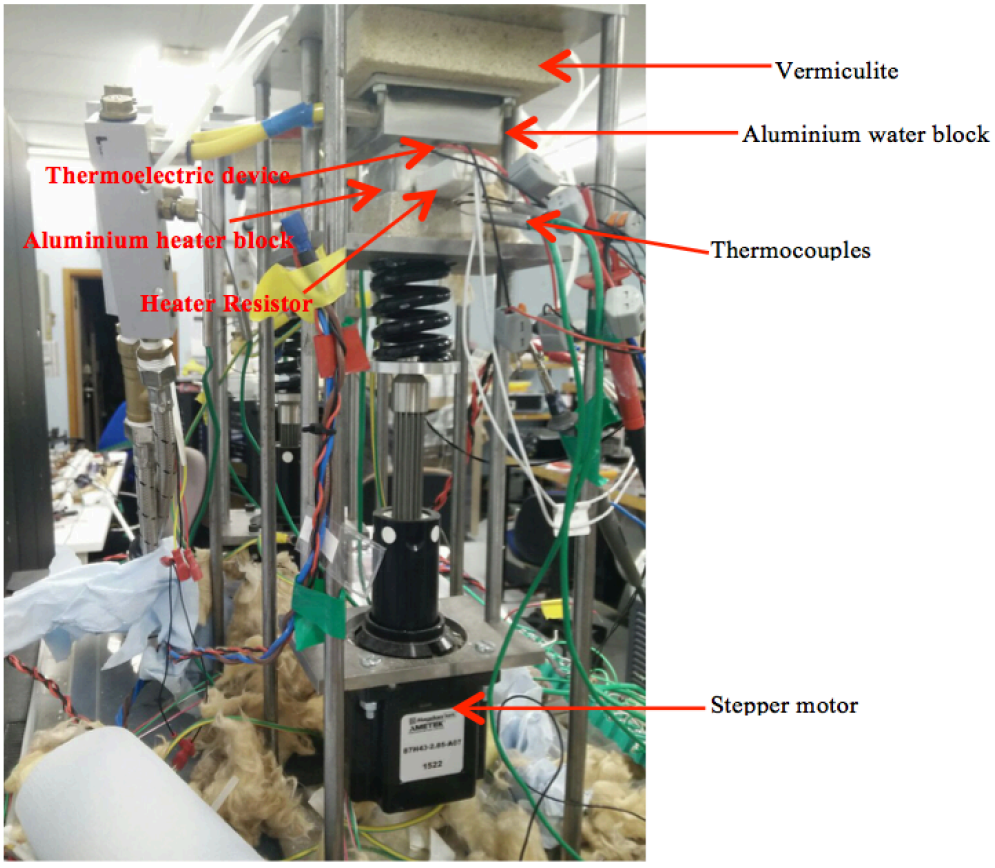

Figure 4–9- Test fixture used to obtained the characteristic curves of the TEG. Reprinted from Applied Energy 212 (2018) 293-303, Transient response of a thermoelectric generator to load steps under constant heat flux, with permission from Elsevier

Heat is provided to the system by a silicon nitride electrical igniter (Glo120-400-370URF) rated to 500 W_{el} placed inside an aluminium heater block, which is placed underneath the TEG. The heater block is placed on a moveable plate that is pushed towards the heat sink block in order to have the TEG sandwiched between the heater block and the heat sink. The heater is connected to a power supply that controls the amount of power delivered to it. The surface of the heater block has the same area as the TEG under test; in this case 40 *mm* x 40 *mm*, and it is made of aluminium having the same thermal conductivity as the heat sink. There are two *K*-type thermocouples symmetrically placed in the heater block used to measure the temperature on the hot face of the TEG. Each thermocouple is introduced from the bottom of the heater block through a 3 *mm* hole, reaching the hot plate of the TEG on the topside of the heater block.

A fumed silica block, with a thermal conductivity equal to $\kappa_{Silica} = 0.02\ W/m{\cdot}K$, is placed between the moving plate and the heater block and is used to thermally isolate the heater block from the moving plate thus enhancing the thermal conductivity across the TEG towards the heat sink. Fibre-glass, with thermal conductivity equal to $\kappa_{Fibre} = 0.04\ W/m{\cdot}K$, is used around the TEG assembly to reduce radiation and convection losses to ambient. Heat absorbed from ambient to the cooling block is also minimized by the use of a vermiculite block, with a thermal conductivity equal to $\kappa_{Verm} = 0.07\ W/m{\cdot}K$, between the heat sink and the topside plate [112].

The clamping force of the TEG between the water-cooled heat sink and heater block is applied using a 179 *N/mm* spring placed underneath the moving plate. The clamping force is controlled using a stepper motor and can be adjusted to any desired setting, up to a maximum clamping force of 180 *Kg*. A load cell is used to measure the clamping force applied to the TEG.

The instruments used to log the data of the different sensors, drive the heater and apply electrical load to the TEG are listed in Table 4-5 and shown in Figure 4–10. Temperature and electrical measurements are performed by a data-logger and all instruments are controlled by a VEE pro[9] PC interface, see Figure 4–11.

[9] www.keysight.com

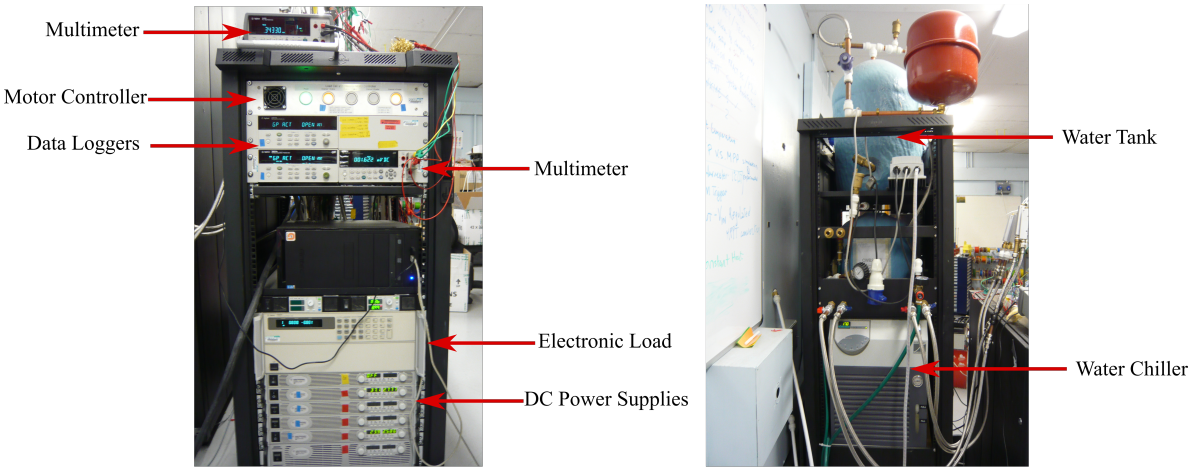

Figure 4–10 – a) Test instruments b) Water chiller and water tank

Equipment	Model	Function
Power Supply Unit	Agilent N5750	Drive the heater inside the heater block
Electronic Load	Agilent N3300A	Apply electrical load to the TEG
Data Acquisition Unit	Agilent 34972A	Measure the hot and cold side temperatures
Digital Multimeter	Agilent 34410A	Measure the output current from the TEG
Digital Multimeter	Agilent 34405A	Measure the output voltage of the TEG

Table 4-5 - Equipment used in the test fixture

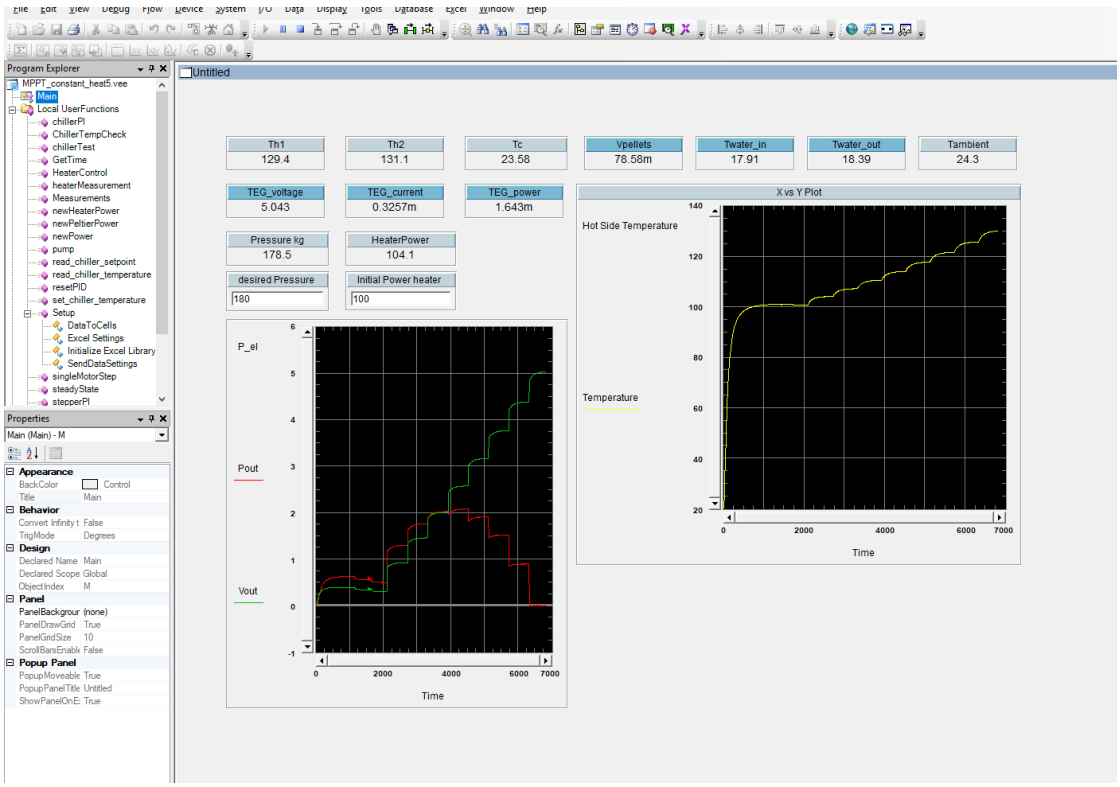

Figure 4–11 - VEE program interface used to test TEGs under constant heat flux

The accuracy of the measurements performed with the instruments described in Table 4-5 will be limited by the accuracy of each instrument. The accuracy of the voltmeter is ±0.025 *%*, the accuracy of the ammeter is ±1.1 to 3.6 *mA* in the range of 1 to 3 *A*. The accuracy of the temperature measurements is ±1 ^{o}C for the data acquisition unit and ±1.6 ^{o}C for the thermocouple up to 400 ^{o}C. Measuring current and voltage is straightforward and it only requires an accurate measurement device, like the devices shown in Table 4-5. Measuring temperature is not a straightforward task, as it requires precise and accurate coupling of the thermal sensor, a *K*-type thermocouple in this specific application, to the element the temperature of which is to be measured. It is therefore important to note that the highest error in the different measurements shown in this work is the error associated to the temperature readings.

4.2.4 Heat losses in the TEG system

The thermal system is not perfectly insulated and part of the heat generated by the heater block is lost to the surrounding environment. The equivalent thermal model of the TEG system is shown in Figure 4–12, where θ_x represents the thermal impedance of an element of the system and T_x the temperature at a given point in the system.

The heat flux is represented by an ideal current source, the thermal resistance of the different elements are represented by resistors and the temperature at the different points of the system by node voltages. The heat lost (absorbed) to (from) ambient is also represented by currents flowing to (from) the ambient temperature, which is also represented by a node voltage ($T_{AMBIENT}$). The different parameters shown in Figure 4–12 are defined in Table 4-6.

The heat flux from the different elements of the system to/from ambient is minimized by the use of the fumed silica and vermiculite blocks and the fibre-glass around the TEG, heater block and heat sink. The insulation provided by these elements is, however, not perfect and there will be heat losses to ambient. These extra losses have been characterized and the heat flux in the system is modified in order to compensate for such losses. The amount of heat lost between the TEG system and ambient, defining ambient as the external boundary of the system, depends on the temperature of the system and the ambient temperature.

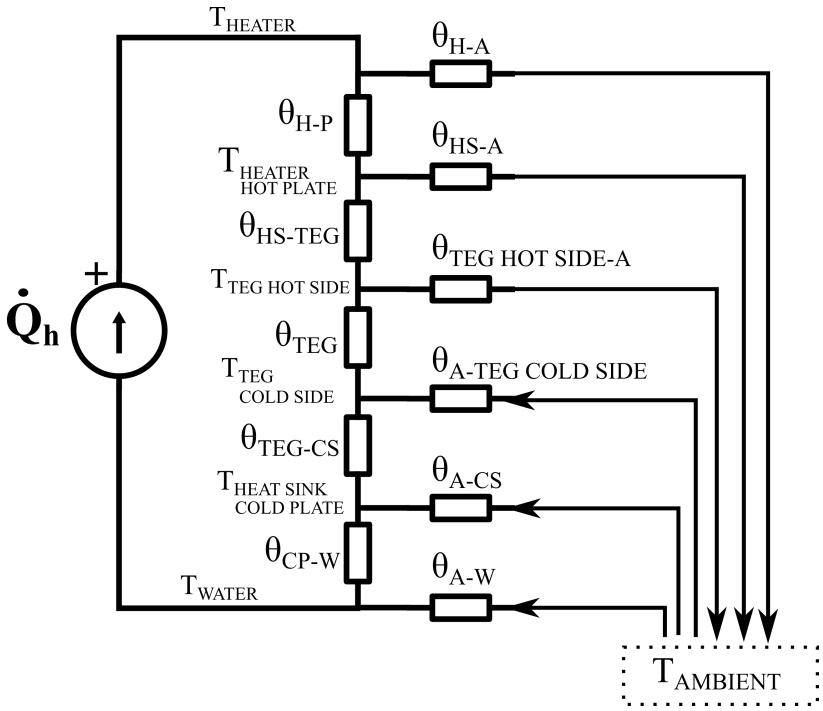

Figure 4–12 - Thermal model of the TEG system

Element	Definition
θ_{H-P}	Thermal resistance between the resistive heater and the surface of the heater block
θ_{HS-TEG}	Thermal resistance of the hot side of the TEG
θ_{TEG}	Thermal resistance of the TEG
θ_{TEG-CP}	Thermal resistance of the cold side of the TEG
θ_{CP-W}	Thermal resistance between the surface of the heat sink plate and the cooling water
θ_{H-A}	Thermal resistance between the resistive heater and ambient
θ_{HS-A}	Thermal resistance between the hot plate of the heater and ambient
$\theta_{TEG\ HOT\ SIDE-A}$	Thermal resistance between the hot side of the TEG and ambient
$\theta_{A-TEG\ COLD\ SIDE}$	Thermal resistance between ambient and the cold side of the TEG
θ_{A-CP}	Thermal resistance between ambient and the surface of the cold plate
θ_{W-A}	Thermal resistance between ambient and the cooling water
T_{HEATER}	Temperature of the resistive heater
$T_{HEATER\ HOT\ PLATE}$	Temperature of the hot plate of the heater block in contact with the TEG
$T_{TEG\ HOT\ SIDE}$	Temperature of the hot side of the TEG (on the pellets)
$T_{TEG\ COLD\ SIDE}$	Temperature of the cold side of the TEG (on the pellets)
$T_{HEAT\ SINK\ COLD}$	Temperature of the cold plate of the heat sink in contact with the TEG
T_{WATER}	Temperature of the cooling water
$T_{AMBIENT}$	Ambient temperature

Table 4-6- Definition of the elements represented in the equivalent thermal model of the TEG system (Figure 4–12)

In order to characterize the heat losses the TEG is replaced by a 40 *mm* x 40 *mm* x 25 *mm* vermiculite block. Knowing the thermal conductivity of the vermiculite, the heat losses can be characterize using Equation (**4-11**):

$$Q_{losses} = P_{HEATER} - Q_{VERM} = P_{HEATER} - \kappa_{VERM} A_{VERM} \frac{T_H - T_C}{l_{VERM}} \quad (4\text{-}11)$$

Where P_{HEATER} is the electric power in the heater resistive element, Q_{VERM} the heat flux across the vermiculite block and κ_{VERM}, A_{VERM}, l_{VERM} the thermal conductivity, surface area and length of the vermiculite block, respectively. T_H is the temperature at the interface between the heater and the vermiculite blocks, and T_C is the temperature at the interface between the vermiculite and the surface of the water-cooled heat sink.

A test performed for input heat power from 2 W_{th} to 10 W_{th}, with increments of 2 W_{th}, was performed, allowing for steady-state thermal conditions to be reached before temperature measurements, across the vermiculite block, were taken. In this experiment it is considered that steady-state conditions are reached when the difference between the maximum and minimum value of the hot side temperature, of 50 consecutive measurements, was less than 0.1 ^oC.

After steady-state conditions are reached the hot and cold side temperatures, T_H and T_C, are recorded. The heat losses are then calculated using Equation (**4-11**), and the results are shown in Table 4-7 and plotted in Figure 4–13. The best-fit trend line of the points plotted in the graph is also shown in Figure 4–13. The hot side temperature T_H has been chosen as the independent variable of the equation, or the variable plotted in the abscissa axis, due to the low dependency of the heat losses on the hot side temperature [112].

Heat Power	T_H	Heat
0 W_{th}	0 ^oC	0 W_{th}
2 W_{th}	71.05 ^oC	1.794 W_{th}
4 W_{th}	118.5 ^oC	3.583 W_{th}
6 W_{th}	162.9 ^oC	5.385 W_{th}
8 W_{th}	204.2 ^oC	7.201 W_{th}
10 W_{th}	242.8 ^oC	9.031 W_{th}

Table 4-7 - Hot side temperature and heat losses for different values of input heat power

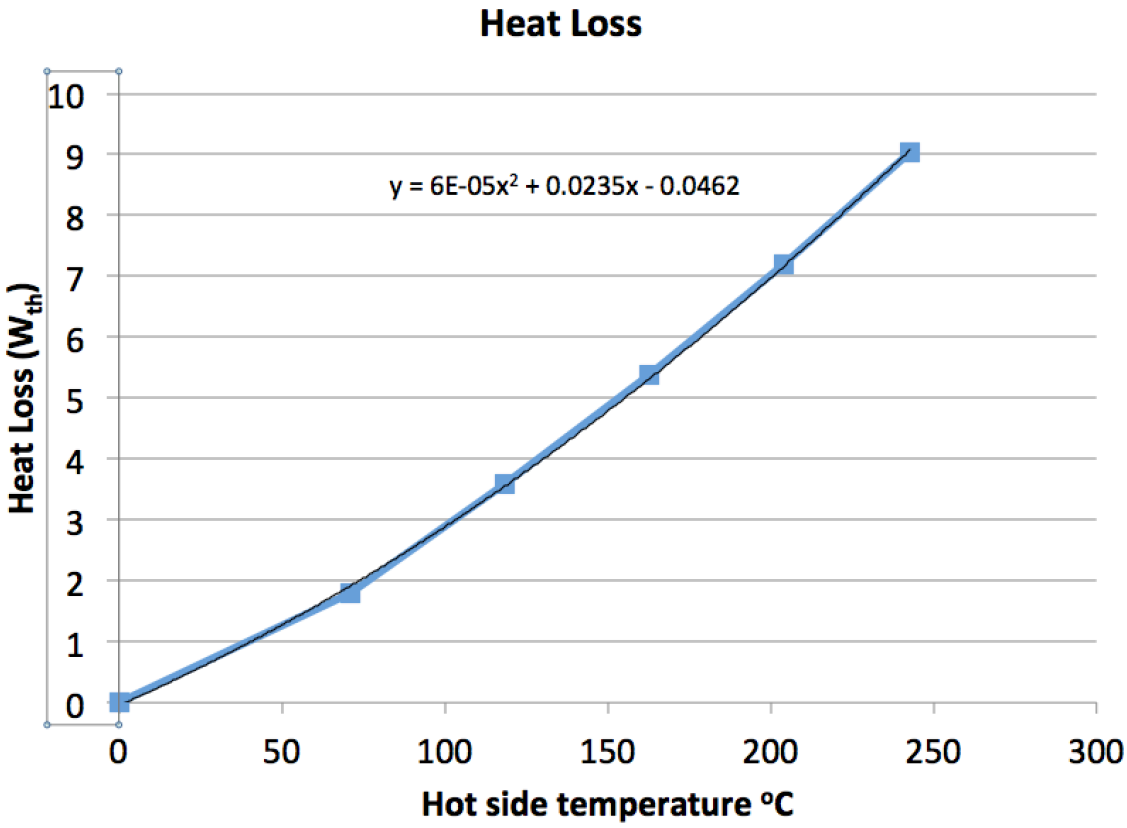

Figure 4–13 - Heat losses plotted against hot side temperature

Once the thermal losses are characterized, a simple method to compensate for them is used in the control of the heater. This method consists of measuring the hot side temperature of the TEG and injecting extra heat to compensate against the losses. The amount of extra heat required to compensate against thermal losses is calculated using Equation (**4-12**).

$$Q_{losses} = 6 \cdot 10^{-5} \cdot {T_H}^2 + 0.0235 \cdot T_H - 0.0462 \quad (4\text{-}12)$$

This equation is valid for temperatures in the hot side above 40 ^{o}C, which are the temperatures reached on the hot side during the experiment and this method is used for the tests performed throughout the work presented in this thesis.

4.2.5 Experimental characteristic curves of a TEG operated under constant heat flux

The experimental curves of the monTE™ have been obtained by performing electrical measurements using the test fixture described in Section 4.2.3. The heat losses are compensated for using the methodology described in Section 4.2.4. Compensating for the heat losses is required in order to ensure a known constant and accurate heat flux through the TEG under test.

A minimum of six equally spaced operating points has proved to be sufficient to obtain accurate characteristic curves. The TEG was driven into such operating points using an electronic load that operated the device to the desired point of the curve. The electronic load described in Table 4-5 was the one used to change the operating point of the TEG.

Six different tests have been performed at different levels of input heat power; that is, 75 W_{th}, 100 W_{th}, 150 W_{th}, 200 W_{th}, 250 W_{th} and 300 W_{th}. Depending on the value of input heat power, the number of operating points was varied between eight and ten. These operating points were set, by changing the load current delivered by the TEG, using the electronic load that applies current steps of the same magnitude on each test. All the operating points were measured once steady-state conditions had been reached. Previous tests demonstrated that steady state conditions were reached after 480 seconds, so the operating point of the TEG was changed every 480-540 seconds, approximately.

The physical distance between TEG and the digital multimeters was around one meter. The impedance of the cabling was around 200 $m\Omega$ so, when the TEG was short-circuited, the TEG output voltage was not zero and was the voltage resulting from the potential divider between the internal resistance of the TEG and the impedance of the cabling. It was, therefore, not possible to obtain zero volts when the output terminals of the TEG were short-circuited. The non-zero voltage when the terminals of the TEG were short-circuited prevented the TEG from operating, strictly speaking, at the actual short circuit operating point. Using curve-fitting techniques it was possible to interpolate the characteristic curves around the zero voltage region.

As stated in Section 4.2.3 there are two thermocouples that measured the temperature at the hot plate of the TEG. The hot side temperature was calculated as the average of the temperature provided by the two sensors.

The monTE™ is a TEG that is made of 196 pairs of nominally identical pellets, three of which are not connected to the main string of pellets and, therefore, are not used for power generation. Instead, they are used as a sensor that provides a voltage that is proportional to the instantaneous open-circuit voltage of the TEG. This information was used to calculate the instantaneous open-circuit voltage allowing the calculations of the beta factor. The ratio between the open-circuit voltages of the 193 main pairs of pellets to the 3 used for sensing is equal to:

$$Pellets\ Ratio = \frac{V_{OC,TEG}}{V_{OC,PELLETS}} = \frac{193}{3} = 64.33 \tag{4-13}$$

This ratio has been measured experimentally using the test fixture and the pellets ratio is plotted in Figure 4–14. The differences between the theoretical calculation of Equation (**4-13**) and the measurements are due to the non-ideal heat and temperature distribution across the TEG. However, a good approximation for the range of temperatures under which the TEG will operate can be done by selecting $V_{OC}/V_{pellets}$ = 63.

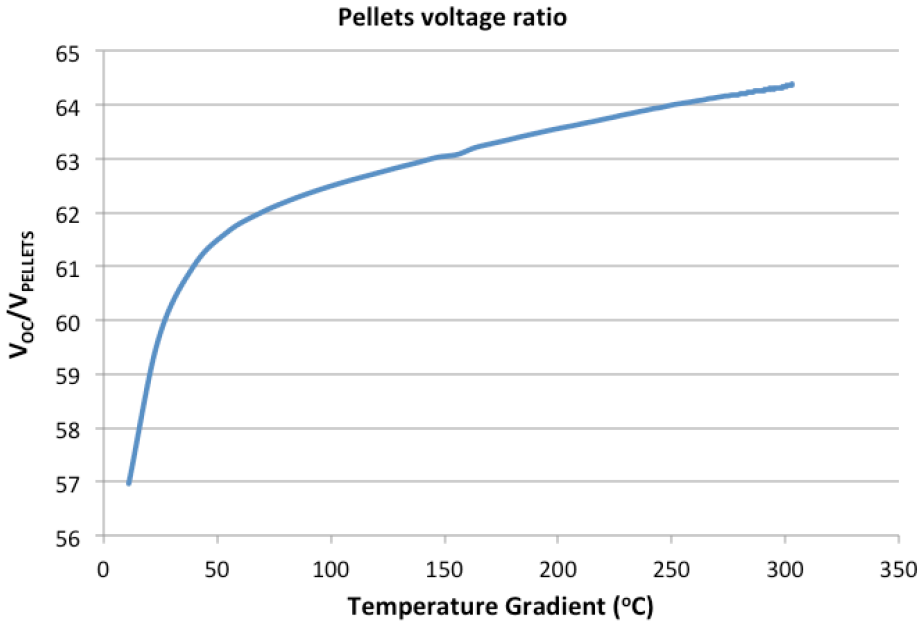

Figure 4–14- Ratio of the open-circuit voltage of the main output to the open-circuit voltage of the sensing pellets

Table 4-8 shows the steady-state values of different TEG parameters at different operating points for an input heat power equal to 75 W_{th}. The operating points have been changed in steps of 200 mA, approximately. TEG power and ΔT curves are plotted against load current

in Figure 4–15. TEG power and load voltage curves, plotted against load current, are shown in Figure 4–16. TEG power and beta factor have been plotted against load voltage in Figure 4–17. All these curves have been obtained with the values in Table 4-8.

T_H (°C)	T_C (°C)	ΔT (°C)	P_{HEATER} (W)	I_{LOAD} (A)	V_{TEG} (V)	$V_{PELLETS}$ (V)	Power (W)	V_{OC} (V)	β
100.532	22.194	78.338	77.964	-0.001	3.647	0.057	-0.002	3.576	1.020
96.617	22.135	74.482	77.831	0.204	3.052	0.054	0.623	3.387	0.901
92.960	22.052	70.908	77.713	0.407	2.479	0.051	1.008	3.212	0.772
89.619	22.125	67.494	77.605	0.607	1.932	0.048	1.172	3.049	0.634
86.433	22.147	64.286	77.481	0.807	1.399	0.046	1.129	2.893	0.483
83.435	22.185	61.250	77.388	1.005	0.881	0.044	0.886	2.747	0.321
80.756	22.522	58.234	77.318	1.224	0.323	0.041	0.396	2.606	0.124

Table 4-8 - Steady-state values of the TEG parameters used to plot the characteristic curves at $Q_h = 75\ W_{th}$

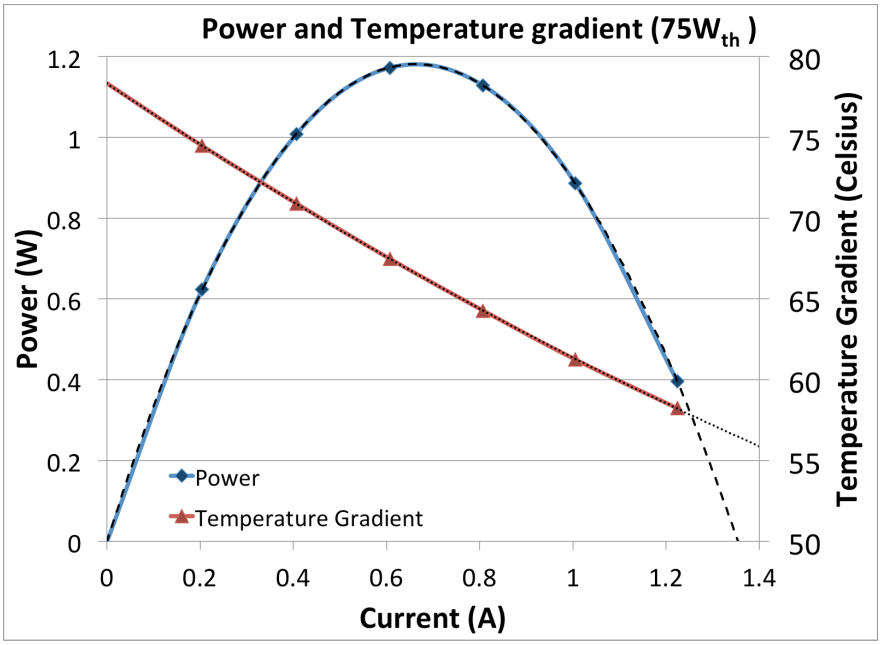

Figure 4–15 - Power and temperature gradient against TEG current for $Q_h = 75\ W_{th}$

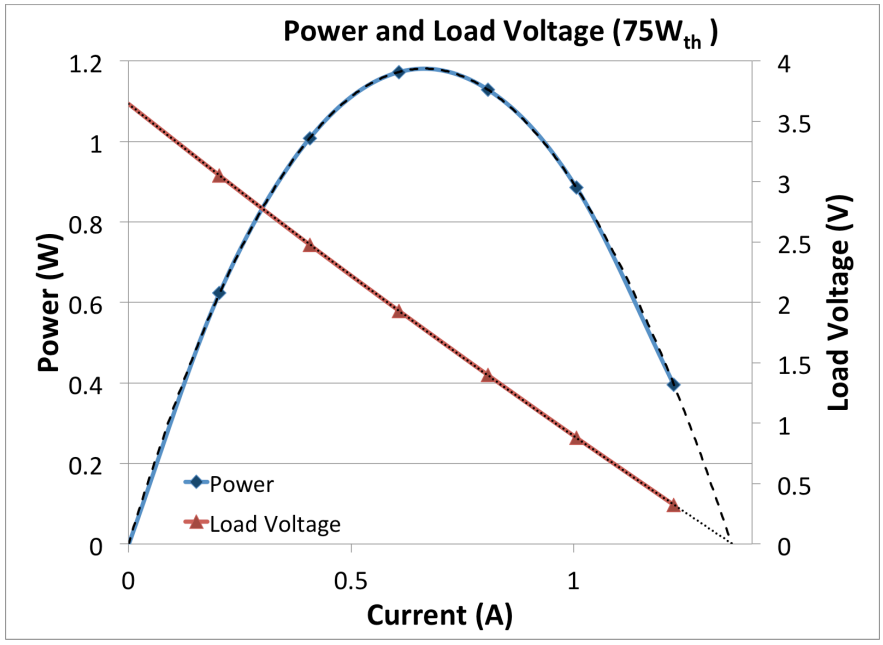

Figure 4–16 - Power and output voltage against TEG current for Q_h = 75 W_{th}

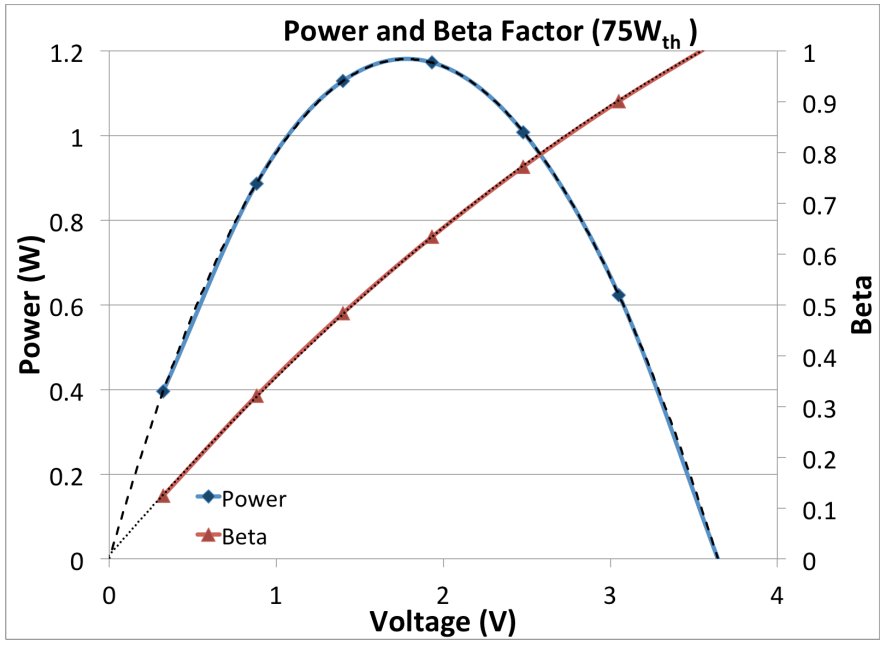

Figure 4–17 - Power and beta factor against output voltage for Q_h = 75 W_{th}

The steady-state values and graphs for input heat fluxes equal to 100 W_{th}, 150 W_{th}, 200 W_{th}, 250 W_{th} and 300 W_{th} are presented in Appendix B.

It can be observed that the temperature and load voltage curves, when plotted against the TEG current, are not straight lines, unlike the case when the TEG operates under constant ΔT.

There is a difference between the experimental values and the theoretical values obtained in Section 4.2.2. The main reason being that the experimental setup used, and described in Section 4.2.3, does not represent an ideal system. Table 4-9 shows the difference between the experimental and theoretical values at the MPP. Besides, the heat loss compensation implemented on the heater control calculates the heat loss based on the hot-side temperature, as per Equation (**4-12**). However, the temperature conditions in the lab, as well as the atmospheric pressure, will have an impact on the heat losses, due to the convection losses, that are not accounted for in Equation (**4-12**). For this reason, it is important to note that the repeatability of the results is subject to the environmental conditions of the lab, and different results can be obtained for the same experiment if they are performed under different conditions.

This dependability on the environmental conditions in the lab has been observed throughout the experiments presented in this work. In some cases, the results obtained (and not presented in this thesis) were not valid; *i.e.* the results differed significantly from the expected results based on simulations, and it was observed that the experiment was affected by the air conditioning system of the lab. In some other cases, it was observed that a window was open. Repeating the experiment after turning off the air conditioning unit or closing the window provided results that much closer to the expected results.

The calculated difference in Table 4-9 is a relative difference with respect to the values obtained in the simulations, and it is calculated using Equation (4-14).

$$Diff.(\%) = 100 \cdot \frac{|VALUE_{EXPERIMENT} - VALUE_{SIMULATION}|}{VALUE_{SIMULATION}} \quad (4\text{-}14)$$

Figure 4–18 shows the optimum values of the beta factor (value of the beta factor at the MPP) plotted against input heat flux. The values are shown for both theoretical (simulation) and experimental results. For values of input heat flux lower than 200 W_{th} the value of beta decreases with input heat flux, which is in agreement with the results reported by [112]. This decreasing trend occurs for both theoretical and experimental curves. For values higher than 200 W_{th} there is not a clear trend but the values seem to stabilize around 0.57.

	$Q_h = 75\ W_{th}$			$Q_h = 100\ W_{th}$		
	Simulation	Experiment	Diff.	Simulation	Experiment	Diff.
β	0.589	0.612	**3.83%**	0.575	0.611	**6.21%**
P_{MPP} (W)	1.339	1.176	**12.18%**	2.249	2.088	**7.14%**
$V_{LOAD,MPP}$ (V)	1.969	1.850	**6.06%**	2.555	2.540	**0.60%**
$V_{OC,MPP}$ (V)	3.341	3.023	**9.53%**	4.441	4.157	**6.40%**
I_{MPP} (A)	0.680	0.640	**5.88%**	0.880	0.830	**5.68%**
	$Q_h = 150\ W_{th}$			$Q_h = 200\ W_{th}$		
	Simulation	Experiment	Diff.	Simulation	Experiment	Diff.
β	0.572	0.590	**3.20%**	0.571	0.564	**1.26%**
P_{MPP} (W)	4.577	4.535	**0.91%**	7.474	7.605	**1.76%**
$V_{LOAD,MPP}$ (V)	3.814	3.785	**0.76%**	5.084	4.880	**4.01%**
$V_{OC,MPP}$ (V)	6.671	6.415	**3.83%**	8.900	8.652	**2.78%**
I_{MPP} (A)	1.200	1.200	**0.00%**	1.470	1.564	**6.39%**
	$Q_h = 250\ W_{th}$			$Q_h = 300\ W_{th}$		
	Simulation	Experiment	Diff.	Simulation	Experiment	Diff.
β	0.568	0.582	**2.39%**	0.574	0.561	**2.26%**
P_{MPP} (W)	10.859	10.954	**0.87%**	14.693	14.135	**3.80%**
$V_{LOAD,MPP}$ (V)	6.314	6.300	**0.22%**	7.653	7.125	**6.90%**
$V_{OC,MPP}$ (V)	11.108	10.825	**2.55%**	13.332	12.701	**4.74%**
I_{MPP} (A)	1.720	1.742	**1.28%**	1.920	1.990	**3.65%**

Table 4-9 - Divergence of TEG parameters at the MPP between the theoretical and experimental characteristic curves, for 75 W_{th}, 100 W_{th}, 150 W_{th}, 200 W_{th}, 250 W_{th}, 300 W_{th} (Diff. = Difference between simulation and experimental results)

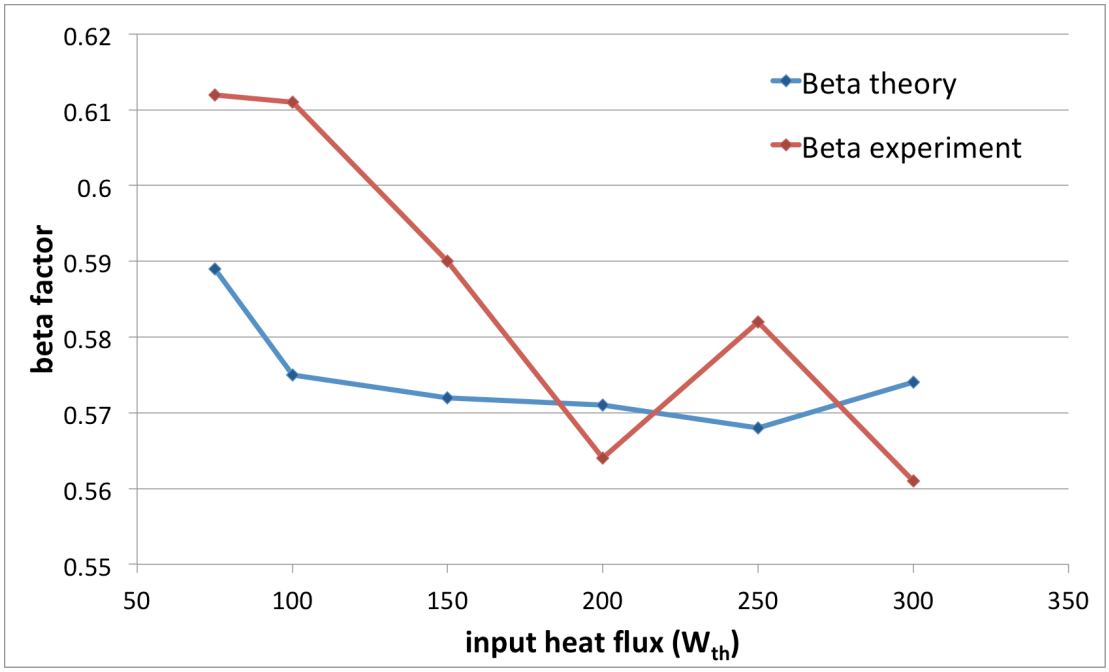

Figure 4–18 - Values of the beta factor at the MPP plotted against input heat flux

4.2.6 Analytical calculation of the maximum power point

The MPP of TEGs operated under constant heat flux can be found by simple inspection of the characteristic curves shown in Sections 4.2.2 and 4.2.5. This is not always practical, and an analytical solution must be found. The solution is found using Equations (**3-23**) and (**3-38**), rewritten in Equations (**4-15**) and (**4-16**), respectively, where $K=\kappa A/L$ (thermal conductance).

$$P_{LOAD} = V_{OC} \cdot I_{LOAD} - R_{INT} \cdot {I_{LOAD}}^2 = I \cdot (\alpha \cdot \Delta T - R_{INT} \cdot I); \text{ with } I = I_{LOAD} \quad (4\text{-}15)$$

$$\dot{Q_h} = K \cdot \Delta T - \frac{1}{2} \cdot R_{INT} \cdot I^2 + \alpha \cdot T_H \cdot I \quad (4\text{-}16)$$

Knowing that:

$$T_H = \Delta T + T_C \quad (4\text{-}17)$$

Equation (**4-16**) becomes:

$$\begin{aligned} \dot{Q_h} &= K\Delta T - \frac{1}{2} R_{INT} I^2 + \alpha(\Delta T + T_C) I \\ &= \Delta T(K + \alpha I) + \alpha I T_C - \frac{1}{2} R_{INT} I^2 \\ &\Rightarrow \Delta T(K + \alpha I) = \dot{Q_H} - \alpha I T_C + \frac{1}{2} R_{INT} I^2 \\ &\Rightarrow \Delta T = \frac{\dot{Q_H} - \alpha I T_C + \frac{1}{2} R_{INT} I^2}{(K + \alpha I)} \end{aligned} \quad (4\text{-}18)$$

Substituting Equation (**4-18**) into Equation (**4-15**):

$$P_{LOAD} = \alpha I \cdot \frac{\dot{Q_H} - \alpha I T_C + \frac{1}{2} R_{INT} I^2}{(K + \alpha I)} - R_{INT} I^2 =$$

$$= \frac{-\frac{1}{2}\alpha R_{INT} I^3 - (\alpha^2 T_C + R_{INT} K) I^2 + \dot{Q_H} \alpha I}{K + \alpha I} \tag{4-19}$$

The MPP is found taking the derivative of Equation (**4-19**) with respect to the load current, and equating the result to zero. This is equivalent to finding the value of output current at which the output power is the maximum the TEG can produce for a given value of input heat flux $\dot{Q_h}$.

$$\frac{dP_{LOAD}}{dI} = \frac{\left[-\frac{3}{2}\alpha R_{INT} I^2 - 2(\alpha^2 T_C + R_{INT} K) I + \dot{Q_h} \alpha\right](K + \alpha I)}{(K + \alpha I)^2}$$

$$- \frac{\alpha\left[-\frac{1}{2}\alpha R_{INT} I^3 - (\alpha^2 T_C + R_{INT} K) I^2 + \dot{Q_h} \alpha I\right]}{(K + \alpha I)^2} \tag{4-20}$$

$$= \frac{-\left[I^3 \alpha^2 R_{INT} + I^2\left(\alpha^3 T_C + \frac{5}{2}\alpha R_{INT} K\right) + I \cdot 2(K\alpha^2 T_C + R_{INT} K^2) - \dot{Q_h} \alpha I\right]}{(K + \alpha I)^2}$$

The MPP is found solving Equation (**4-21**). It is a third order equation that will provide 3 solutions (or roots). Only one of these values is the valid solution, the other two solutions are complex conjugates that can be discarded.

$$I^3 \alpha^2 R_{INT} + I^2\left(\alpha^3 T_C + \frac{5}{2}\alpha R_{INT} K\right) + I \cdot 2(K\alpha^2 T_C + R_{INT} K^2) - \dot{Q_h} \alpha I = 0 \tag{4-21}$$

The maximum output power, the temperature and the voltage at the MPP can be found after solving Equation (**4-21**).

Equation (**4-21**) provides an approximation of the actual current at the MPP and, therefore, all the other parameters obtained with the value of current are also an approximation. This

approximation comes from the fact that the parameters α and R_{INT} are represented by fixed values rather than second order polynomials (see Table 4-1). For the case of the monTE™, the error is only due to the value of R_{INT} since α is already a fixed value (equal to 0.0517).

The error between the theoretical values at the MPP presented in Section 4.2.2 and the values obtained with Equation (**4-21**) are presented hereafter. First, the values of R_{INT} for the values of heat input power must be calculated so that the average value can then be calculated and used in Equation (**4-21**). The values of R_{INT} for different values of ΔT are presented in Table 4-10 and Figure 4–19. The average value of R_{INT} is equal to 2.531 Ω, and this is the value that will be used in Equation (**4-21**).

ΔT (^oC)	R_{INT} (Ω)	Error	Relative Error (%)
0	1.603	0.928	0.578
50	1.928	0.603	0.312
100	2.223	0.308	0.138
150	2.488	0.043	0.017
200	2.723	0.193	0.071
250	2.928	0.398	0.136
300	3.103	0.573	0.184
350	3.248	0.718	0.221
$R_{INT,AVG}$	2.531		

Table 4-10- Values of R_{INT} and average value of R_{INT}

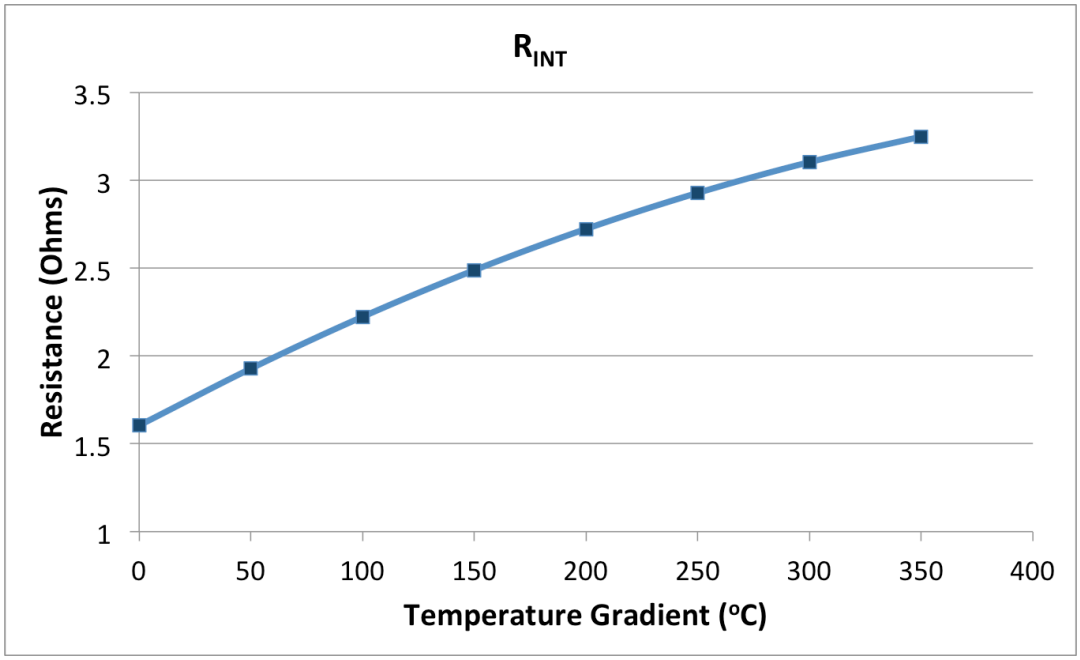

Figure 4–19 – Internal resistance of the monTE™ plotted against ΔT

The difference between the theoretical parameters using the simulations presented in Section 4.2.2 and the same parameters obtained using Equation (**4-21**) are presented in Table 4-11. The relative difference, with respect to the values obtained from the simulations, are also presented in the table.

	Q_h = 75		Q_h = 100		Q_h = 150	
	Difference		Difference		Difference	
β	0.004	**0.70%**	0.011	**1.99%**	0.018	**3.14%**
P_{MPP} (W)	0.308	**23.00%**	0.438	**19.47%**	0.598	**13.08%**
$V_{LOAD,MPP}$ (V)	0.050	**2.56%**	0.004	**0.17%**	0.010	**0.27%**
$V_{OC,MPP}$ (V)	0.063	**1.87%**	0.094	**2.12%**	0.220	**3.30%**
I_{MPP} (A)	0.143	**20.99%**	0.170	**19.34%**	0.154	**12.84%**
	Q_h = 200		Q_h = 250		Q_h = 300	
	Difference		Difference		Difference	
β	0.021	**3.71%**	0.027	**4.69%**	0.024	**4.10%**
P_{MPP} (W)	0.561	**7.51%**	0.295	**2.71%**	0.199	**1.35%**
$V_{LOAD,MPP}$ (V)	0.042	**0.82%**	0.046	**0.72%**	0.172	**2.25%**
$V_{OC,MPP}$ (V)	0.388	**4.36%**	0.574	**5.17%**	0.813	**6.10%**
I_{MPP} (A)	0.099	**6.74%**	0.034	**2.00%**	0.071	**3.68%**

Table 4-11 - Difference between the values of different TEG parameters, at the MPP, obtained using theoretical simulations and Equation (4.21)

4.2.7 The maximum power point and the maximum power transfer theorem

The maximum power transfer theorem states that, for a circuit like the one shown in Figure 4–1, the maximum power transferred to R_{LOAD} occurs when $R_{LOAD} = R_{INT}$. The results presented in this chapter show that when a TEG operates under constant heat flux, the MPP occurs for values of $\beta > 0.5$, which requires $R_{LOAD} > R_{INT}$.

The maximum power transfer theorem applies to circuits like the one shown in Figure 4–1, which is the equivalent circuit of a TEG operated under constant ΔT. However, when a TEG is operated under constant heat flux, the voltage source is variable, and a different value of voltage corresponds to each operating point of the TEG.

Figure 4–20 shows the power curve of the GM250-241-10-12™ TEG operated under 35 W_{th} constant heat flux (red solid line) and operated under different constant temperature gradients (dashed lines and solid blue line). When the TEG operates at the MPP under constant heat flux (35 W_{th}), the temperature across the TEG is equal to 42.4 ^{o}C. At this point the internal resistance of the TEG is not equal to the load resistance, but the TEG is not operated at the MPP of the ΔT = 42.4 ^{o}C curve. However, when the TEG operates at the MPP of the ΔT = 42.4 ^{o}C curve, the load resistance is equal to the internal resistance. This means that the maximum power transfer theorem still applies to the TEG, but only to the power curves for constant ΔT.

Note that the TEG cannot be considered in isolation in a constant heat system. The thermal impedances on each side of the TEG have an impact in the overall system performance due to the temperature drop across them.

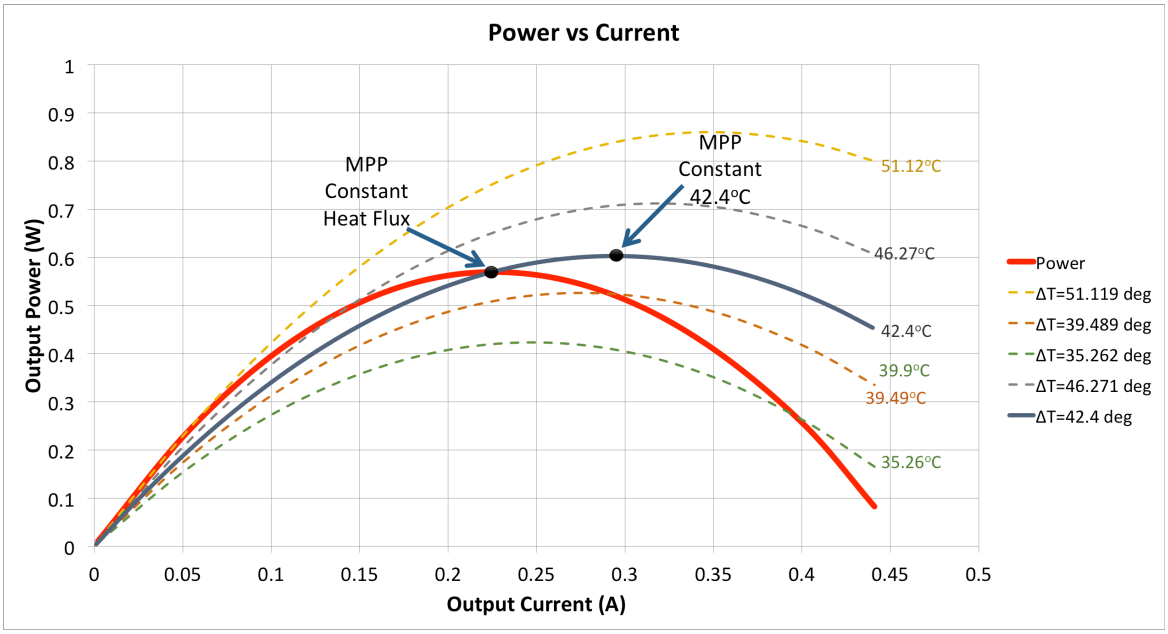

Figure 4–20- Power curves (constant heat flux and constant ΔT) for the GM250-241-10-12™. Reprinted from Applied Energy 212 (2018) 293-303, Transient response of a thermoelectric generator to load steps under constant heat flux, with permission from Elsevier

4.3 Dynamic response of TEGs operated under constant heat flux

The characteristic curves of a TEG operated under constant ΔT have been presented in Section 4.1.2. The operating points presented in these curves represent the operating points in steady-state conditions. Assuming that the temperature gradient ΔT across the TEG does not change when the operating point is changed; that is, the TEG operates under true constant ΔT, the transitions from one operating point to another will also occur across the same curves.

On the other hand, the characteristic curves of a TEG operated under constant heat flux have been presented in Section 4.2.2 and 4.2.5, for the theoretical and experimental results, respectively. These curves, however, only represent the operating point of the TEG under steady-state conditions. Due to the inherent thermal time constant of the TEG system (thermal delays introduced by the thermal capacitance of the different elements in the system), and the fact that the temperature gradient across the TEG is not maintained at a constant value; transitions from one operating point to another will occur across different constant ΔT curves. This happens because, when the operating point of the TEG is changed the ΔT across the TEG also changes, until it reaches the new steady-state operating point.

A graphic description of the transitions between power curves will be used to explain the dynamic, or transient, response of the TEG. The TEG that will be used is the GM250-241-10-12™ with values of α and R_{INT} defined in Table 4-1. Figure 4–21 shows the power curve under constant heat flux; and also the power curves for several constant temperatures under steady-state conditions. The solid red line shows the curve for constant heat flux and the dashed lines represent power curves for constant ΔT at different values of temperature difference. The constant heat flux power curve has been obtained experimentally with an input heat flux of 35 W_{th}, using the same test setup as described in Section 4.2.3, whereas the constant ΔT power curves have been obtained using the TEG equations as described in Section 4.2.2. The solid blue line represents the temperature difference across the TEG. The solid black points marked in the curves correspond to different electrical points when the output load increases and are summarized in Table 4-12.

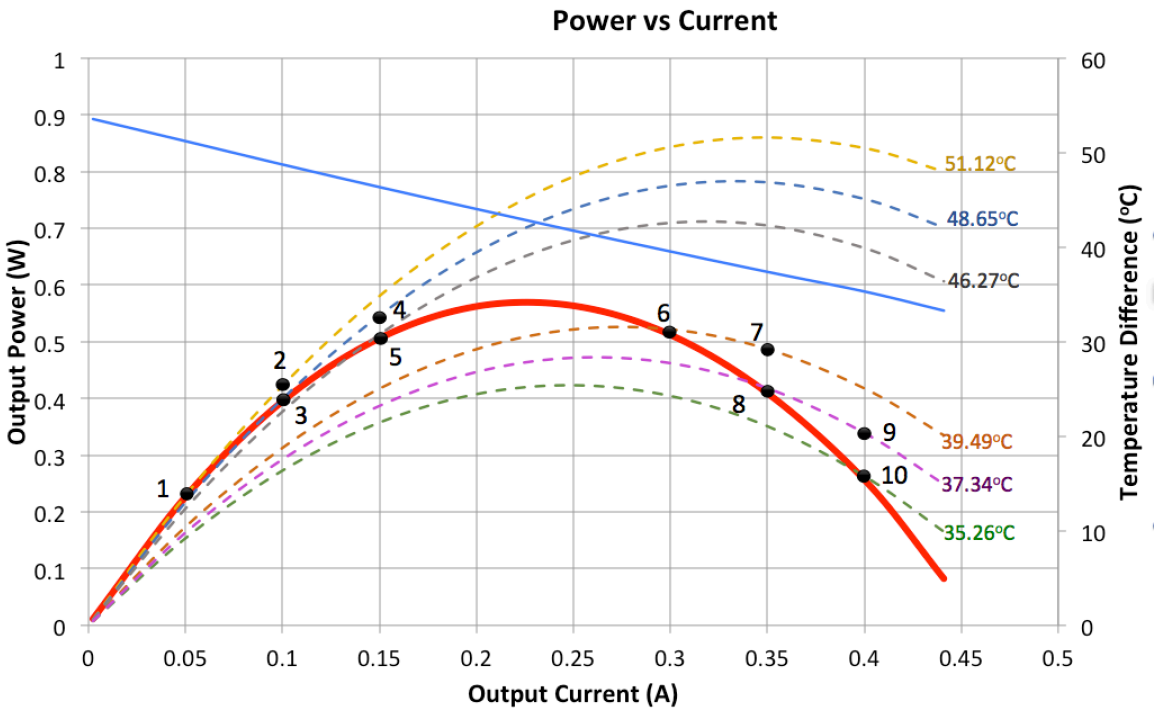

Figure 4–21 - Power curves for constant heat flux (35 W_{th}, solid red line) and constant ΔT (dashed lines) with increasing load changes. Reprinted from Applied Energy 212 (2018) 293-303, Transient response of a thermoelectric generator to load steps under constant heat flux, with permission from Elsevier

Point	Current (mA)	Power (mW)	ΔT (^oC)
1	50	237	51.12
2	100	430	51.12
3	100	400	48.65
4	150	541	48.65
5	150	509	43.96
6	300	510	39.49
7	350	472	39.49
8	350	406	37.34
9	400	321	37.34
10	400	253	35.26

Table 4-12– Values of current, power and ΔT for the labeled points in Figure 4–21

If the TEG reaches steady-state conditions at point 1, with 51.12 ^oC across it, and a sudden load step from 50 mA to 100 mA is applied, the temperature difference across the TEG will

not change immediately at the time the load step is applied. This is because the thermal capacitances of the system prevent the temperature from changing instantaneously. Hence the TEG continues to operate under the constant ΔT curve corresponding to 51.12 ^{o}C, and the output power changes from 237 mW (point 1) to 430 mW (point 2). The output power then exponentially decreases, following the reduction in temperature gradient dictated by the thermal time constant of the system, from 430 mW to a steady-state power of 400 mW (point 3). Once steady-state is reached, the temperature difference across the TEG has decreased from 51.12 ^{o}C to 48.65 ^{o}C. When a second load step is applied from 100 mA to 150 mA the output power changes immediately from 400 mW (point 3) to 541 mW (point 4). Progressively the TEG reaches steady-state conditions delivering 509 mW with a ΔT of 43.96 ^{o}C (point 5). This behaviour will be observed with increasing load changes up to the MPP.

When increasing load changes are applied past the MPP, *i.e.* to the right of the MPP as shown in Figure 4–21, the behaviour is similar to the previous situation, following the transitions across constant ΔT curves, with decreasing output power and temperature. If the TEG was operated under steady-state condition at point 6, with ΔT =39.49 ^{o}C, and a step load is applied from 300 mA to 350 mA, the power decreases immediately from 510 mW to 472 mW (point 7). Once the system reaches steady-state (point 8) the power decreases further to 406 mW and the temperature decreases to 37.34 ^{o}C. When another load step is applied from 350 mA to 400 mW the output power decreases immediately from 406 mW to 321 mW (point 9) and at steady-state it becomes 253 mW with ΔT = 35.26 ^{o}C.

Figure 4–22 shows the transitions in the time domain between points 3, 4 and 5 described in Table 4-12, and provides an insight into the transitions described in Figure 4–21. On the left side of Figure 4–22, point 3, the TEG is operating in steady-state conditions with a load current of 100 mA and an output power of 400 mW. When the load changes from 100 mA to 150 mA the output power increases instantaneously from 400 mW to 541 mW and then it decreases exponentially down to 509 mW. The output voltage also changes following the same principles. In steady-state conditions the output voltage is 3.92 V and it then changes instantly to 3.57 V. This corresponds to an instantaneous change of voltage across the same ΔT = 48.65 ^{o}C constant temperature curve, then reaching steady-state at 3.35 V.

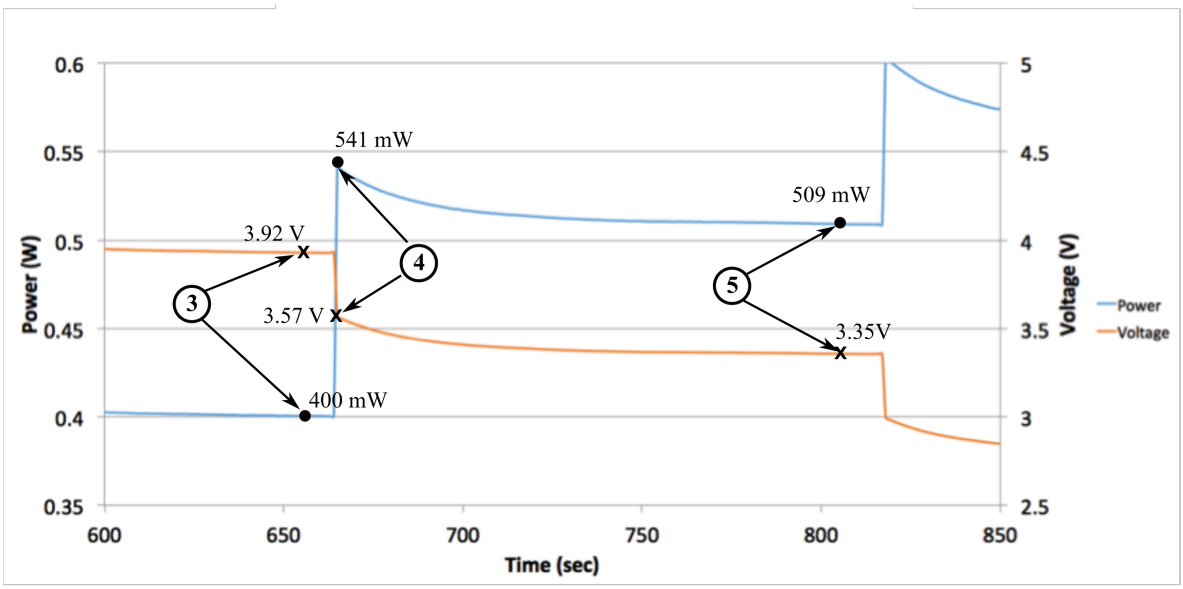

Figure 4–22 - Transient response between points 3, 4 and 5 represented in the time domain.

Figure 4–23 shows the different transitions when the load current is stepped down. The same principles apply when moving from higher to lower load currents. The temperature difference across the TEG does not change immediately due to the thermal capacitance of the system and there will be transitions between constant ΔT and constant heat flux power curves. The points marked in Figure 4–23 are numbered in the order the transitions occur. Transitions across the same constant ΔT curve occur immediately whereas the transitions between a constant ΔT curve and the constant heat flux curve correspond to exponentially decaying transitions dictated by the thermal resistances and capacitances of the system. The difference between the thermal and electrical time constants is several orders of magnitude: depending on the electrical reactances in the circuit, settling time is usually measured in nanoseconds [113] whereas for the thermal response the settling time is many minutes. This difference in time constants poses a particular challenge to the development of an MPPT algorithm that is able to simultaneously accommodate the thermal and electrical responses to determine the true MPP.

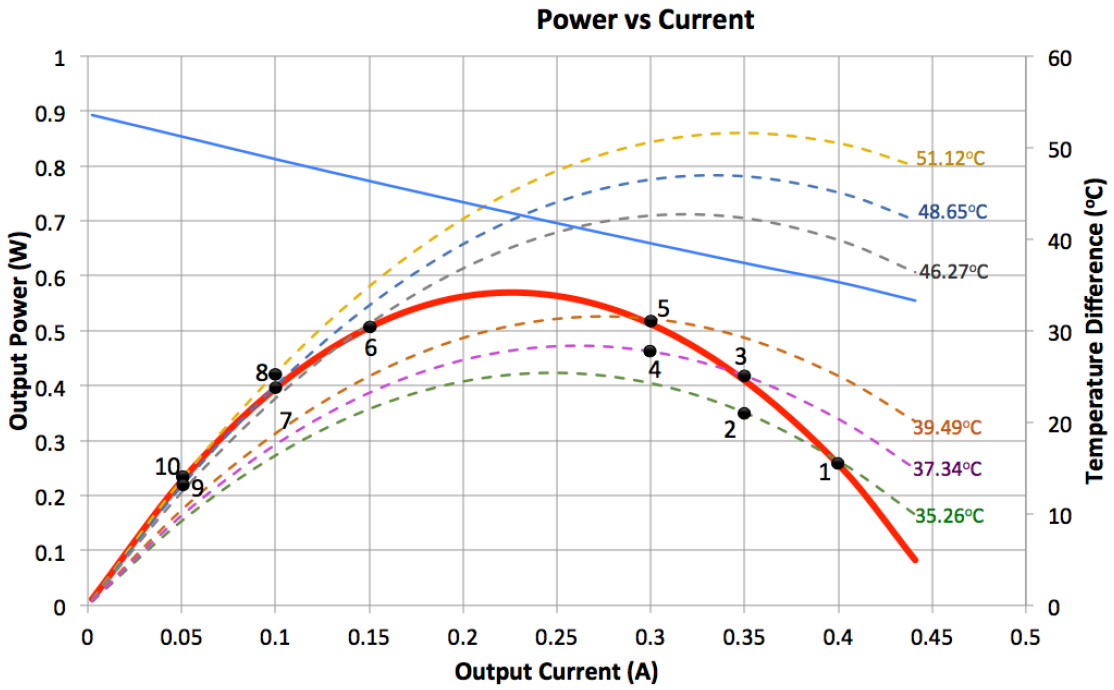

Figure 4–23 - Power curves for constant heat flux and constant ΔT with decreasing load changes. Reprinted from Applied Energy 212 (2018) 293-303, Transient response of a thermoelectric generator to load steps under constant heat flux, with permission from Elsevier

4.3.1 Experimental dynamic curves of a TEG operated under constant ΔT

The dynamic behaviour of the monTE™ has been obtained experimentally using the test setup described in Section 4.2.3. The dynamic response has been obtained at 75 W_{th}, 100 W_{th}, 150 W_{th}, 200 W_{th}, 250 W_{th} and 300 W_{th}. For each level of input heat flux, two transitions have been performed using current steps of equal magnitude: from open-circuit to short-circuit and vice-versa. The current steps are applied in time interval between 540 and 600 seconds.

Figure 4–24 to Figure 4–27 show the transient behaviour of the TEG when the input power is 75 W_{th} and the load current is changed with steps of 200 *mA*. In Figure 4–24 and Figure 4–25 the current is stepped from zero to the short-circuit current, whereas in Figure 4–26 and Figure 4–27 the current is stepped from the short-circuit current down to zero.

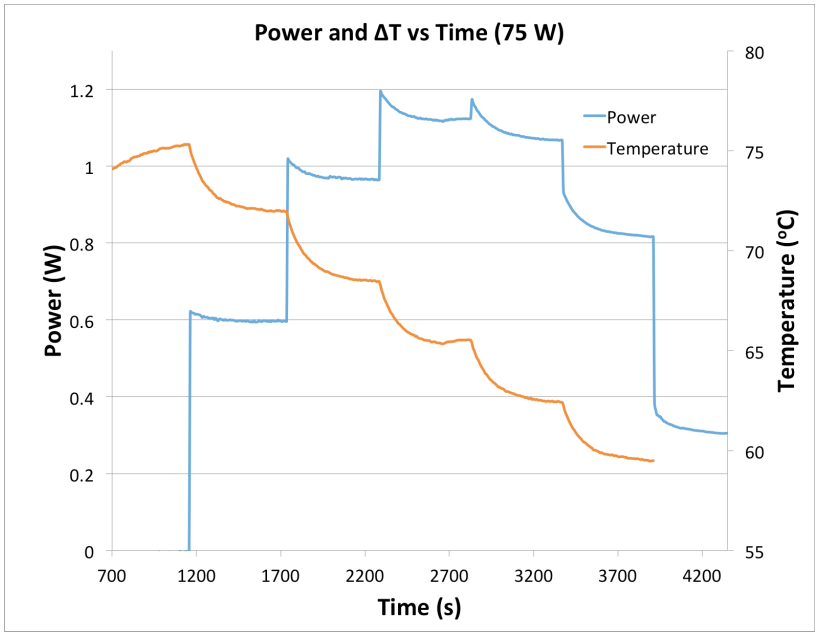

Figure 4–24 - Transient behaviour of the output power and ΔT for increasing steps of output current with 75 W_{th} input heat flux

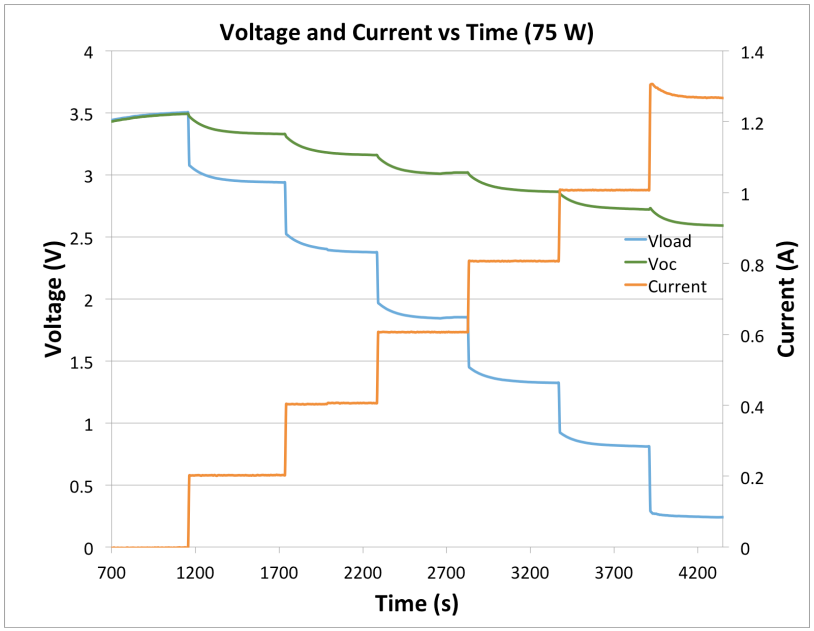

Figure 4–25 - Transient behaviour of the load and open-circuit voltages and load current increasing steps of output current with 75 W_{th} input heat flux

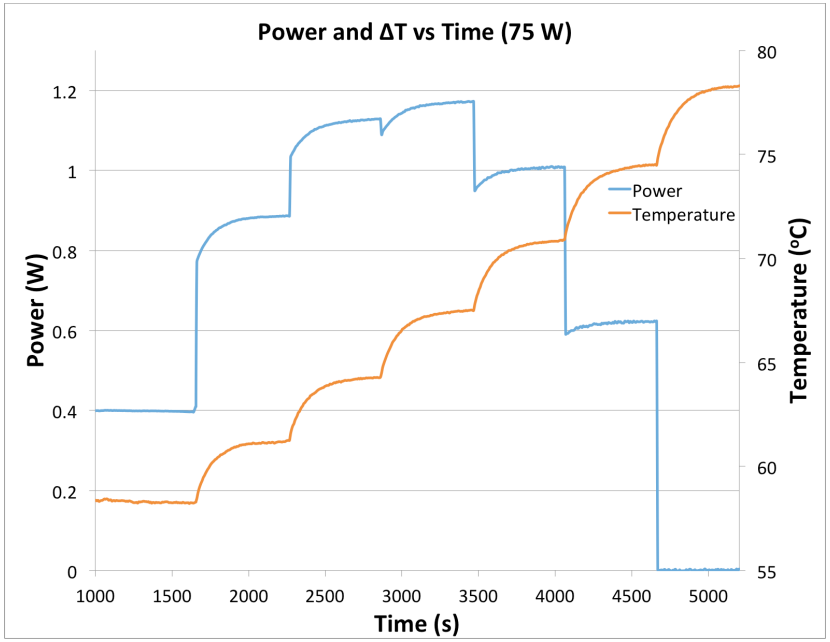

Figure 4–26 - Transient behaviour of the output power and ΔT for decreasing steps of output current with 75 W_{th} input heat flux

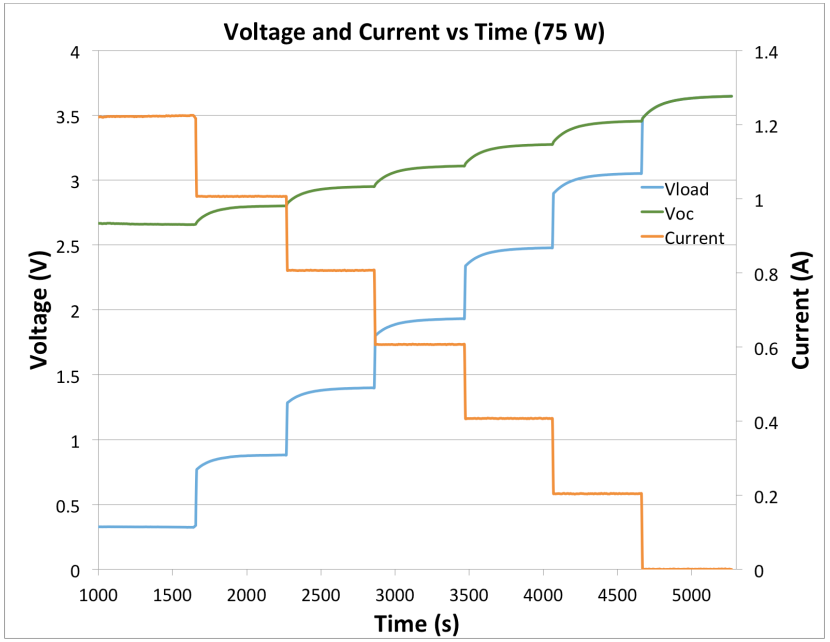

Figure 4–27 - Transient behaviour of the load and open-circuit voltages and load current decreasing steps of output current with 75 W_{th} input heat flux

4.4 Conclusions

There are several quantitative differences between the MPP of TEGs operated under constant ΔT and constant heat flux. The first is that the MPP for the constant ΔT case is found at $\beta = 0.5$ whereas for constant input heat flux the MPP is found at $\beta > 0.5$. The second is that, for TEGs operated under constant heat flux, the temperature gradient across the TEG changes when the operating point of the TEG changes as well. Another difference is the point of maximum efficiency of the TEG. For a TEG operated under constant heat flux, the MPP corresponds to the point of maximum efficiency, whereas these two points are different when the TEG operates under constant ΔT.

Equation (**4-21**) can be used to calculate the MPP when the TEG operates under constant heat flux with the caveat that an error is introduced due to the variations of α and R_{INT} with temperature. This error can be eliminated when Equations (**4-9**) are used in an iterative manner.

Simulated curves for output voltage, TEG power and temperature difference have been produced for different values of input heat flux. The beta factor has also been plotted, which highlights that the optimum value of beta, at the MPP, is higher than 0.5. The same curves have been produced experimentally, which show a very good correlation between the simulations and the experimental measurements. The value of the beta factor at the MPP has been plotted against input heat flux, for both experimental and theoretical results. For low values of input heat flux (lower than 200 W_{th}), the values of beta factor decrease with input heat flux, as reported by [112]. For higher values of input heat flux the optimum value of beta stabilizes around a value which, for the monTE™, is equal to 0.57. Note that a MPP with a value of beta of less than 0.5 is thought to be impossible in any physical system.

Temperature variations, following a change in load current, are not instantaneous due to the thermal capacitance of the different elements in the TEG system and there is therefore a dynamic response associated to the thermal time constant of the TEG system. Transitions between different operating points occur across constant ΔT power curves. The dynamic response corresponds to the transitions explained in Figure 4–21 and Figure 4–23. These transitions have been explained graphically in Section 4.3. The transient response of the

TEG has been characterized through experimental measurements, for different values of input heat flux, and have been presented in Section 4.3.1. (and Appendix C). There may be up to 12 orders of magnitude difference between the thermal and electrical time constants and this is a significant challenge to incorporate in an MPP algorithm that utilizes beta.

Chapter 5 TEG system model and MPPT algorithm

Modeling techniques are used to represent the physical behaviour of systems in a mathematical form, named *model*. A model can represent a mechanical, electrical or thermal system, amongst others, and it is based on the equations that define its physical behaviour. Working with models allows the integration of systems with different natures into a single common system that interprets the equations of each part. The accuracy, or fidelity, of a model is related to how closely it represents the physical behaviour of the actual system. In many cases, the level of accuracy translates into the complexity of the model and accurate models might require large amounts of computational resources in order for them to be utilized. In some cases a very accurate model is not required and a less detailed solution is preferred since it often provides a tool that can be run more quickly than a more complex version.

A model of a TEG system is very useful as it provides a tool that allows the development of an algorithm capable of operating the TEG at the MPP. Several maximum power point tracking (MPPT) techniques, most of them based on methods developed for photovoltaic (PV) applications, are currently used in TEG systems. Most were developed and optimized for applications where the TEG operates under constant ΔT, however, they are not optimized for TEGs operated under constant heat flux.

This chapter presents a model of the TEG system that comprises the TEG device and a power converter controlled by an MPPT algorithm with a superior performance when compared to the two main algorithms used in the literature: the *Fractional Open-circuit Voltage* (FOV) and *Perturb and Observe* (P&O) methods. The performance of the new algorithm is compared against FOV and P&O for different levels of input heat flux.

5.1 Model of the thermoelectric device

Several TEG models have been presented in the literature [22], [100]–[103], but some of them are not accurate for applications where the TEG operates under constant heat flux. Others are very complex and the amount of computational resources they require often means that the model is very slow. The simulation speed is an important aspect when the model has to be used along with other models, like the power conversion stage, to reproduce several seconds of operation of the overall system.

A model of the TEG is developed in Matlab/Simulink® and its purpose is to simulate the behaviour of the TEG in order to use it for the development of the controlling power converter. The model uses approximate values for the thermal resistances and thermal capacitances (specific heat) of the system and it reproduces, with a good degree of accuracy, the transient response of a real TEG.

The model uses the set of equations described in Equation (**4-9**), which represents the operating points of a TEG in steady-state conditions. The system dynamics, influenced by the equivalent thermal capacitance and resistance of the TEG system, are simulated using a first-order transfer function that represents the equivalent thermal impedance of the overall system. Figure 5–1 shows a simplified diagram of the TEG system (a) and the equivalent thermal circuit used to implement the thermal dynamics of the system (b), where θ_{TEG} and C_{TEG} are the thermal resistance and capacitance of the TEG system, respectively.

The thermal circuit of Figure 5–1 b) implements the system delay to temperature changes using the difference between two consecutive values of steady-state temperature gradient across the TEG as the input to the circuit; that is, $\Delta T_{SS}=\Delta T_{SS}(j)-\Delta T_{SS}(j-1)$. Based on this circuit model, the first order equation that models the temperature dynamics of the system can be obtained, and shown in Equation (**5-1**), where τ_{TEG} is the thermal time constant of the system. When steady state conditions are reached then $\Delta T_{C_{TEG}}=\Delta T_{SS}$.

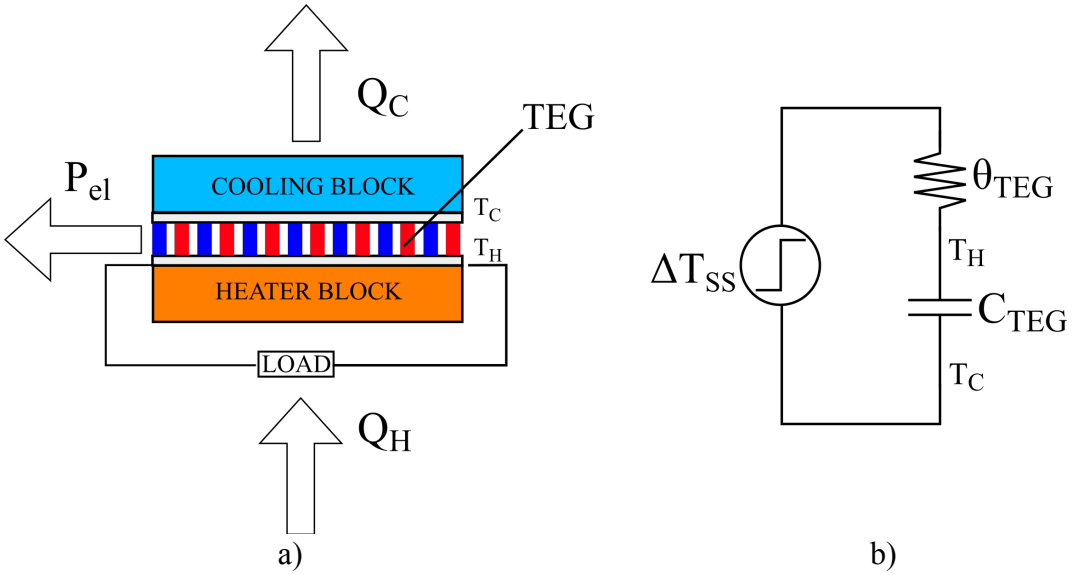

Figure 5–1 – a) Simplified diagram of the TEG setup and b) simplified equivalent model of the thermal element

$$\Delta T_{C_{TEG}}(S) = \Delta T_{SS} \cdot \frac{\frac{1}{\theta_{TEG} C_{TEG}}}{s\left(s + \frac{1}{\theta_{TEG} C_{TEG}}\right)} + \frac{\Delta T_{SS,j-1}}{s}$$
$$= \Delta T_{SS} \cdot \frac{\frac{1}{\tau_{TEG}}}{s\left(s + \frac{1}{\tau_{TEG}}\right)} + \frac{\Delta T_{SS,j-1}}{s} \quad (5\text{-}1)$$

The Simulink model of the TEG is shown in Figure 5–2, where the main block "*TEG Equations*" contains a script that processes the set of equations shown in Equation (**4-9**) sequentially. The inputs to the block are the heat flux (*Qh*), the cold side temperature (*Tc*), the temperature difference from the previous iteration (*To*) and the output current of the TEG (*Io*). The outputs are the temperature gradient *(T*), the output power (*P*), the load voltage (*Vout*) and the instantaneous open circuit voltage (*Voc*).

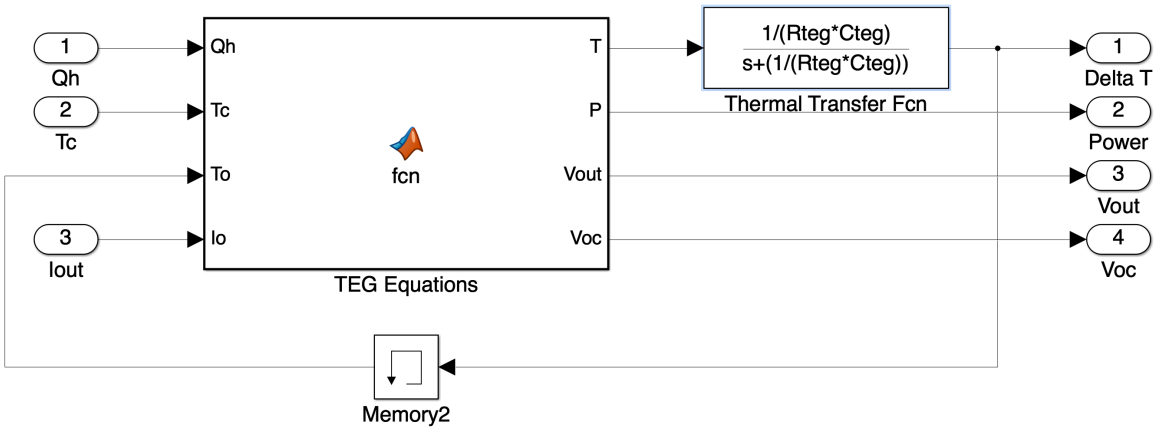

Figure 5–2 - Simulink model of the TEG

Figure 5–3 shows the Simulink model used to characterize the TEG model. The main block "*TEG*" contains the block shown on the left hand side of Figure 3. The block "*Resistor*" simulates a load and provides the output current that is fed-back into the TEG block. The characterization model contains three blocks, "*Temp_TEG*", "*Power_TEG*" and "*Volt_TEG*" that take external data saved in a matrix format. This data is taken from real measurements on actual TEGs and it is fed into the simulation to provide a method of direct comparison between the simulation and the real performance of the TEG.

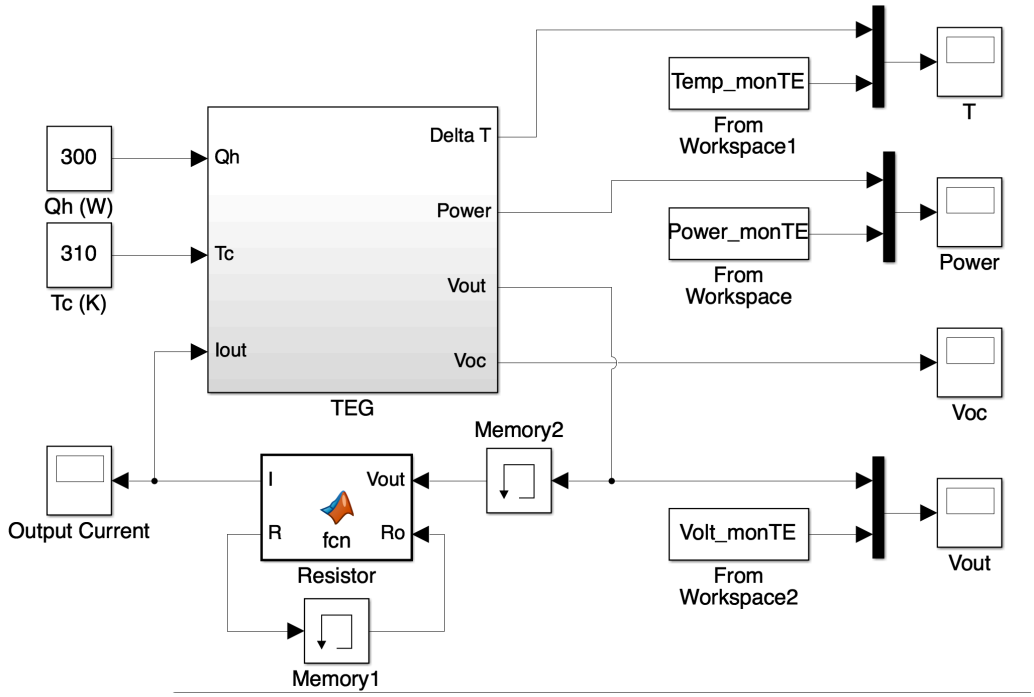

Figure 5–3 - Test bench used to characterize the TEG model

The cold side temperature is considered as fixed and it is equal to 310 *K*, which corresponds to the cold side temperature on the cold side of the TEG measured from the experimental characterization at 300 W_{th}. The block "*Resistor*" implements the TEG load step changes by increasing the output current of the TEG using fixed, or variable step changes. In this case the load step changes are fixed, and correspond to the load step changes of the same magnitude as those applied in the transient characterization in Section 4.3.1.

In order to verify the accuracy of the simulated TEG, a test is performed using a real TEG and the results are compared against the results from the simulation. The TEG used for the verification of the model is the monTE™, and the parameters used by the Simulink model are taken from the manufacturer's datasheet and are shown in Table 5-1.

Parameter	Value	Units
α	0.0517	*V/K*
$\mathbf{R_{int}}$	$-0.000006 \cdot T^2+0.0068 \cdot T+1.6033$	*Ω*
$\mathbf{T_C}$	310	*K*
$\mathbf{Q_H}$	300	W_h
$\mathbf{\theta_{TEG}}$	1.03	*K/W*

Table 5-1- Parameters of the monTE™ used in the simulation

The thermal time constant of the TEG system, τ_{TEG}, can be obtained by inspection of the experimental dynamic characterization undertaken in Section 4.3.1. Figure 4–24 and Figure C-17 are used to obtain the thermal time constant as they correspond to the minimum and maximum input heat flux used in the characterization, 75 W_{th} and 300 W_{th} respectively. When a system is excited with a step function, the time constant is defined as the time it takes the output of the system to reach 63.2% of the input step. The system is considered to have reached 98.16% of the value of the input step after four time constants. In this case the input of the system is the defined as $\Delta T_{SS}=\Delta T_{SS}(j)-\Delta T_{ss}(j-1)$, which can be obtained by inspection of the curves.

A zoomed-in view of a transient of Figure 4–24 is shown in Figure 5–4 a). The time constant is measured when the temperature gradient across the TEG has reached 63.2% of the difference between the initial and the final value of temperature. For 75 W_{th}, τ_{TEG} = 114.43 seconds. The time constant can also be measured by looking at the time it takes the temperature across the TEG to reach the steady-state value. The temperature gradient

across the TEG is considered to be at steady-state or, at least, is higher than 98.16% of the steady-state value after 464.17 seconds, so $4\tau_{TEG} = 464.17\ s$. Based on this assumption, the value of the time constant is one fourth of that value; that is, $\tau_{TEG} = 116.04\ s$. The error produced between these two figures, with respect to the 63.2% value, is 1.4%.

The same exercise can be repeated for 300 W_{th}, using Figure C-17. A zoomed-in view of a transient in this figure is shown in Figure 5–4 b). Using the 63.2% of the final steady-state value, the time constant is found to be 114.18 seconds. On the other hand, using the 98.16% value for four times the value of the time constant, the value is 117.65 seconds. The error produced between these two figures, with respect to the 63.2% value figure, is 3.09%.

Based on the previous observations, the value of the thermal time constant of the system can be approximated as 115 seconds, without great loss of accuracy.

The model of the thermal time constant of the TEG system using the first order equation, Equation (**5-1**), will be verified in the time domain and then plotting the resulting curve against the experimental data. The time domain representation of Equation (**5-1**) is shown in Equation (**5-2**) for the temperature difference ΔT and Equation (**5-3**) for the TEG output power.

$$\Delta T_{TEG}(t) = \Delta T_{SS,j-1} + \Delta T_{SS} \cdot e^{-\frac{t}{\tau_{TEG}}} \tag{5-2}$$

$$P_{TEG}(t) = P_{TEG,j-1} + (P_{TEG,j} - P_{TEG,j-1}) \cdot e^{-\frac{t}{\tau_{TEG}}} \tag{5-3}$$

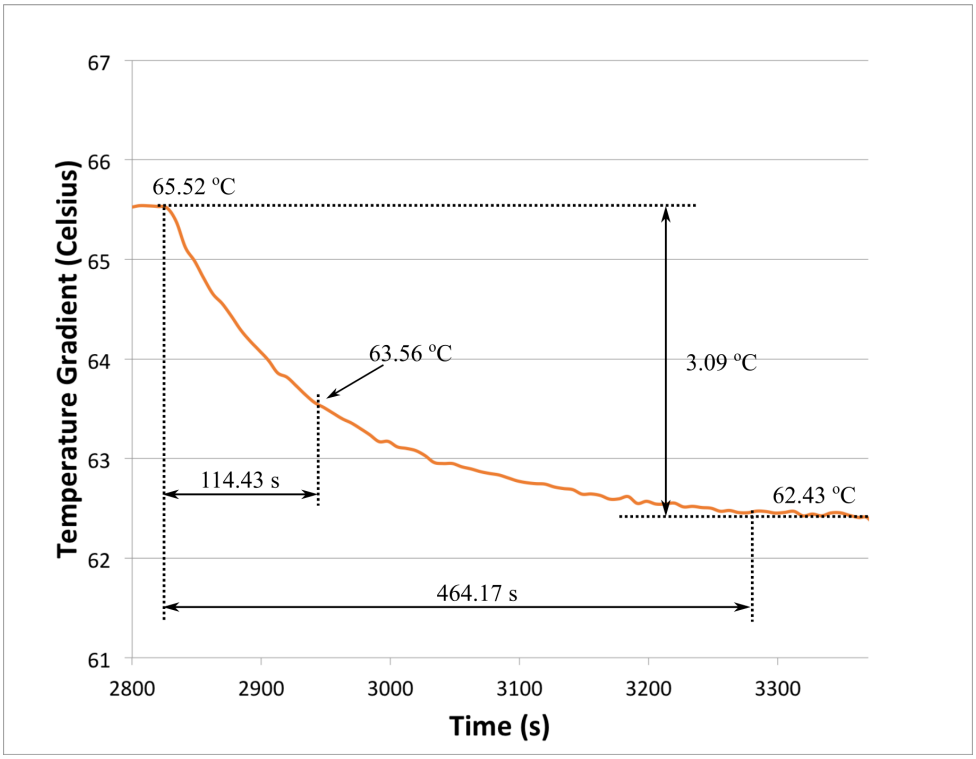

a)

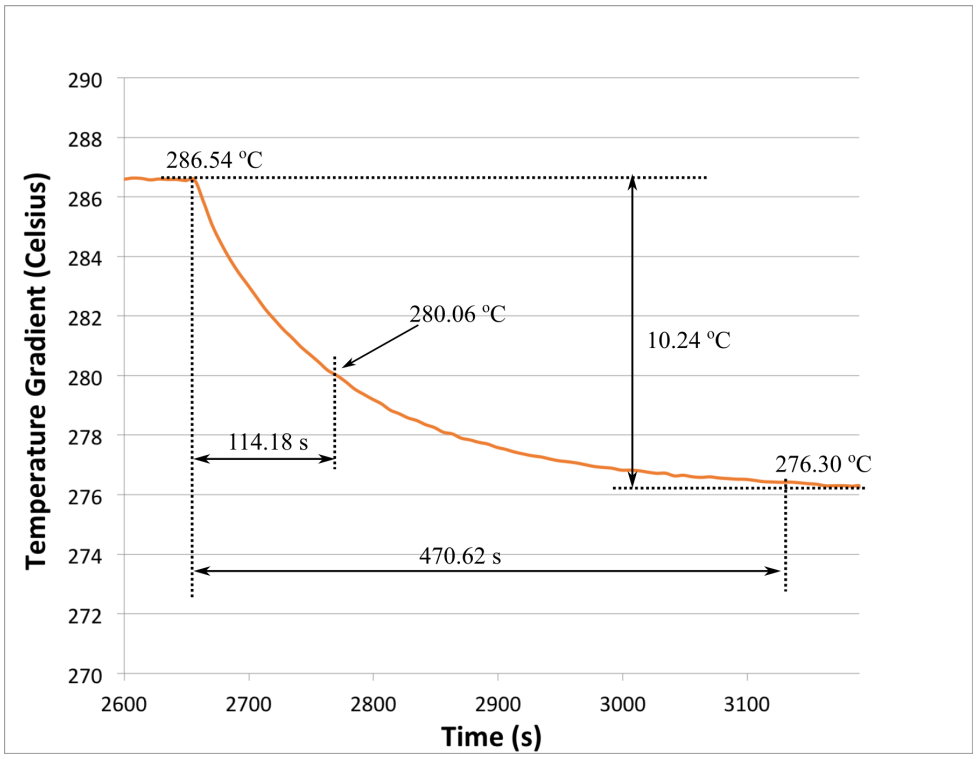

b)

Figure 5–4 - Time constant for a) 75 W_{th} and b) 300 W_{th}

The encircled portions of TEG power and temperature gradient ΔT shown in Figure 5–5 are used to check Equations (**5-2**) and (**5-3**) for the case of decreasing exponentials. The theoretical decreasing exponentials curves are plotted against the measured curves in Figure 5–6 a) and b) for TEG power and ΔT, respectively.

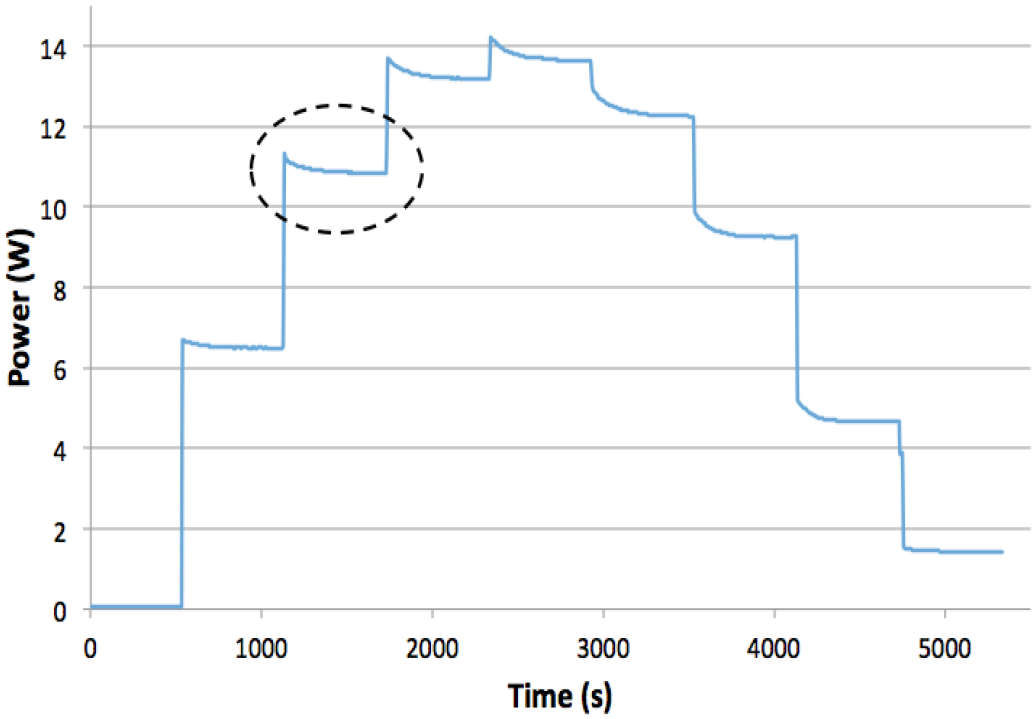

a)

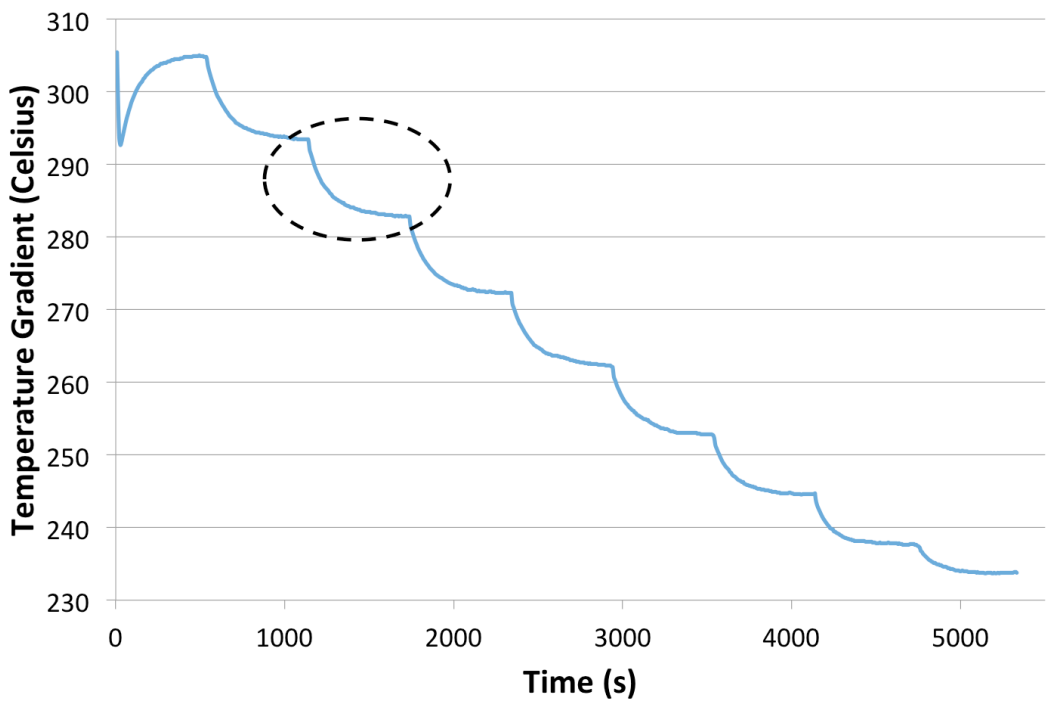

b)

Figure 5–5 - Portions of the power (a) and ΔT (b) used to check the modeled thermal delay for decreasing exponentials

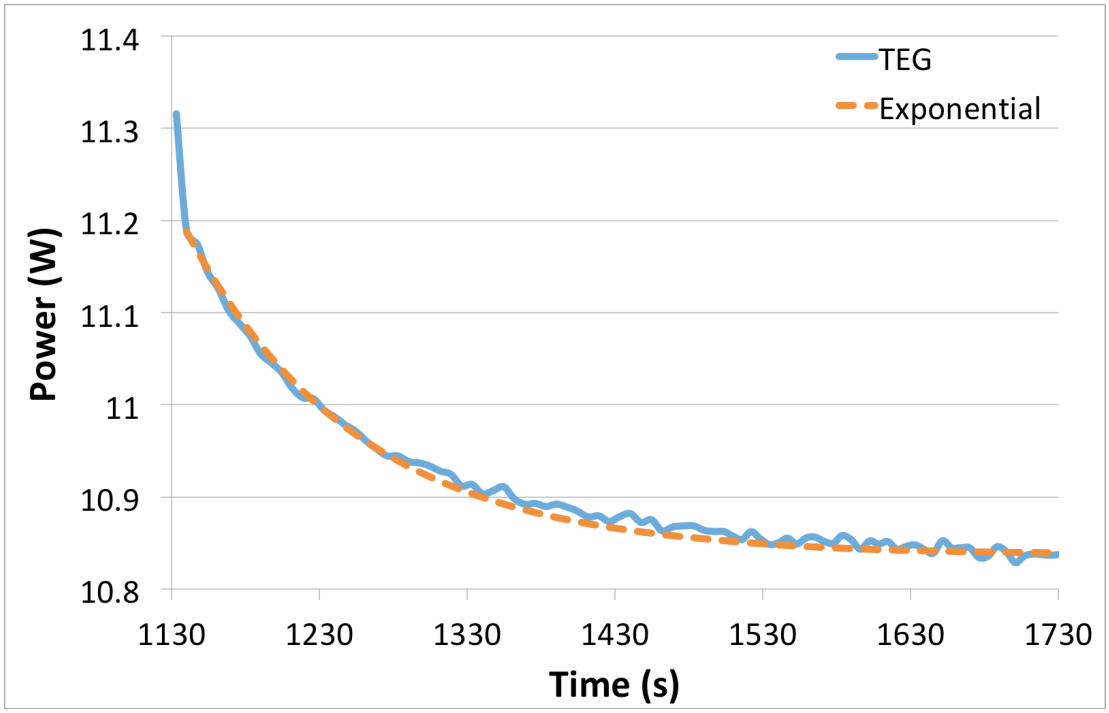

a)

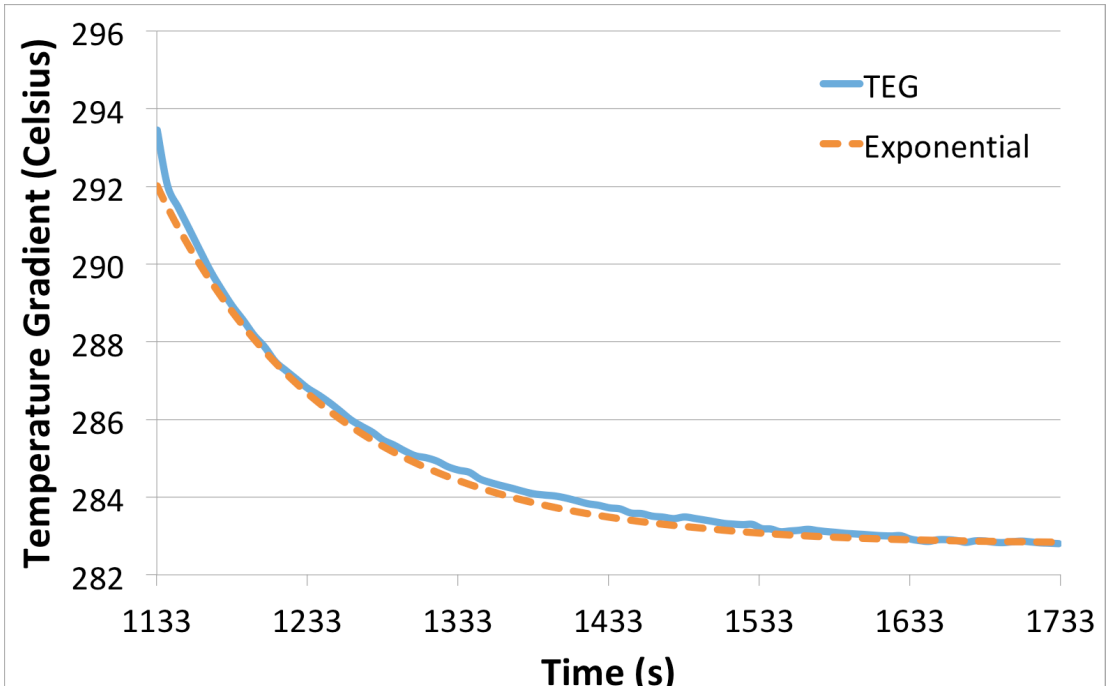

b)

Figure 5–6 - Decreasing theoretical exponentials (encircled areas) plotted against experimental waveforms of Power (a) and ΔT (b)

The encircled portions of TEG power and temperature gradient ΔT shown in Figure 5–7 are used to check Equations (**5-2**) and (**5-3**) for the case of increasing exponentials. The theoretical increasing exponentials curves are plotted against the measured curves in Figure 5–8 a) and b) for TEG power and ΔT, respectively.

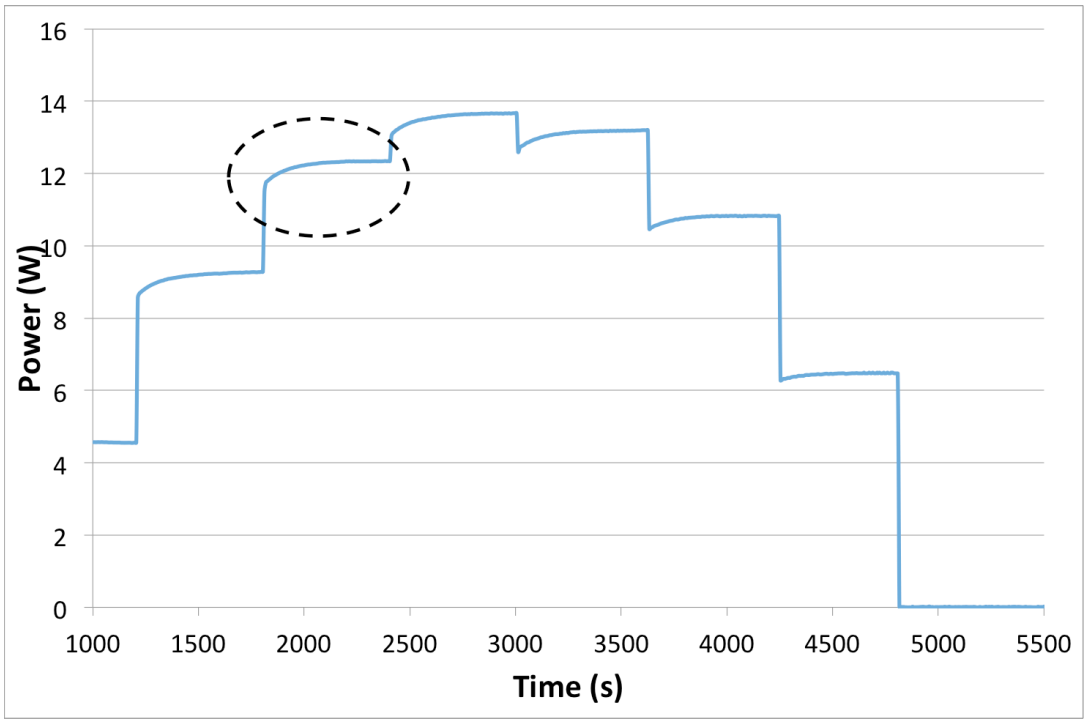

a)

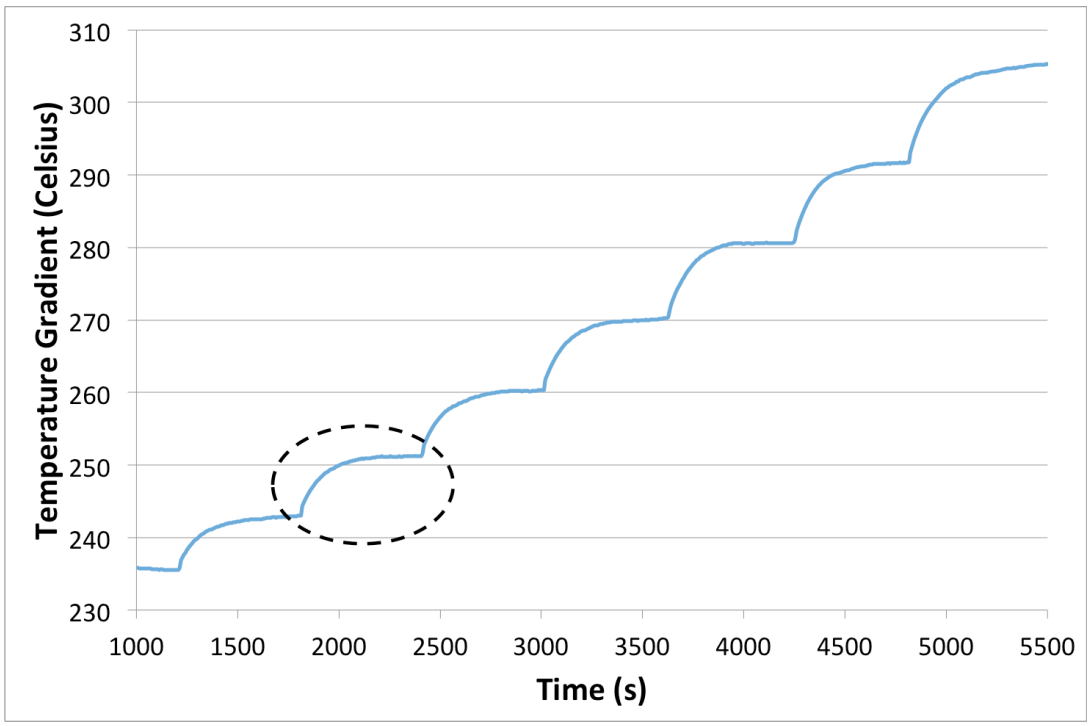

b)

Figure 5–7 - Portions of the power (a) and ΔT (b) used to check the modeled thermal delay for increasing exponentials

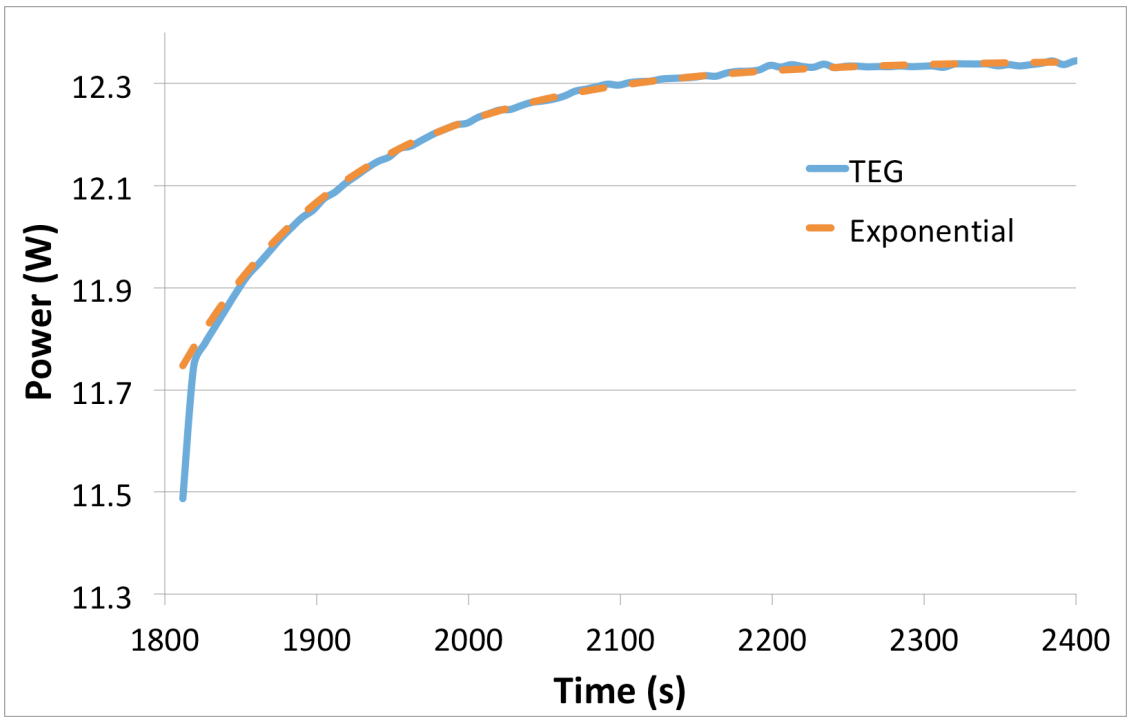

a)

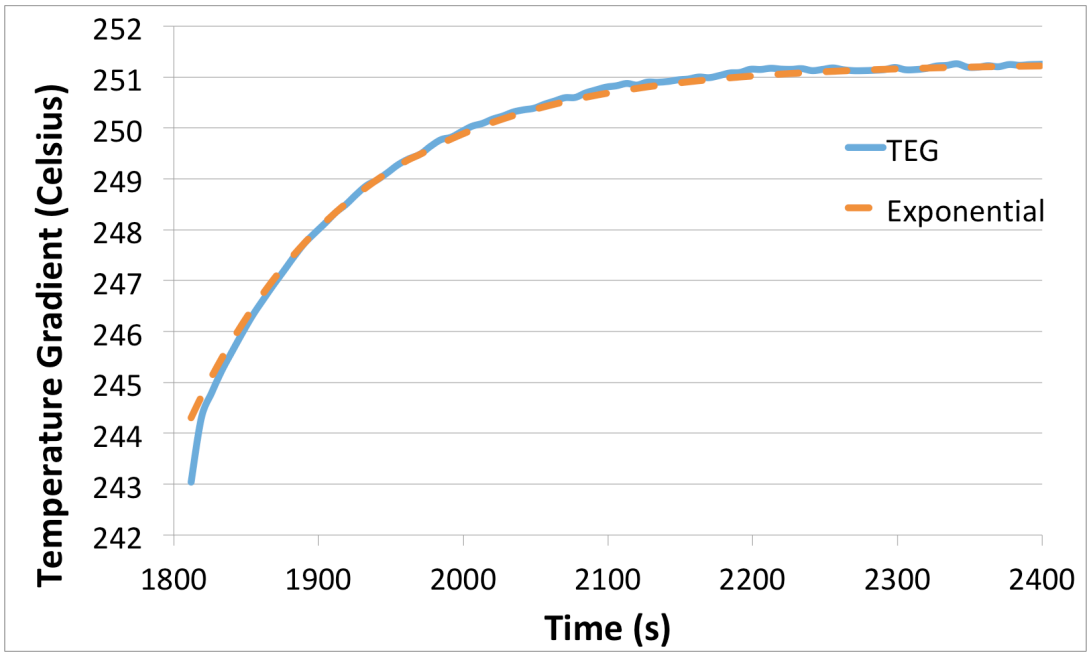

b)

Figure 5–8 - Increasing theoretical exponentials (encircled areas) plotted against experimental waveforms of Power (a) and ΔT (b)

The results shown in Figure 5–6 and Figure 5–8 show that the first order circuit in Figure 5–1 b), and therefore Equation (**5-1**), represents the thermal delay introduced by the thermal capacitances of the TEG system. The accuracy of the model will be checked running a simulation where the current is changed in steps of 500 *mA*. The TEG power, load voltage and temperature gradient will be plotted against the experimental results in order for the accuracy to be evaluated. The results are presented in Figure 5–9 a), b) and c). The parameters of the monTE™ are shown in Table 5-1.

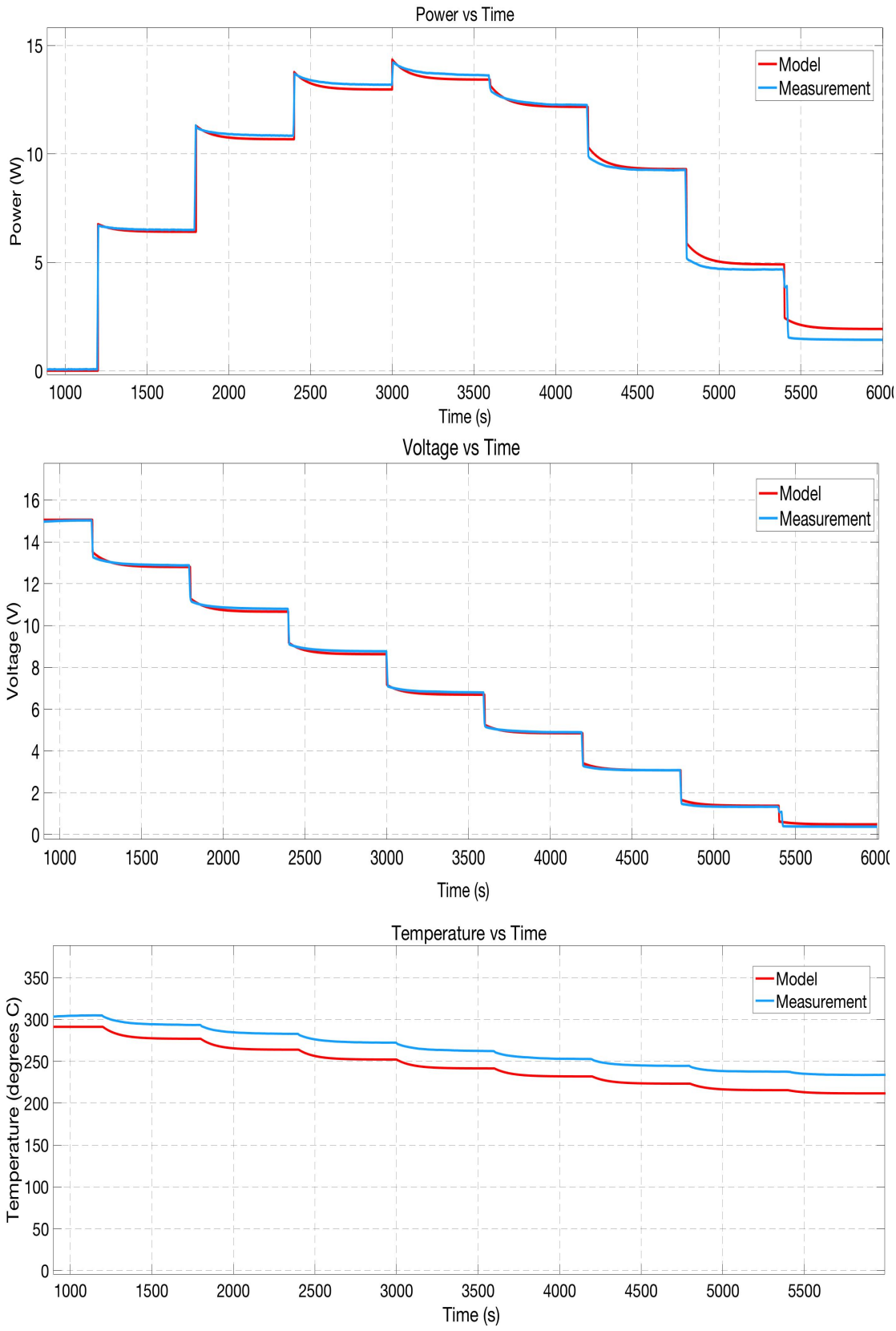

Figure 5–9 - Model and TEG results. a) Power curves b) Voltage curves c) Temperature curves

The maximum steady-state power and voltage errors, between the model and the TEG, are 1.8 % and 1.54 %, respectively. The maximum steady-state temperature error is 9.31 % with respect to the measured temperature across the TEG. It is important to note that the model provides the temperature between the hot and cold plates of the TEG, whereas the measurements are not taken exactly at the plates. This is because the thermocouples are inside the hot and cold blocks and, although they are very close to the TEG plates, they are not in perfect contact with them, and this contributes to the difference observed. These measurement errors have been discussed in Section 4.2.3.

The model and the TEG generally show very good correlation with a very small error, and the dynamic behaviour of the TEG is replicated which is important in order to evaluate MPPT techniques when the TEG operates under constant heat flux.

The experimental dynamic response of the monTE™ was plotted for different values of input heat flux in Section 4.3.1 The results are plotted in Figure 4–24 to Figure 4–27, and in Appendix C, using six different values of input heat flux: 75 W_{th}, 100 W_{th}, 150 W_{th}, 200 W_{th}, 250 W_{th} and 300 W_{th}. The power curves obtained from the TEG model for increasing and decreasing load current are represented in Figure 5–10 and Figure 5–11, respectively. These curves have been obtained using the same current steps used in the experimental measurements using the same values of input power. The value of the steps is presented in Table 5-2.

Input heat flux	Load step
75 W_{th}	200 mA
100 W_{th}	200 mA
150 W_{th}	300 mA
200 W_{th}	400 mA
250 W_{th}	400 mA
300 W_{th}	500 mA

Table 5-2 - Magnitude of the load steps versus input heat flux for the curves obtained from the model

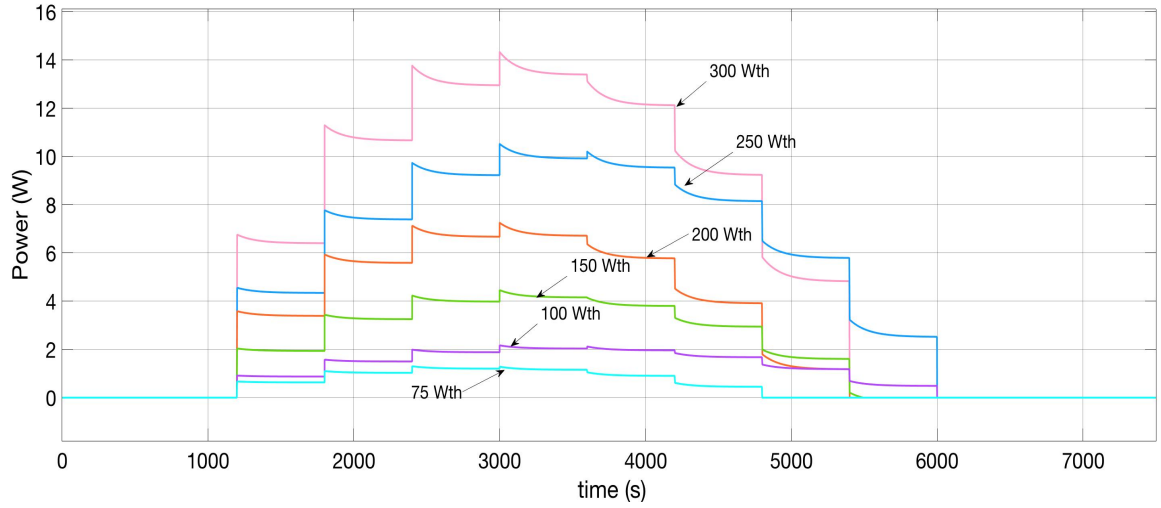

Figure 5–10 - Power curves obtained from the TEG model for different values of input heat flux. The current is stepped from zero to the short-circuit current

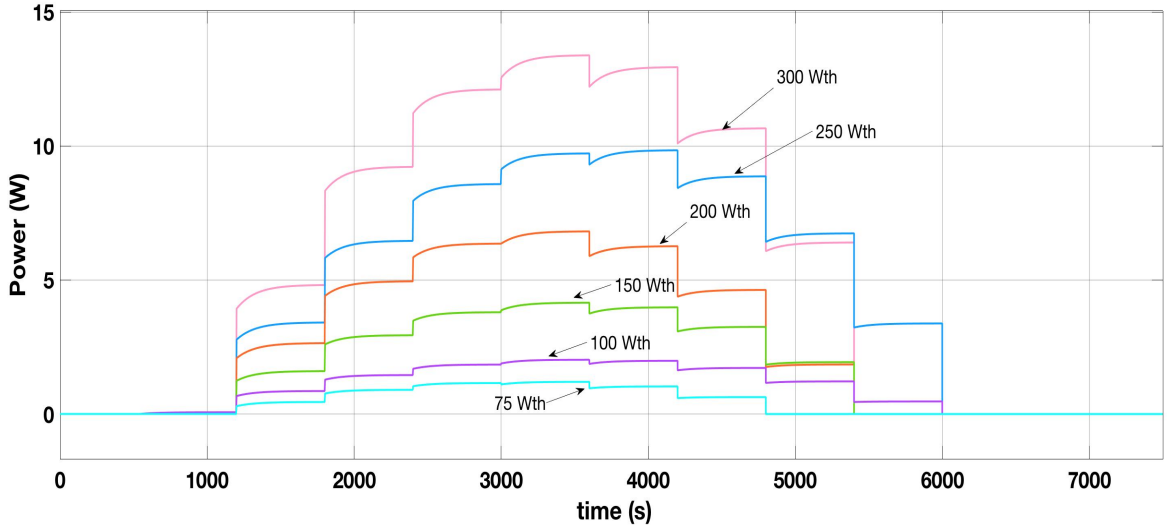

Figure 5–11 - Power curves obtained from the TEG model for different values of input heat flux. The current is stepped from the short-circuit to zero current

5.2 Model of the power converter

The basic principle of Maximum Power Point Tracking consists of changing the operating point of the TEG in order to find the MPP. The operating point of the TEG can be controlled by changing either the output current or the voltage produced at the output terminals. For instance, by connecting a variable resistor at the output of the TEG, the operating point could be changed by changing the resistance value. In this case, the value of the output resistance would set the output current of the TEG and, therefore, its operating point. On the other hand, the TEG could also be connected to a power supply

and an electronic load. The voltage of the power supply would control the operating point of the TEG by controlling the output voltage, and the electronic load would sink the output current of the TEG. Even though the operating point of the TEG could be controlled by either of the two previous examples, they do not present any benefit from the power generation point of view since the power generated by the TEG is dissipated in form of heat either in the output resistor or in the electronic load. It is therefore desirable to be able to control the operating point of the TEG while using the output energy to either supply power to a useful load or to store it in a battery. *It is important to note that unless the total power exported from the TEG is absorbed in the load it is impossible for the TEG to be operated at the MPP.*

A DC/DC converter (power converter) is a type of electronic circuit with an input port and an output port. With the presence of a voltage at the input, it is possible to regulate the current or voltage at the output port. Conversely, if a regulated voltage is present at the output port and a source is connected to the input port, it is possible to regulate the voltage (or current) of the source. A DC/DC converter is made of reactive elements and switches, which present very low losses (switching and very low on-conduction losses). Exploiting the capability of a DC/DC converter of regulating the source voltage when a regulated, or quasi-regulated, voltage is present at the output port, the power converter can appear to the TEG (the source connected to the input port) as a controllable resistor.

There are different DC/DC converter topologies depending on whether the input is higher or lower than the output voltage or whether the output is isolated, or not, from the input port, amongst others. The most common topologies are the buck (step down) converter [63], boost converter (step up) [64], buck-boost (step up and down) converter [66] and flyback converter (step up and down with isolation).

5.2.1 The boost converter

The TEG will be used to charge a 28 V (nominal voltage) battery, which represents a battery made of eight lithium-ion (Li-Ion) battery cells connected in series. The nominal voltage of each battery cell is, typically, 3.5-3.7 V varying from typically 3 V for a discharged cell and 4.2 V for a fully charged (or at end-of-charge, EoC) cell. Beyond these limits, the battery cells can suffer irreversible damage. The battery voltage will therefore vary between 24 V and 33.6 V. This battery voltage presents a widely used voltage in satellite applications.

The monTE™ presents an output open-circuit voltage between 2.58 *V* and 17.06 *V* when it operates under a temperature gradient between 50 ^{o}C and 330 ^{o}C. Below 50 °*C* the TEG output power is so low it is not considered useful, and this places a lower boundary on the input voltage range the converter is required to operate over. With this range of input voltage and the range of output voltage given by the selected battery, the input voltage will always be lower than the output voltage. A boost converter presents the topology that will allow to step-up the voltage from the input to the output.

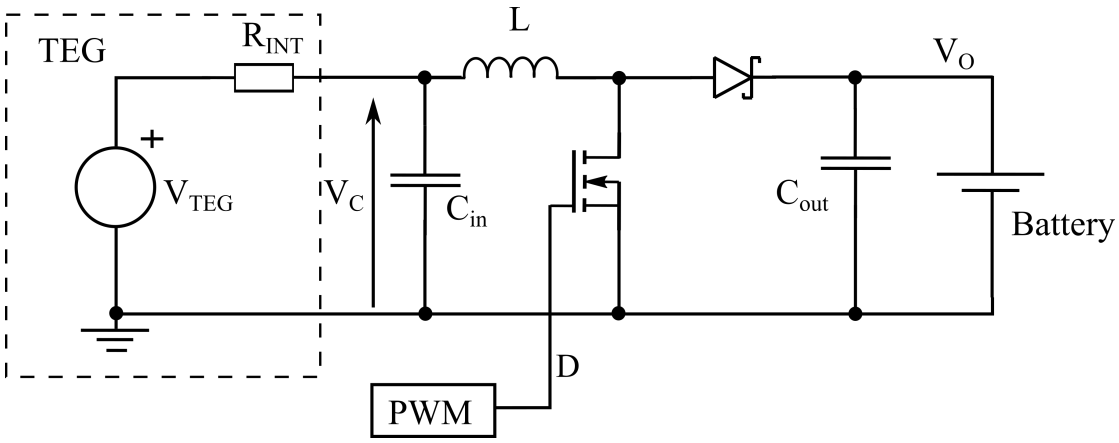

Figure 5–12 - Boost converter

The boost converter is presented in Figure 5–12, where the equivalent circuit of a TEG is connected to the input. The boost converter is made of reactive components, and switch elements that dissipate very low power (ideally zero losses). The two switches are the low-side switch and the high-side switch, implemented with a MOSFET and a diode, respectively. The MOSFET is switched ON and OFF with a fixed frequency but variable duty cycle, which allows the energy transfer between the reactive components and, ultimately, from the input to the output.

The two operating modes of the converter are *continuous conduction mode* (CCM) and *discontinuous conduction mode* (DCM) depending on whether the inductor current reaches zero *Amps*, or not, at the end of the OFF period, respectively. The boost converter used for the MPPT operation of the TEG is designed to operate in CCM. The CCM operation of the boost is represented by two different states: the ON state, that corresponds to the state of the converter when the MOSFET is ON, and the OFF state, that corresponds to the state of the converter when the MOSFET is OFF. The two states of the power converter are represented in Figure 5–13 and may be conveniently thought of as either charging or discharging the inductor respectively.

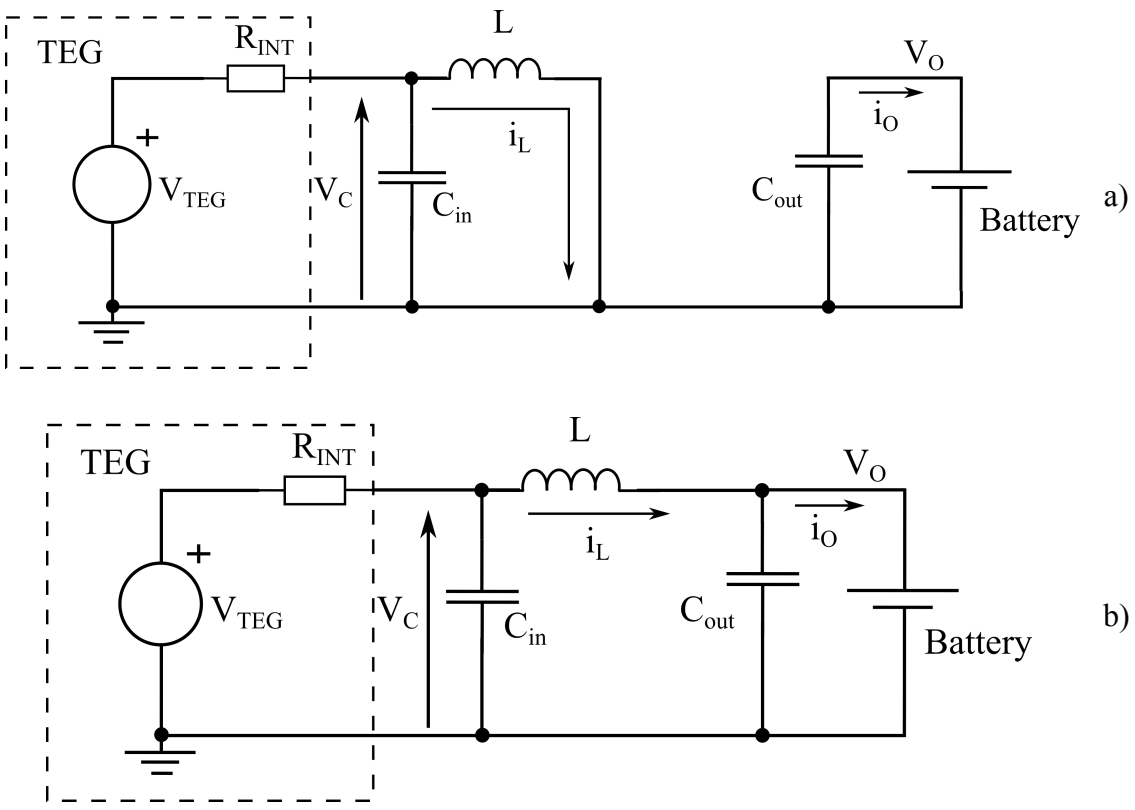

Figure 5–13 - Equivalent circuit of the boost during a) the ON state and b) the OFF state

Based on the two states of the power converter presented in Figure 5–13 it is possible to obtain the steady-state transfer function of the boost converter in CCM.

During the ON time, the diode becomes reversed biased, and the input is isolated from the output. During this period of time, the inductor current ramps up and the energy stored in the inductor increases. The voltage across the inductor during the ON time and the current excursion through the inductor are defined in Equations (**5-4**) and (**5-5**), respectively.

$$V_L|_{ON} = V_C \tag{5-4}$$

$$\Delta i_L|_{ON} = \frac{1}{L}\int_0^{t_{ON}} V_C \, dt = \frac{V_C \cdot t_{ON}}{L} \tag{5-5}$$

During the OFF time, the diode conducts the inductor current to the output; in other words, the current stored in the inductor during the ON time is transferred to the output. During this period of time, the inductor current ramps down and the energy in the inductor

decreases. The voltage during the OFF time and the current excursion through the inductor are defined in Equation (**5-6**) and (**5-7**), respectively.

$$V_L|_{OFF} = V_C - V_{OUT} \tag{5-6}$$

$$\Delta i_L|_{OFF} = \frac{1}{L}\int_0^{t_{OFF}} (V_C - V_{OUT})\, dt = \frac{(V_C - V_{OUT}) \cdot t_{OFF}}{L} \tag{5-7}$$

V_C is the voltage across the input capacitor, which is equivalent to the output voltage of the TEG.

The main voltage and current waveforms in the boost converter, operating in CCM, are shown in Figure 5–14. The inductor current is continuous and presents an average value $\overline{i_L}$ with a current ripple Δi_L. During the ON time, the inductor current flows through the MOSFET and during the OFF time it flows through the diode. Under steady-state conditions, the current excursion during the ON time (Equation (**5-5**)) is equal to the current excursion during the OFF time (Equation (**5-7**)), otherwise there would be a net increase or decrease of current during one switching period, and the converter would not operate under steady-state. The steady-state input to output transfer function of the boost converter can be found by making the sum of Equation (**5-5**) and Equation (**5-7**) equal to zero:

$$\frac{V_C \cdot t_{ON}}{L} + \frac{(V_C - V_{OUT}) \cdot t_{OFF}}{L} = 0 \implies \frac{V_C}{V_{OUT}} = 1 - D \tag{5-8}$$

Where $D = t_{ON}/T$, also called duty-cycle. The duty-cycle D is the ratio of the ON time to the switching period. For a fixed output voltage, the control of the duty-cycle allows the control of the input voltage. The control of t_{ON} between 0 and T is equivalent to a variation of the duty-cycle between 0 and 100 %. Modulation of the duty-cycle is translated in the modulation of the input voltage and this technique is known as Pulse-Width Modulation, or PWM.

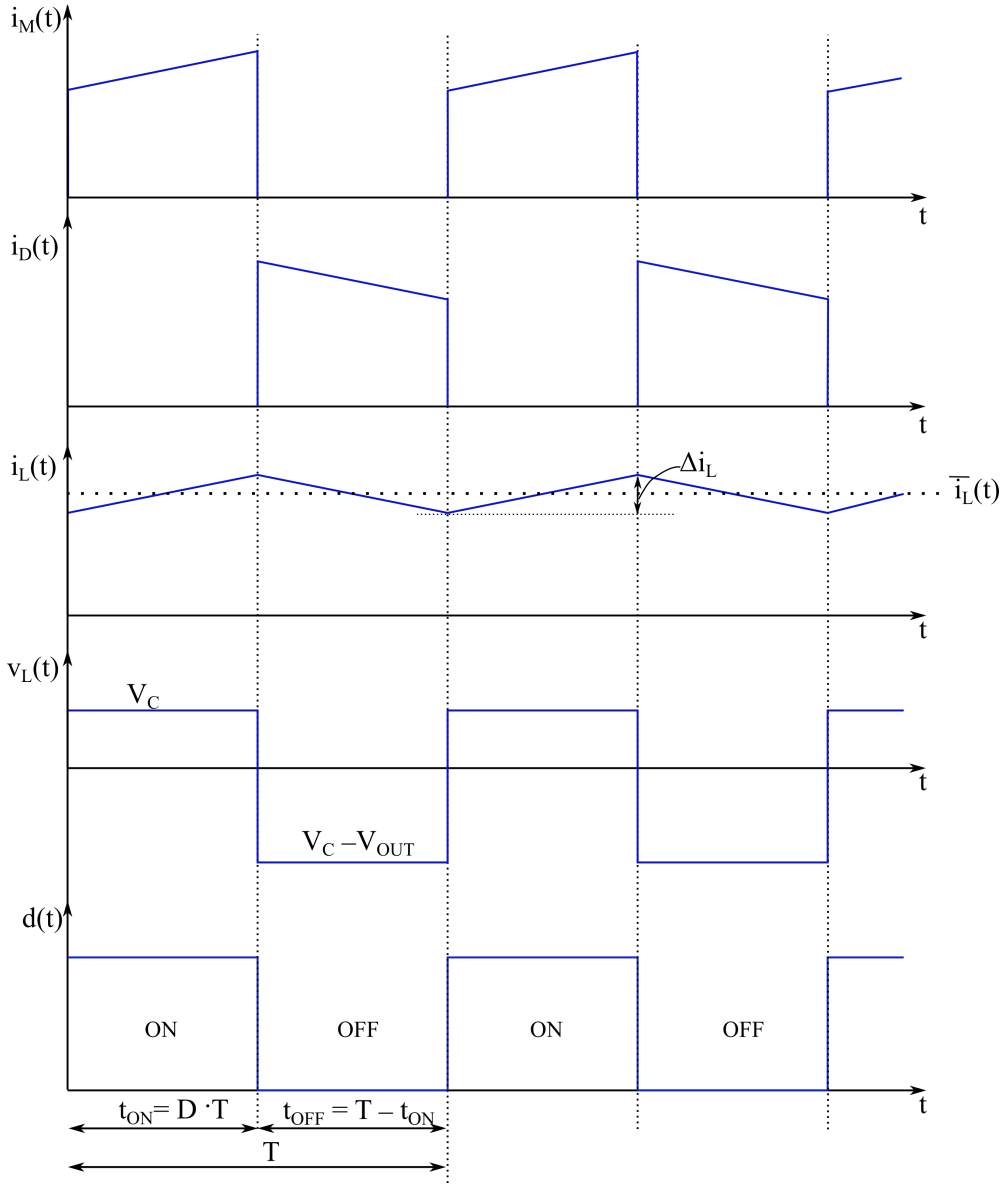

Figure 5–14 - Main boost voltage and current waveforms operating in CCM

5.2.2 Switched model of the boost converter

The model of the boost converter is built using the equations of the inductor and input (TEG) current as well as the input capacitor voltage during the ON and OFF periods of the switching cycle [114]–[118]. During the ON period, these equations can be written as:

$$
\begin{aligned}
i_L|_{ON} &= \frac{1}{L}\int V_C dt \\
i_{TEG}|_{ON} &= \frac{V_{TEG} - V_C}{R_i} \\
i_{C_{in}}|_{ON} &= i_{TEG}|_{ON} - i_L|_{ON} \\
v_{C_{in}}|_{ON} &= \frac{1}{C_{in}}\int_0^{t_{ON}} i_{C_{in}}|_{ON}\, dt
\end{aligned}
\tag{5-9}
$$

During the OFF period, the equations can be written as:

$$
\begin{aligned}
i_L|_{OFF} &= \frac{1}{L}\int V_C - V_O dt \\
i_{TEG}|_{OFF} &= \frac{V_{TEG} - V_C}{R_i} \\
i_{C_{in}}|_{OFF} &= i_{TEG}|_{OFF} - i_L|_{OFF} \\
v_{C_{in}}|_{OFF} &= \frac{1}{C_{in}}\int_0^{t_{OFF}} i_{C_{in}}|_{OFF}\, dt
\end{aligned}
\tag{5-10}
$$

The only difference between the ON and OFF equations is for the inductor current. Based on these sets of equations a model is built in Simulink. The PWM is implemented using a *Switch* block that allows changing the equation of the inductor current during the ON and OFF period. The switched model of the boost converter is shown in Figure 5–15.

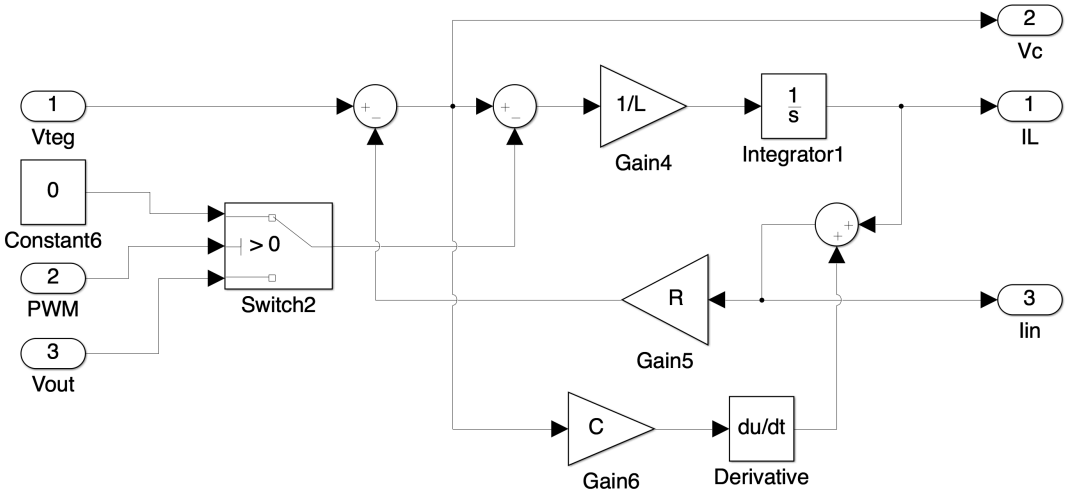

Figure 5–15 - Switched model of the boost converter

Figure 5–16 a) and b) show the voltage across the input capacitor and the inductor current waveforms, respectively, for a battery voltage equal to 28 *V* and a value of R_{INT} equal to 2.75 *Ω*. The values used for the input capacitor C_{IN}, the boost inductor *L* used in the simulation are shown in Table 5-3. The duty-cycle is set to 75 *%* and the open-circuit voltage of the TEG, V_{TEG}, changes from 15 *V* to 10 *V* every 3 *ms*. The switching frequency is 100 *kHz* so t_{ON} is equal to 7.5 *μs* and t_{OFF} equal to 2.5 *μs*. A zoomed-in view of the voltage and current ripple of the waveforms of Figure 5–16 is shown in Figure 5–17 a) and b), respectively.

From Figure 5–16 it can be observed how the input voltage remains constant under steady-state conditions, regardless of the open-circuit voltage of the TEG, V_{TEG}. The input voltage of the boost converter is equal to $V_C = 28 \cdot (1-0.75) = 7\ V$. The DC value of the inductor current is equal to the input current. When the TEG voltage is equal to 15 *V*, the DC value of the inductor current is equal to $(15 - 7)/2.75 = 2.9\ A$ and, when the TEG voltage is equal to 10 *V*, the current becomes $(10 - 7)/2.75 = 1.09\ A$. At the moment V_{TEG} steps up from 10 *V* to 15 *V* the input voltage presents an overshoot until the inductor current increases up to the new DC value. On the other hand, when V_{TEG} steps down from 15 *V* to 10 *V*, the input voltage presents an under-shoot until the inductor current decreases to the new DC value

Parameter	Value
L	270 *μH*
C_{in}	4.7 *μF*
V_O	28 *V*
R_{int}	2.75 *Ω*

Table 5-3 - Parameters used in the switched model of the boost converter

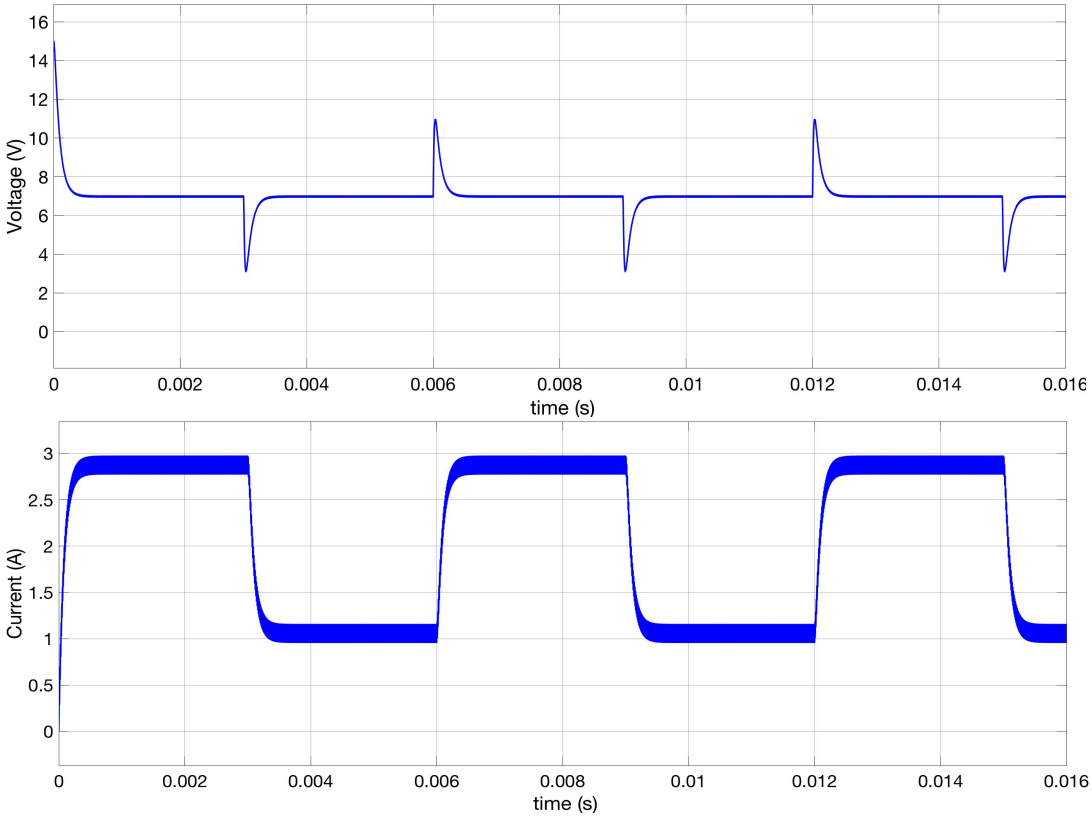

Figure 5–16 – a) Input voltage and b) inductor current waveforms of the switched boost model

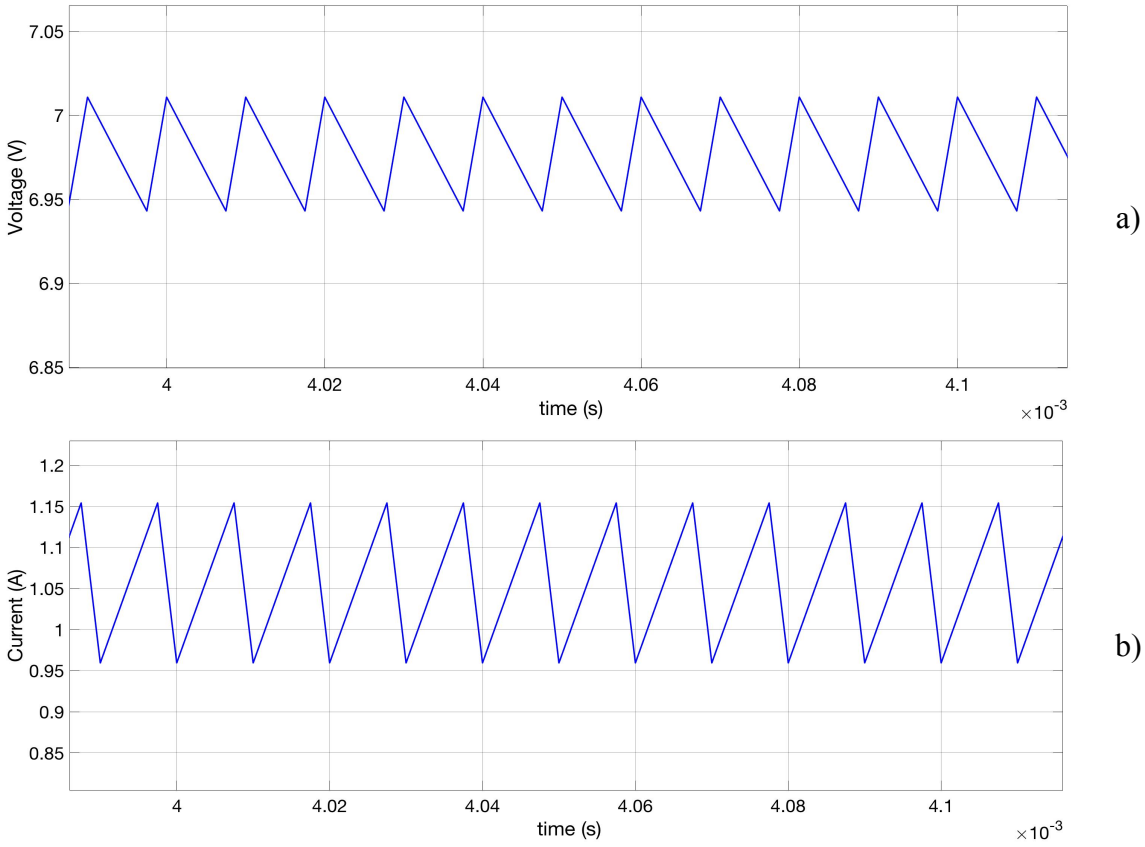

Figure 5–17 - Voltage and current ripple in the input voltage and inductor current

5.2.3 Average model of the boost converter

The switched model of the boost converter provides a model in which the voltage and current waveforms contain both DC and AC information. For the case of the input voltage, the DC value represents the average value of the voltage waveform, and the AC value the voltage ripple. For the case of the inductor current, the DC value represents the average value of the current through the inductor and the AC value the current ripple. In some cases it is important to know the maximum magnitude of the AC values, as it is the case when the maximum current ratings of the current through the switches needs to be calculated, or to ensure magnetic saturation of the inductor core is avoided. In other cases, however, the AC information is not required. This is the case when the efficiency needs to be calculated, or when the stability of the converter needs to be studied. In these cases only the average, or DC values, are of interest.

Conversely, the switching information requires simulation time steps shorter than the switching period in order for it to be properly processed; otherwise the signals are not calculated accurately. This information takes time and computing resources to be processed considerably increasing the simulation times. Reducing the simulation computation time is required in order to be able to run simulations covering an extended period of TEG system operation.

An average model [119] removes all the switching information by averaging the values of voltage and current over a switching cycle, leaving the DC information intact. The average model is faster than the switched version and it also allows the equations required to analyze the stability of the converter to be obtained.

The average model, Figure 5–18, is developed based on the steady-state converter equations shown in the set of Equations (**5-11**). $v_L(t)$ and $i_L(t)$ are the voltage and current in the inductor, respectively; $v_C(t)$ and $i_C(t)$ are the voltage and current in the input capacitor, respectively; R_{INT} is the internal resistance of the TEG; V_{TEG} is the TEG voltage, corresponding to the open-circuit voltage of the TEG; and D is the duty-cycle of the converter. Based on these equations, the average model can be built in Simulink, and it is shown in Figure 5–19.

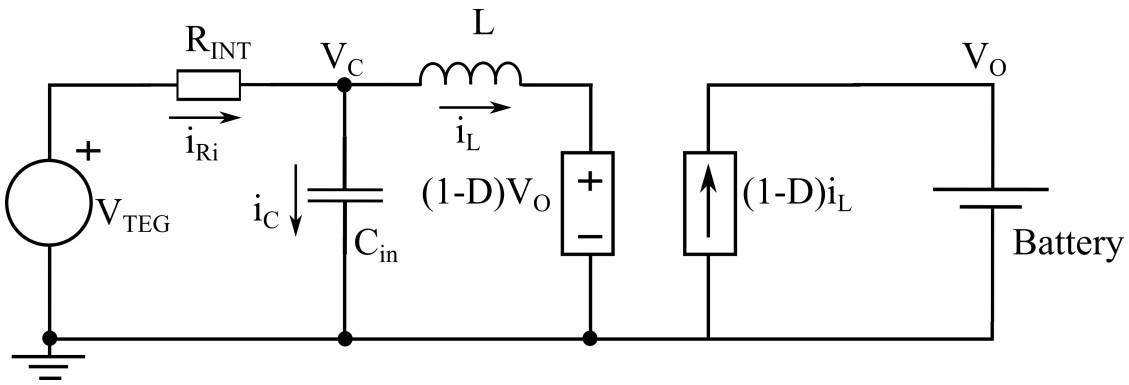

Figure 5–18 - Average model of the boost converter

$$v_L(t) = L\frac{di_L(t)}{dt} = v_C(t) - (1-D)V_o \Rightarrow i_L(t) = \frac{1}{L}\int V_C - (1-D)V_o\, dt$$

$$i_C(t) = C\frac{dv_C(t)}{dt} = i_{R_{INT}}(t) - i_L(t) \Rightarrow v_C(t) = \frac{1}{C}\int i_{R_{INT}}(t) - i_L(t)\, dt \quad (5\text{-}11)$$

$$i_{R_{INT}}(t) = \frac{v_{TEG}(t) - v_c(t)}{R_{INT}}$$

$$\frac{V_O}{V_{TEG}} = 1 - D$$

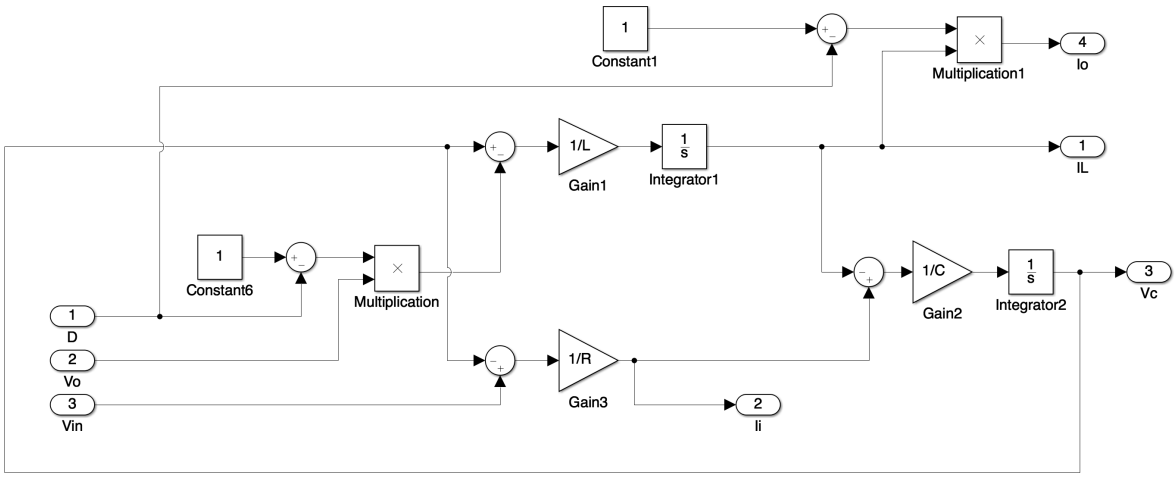

Figure 5–19 - Simulink model of the average boost

The same simulation performed and shown in Figure 5–16 is run again, but this time on the average model. The same conditions for the switched model of Section 5.2.2 are applied, with the same component values specified in Table 5-3. The design and calculations of the

component values is undertaken in Section 6.2.3. The waveforms are shown in Figure 5–20 where it can be seen from the inductor current waveform, Figure 5–20 b), that the switching components have been eliminated. The input capacitor voltage waveform, Figure 5–20 a), does not contain any switching components either.

A comparison between the switched and average models is shown in Figure 5–21, where the TEG open-circuit voltage changes from 10 *V* to 11 *V*. It can be seen how the switching components are not present in the average model while the average value of the converter input voltage and inductor current is the same in both cases.

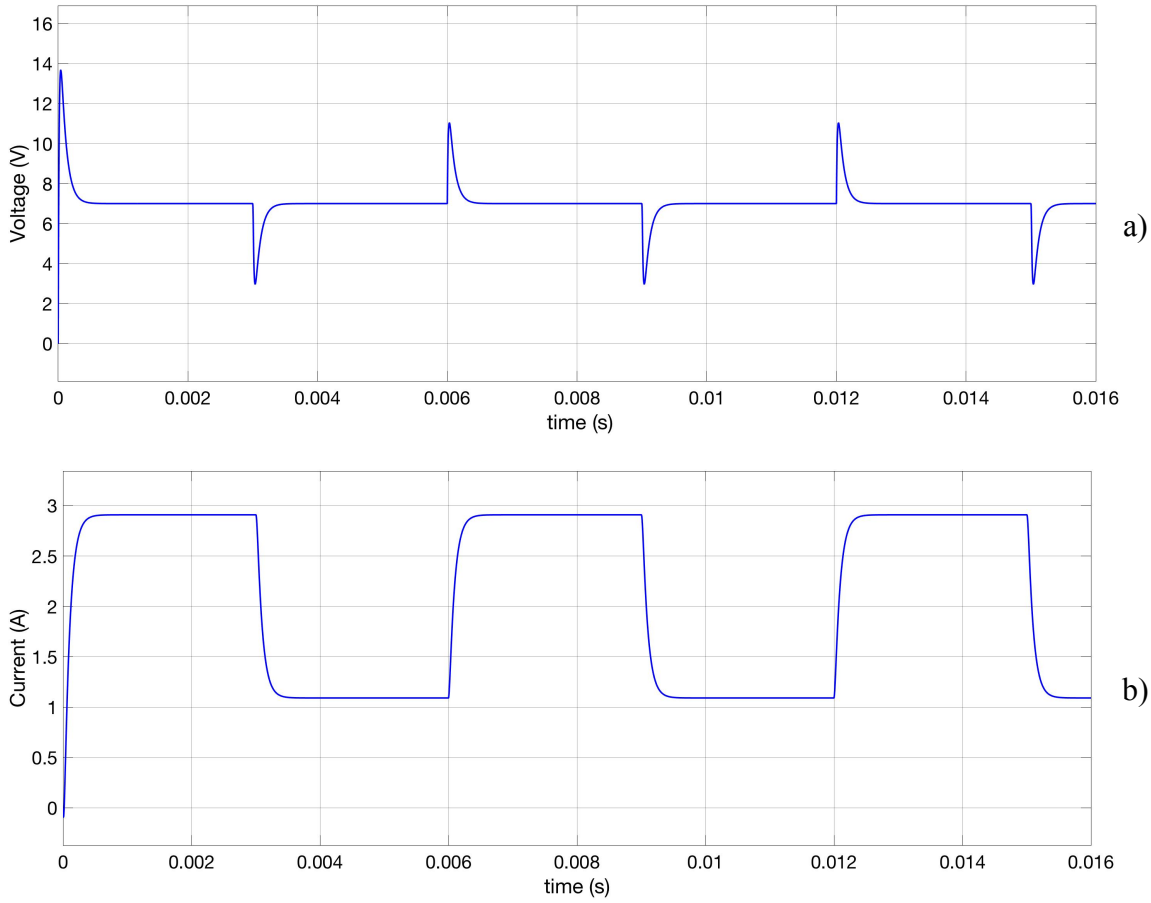

Figure 5–20 – a) Input voltage and b) inductor current waveforms of the average boost model

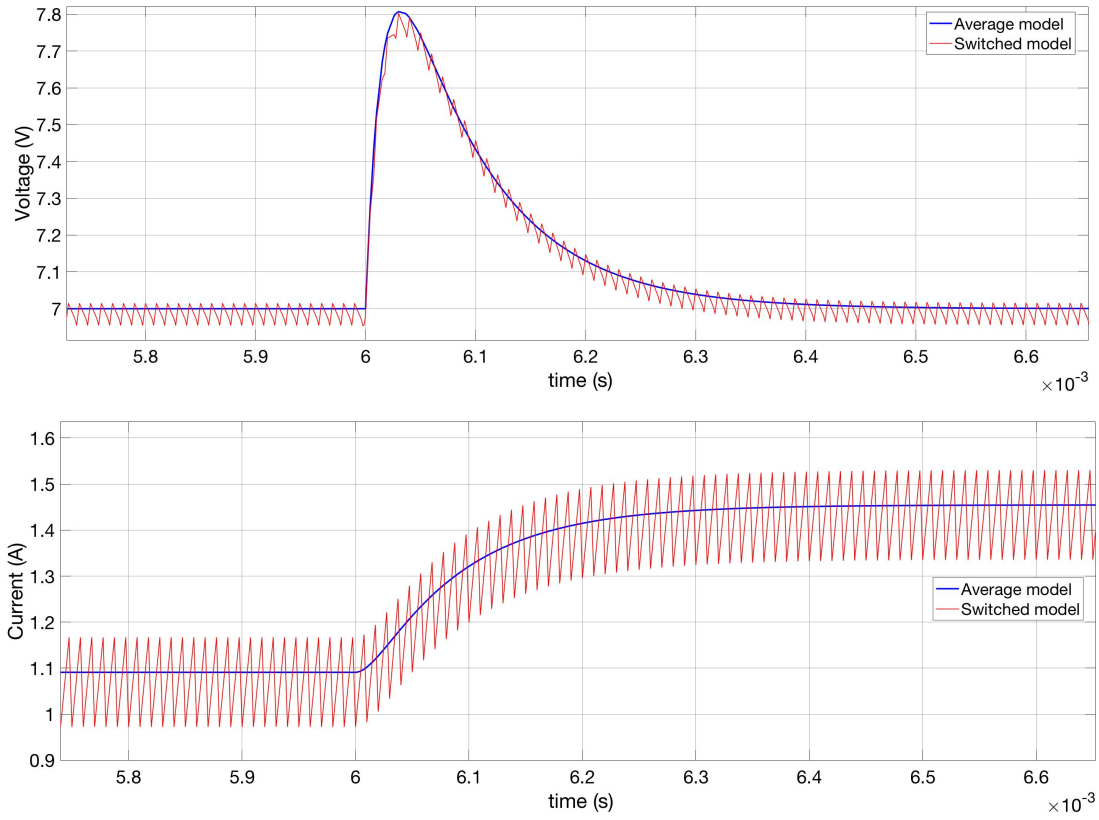

Figure 5–21 - Comparison between the average model (blue traces) and the switching model (red traces) for a) the input voltage and b) the inductor current

5.3 Maximum Power Point Tracking algorithm

As stated at the beginning of Section 5.2, the basic principle of MPPT techniques consists of changing the operating point of the TEG in order to find the MPP. The boost converter is the "*tool*" or "*instrument*" used to change the operating point of the TEG in order to find the MPP. However, the MPPT algorithm is the element that will decide *how* and *when* to change the operating point. There are three main well-known and well-established MPPT algorithms: Fractional Open-Circuit Voltage (FOV or FOC), Incremental Conductance (INC) and Perturb and Observe (P&O) [67], [68].

FOV consists of regulating the TEG voltage to a fixed voltage, usually a fraction of the open-circuit voltage. In TEGs operating under constant ΔT, the MPP voltage corresponds to 50 % (β = 0.5) of the open-circuit voltage so the MPPT algorithm monitors constantly the open-circuit voltage in order to track accurately the MPP of the TEG. The typical flow chart of the FOV MPPT algorithm is displayed in Figure 5–22. However, when a TEG operates under constant heat flux, the MPP is not found at 50 % of the open-circuit

voltage; furthermore, the β factor changes with the input heat flux and with the type of TEG [112]. FOV will therefore not optimize the operation of the TEG at the MPP as the β factor will change under different operating conditions.

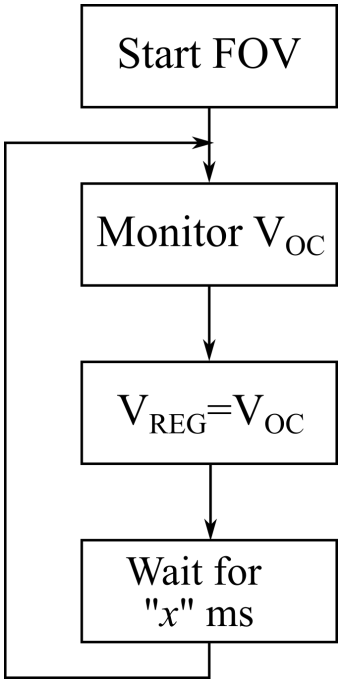

Figure 5–22 - Simplified flow chart of FOV MPPT algorithm

P&O algorithm monitors constantly the TEG power and, depending on whether the current value of power is higher or lower than the previous value, the operating point is changed in one direction or in the opposite one. The simplified flow chart of P&O is displayed in Figure 5–23, where the first operating point is set to 50 % of the instantaneous open-circuit voltage in order to move faster towards the MPP at start-up.

The P&O sampling period, defined in Figure 5–23 as "x" milliseconds, is usually in the order of few hundred of milliseconds to few seconds. A short sampling period, equivalent to a fast P&O frequency, is desirable in applications where the TEG operates under (nearly) constant ΔT because it allows fast tracking of the MPP. In constant heat applications, and due to the "long" thermal transients, a "fast" P&O algorithm will produce an oscillatory behaviour and will not track efficiently the MPP. The reason for this is that without measuring the power generated under steady-state conditions, the algorithm will not be able to find a steady-state operating point at which the TEG operates at the MPP.

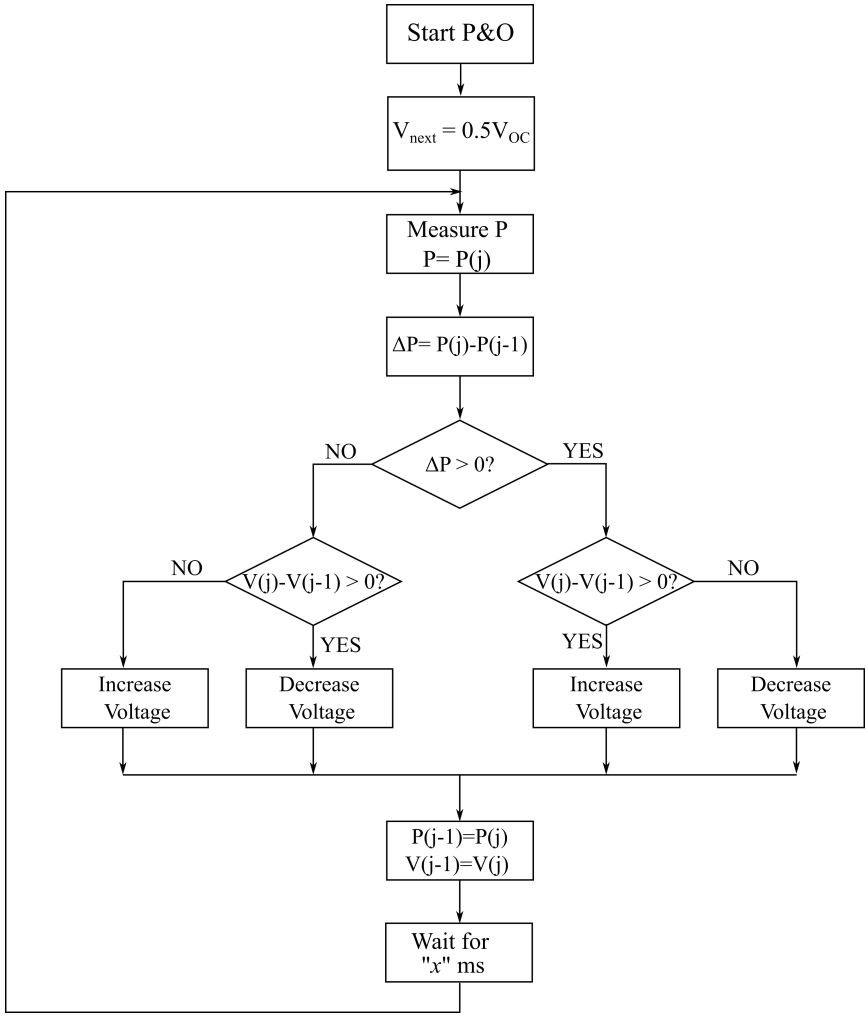

Figure 5–23 - Simplified flow chart of P&O MPPT algorithm

INC is very similar to P&O but it changes the operating point of the TEG based on the slope of the power-voltage curve. When the operating point lies to the right of the MPP, $dP/dV < 0$ and, when the operating point lies to the left of the MPP, $dP/dV > 0$. These conditions can be verified by measuring the TEG output voltage and current, as shown in the simplified flow chart shown in Figure 5–24. As with “fast” P&O algorithms, a “fast” INC algorithm will not be able to find the steady-state operating point at which the TEG is at the MPP.

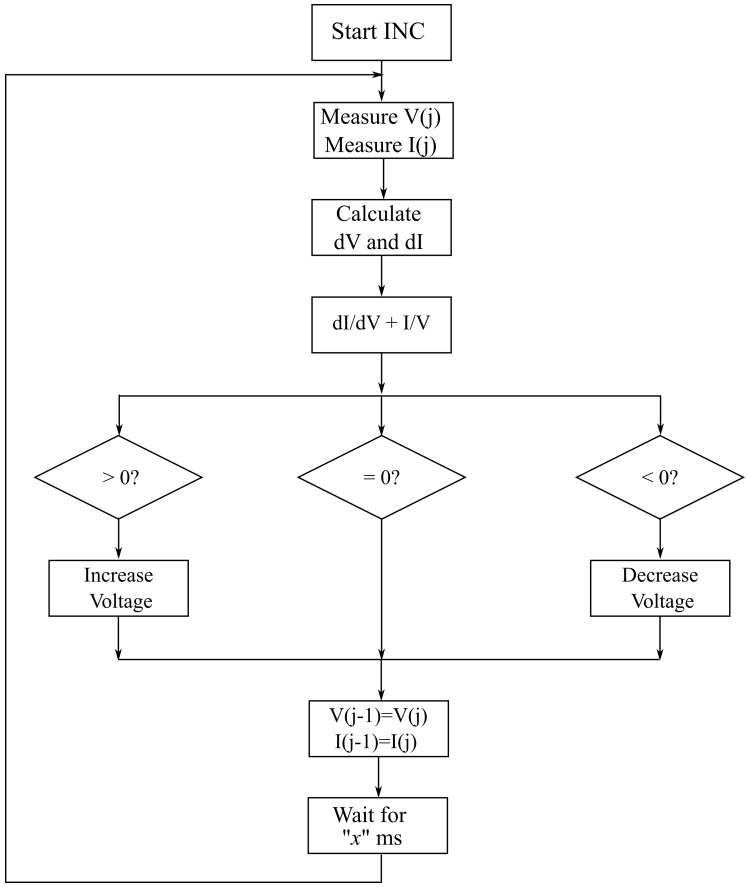

Figure 5–24 – Simplified flow chart of the INC algorithm

The proposed MPPT algorithm takes into consideration the "long" thermal time constant of typical TEG systems and it adapts the perturbation step dynamically based on the steady-state value of the instantaneous open-circuit voltage. The algorithm builds on previous literature that explored how in constant heat TEG systems the MPP is found with TEG voltages between 50-60 % of the instantaneous open-circuit voltage [55], [111].

The flow chart of the proposed algorithm is shown in Figure 5–25. The first operating point is set to 50 % of the open-circuit voltage. Since the MPP is in the region between 50-60 %, the first operating is set in the proximity of the MPP. The subsequent operating points are set using a conventional P&O whereby the voltage is perturbed depending on the TEG power. When the TEG power measured at instant "*i*" is higher than the power measured at instant "*i*-1", then the voltage is perturbed in the same direction it was set at instant "*i*-1", otherwise the direction of the perturbation is changed. If at any point the calculated target voltage is lower than 50 % or higher than 60 % of the instantaneous open-circuit voltage, the voltage is set to 52 % or 58 %, respectively. This aids the MPPT algorithm not to operate at points outside the MPP range, rendering the algorithm faster than it would be without applying these limits. The step size used in the P&O, stated as

"step" in the flow chart, is proportional to the instantaneous open-circuit voltage with a factor of proportionality equal to $V_{NEXT} = 0.015V_{OC}$. This value has been calculated so that the perturbation step is higher than the V_{LSB} of the ADC converter used to calculate the value of TEG power but low enough to avoid setting the operating point too far from the true MPP. The factor 0.015 is obtained from an approximation to the power-voltage characteristic curve, assuming a fix value of R_{INT} and V_{OC}. Knowing that:

$$P_{TEG} = {V_{OC}}^2 \frac{R_L}{(R_L + R_{INT})^2}$$

and

$$P_{TEG}|_{MAX} = \frac{{V_{OC}}^2}{4 \cdot R_{INT}}$$

for

$$P_{TEG} = k \cdot P_{TEG}|_{MAX}$$

$${V_{OC}}^2 \frac{R_L}{(R_L + R_{INT})^2} = k \cdot \frac{{V_{OC}}^2}{4 \cdot R_{INT}} \Longrightarrow R_L = \frac{-R_{INT}\left[(k-2) \pm 2\sqrt{1-k}\right]}{k}$$

and therefore:

$$V_{TEG} = V_{OC} \frac{R_L}{R_L + R_{INT}} = V_{OC} \frac{-\left[(k-2) \pm 2\sqrt{1-k}\right]}{k - \left[(k-2) \pm 2\sqrt{1-k}\right]}$$

The maximum voltage step from the MPP, normalized to the MPP voltage is:

$$\frac{V_{TEG} - V_{TEG}|_{MPP}}{V_{TEG}|_{MPP}} = \sqrt{1-k}$$

$$\frac{V_{TEG} - V_{TEG}|_{MPP}}{0.5 \cdot V_{OC}} = \sqrt{1-k} \Longrightarrow V_{TEG} - V_{TEG}|_{MPP} = V_{OC} \frac{\sqrt{1-k}}{2}$$

The V_{LSB} of a 12-bit ADC with $V_{REF} = 3.3\ V$ is:

$$V_{LSB} = \frac{3.3}{2^{12} - 1} = \frac{3.3}{4095} = 805.86\ \mu V$$

With:

$$V_{TEG} - V_{TEG}|_{MPP} = 0.015 \cdot V_{OC}$$

Assuming a minimum V_{OC} equal to 1 V, the minimum step is 18 times higher than V_{LSB} and a step away from the MPP places the operating point at 0.9991 % of P_{MPP}.

Derivative adaptive steps increase the speed and accuracy of the MPPT algorithm; however, in real digital MPPT implementations there are limitations imposed by different factors like the numerical stability and discretization and quantization errors [97]. For instance, when using a step equal to *dP/dV*, when the converter operates in the vicinity of the MPP, the perturbations are very small hence *dV* and *dP* are also very small. A quantization error that makes *dV* smaller than *dP* might lead to an excessive step that would send the next operating point far from the MPP.

When the converter operates in P&O mode the power delivered by the TEG is monitored, and the operating point changed, after 4 system thermal time constants, that is, after $4\tau_{TEG}$. By doing so, the actual value of steady-state power is evaluated.

In order to track the changes in the input heat flux and quickly respond to these variations, the open-circuit voltage is monitored constantly after each perturbation step. First, after two system thermal time constants, $2\tau_{TEG}$, and then it is monitored continuously until the next perturbation step. If the difference in the instantaneous open-circuit voltage is greater than 0.1 V then the operating point is immediately changed to $0.5V_{OC}$, because this means that there is a change in the input heat flux. This action is performed in order to make sure the algorithm responds to external changes without having to wait for a time equal to $4\tau_{TEG}$. One might think that the algorithm could react faster if the open-circuit voltage was monitored immediately after a perturbation step; however, during the first $2\tau_{TEG}$ the open-circuit voltage changes considerably as a consequence of the thermal transient. If this was the case, the algorithm would be deceived by the natural change in open-circuit voltage due to the transient response and the algorithm would become unstable.

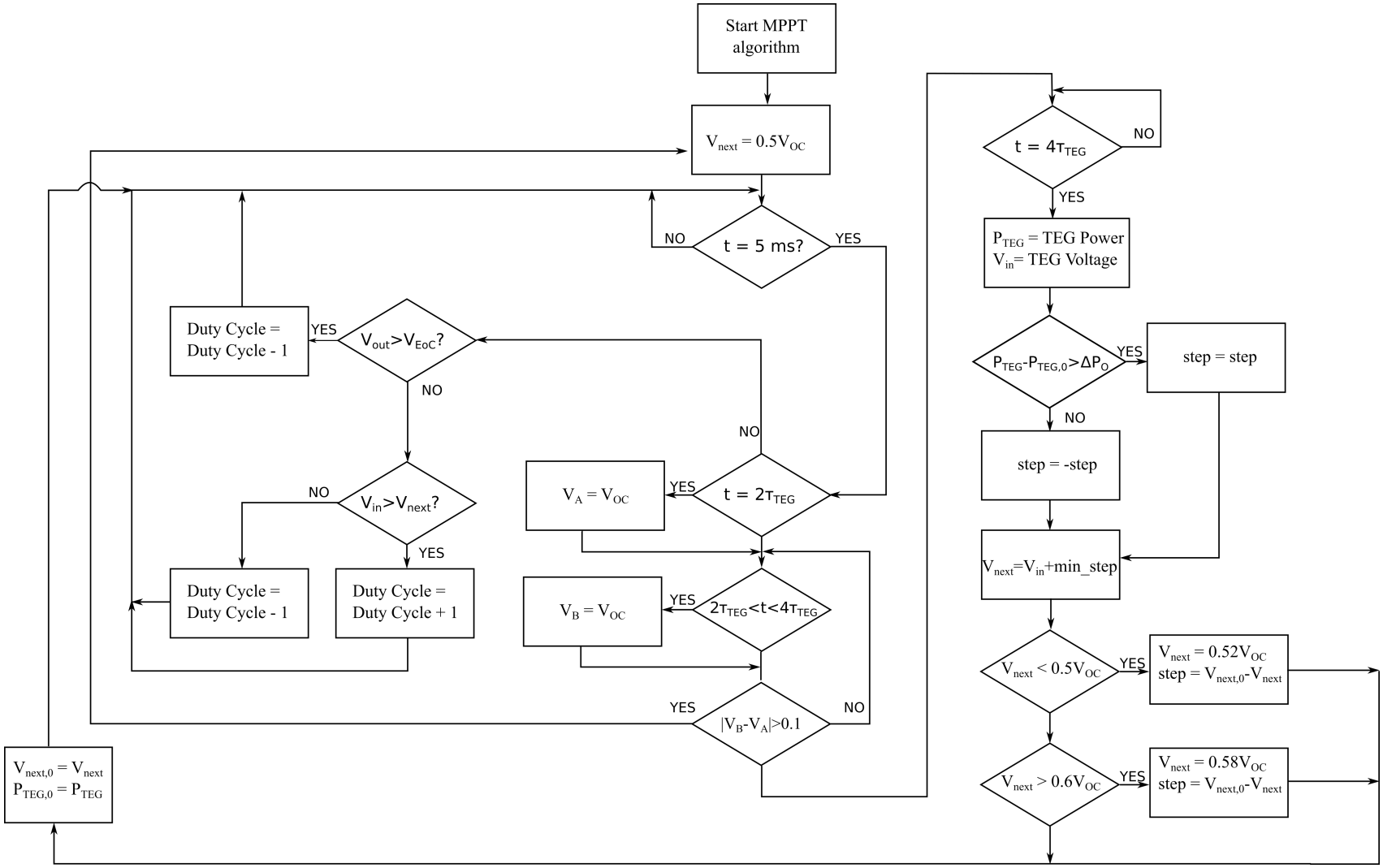

Figure 5–25 - Flow chart of the new proposed MPPT algorithm

The power converter regulates the input voltage using a control loop that monitors the TEG voltage every 5 *ms* and compares it to the target voltage V_{NEXT}. The operating point is varied accordingly, increasing or decreasing the duty-cycle by the minimum duty-cycle step the control system can apply. This control loop is implemented in order to avoid loss of control due to drifts in the duty-cycle-to-input control of the PWM, aging of components or other events like injection of external signals like noise.

If the output voltage (battery voltage) reaches the maximum charge voltage of the battery, also known as End of Charge voltage, the power converter starts decreasing the duty cycle until it becomes 0 *%* and the converter delivers zero energy to the battery, *i.e.*, the battery is fully charged.

The effectiveness of this algorithm will be verified in the next section, where the whole TEG system, along with the MPPT algorithm, is implemented in Matlab/Simulink.

5.4 TEG System Model

With the model TEG and the power converter, the model of the TEG system is built. The output of the TEG model will be connected to the input of the model of the power converter, and the *duty-cycle* input to the power converter will be the control input of the operating point of the TEG. The MPPT algorithm will set the duty-cycle, and for that purpose a block that contains the algorithm instructions needs to be added to the system. With the MPPT algorithm the control loop of the system will be closed and the electrical power delivered by the TEG will be controlled as per the MPPT algorithm.

The model of the overall system is shown in Figure 5–26. The input heat flux is set by the red block, which reads the parameters from an external spreadsheet that contains the input power profile. This aids the simulation of the TEG system under different input heat flux profiles. The cyan block is the TEG model which has the output *"Vout"* connected to the *"Vin"* input of the boost model (orange block). The model of the boost used is the average one, which yields faster simulations than the switched model. The green block contains the MPPT algorithm. The inputs *"vin"* and *"iin"* take the voltage and current readings for the TEG, which are filtered using a first order low-pass filter block before they are fed into the MPPT algorithm block. These filter blocks implement the low-pass *RC* filters used in the actual hardware.

The purpose of the model of the TEG system is to run simulations implementing the conventional P&O described in Figure 5–23, the FOV algorithm described in Figure 5–22 and the new algorithm described in Figure 5–25; and compare the results of all three algorithms. Four blocks (*"FracVoc"*, *"PO"*, *"FracVoc_V"* and *"PO_V"*) are used to store and plot the output power and voltage obtained using conventional P&O and conventional FOV against the results obtained with the new algorithm.

The monTE™ generator comprises of 196 pairs of pellets, three of which are not connected to the main string of pellets and are used for open-circuit and temperature sensing. The output voltage of these pellets is proportional to the voltage of the main string of pellets by a factor of 1/63. The voltage reading from these pellets can be used to sense the instantaneous open-circuit voltage of the TEG while working at load without having to disrupt the operation of the power converter. The Simulink model of the monTE™ also implements this output and it is fed into the MPPT algorithm block to obtain the reading of the instantaneous open-circuit voltage.

Finally, the blue block is a constant that is used to fix the temperature on the cold side of the TEG, and the yellow block is a constant that represents the battery voltage at the output of the boost converter.

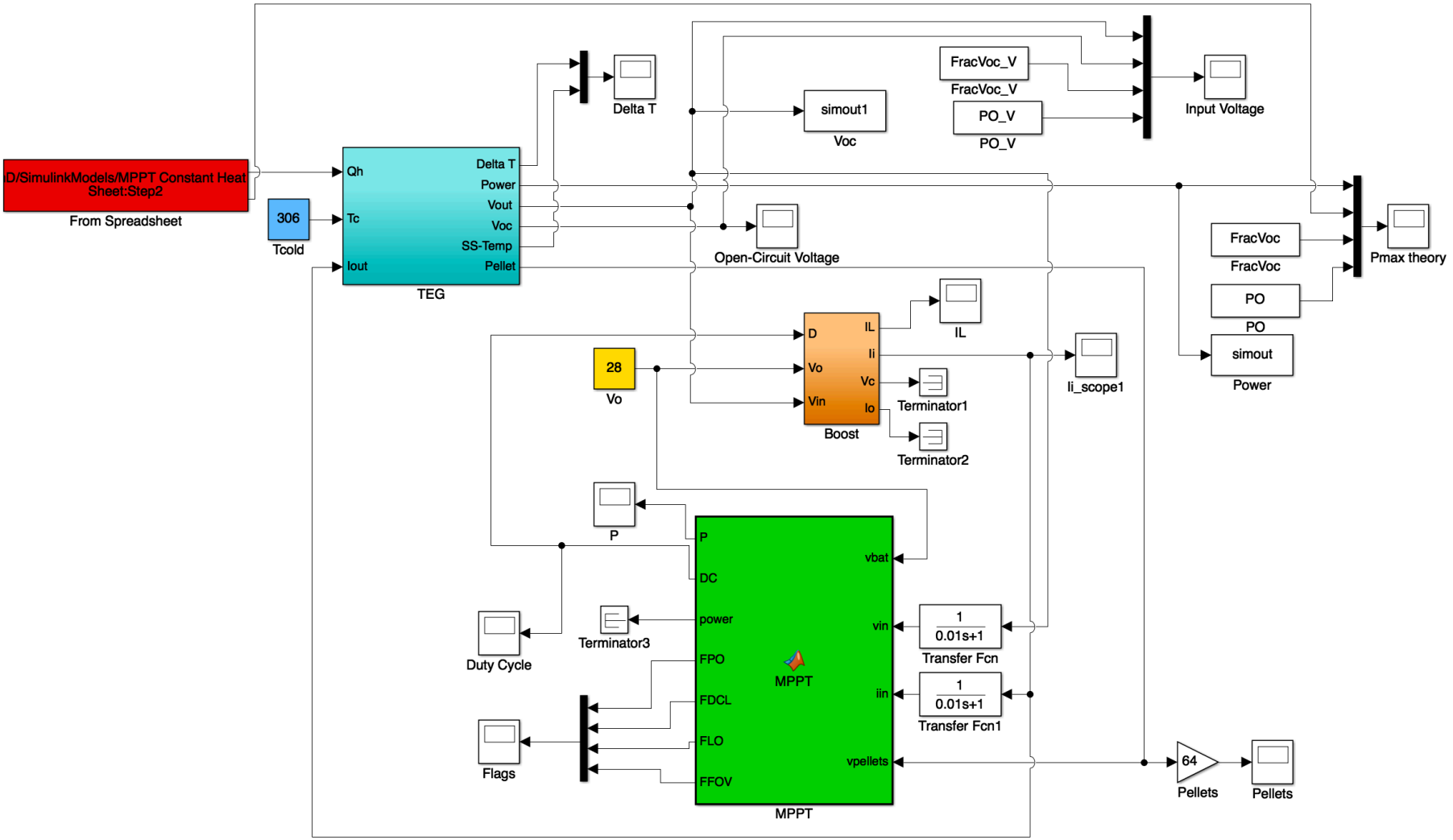

Figure 5–26 - Simulation model of the TEG system including the MPPT algorithm

The thermal time constant of the monTE™ is equal to 115 *s*, as discussed in Section 5.1. This means that $4\tau_{TEG}$ is equal to 460 *s*. The P&O frequency of the new algorithm needs to be higher than 460 *s* ($\tau_{MPPT} > 4\tau_{TEG}$). The new algorithm will implement a $\tau_{MPPT} = 500$ *s*. On the other hand, the time constant of the power converter is in the order of microseconds, which is dictated by the values of the boost inductor and input capacitor. If the step size of the simulation is set to be compatible with the time constant of the power converter, it would be impractical to run simulations using the actual time constants of the TEG system as each simulation would take several hours. The thermal time constant of the TEG will be decreased by a factor of 1000 in order to reduce the simulation times. Once this is done, the MPPT sampling time of the three different algorithms that will be simulated will also be reduced. Also, the regulation period is reduced by a factor of 10, from 5 *ms* to 500 μs. The simulation and the actual time constant and sampling periods are shown in Table 5-4.

On the other hand, it is desirable to simulate the power converter with the actual time constant of the circuit; that is, without modifying its dynamic response. By doing so, it is possible to simulate and observe the dynamic behaviour of the converter to changes in the operating point of the TEG. The relatively low time constant of the power converter is therefore the limiting factor in terms of simulation speed.

For the new proposed algorithm presented in this work, the MPPT sampling period, during perturb and observe operation, is equal to 500 *s*. This is considered in this work as a "slow" P&O. For the other two conventional algorithms, the new one will be compared against, the MPPT sampling period will be 5 *s*. This sampling rate, being 100 times lower than the MPPT sampling rate of the new algorithm (in the real system, 50 times lower in the simulation), is considered a "fast" rate. That is why in this work the conventional P&O is also referred to as "fast" P&O.

Even if an MPPT sampling rate of 5 *s* would be considered a slow sampling rate in other applications, like photovoltaic, it is a fast rate for TEG applications.

Parameter	Simulation	Real System
Regulation Period	500 μs	5 ms
TEG time constant	1.15 s	115 s
New algorithm MPPT sampling period	500 ms	500 s
FOV MPPT sampling period	10 ms	5 s
P&O MPPT sampling period	10 ms	5 s

Table 5-4 - Time constants of the simulated and real system

5.5 Simulation results

The performance of the MPPT algorithm described in Section 5.3, compared to conventional FOV and "fast" P&O, was tested using the model of the TEG system described in Section 5.5.

A first set of simulations was run at constant values of input heat flux. The values of input heat flux were 100 W_{th}, 200 W_{th} and 300 W_{th}. The difference in performance of all three algorithms can be compared under fixed values of input heat flux. Another simulation was performed where the input heat flux was stepped from 75 W_{th} to 250 W_{th}, and then back down to 150 W_{th}, see Figure 5–27. The purpose of this simulation was to check the response of the algorithm to sudden changes in the input heat flux.

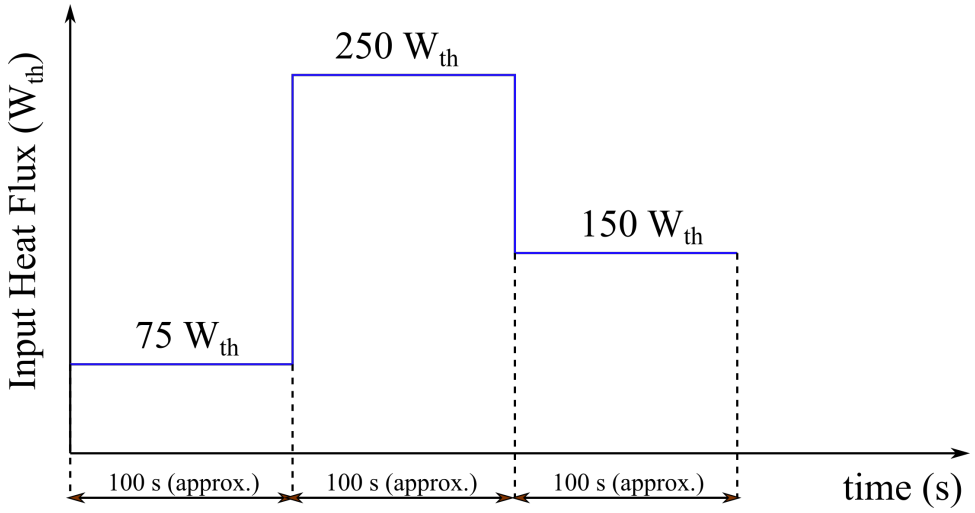

Figure 5–27 - Input thermal profile used to simulate the input power step transients

Finally, the three algorithms were simulated by applying the input heat flux in the form of a ramp. Three different ramps were used. First, a ramp from 100 W_{th} to 250 W_{th}, and then

back down to 100 W_{th}. The time delay of each ramp was equal to 1000 s. The second ramp was slower, where the power limits were the same as in the first case but the ramp time was equal to 3000 s. The third ramp was faster, where the value of input power changes from 75 W_{th} to 330 W_{th} and then back down to 75 W_{th} with a ramp time of 1000 s. The three ramp profiles are defined in Table 5-5 and Figure 5–28. The purpose of this simulation was to check the performance of the algorithm under increasing and decreasing heat flux conditions.

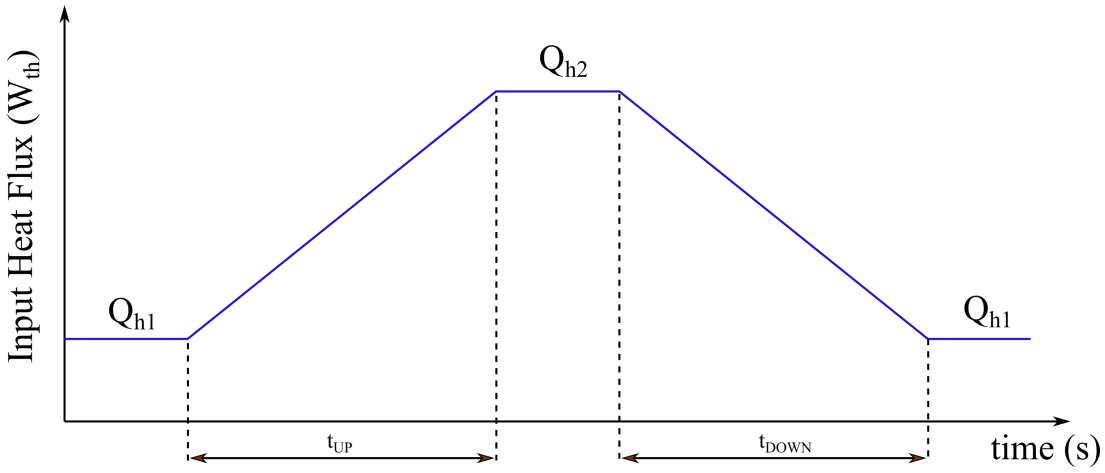

Figure 5–28 - Input thermal profile used to simulate the input power ramp transients

Parameter	1st ramp	2nd ramp	3rd ramp
Q_{h1}	100 W_{th}	100 W_{th}	75 W_{th}
Q_{h2}	250 W_{th}	250 W_{th}	330 W_{th}
t_{UP}	1000 s	3000 s	1000 s
t_{DOWN}	1000 s	3000 s	1000 s
Rate	150 mW_{th}/s	50 mW_{th}/s	225 mW_{th}/s

Table 5-5 - Parameters used in the ramp test

Figure 5–29 a) shows the simulation with an input heat flux of 100 W_{th}. Figure 5–29 b) shows a zoomed-in view during steady-state operation, where the superior performance of the new algorithm can be observed.

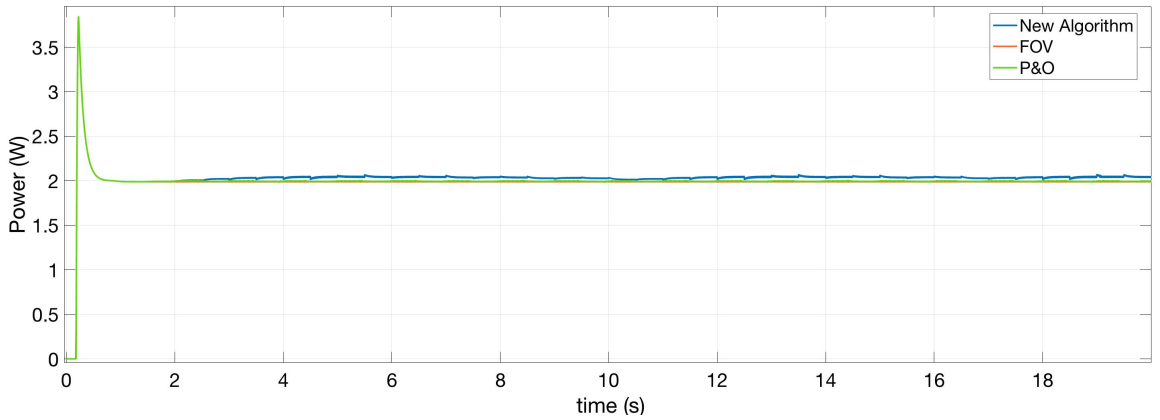

a)

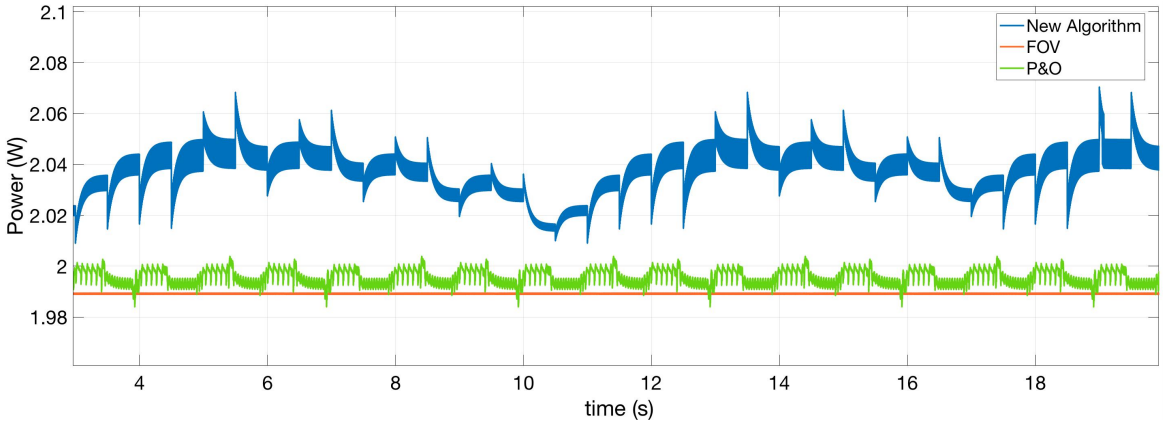

b)

Figure 5–29 - Simulation run at constant input heat flux equal to 300 W_{th}, a) Entire simulation result b) Zoomed-in view of the steady-state portion

The initial transient shows that all three algorithms present the same initial operating point as a result of all three algorithms setting the first operating point at 50 % of the instantaneous open-circuit voltage. This is shown in Figure 5–30 where all three power traces are superimposed on top of each other (P&O plotted last).

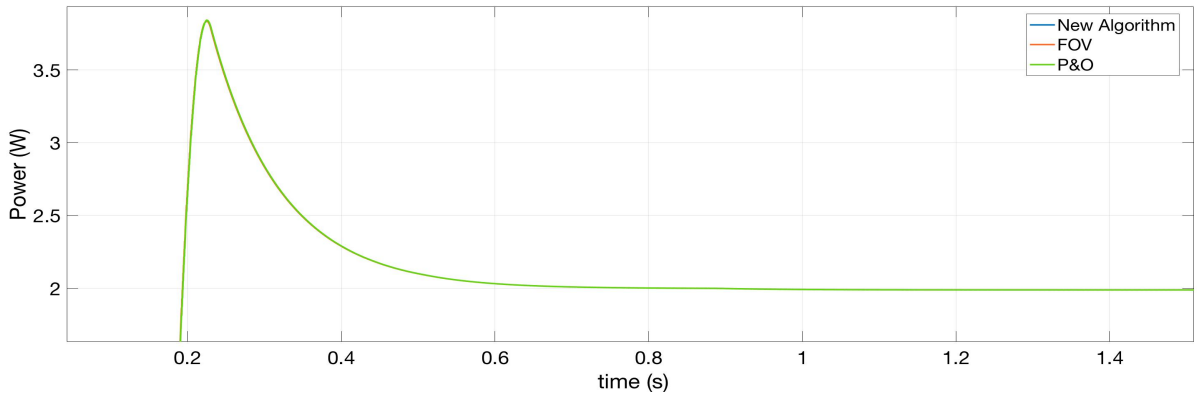

Figure 5–30 - Initial transient and operating point of all three algorithms with an input heat flux equal to 100 W_{th}

Each MPPT cycle of the new algorithm takes 500 *ms*, as stated in Table 5-4, and it can be seen in Figure 5–31. In this figure it can be appreciated that, when the steady-state value of TEG power is sampled by waiting for $4\tau_{TEG}$ before changing to the next operating point, the output power is more stable than with "fast" P&O. Another observation is that there is a "ripple" on the power trace of all three algorithms, more noticeable on the power trace of the new algorithm. This ripple is the result of the regulation cycle implemented on the input voltage, which is shown in Figure 5–32. Figure 5–32 a) shows the ripple on the power trace while Figure 5–32 b) shows the ripple on the voltage trace. The ripple has a period of 500 μs; that is, a frequency of 2 *kHz*, which is equivalent to the frequency of the input voltage control loop.

Another important observation to make is that the variations in TEG power, due to the input voltage or MPPT regulation cycles, are smaller than the variations in TEG voltage. This is because, as shown in Figure 4–4, variations in TEG voltage around the MPP produce smaller variations in the output power. From Figure 5–32 it can be seen that a variation of 30.5 *mV* produces a variation of only 8.5 *mW* in the output power.

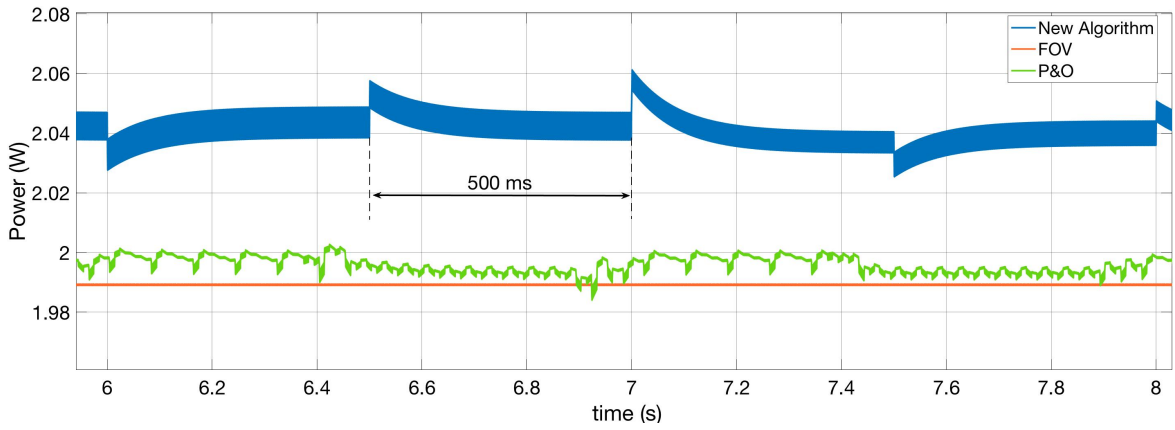

Figure 5–31 – Zoomed-in view of the MPPT cycles of the new algorithm

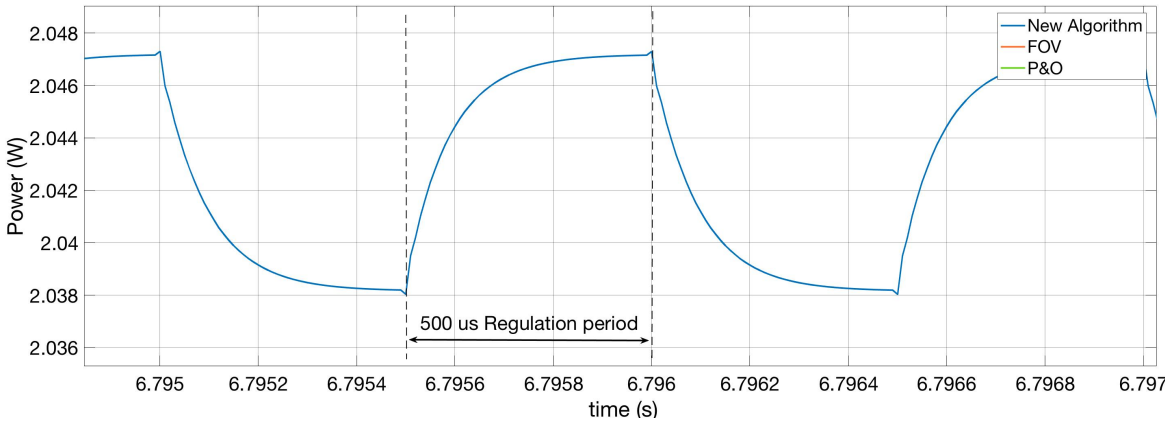

a)

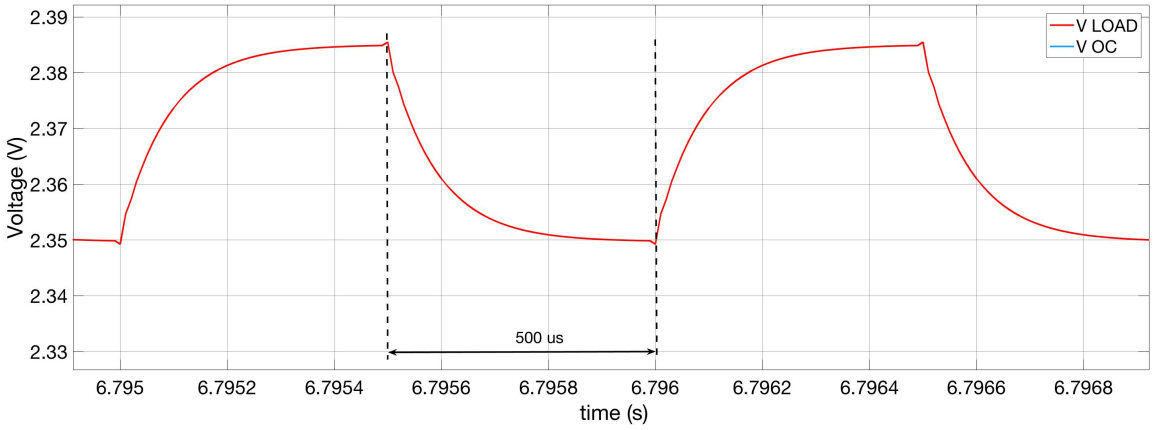

b)

Figure 5–32 – Zoomed-in view of the power and voltage ripple as a consequence of the input voltage regulation loop

For the case of "fast" P&O and FOV, the MPPT sampling period is equal to 10 *ms*, which is equal to a sampling frequency of 100 *Hz*. Figure 5–33 shows a zoomed-in view of the power traces for "fast" P&O and FOV during steady-state operation, where both the MPPT and input voltage regulation periods are shown. Whereas the FOV operation is very stable, since the TEG voltage is not changed during steady-state, the variations in the operation point of the "fast" P&O algorithm are larger than with the new algorithm. This means that the "stability" of the new algorithm, during steady-state operation, is better than with "fast" P&O.

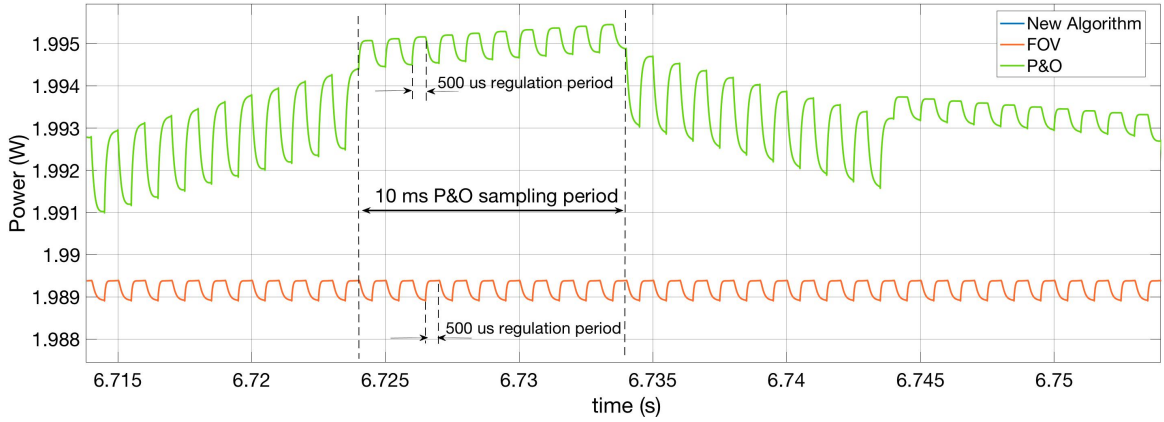

Figure 5–33 - Zoomed-in view of the steady-state ouptut power when using "fast" P&O and FOV

Both the TEG output voltage and the open-circuit voltage, obtained with the new algorithm, are shown in Figure 5–34. Figure 5–34 b) shows a zoomed-in version of Figure 5–34 a). In this figure both the MPPT and regulation cycles can be distinguished. The TEG output voltage oscillates around a steady-state value equal to 2.306 V. In other words, the operating point of the TEG "perturbs" the operating point of the TEG around that steady-state point meaning that the operation of the TEG is stable. This can also be seen from Figure 5–31, where the output power of the TEG is stable around 2.04 W.

The start-up operation of the algorithm can be explained using Figure 5–35. During the first 1.5 seconds, the algorithm performs FOV, setting the initial operating point of the TEG at 50 % of the initial open-circuit voltage. After 1.5 seconds, the algorithm starts performing P&O with an MPPT sampling frequency of 2 Hz. After operating at 50 % of V_{OC} the voltage climbs up to a voltage that is higher than $0.5V_{OC}$, meaning that the MPP is found at output voltages that are higher than 50 % of the TEG open-circuit voltage. Once the MPP is found, the operating point of the TEG oscillates around it.

The TEG output current is shown in Figure 5–36. The same observations, with regards the MPPT and input voltage regulation cycles, made for the power and voltage traces are also applied to the TEG output current.

The simulation performed under an input heat flux of 100 W_{th} is run for 20 seconds. Under these conditions, the total energy delivered with the TEG, using the proposed algorithm, is equal to 40.48 J. With the "fast" P&O the energy delivered is 39.76 J, and with FOV 39.64 J. This means that the new algorithm produces 1.81 % more energy than the "fast" P&O, and 2.12 % more energy than FOV. Also, when the TEG reaches steady-state conditions,

the output and open-circuit voltages are 2.30 *V* and 4.17 *V*, respectively. The beta factor during steady-state operation is equal to 0.5524. These results are summarized in Table 5-6.

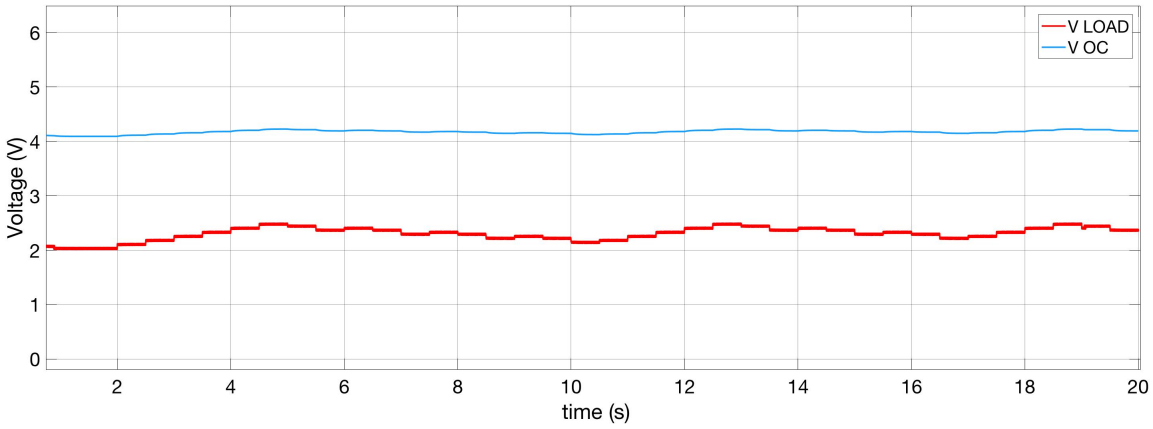

a)

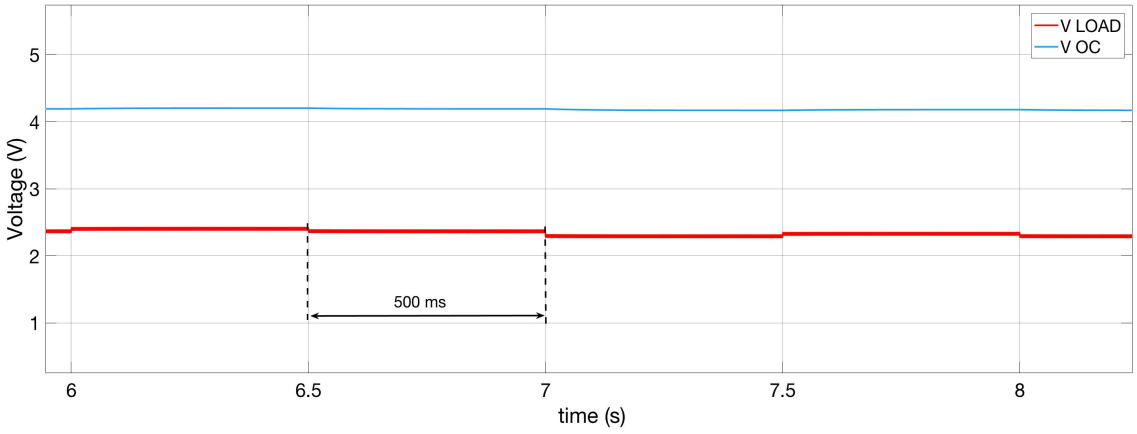

b)

Figure 5–34 - TEG open-circuit (blue trace) and output voltage (red trace) voltages when the TEG operates under a constant heat flux equal to 100 W_{th}. a) Steady-state waveforms b) zoomed-in view of the MPPT regulation period

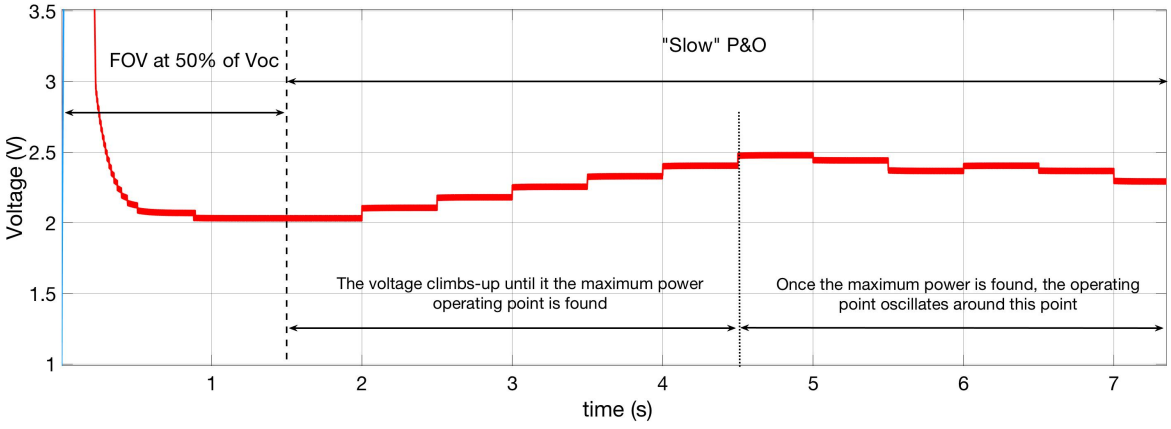

Figure 5–35 - TEG output voltage during start-up using the new algorithm

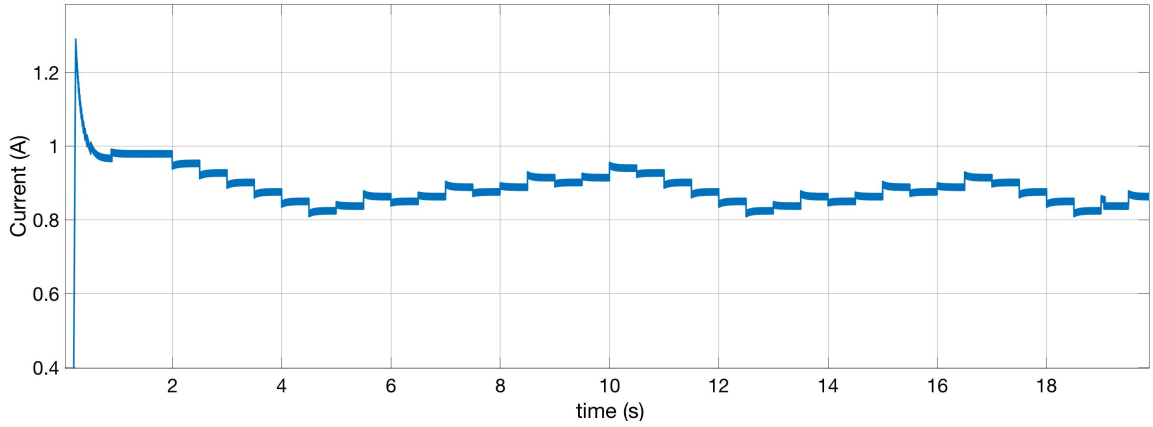

Figure 5–36 - Output current of the TEG operated under a constant heat flux equal to 100 W_{th}

The same simulation has been performed for values of input heat flux equal to 75 W_{th}, 150 W_{th}, 200 W_{th}, 250 W_{th} and 300 W_{th}. The steady-state power and voltage simulation results for 200 W_{th} and 300 W_{th} are shown in Figure 5–37 and Figure 5–38, respectively. Figure 5–38 b) shows a zoomed-in view of the output power when the TEG is driven using "fast" P&O and FOV. Both simulations, for 200 W_{th} and 300 W_{th} run for 20 seconds.

For the 200 W_{th}, the total energy delivered with the TEG, using the proposed algorithm, is equal to 135.41 *J*. With the "fast" P&O the energy delivered is 133.33 *J*, and with FOV 133.12 *J*. This means that the new algorithm produces 1.56 % more energy than the "fast" P&O, and 1.72 % more energy than FOV. Also, when the TEG reaches steady-state conditions, the output and open-circuit voltages are 4.68 *V* and 8.40 *V*, respectively. The beta factor during steady-state operation is equal to 0.5571.

For the 300 W_{th}, the total energy delivered with the TEG, using the proposed algorithm, is equal to 267.01 *J*. With the "fast" P&O the energy delivered is 263.22 *J*, and with FOV 263.24 *J*. This means that the new algorithm produces 1.44 % more energy than the "fast" P&O, and 1.43 % more energy than FOV. Also, when the TEG reaches steady-state conditions, the output and open-circuit voltages are 7.18 *V* and 12.63 *V*, respectively. The beta factor during steady-state operation is equal to 0.5684.

These results are summarized in Table 5-6 and Figure 5–44.

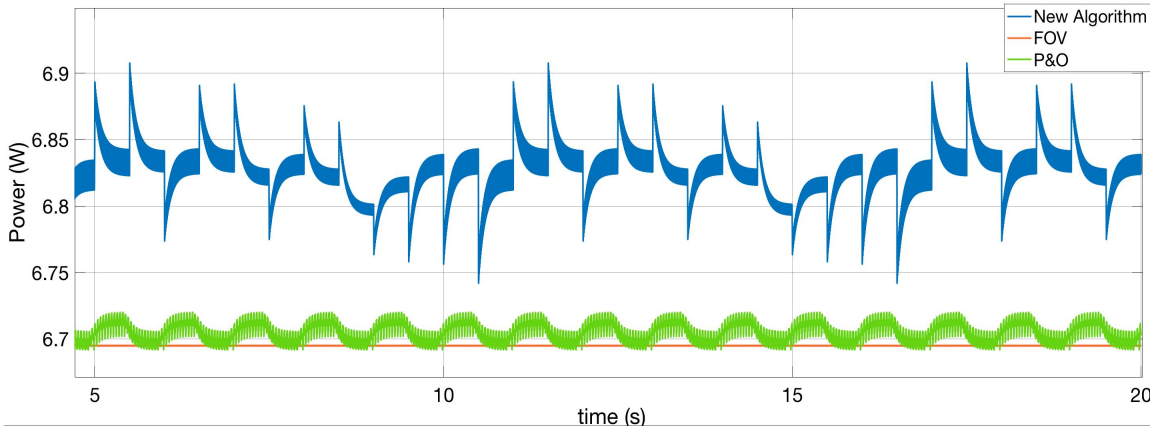

a)

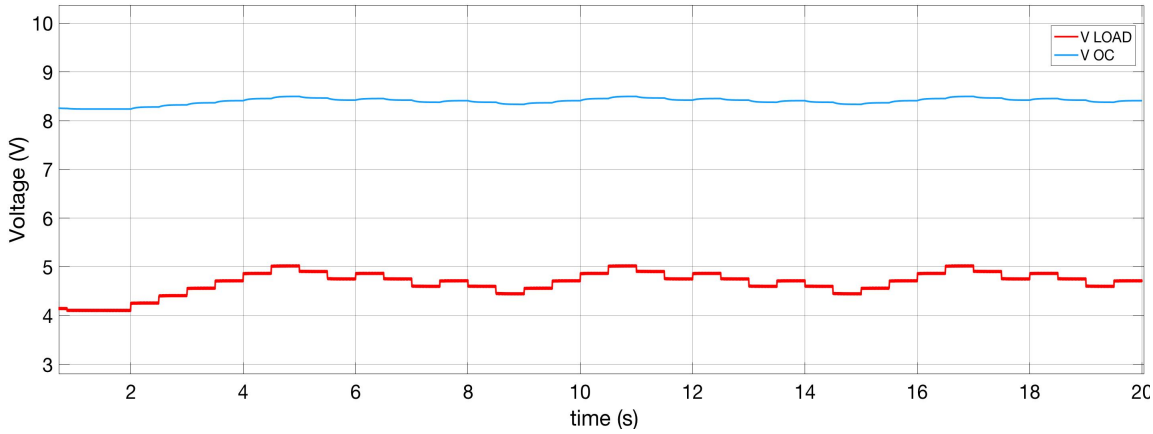

b)

Figure 5–37 - Simulation results during steady-state conditions, with an input heat flux equal to 200 W_{th}. a) TEG Power b) Zoomed-in view of the "fast" P&O and FOV

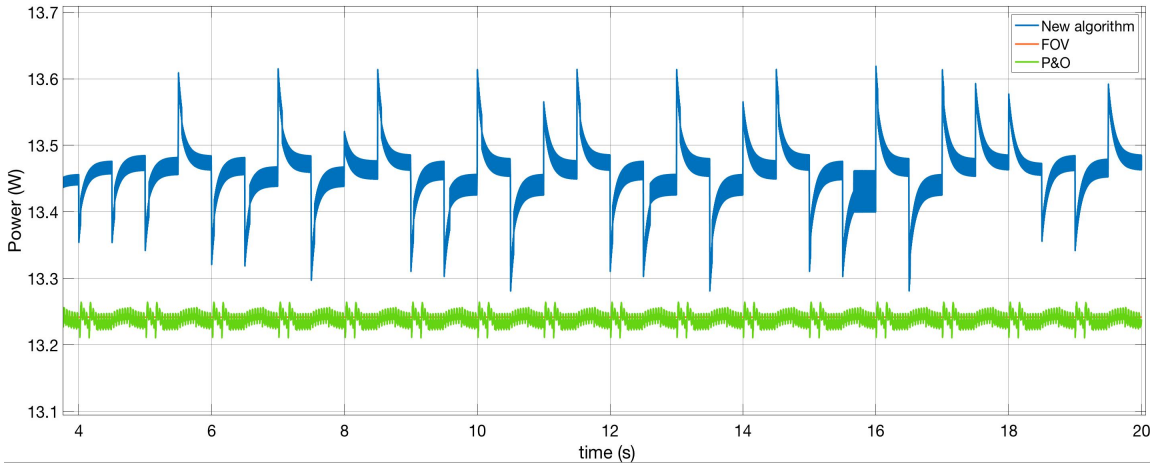

a)

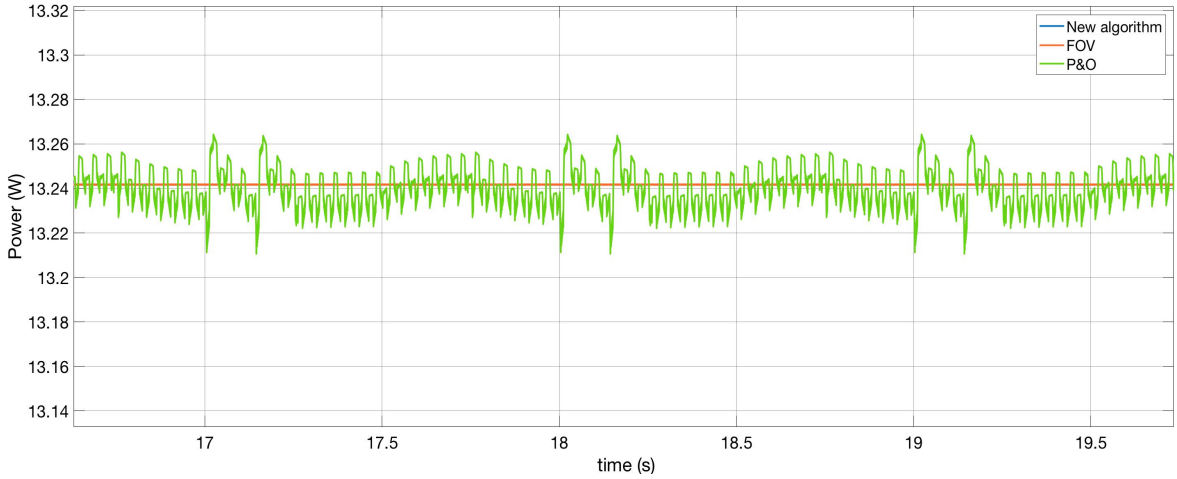

b)

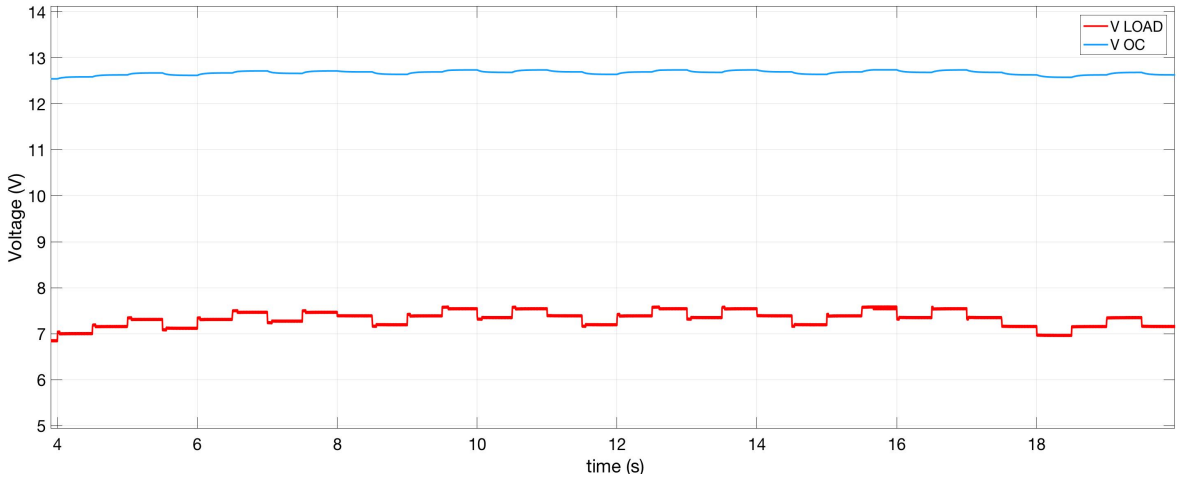

c)

Figure 5–38 - Simulation results during steady-state conditions, with an input heat flux equal to 300 W_{th}. a) TEG Power b) Zoomed-in view of the output power when using "fast" P&O and FOV c) TEG open-circuit and output voltage when the TEG is driven using the new algorithm

Another simulation has been run applying step changes in the input heat flux as described in Figure 5–27. The output power, for all three algorithms is shown in Figure 5–39.

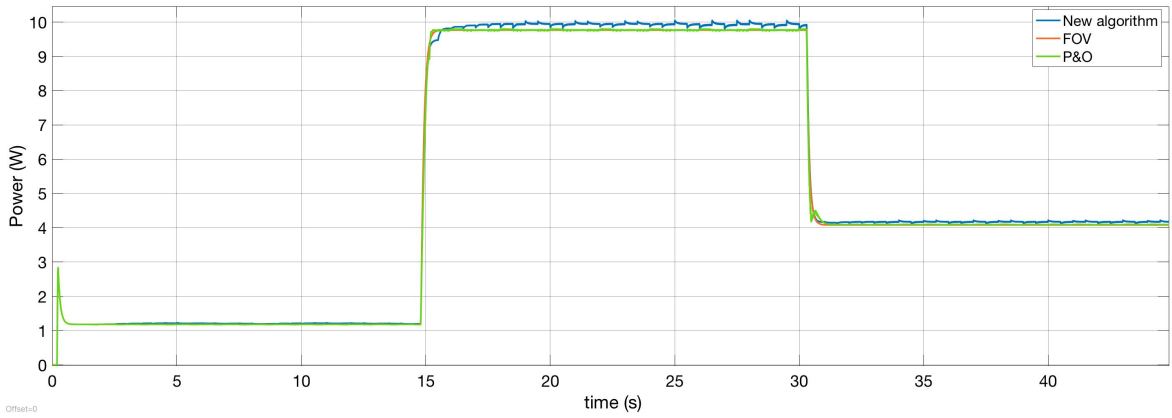

Figure 5–39 - TEG output power using the new algorithm, "fast" P&O and FOV, when applying step changes in the input heat flux, from 75 W_{th} to 250 W_{th} and from 250 Wth to 150 W_{th}.

The most interesting result from this simulation is the tracking speed of the new algorithm during the step changes. Figure 5–40 a) shows a zoomed-in view of the response of all three algorithms to the step in input heat flux from 75 W_{th} to 250 W_{th}. Figure 5–40 b) shows a zoomed-in view of the response of all three algorithms to the step in input heat flux from 250 W_{th} to 150 W_{th}. The "fast" P&O algorithm is not capable of tracking the thermal transient response of the TEG system. This is because, since the TEG power continues to increase due to the exponential increase in ΔT across the TEG plates, the algorithm continues to change the operating point in the same direction without considering the location of the actual operating point with respect to the actual MPP. This means that, once the operating point passes through the actual MPP, the "fast" P&O algorithm keeps moving the operating point of the TEG away from it thus decreasing the output power. For the case of the new algorithm and FOV, the tracking speed is the same, because the new algorithm implements FOV as soon as a change in the input heat flux is detected. This means that both algorithms keep the operating point near the MPP, exactly at 50 % of the instantaneous open-circuit voltage, without being deceived by the change in magnitude of the TEG power.

Keeping into consideration the entire simulation, and not only the transients, the total energy delivered with the TEG, using the proposed algorithm, is equal to 232.29 *J*. With the "fast" P&O the energy delivered is 228.40 *J*, and with FOV 228.35 *J*. This means that

the new algorithm produces 1.70 % more energy than the "fast" P&O, and 1.72 % more energy than FOV.

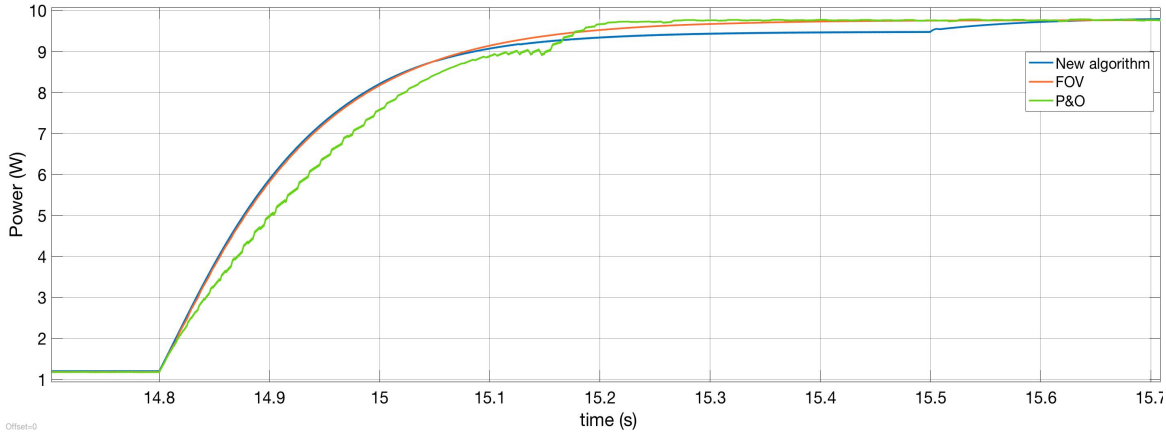

a)

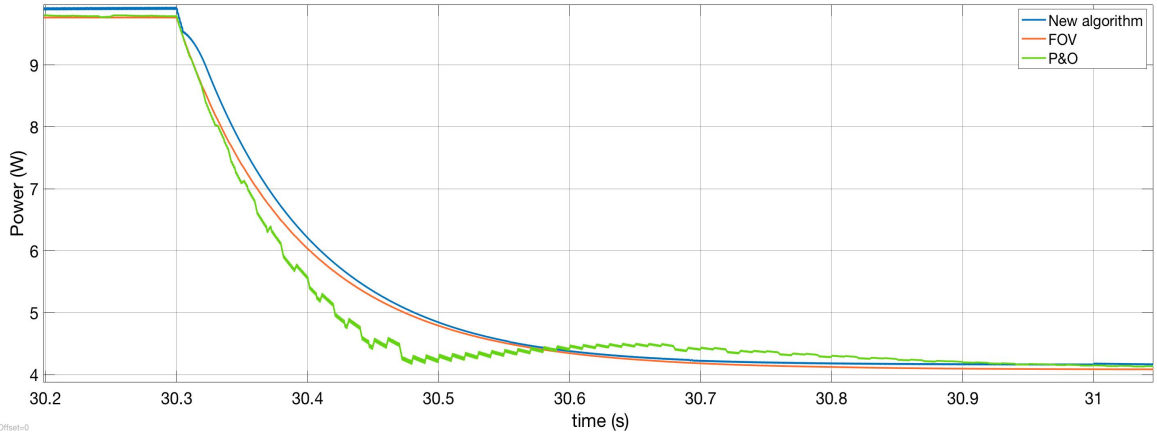

b)

Figure 5–40 – Zoomed-in view of the step transients a) from 75 W_{th} to 250 W_{th} and b) from 250 W_{th} to 150 W_{th}

The next simulations are run applying the input heat flux ramps shown in Figure 5–28 and defined in Table 5-5. The results applying the first ramp are shown in Figure 5–41. Figure 5–41 b) and c) shows a zoomed-in view on the rising and falling slopes, respectively. The energy delivered during the rising slope with the new algorithm is equal to 54.37 *J*, with "fast" P&O is equal to 54.59 *J* and 54.35 *J* with FOV. During the falling slope, the energy delivered with the new algorithm is equal to 56.95 *J*, with "fast" P&O is equal to 56.07 *J* and 55.94 *J* with FOV. During the rising slope, the "fast" P&O algorithm produces 0.4 % more power than the new algorithm; and the new algorithm produces only 0.03 % more than FOV. During the falling slope, the new algorithm produces 1.57 % more than "fast" P&O and 1.80 % more than FOV.

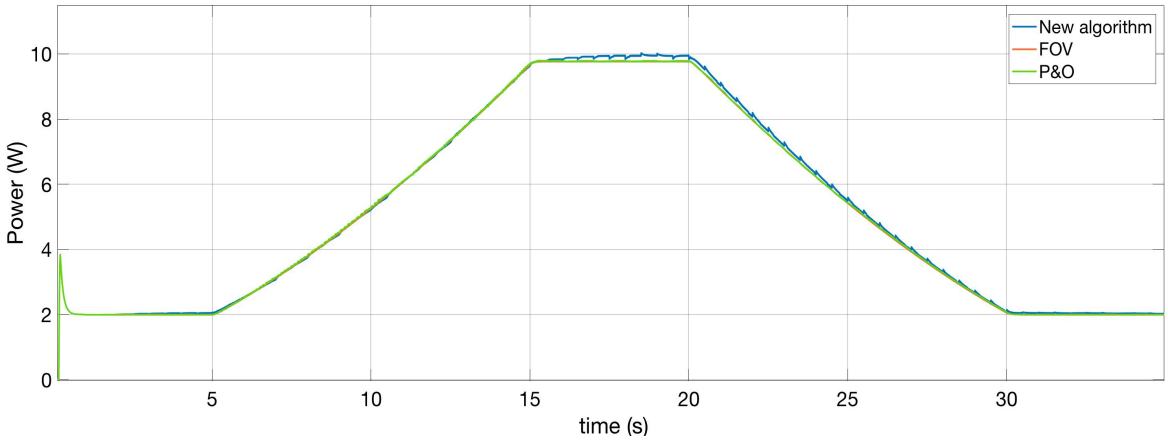

a)

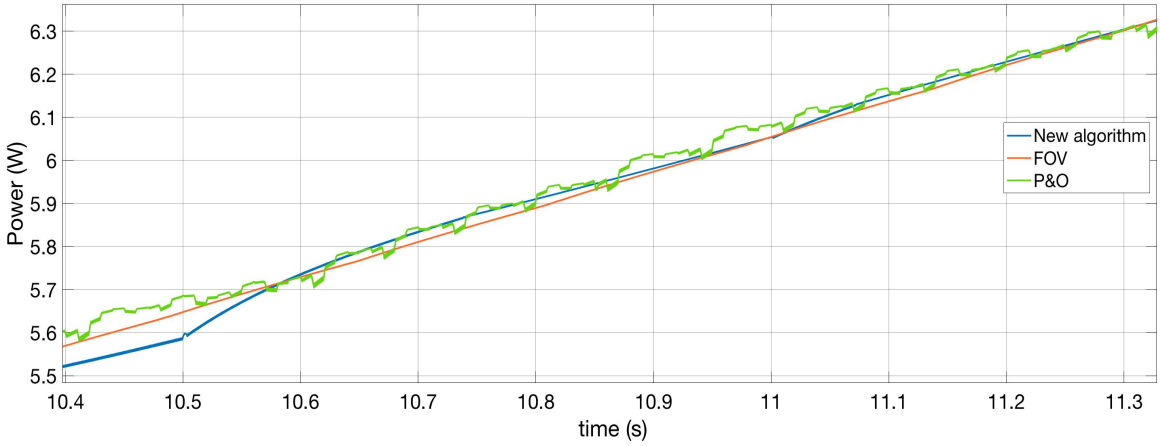

b)

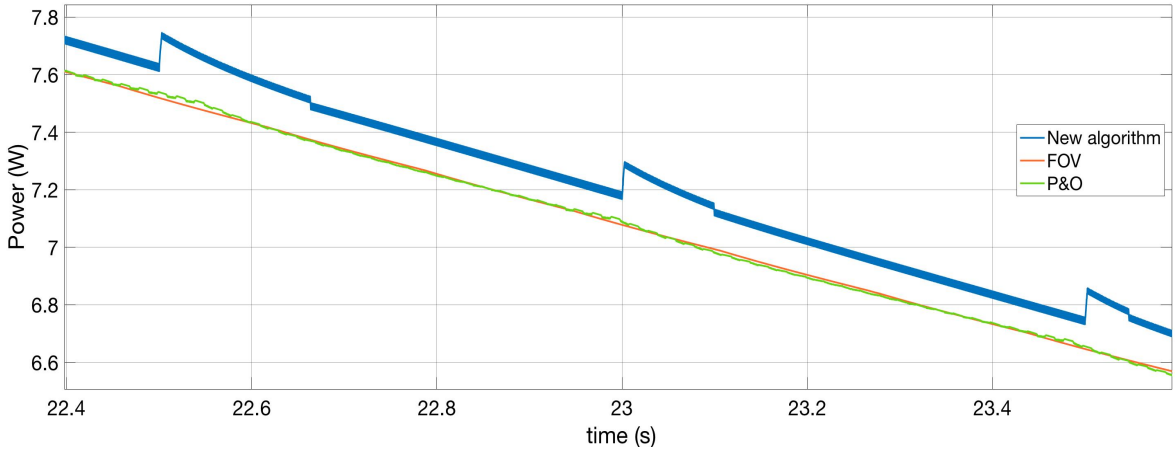

c)

Figure 5–41 - Output power applying the first input ramp (150 mW_{th}/s - Table 5-5)

The results applying the second ramp are shown in Figure 5–42. Figure 5–42 b) and c) shows a zoomed-in view on the rising and falling slopes, respectively. The energy delivered during the rising slope with the new algorithm is equal to 167.28 *J*, with "fast" P&O is equal to 165.02 *J* and 164.62 *J* with FOV. During the falling slope, the energy delivered with the new algorithm is equal to 169.45 J, with "fast" P&O is equal to 166.35 *J*

and 166.24 *J* with FOV. During the rising slope, the new algorithm produces 1.3 % more power than the "fast" P&O and 1.62 % more than FOV. During the falling slope, the new algorithm produces 1.86 % more than "fast" P&O and 1.93 % more than FOV.

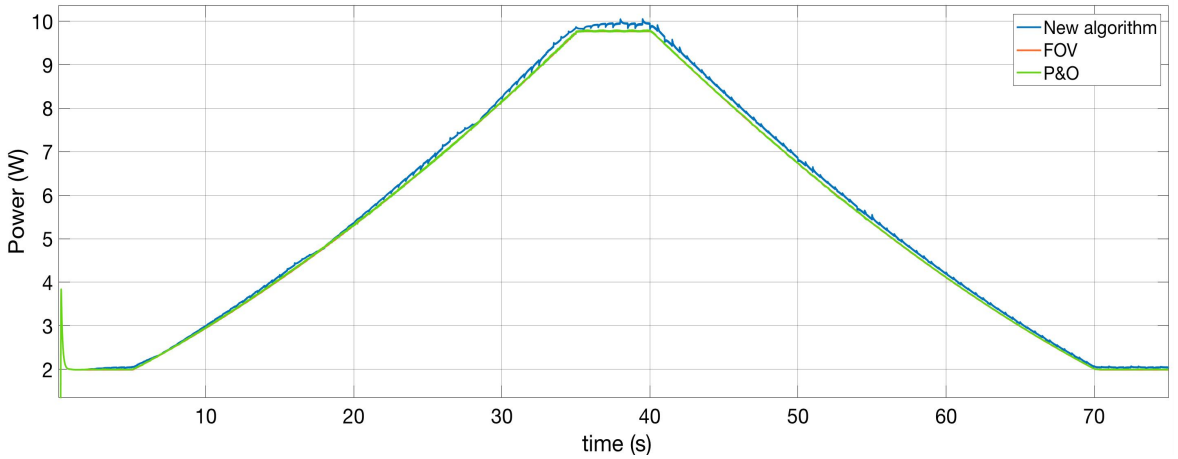

a)

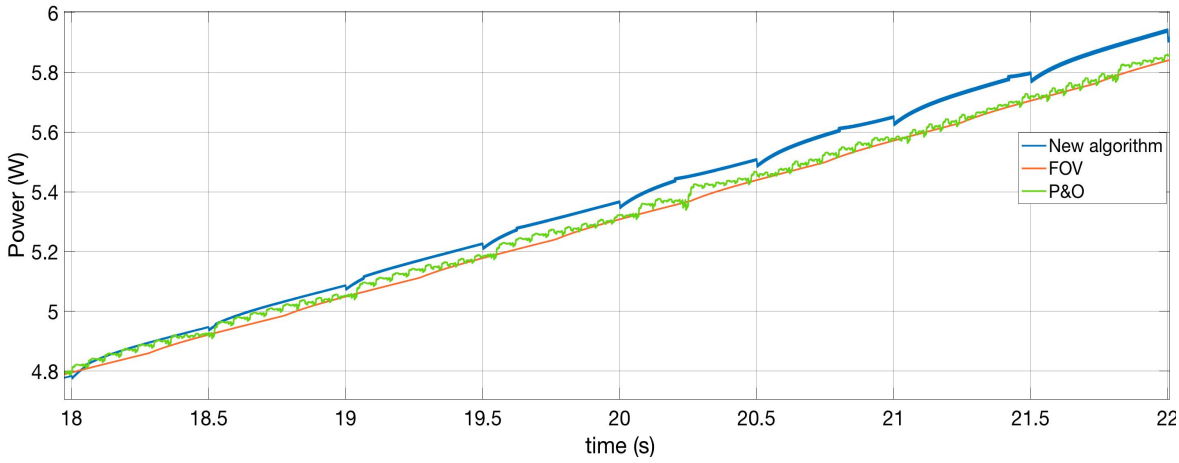

b)

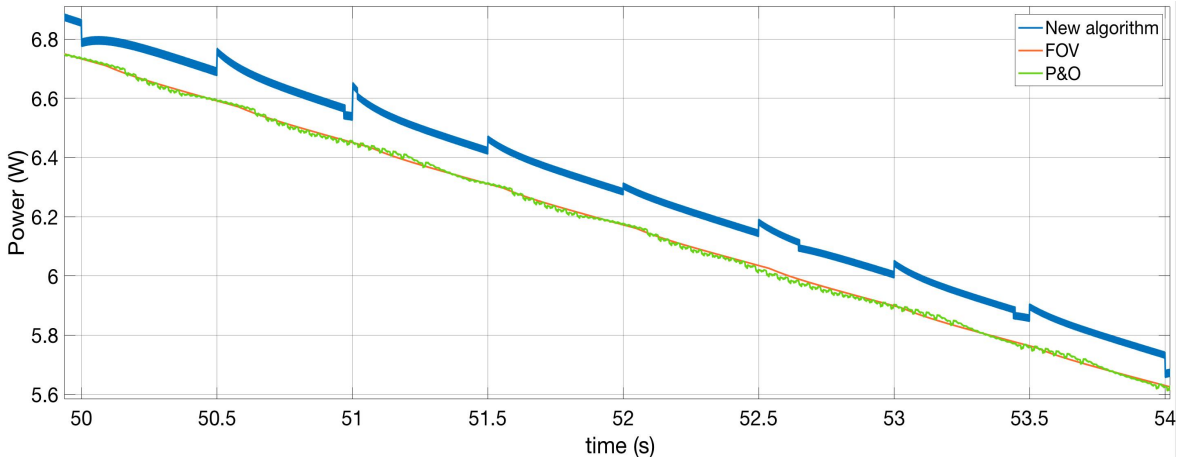

c)

Figure 5–42 - Output power applying the second input ramp (50 mW_{th}/s - Table 5-5)

The results applying the third ramp are shown in Figure 5–43. Figure 5–43 b) and c) shows a zoomed-in view on the rising and falling slopes, respectively. The energy delivered during the rising slope with the new algorithm is equal to 71.49 *J*, with "fast" P&O is equal to 72.26 *J* and 71.89 *J* with FOV. During the falling slope, the energy delivered with the new algorithm is equal to 75.32 *J*, with "fast" P&O is equal to 75.18 *J* and 74.82 *J* with FOV. During the rising slope, the "fast" P&O algorithm produces 1.08 *%* more power than the new algorithm; and FOV, 0.56 *%*. During the falling slope, the new algorithm produces 0.19 *%* more than "fast" P&O and 0.67 *%* more than FOV.

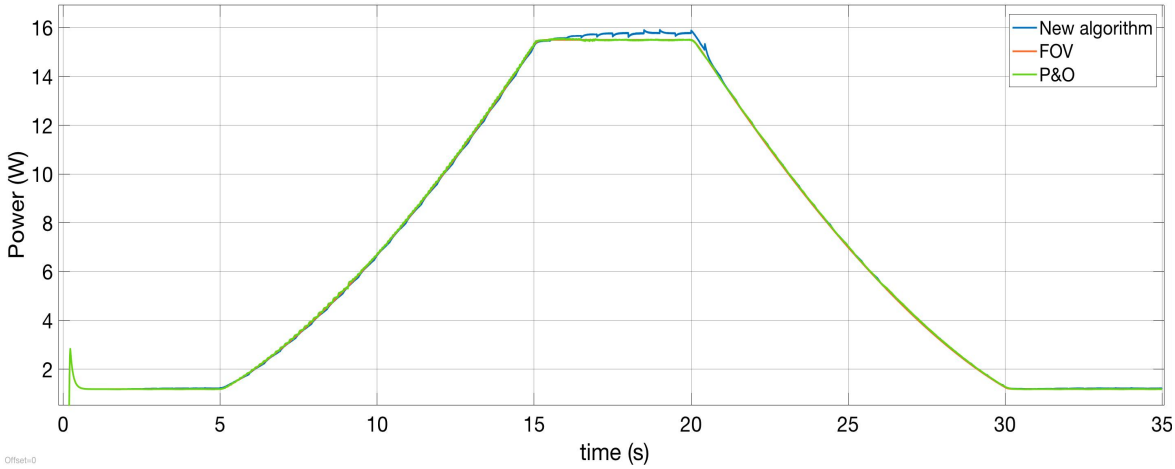

a)

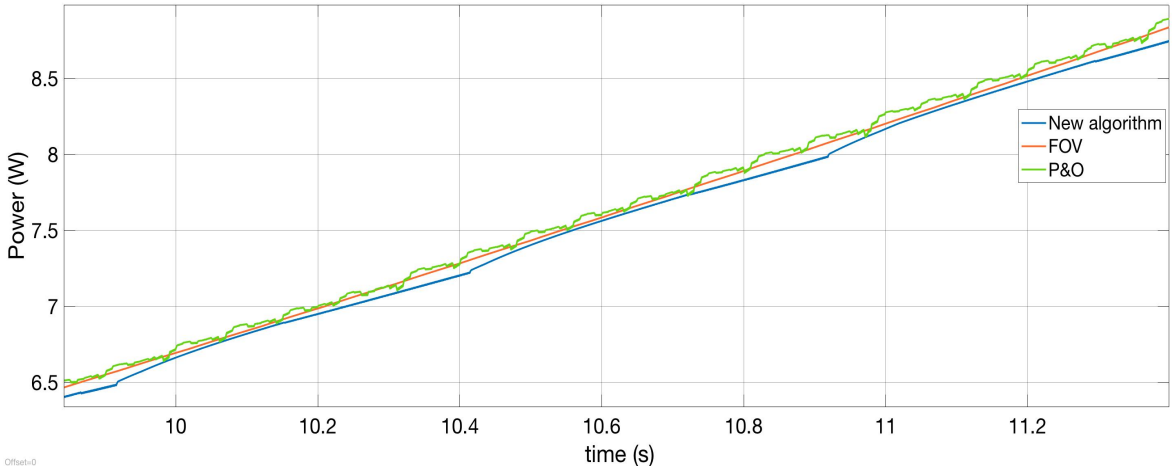

b)

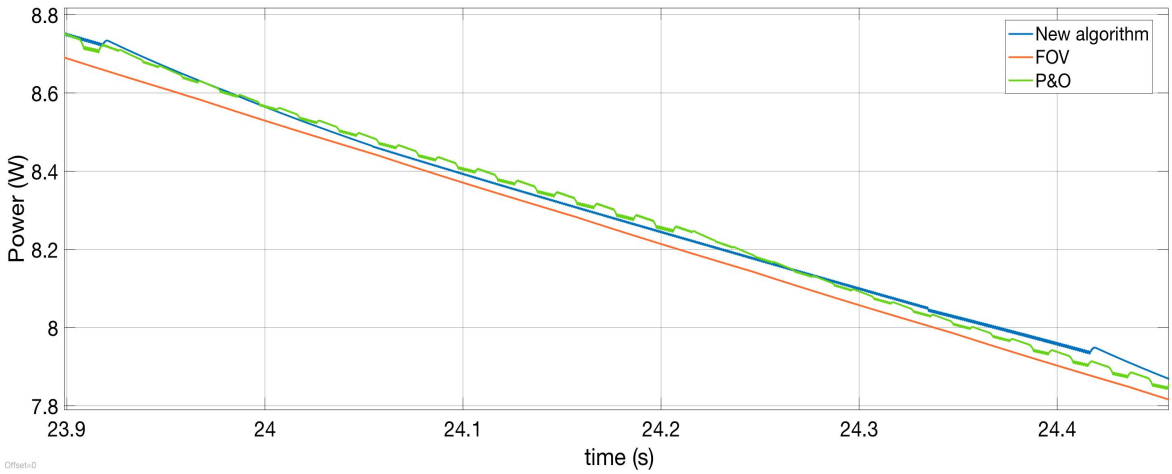

c)

Figure 5–43 - Output power applying the third input ramp (225 mW_{th}/s - Table 5-5)

5.6 Summary of the simulation results

Table 5-6 summarizes the results obtained with all three algorithms for constant values of input heat flux. The parameter that is used to compare the performance of each one of the

algorithms is the energy delivered by the TEG. It can be observed that both the "fast" P&O and FOV operate, under steady-state conditions, with a beta value equal to 0.5, approximately. With the new algorithm the beta factor is higher than 0.5, and it does not follow a particular trend. Figure 5–44 shows the values of beta plotted against the values of input heat flux. In this figure the beta values obtained from the experimental measurements presented in Section 4.2.5 are also plotted. The new MPPT algorithm operates the TEG very close to the actual MPP; or, in other words, at a beta factor that it is very close to the values obtained from the steady-state characterization of the TEG under constant heat flux. At low values of input heat flux, the difference between the operating point set by the MPPT algorithm and the true operating point obtained during the electrical characterization is higher than at high values of input heat flux.

	Q_h = 75 W_{th}			Q_h = 100 W_{th}		
	New	"Fast" P&O	FOV	New	"Fast" P&O	FOV
E_{OUT} (*J*)	**24.078**	23.599	23.598	**40.48**	39.76	39.64
$V_{LOAD,AVG}$ (*V*)	**1.73**	1.54	1.53	**2.31**	2.06	2.03
$V_{OC,AVG}$ (*V*)	**3.12**	3.07	3.06	**4.17**	4.10	4.09
Beta Factor	**0.554**	0.501	0.500	**0.554**	0.501	0.496
	Q_h = 150 W_{th}			Q_h = 200 W_{th}		
	New	"Fast" P&O	FOV	New	"Fast" P&O	FOV
E_{OUT} (*J*)	**82.74**	81.43	81.24	**135.41**	133.33	133.12
$V_{LOAD,AVG}$ (*V*)	**3.63**	3.12	3.08	**4.68**	4.14	4.11
$V_{OC,AVG}$ (*V*)	**6.33**	6.18	6.17	**8.40**	8.25	8.24
Beta Factor	**0.573**	0.504	0.499	**0.557**	0.502	0.498
	Q_h = 250 W_{th}			Q_h = 300 W_{th}		
	New	"Fast" P&O	FOV	New	"Fast" P&O	FOV
E_{OUT} (*J*)	**197.11**	194.35	194.14	**267.01**	263.22	263.24
$V_{LOAD,AVG}$ (*V*)	**5.99**	5.19	5.15	**7.18**	6.20	6.19
$V_{OC,AVG}$ (*V*)	**10.54**	10.32	10.31	**12.63**	12.37	12.36
Beta Factor	**0.568**	0.503	0.499	**0.568**	0.501	0.500

Table 5-6 - Summary of simulation results for different values of constant input heat flux

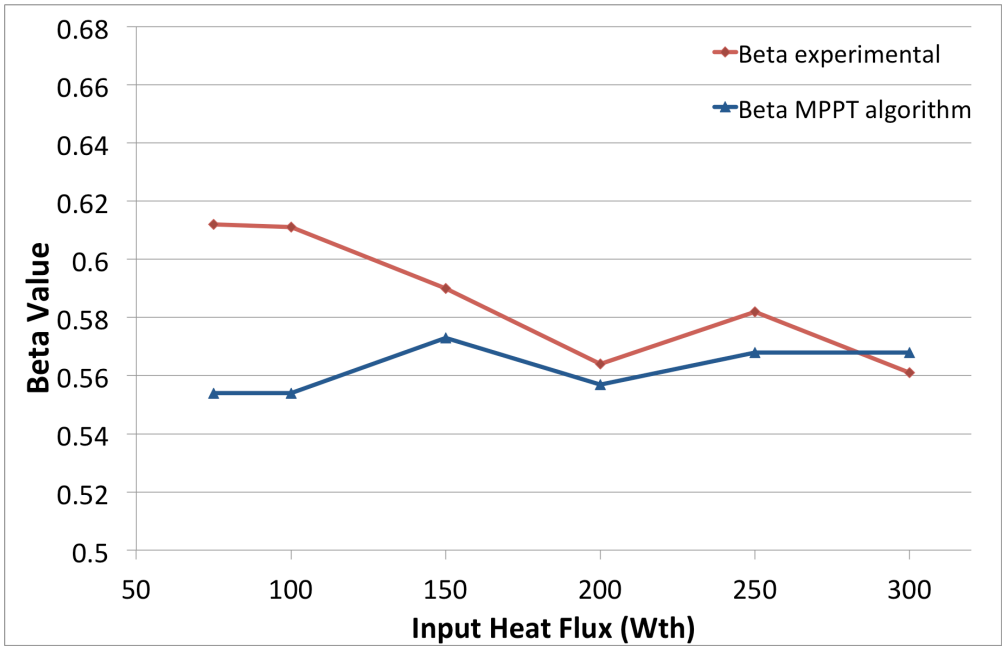

Figure 5–44 - Values of the Beta factor at the MPP, using the new proposed algorithm, for different values of input heat flux (TEG characterization and MPPT simulation)

Table 5-7 and Figure 5–45 show the performance of the new algorithm compared to "fast" P&O and FOV. The performance is shown in terms of the percentage of extra energy that the new algorithm generates compared to the other two (third and fourth column). The maximum energy, obtained using the new algorithm, is presented in the second column. The gain is calculated using the following formulae:

$$Gain\_P\&O\ (\%) = 100 \cdot \frac{\left|Energy_{NEW} - Energy_{fast\ P\&O}\right|}{Energy_{fast\ P\&O}} \tag{5-12}$$

$$Gain\_FOV\ (\%) = 100 \cdot \frac{\left|Energy_{NEW} - Energy_{FOV}\right|}{Energy_{FOV}} \tag{5-13}$$

Input Heat Flux	New algorithm	"Fast" P&O	FOV
75 W_{th}	24.08 J	2.03 %	2.03 %
100 W_{th}	40.48 J	1.82 %	2.13 %
150 W_{th}	82.74 J	1.61 %	1.85 %
200 W_{th}	135.41 J	1.50 %	1.72 %
250 W_{th}	197.11 J	1.42 %	1.66 %
300 W_{th}	267.01 J	1.44 %	1.43 %

Table 5-7 - Performance of the new algorithm compared to "fast" P&O and FOV (simulation results)

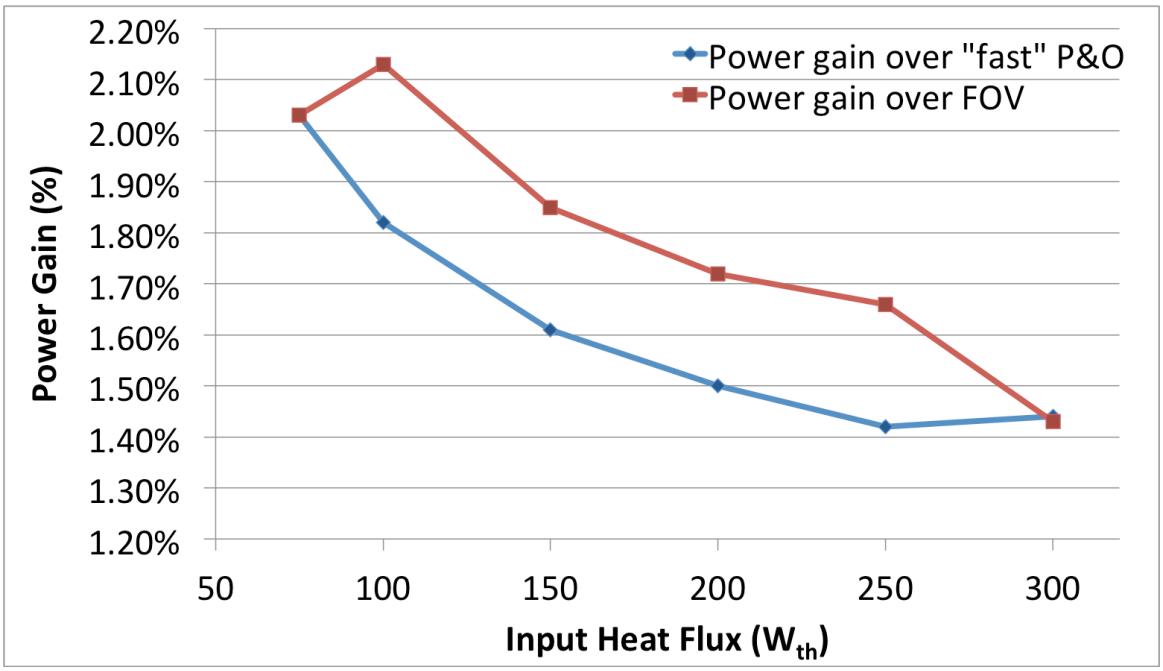

Figure 5–45 - Power gain of the new algorithm over "fast" P&O and FOV for different values of constant input heat flux (simulation results)

During step changes in the input heat flux, the new algorithm detects the transient by monitoring the instantaneous open-circuit voltage and reacts to it performing FOV. FOV sets the operating point of the TEG to 50 % of the open-circuit voltage thus driving the TEG into the vicinity of the MPPT. The error produced between the actual power point and the output voltage power obtained by applying FOV can be approximated by the error values that can be inferred from Figure 5–45, with the assumption that the new algorithm operates at the actual MPP. Another element of the error is due to the MPPT frequency. Once the new operating point is calculated, the temperature difference across the TEG will change, thus changing the actual MPP. The algorithm will not track the actual MPP until

the next MPP sampling action. The main difference between the new algorithm and FOV is that, while FOV is constantly setting the operating point of the TEG at 50 % of the open-circuit voltage at a relatively fast MPPT frequency, the new algorithm can take up to $2\tau_{TEG}$ to react to the step change, see Figure 5–25.

For "fast P&O", the problem is different. For the case of a power increase, if the MPPT frequency is lower than the speed it takes the TEG power to increase, due to the thermal time constant of the TEG system; the power increase due to the step change will most likely be higher than any potential increase due to the P&O perturbation. This effect will be subject to the type of perturbation step (adaptive, non-adaptive…). In that case, the perturbation step will be in the same direction as before the input heat flux step was applied to the input, until the input power stabilizes and stops increasing at a fast speed.

For the case of a power decrease step change the effect is smaller than with the increasing step, the reason being that with a decreasing power the perturbation step will change constantly and the algorithm does not keep perturbing the TEG in the same direction.

The performance of all three algorithms during step changes in the input heat flux can be seen in Figure 5–40.

For the case of ramp changes, the issue is somewhat similar to what happens during the step changes. For FOV, the operating point is set to 50 *%* of the instantaneous open-circuit voltage, and the error will be produced by the difference of the actual value of beta and the value of 0.5 imposed by FOV, and the time it takes to refresh the operating point.

For the case of FOV the situation has been already explained in [112]. If the change in TEG power caused by the temperature gradient (due to the change in input power) is larger than the change in power caused by the perturbation, the TEG will consider the change as produced by the perturbation and the algorithm will be deceived. This will happen at low MPPT frequencies compared to the rate of change of the input heat flux. For the case of the ramp simulations performed in Section 5.4, the MPPT frequency of all three algorithms is fixed, equal to 100 *Hz* and 2 *Hz* for "fast" P&O and the new algorithm, respectively. On the other hand, three different ramp rates have been applied as defined in Figure 5–28 and Table 5-5. The results show that the for the case of the fastest ramp, 225 *mW/s*, the "fast" P&O algorithm is capable of producing more energy, during the rising ramp, than the other three algorithms. For the slowest ramp, 50 *mW/s*, the low MPPT frequency of the new

algorithm has less effect on the MPP tracking capability hence producing more energy than the other two algorithms. For the 150 mW_{th}/s ramp, "fast" P&O generates more energy than the new algorithm, but just 0.4 % more. The energy generated by each algorithm during the ramps is shown in Table 5-8.

The percentage of extra energy generated by the new algorithm with respect to the "fast" P&O and FOV is shown in Table 5-9. In this table, positive values represent the extra energy produced by the new algorithm whereas a negative value represents the loss of energy of the new algorithm with respect to one of the other two. The results presented in Table 5-9 are visually presented in the graphs of Figure 5–46. These graphs represent the gain (positive percentages) and loss (negative percentages) plotted against the different ramp rates (mW_{th}/s). The trend shows that as the rate of change of input heat flux decreases, the new algorithm tends to increase the power generated. For an increasing ramp, "fast" P&O tracks better the MPP only with fast ramps. For a decreasing ramp, the new algorithm is capable of tracking better the MPP even at fast ramps.

	1st Ramp – 150 mW_{th}/s		
	New	"Fast" P&O	FOV
Rising ramp E_{OUT} (J)	54.37	**54.59**	54.35
Falling ramp E_{OUT} (J)	**56.95**	56.07	55.94
	2nd Ramp – 50 mW_{th}/s		
	New	"Fast" P&O	FOV
Rising ramp E_{OUT} (J)	**167.28**	165.02	164.62
Falling ramp E_{OUT} (J)	**169.45**	166.35	166.24
	3rd Ramp – 225 mW_{th}/s		
	New	"Fast" P&O	FOV
Rising ramp E_{OUT} (J)	71.49	**72.26**	71.89
Falling ramp E_{OUT} (J)	**75.32**	75.18	74.82

Table 5-8 - Energy generated by all three algorithms during increasing and decreasing ramp changes in input heat flux (simulation results)

	1st Ramp – 150 mW_{th}/s		
	New	"Fast" P&O	FOV
Rising ramp E_{OUT} (J)	54.37	-0.40 %	0.04 %
Falling ramp E_{OUT} (J)	56.95	1.56 %	1.82 %
	1st Ramp – 150 mW_{th}/s		
	New	"Fast" P&O	FOV
Rising ramp E_{OUT} (J)	167.28	1.37 %	1.62 %
Falling ramp E_{OUT} (J)	169.45	1.86 %	1.93 %
	1st Ramp – 150 mW_{th}/s		
	New	"Fast" P&O	FOV
Rising ramp E_{OUT} (J)	71.49	-1.07 %	-0.56 %
Falling ramp E_{OUT} (J)	75.32	0.19 %	0.66 %

Table 5-9 - Percentages of energy gain generated by the new algorithm with respect to "fast" P&O and FOV (simulation results)

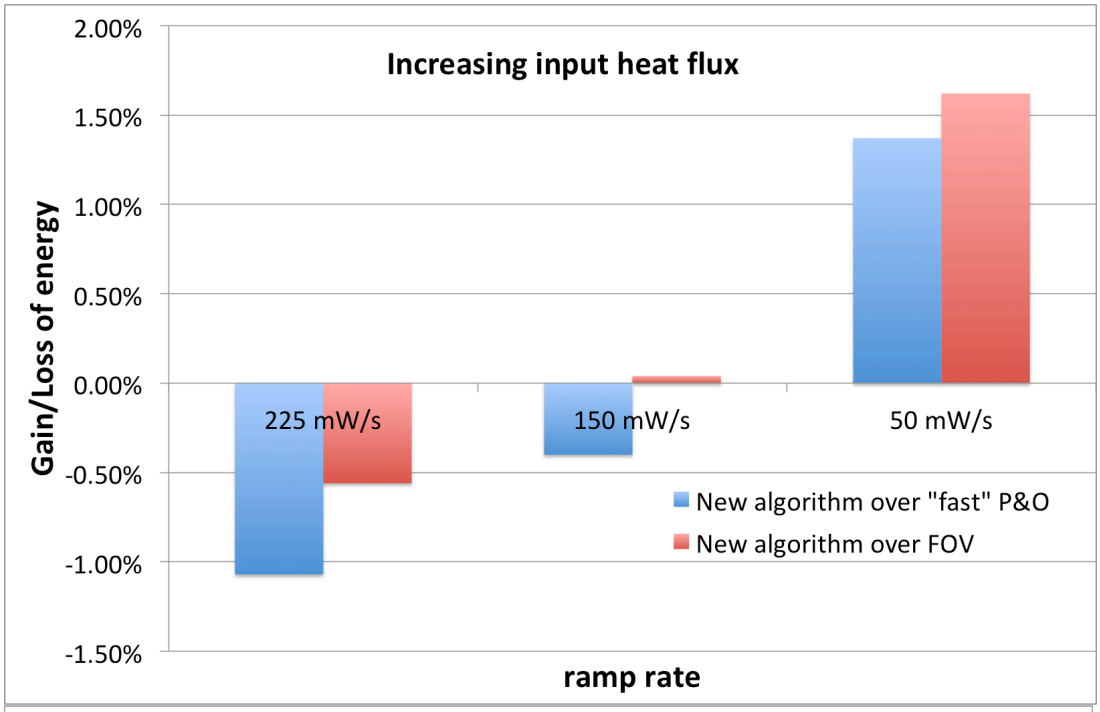

a)

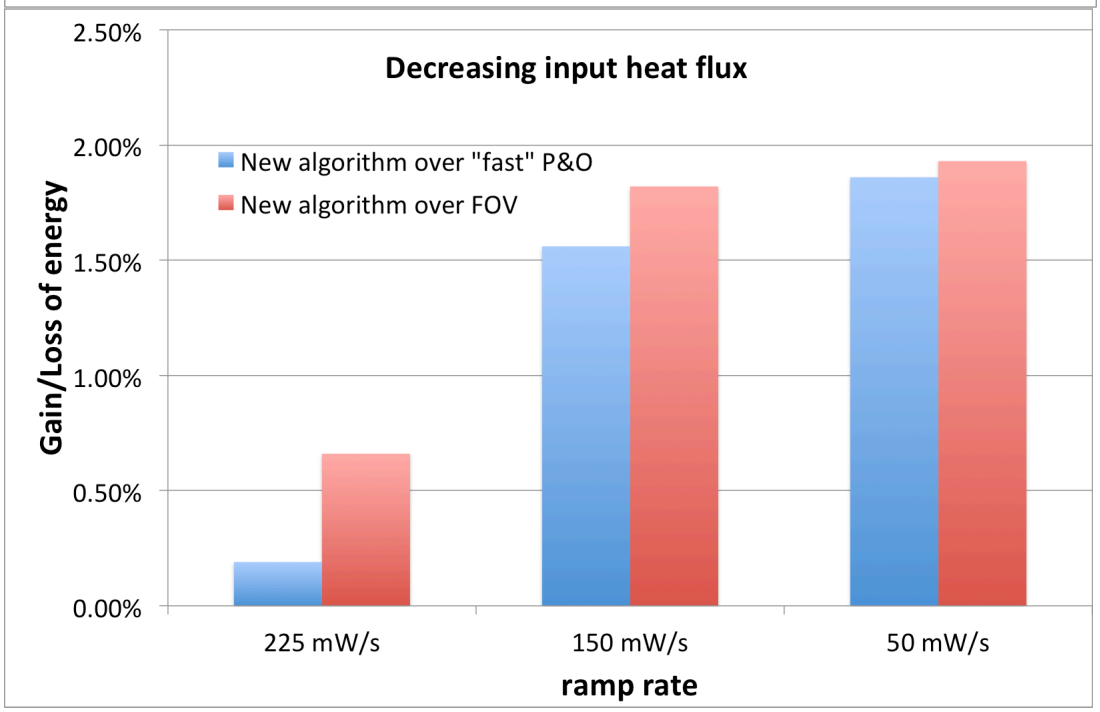

b)

Figure 5–46 - Gain/Loss of energy of the new algorithm with respect to "fast" P&O and FOV (simulation results) a) Rising ramp b) Falling ramp

5.7 Conclusions

A model of the TEG system has been presented in this chapter. The model will aid the development of a new MPPT algorithm that will be used for constant heat flux applications. Three elements are required to be modeled: the TEG device, the power converter and the MPPT algorithm. The model of the TEG device takes into consideration

the thermal capacitances of the system it is coupled to. The thermal time constant of the TEG system can be inferred from a load step on the TEG, as shown in Section 5.1. The model uses the average model of a boost converter, which contains all the average information while removing all the switching information that requires most of the computational resource.

A new algorithm has been developed to optimize power generation for TEGs operated under constant heat flux. The thermal time constant of the TEG system has an impact on the MPPT sampling frequency of the MPPT algorithm and the current state of the art algorithms do not take it into consideration. For this reason, they are not optimized for operation under constant heat flux conditions. The new algorithm is explained in this chapter, and its performance has been compared against two of the most common currently used algorithms in TEG applications: the fractional open-circuit method (FOV) and perturb and observe (P&O) with a relatively high MPPT sampling frequency (a sampling period that it is much shorter than the thermal time constant of the TEG system).

The three algorithms have been implemented in the TEG model where the time constants of the system have been decreased in order to optimize the computational time of the simulations. The time constants used in the model as well as the actual physical time constants of the TEG system and those that will be implemented in the actual algorithm have been shown in Table 5-4. The new algorithm shows a better performance during steady-state conditions with constant values of input heat flux. During step transients, the new algorithm performs in a very similar way as FOV, which, in turn, performs better than the "fast" P&O algorithm. During gradual, or ramp, increases of the input heat flux, the new algorithm performs better than the other two at low rates, with P&O being the best performing algorithm at fast rates. For the decreasing gradual changes of input heat flux, the new algorithm performs better than the other two even though the performance decreases as the rate of change of input heat flux increases. These results are in agreement with some of the results presented in [112]. The simulation results have been presented in Section 5.5 and a summary of the results can be found in Section 5.6

It can be seen that for constant values of input heat flux, the new algorithm operates the TEG very close to the actual optimum value of beta, see Figure 5–44, with the biggest divergence occurring at low values of input heat flux.

Chapter 6 Experimental hardware implementation of the MPPT algorithm

Chapter 5 presented the simulation model of the TEG and maximum power point tracking system. The model included the TEG, considering the thermal capacitance of the TEG system, the DC/DC power converter and the MPPT algorithm. The DC/DC power converter was a boost topology, and the TEG voltage was stepped up to the 28 V nominal battery voltage. A new MPPT algorithm has been presented, which is a combination of two state of the art algorithms: the fractional open-circuit voltage method, or FOV, and perturb and observe, or P&O. The new algorithm performs P&O when the input heat flux remains constant and it implements FOV whenever a variation in the heat flux is detected. The algorithm has been developed for applications where the TEG operates under constant heat flux conditions; and it takes into consideration the thermal transient response of the TEG system in order to be able to sample the TEG output power during steady-state conditions. By direct comparison of the new algorithm against FOV and P&O, it has been shown that it is required to measure steady-state values of the TEG output power in order to be able to operate at the true MPP.

Different simulations have been run for different heat flux conditions, and the results have also been presented in Chapter 5. The different conditions were: constant heat flux, slow and fast changing ramps and step changes. The experimental results have also been discussed and the superior performance of the newly proposed algorithm has been discussed.

In this section a hardware implementation of the simulation model of Chapter 5 is presented. A power converter is designed and built, and it is used to operate a TEG under constant heat flux conditions. All three algorithms (new, “fast” P&O and FOV) have been tested and the experimental results are presented and discussed.

6.1 System overview

The block diagram of the system is shown in Figure 6–1. The system involves the TEG system, the DC/DC power converter with the control electronics and the battery. The TEG system comprises the heat source with the TEG device coupled to it using heat exchangers. The DC/DC power converter and the control electronics have been designed in a single printed circuit board (PCB). A liquid crystal display (LCD) has been included in the PCB in order to monitor the main parameters of the converter: the input and output voltages and currents. The input voltage and input current represent the TEG load voltage and the output TEG current, respectively. The output voltage and output current represent the battery voltage and battery charge current, respectively.

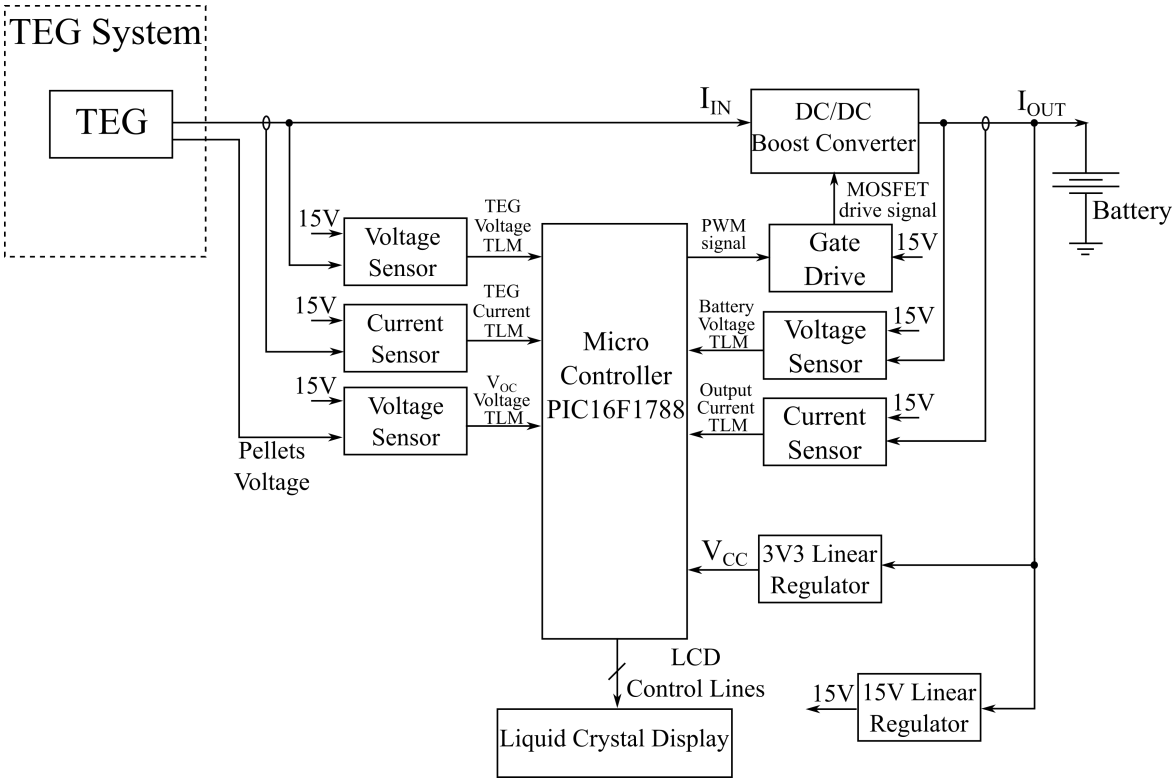

Figure 6–1 - Block diagram of the system

The control of the power converter implements three control loops. The first loop is the MPPT loop, which regulates the TEG voltage in order to operate at the MPP. This loop is referred to as the MPPT loop. The second loop monitors the TEG voltage and regulates it to the voltage set by the first loop. This is done to avoid drifts in TEG operating point due to external factors. The third loop monitors the battery voltage and implements taper charge when the battery reaches the EoC voltage. This loop is referred to as the EoC loop.

The two control loops control the power flow from the TEG to the battery by controlling the duty-cycle of the DC/DC power converter.

The DC/DC converter is a boost converter, which has two ports: an input port, connected to the TEG terminals, and an output port, connected to the system battery. Both the TEG and the system battery are external to the control PCB and the connections are made using screw-block terminal connectors. A third input is provided to attach the terminals that are directly connected to the three pairs of pellets of the monTE™, and used to obtain a measurement of the TEG open-circuit voltage.

Two linear regulators are fed from the battery voltage and produce two regulated output voltages. The voltages are 3.3 *V*, used to supply power to the PIC microcontroller and the LCD, and 15 *V*, used to supply the telemetry sensors.

The PCB is shown in Figure 6–2.

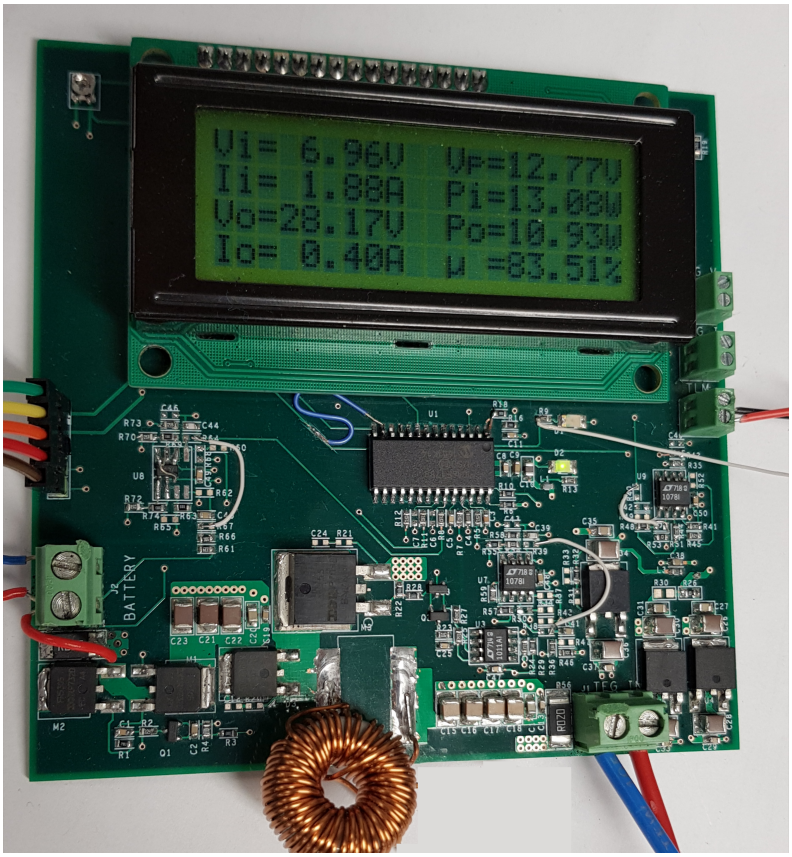

Figure 6–2 - Prototype of the DC/DC power converter used to implement MPPT control

6.2 Microcontroller embedded blocks and design calculations

The following sections present the embedded modules of the microcontroller as well as the design calculations of the different circuits implemented in the system shown in Figure 6–1 and Figure 6–2.

6.2.1 Microcontroller PIC16F1788

The PIC16F1788 is a microcontroller manufactured by Microchip[10]. It is a RISC (Reduced Instruction Set Computer) based architecture microcontroller, meaning that it allows implementing fewer cycles per instruction than CISC (Complex Instruction Set Computer) based microcontrollers. The PIC16F1788 has been selected because of it contains a PWM module, called PSMC module, that is capable of generating a duty-cycle with a precision of 15.6 *ns* with a switching frequency of 100 *kHz*. The microcontroller processes the values of TEG voltage and current to operate the MPPT, and TEG voltage, control loops and the value of battery voltage for the EoC loop. The microcontroller has 16 kilo-Word (*KW*) flash program memory, 256 bytes of data EEPROM and 2048 bytes of RAM.

The embedded resources of the microcontroller used in the MPPT application presented in this section are:

- 32 *MHz* internal clock oscillator.
- 12-bit analogue to digital converter, ADC.
- Internal timer with timer interrupt.
- 8-bit digital to analogue converter, DAC.
- Internal comparator module.
- Programmable Switch Mode Control (PSMC), for PWM operation.

The PIC16F1788 has an internal clock that runs at 32 *MHz* when the internal 4x PLL is enabled.

The 12-bit ADC is used to convert the analogue value at the output of the voltage and current sensors to a digital value that the microcontroller can handle. The voltage reference

[10] www.microchip.com

of the ADC is the supply voltage of the microcontroller and the result is represented in 2's complement format.

The internal timer is used to time precisely four different loops or events: the voltage regulation loop, the detection of changes in the input heat flux, the print telemetry loop and the MPPT sampling loop. The internal timer generates an interrupt every millisecond. During that interrupt four timing variables are incremented. These timing variables are: *timer_regulation*, *timer_pellets_A*, *timer_TLM* and *timer_MPPT*. By doing so, each one of the timing variables increments its value every millisecond.

The first loop is the regulation loop, which monitors the TEG voltage and regulates it to the target voltage, decided by the MPPT loop. This loop is repeated every 5 *ms*.

The second loop is the loop that detects the changes in the input heat flux. This loop is divided in two loops. The first part measures the open-circuit voltage 200 *s* after the operating point is changed; that is, after the decision made by the MPPT loop. The measured value is stored in the variable *Vpellets_A*. The second part of the input heat flux detection loop measures the open-circuit voltage of the TEG is timed every 500 *ms* after the measurement of *Vpellets_A* is taken. The measured value is stored in the variable *Vpellets_B*. During the second part of the loop the values of *Vpellets_A* and *Vpellets_B* are constantly compared in order to detect changes in the input heat flux.

The print telemetry loop is repeated every second, and the telemetries are printed in the LCD screen. Finally, the MPPT loop is repeated every 500 *s* and the TEG power is sampled in order to perform the "slow" P&O. The print telemetry loop is not shown in the flow chart of Figure 5–25 as it is not part of the MPPT actions.

The internal comparator, along with the 8-bit DAC, is used as a battery overcharge protection. The battery should not be charged beyond the absolute maximum voltage of 34 *V*. The MPPT algorithm implements an EoC control loop that decreases the duty-cycle when the battery voltage reaches 33.6 *V*. By doing so, taper charge is applied as the battery reaches the EoC voltage and never increases beyond 33.6 *V*. In the event of a failure on the EoC control loop, the internal comparator will switch the PWM module off. This is done using the modulation of the PWM signal with the output of the internal comparator. The non-inverting input of the comparator is connected to the output of the DAC, which will

provide the voltage reference the battery voltage will be compared against. The inverting input will be connected to the output of the battery voltage telemetry circuit.

The PSMC block generates a PWM signal using a 64 *MHz* internal clock. With a switching frequency of 100 *kHz* the duty-cycle can be changed in 639 steps between 0 and 100 *%*. This means that the duty-cycle can increase, or decrease, in steps of 0.156 *%*. For a nominal battery voltage of 28 *V* this implies a change of input voltage of 43.7 *mV* for every step of duty-cycle.

6.2.2 Auxiliary supply voltages

The voltage sources available in the system are the TEG and the battery. The output of the TEG is regulated by the MPPT algorithm and will change with input heat flux. The battery voltage is unregulated, from 24 to 33.6 *V*, and depends on the state-of-charge, which will change with output load and charge current.

Neither of these sources can be used to power the microcontroller and the control circuitry, which require regulated supply voltages. The microcontroller requires 3.3 *V* and the rest of the circuitry can be powered from 15 *V*. It is required for the OpAmps to be powered from a voltage that is higher than 3.3 *V* to avoid limitations on the input voltage, like the maximum common-mode input voltage.

These two auxiliary supply voltages, 3.3 *V* and 15 *V*, will be generated from the battery voltage using linear regulators. The 3.3 *V* auxiliary power supply is generated using the TLF80511TFV33 linear regulator, Figure 6–3, and the 15 *V* auxiliary power supply is generated using the LT7815 linear regulator, Figure 6–4.

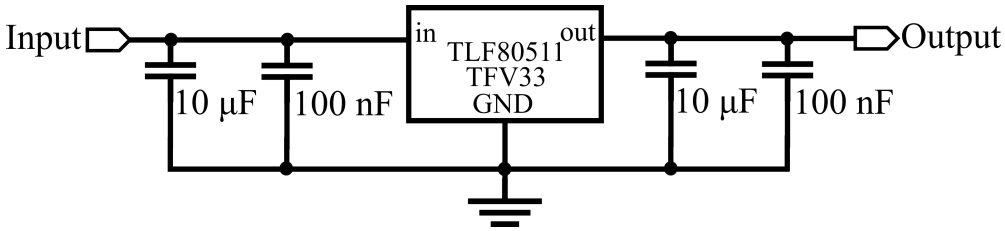

Figure 6–3– 3.3 *V* linear regulator

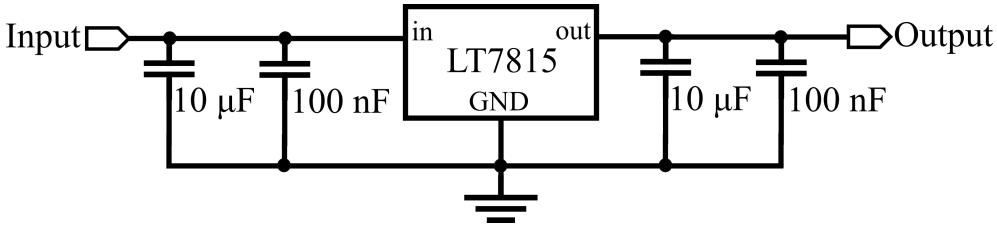

Figure 6–4 – 15 *V* linear regulator

6.2.3 Boost converter component values

The design of the boost converter, Figure 6–5, involves the selection the component values (L and C_{IN}) and the switch ratings based on the maximum and minimum voltage and current values of the input source. In order to find these values is it important to establish the maximum desired current ripple, the switching frequency and the behaviour of the converter to step changes in either the TEG open circuit voltage or battery voltage.

The output voltage of the converter cannot change instantaneously due to the capacitive nature of the battery connected to it; and the TEG open-circuit voltage cannot change instantaneously due to the thermal capacitance of the TEG system. Even though neither the battery voltage nor the TEG open-circuit voltage of the TEG can change instantaneously, the response of the converter to step changes in both the input and output determines the oscillatory behaviour of the voltage at the TEG output terminals.

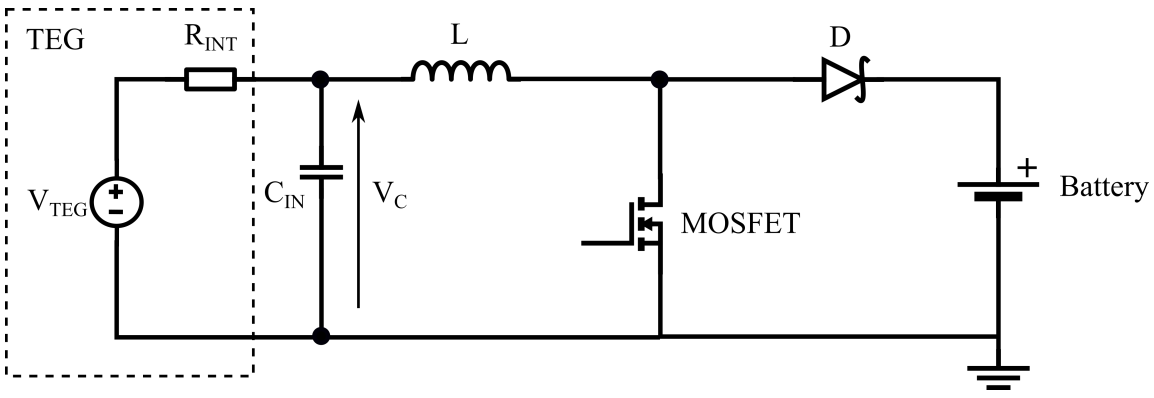

Figure 6–5 - Schematic diagram of the boost converter

The intended operation of the boost converter is in CCM, so it is important to minimize the maximum current ripple through the inductor in order for the current to never reach zero amperes when operating at low loads. The converter is designed to operate a TEG with a minimum input heat flux of 75 W_{th}. Under this value of input heat flux, the TEG current,

around the MPP, is equal to 600 *mA* and the TEG voltage is equal to 1.93 *V*, approximately (see Table 4-8 in Section 4.2.5). The inductor current ripple can be calculated using Equation (**5-5**), where the maximum current ripple, at 75 W_{th}, will occur at the highest t_{ON}. From Equation (**5-8**), and knowing that $t_{ON}=D \cdot T$, the maximum t_{ON} will occur at the maximum value of *D*, that is, at the maximum output voltage. The maximum battery voltage is 33.6 *V*, and it is dictated by the battery cell technology. Using Equation (**5-5**) for a maximum current ripple of 100 *mA*, the minimum inductor value will be:

$$L = \frac{1}{\Delta I}\int_0^{t_{ON}} V_C\, dt = \frac{V_C \cdot t_{ON}}{\Delta I} = \frac{V_C \cdot T\left(1 - \frac{V_C}{V_{OUT}}\right)}{\Delta I} = \\ = \frac{1.93 \cdot 10 \cdot 10^{-6} \cdot \left(1 - \frac{1.93}{33.6}\right)}{0.1} = 181.91\ \mu H \tag{6-1}$$

An inductance higher than 181.91 μH will provide a current ripple lower than 100 *mA*. The inductor has been designed with an inductance equal to 270 μH, and the current ripple will be, under the conditions presented in Equation (**6-1**), equal to 67.4 *mA*. The inductor will be built using a high flux, distributed gap, toroid core; the C058380A2, from Magnetics[11]. The A_L value of the core is equal to 89 nH/T^2 ±8 %, so 55 turns will provide the desired inductance of 270 μH.

From the manufacturer's datasheet of the monTE™, the maximum output current of the TEG is 5 *A* for a ΔT of 300 ^oC, so the boost MOSFET and diode must be able to withstand the peak current of the TEG plus half the value of the current ripple. The selected MOSFET is the IRF3415S from Infineon Technologies[12] and the output diode is the V1S-50WQ06FN from Vishay[13]. The absolute maximum ratings of the MOSFET and the diode are shown in Table 6-1.

Component	Manufacturer Part Number	Maximum Current
MOSFET	IRF3415S	30 *A* @ Tc=100 ^oC
Diode	V1S-50WQ06FN	5.5 *A*

Table 6-1 - Maximum current ratings of the MOSFET and diode

[11] www.mag-inc.com

[12] www.infineon.com

[13] www.vishay.com

The converter dynamics have an impact on the maximum sampling speed of the MPPT algorithm [99]. Sampling voltage/current overshoots/undershoots caused by high *Q*-factors could deceive the algorithm. Also, high ringing also means longer settling time before steady-state values can be measured.

The value of the input capacitance is calculated to avoid excessive ringing when the duty-cycle is changed. The amount of ringing and overshoot the boost converter will exhibit at its input, with step changes in duty-cycle, is related to the quality factor (*Q*-factor) of the input voltage to duty-cycle transfer function [120].

In order to find out the input voltage to duty-cycle transfer function, the small-signal model of the boost converter has to be developed, for the case of the input voltage being the controlled variable.

Based on Figure 5–18, the small-signal linearized equations that define the input-controlled boost converter are shown in the set of Equations (**6-2**). These equations are obtained averaging, perturbing and linearizing the equations for the inductor voltage, input capacitor current and input current [120]. Rearranging these equations the small-signal model of the input controlled boost converter can be obtained. The model is shown in Figure 6–6 and can be used to find the transfer function $G_{vd}(s) = \hat{v}_C(s)/\hat{d}(s)$. Solving for the $\hat{d}(t)V_O$ independent source, the circuit of Figure 6–7 is obtained. With the circuit of Figure 6–7 the transfer function $G_{vd}(s)$ is obtained, and it is shown in Equation (**6-3**).

$$L\frac{d\hat{\imath}_L(t)}{dt} = \hat{v}_C(t) - D'\hat{v}_O(t) + \hat{d}(t)V_O$$

$$C\frac{d\hat{v}_c(t)}{dt} = \hat{\imath}_{R_{INT}}(t) - \hat{\imath}_L(t) \qquad (6\text{-}2)$$

$$\hat{\imath}_{R_{INT}}(t) = \frac{\hat{v}_{TEG}(t) - \hat{v}_C(t)}{R_{INT}}$$

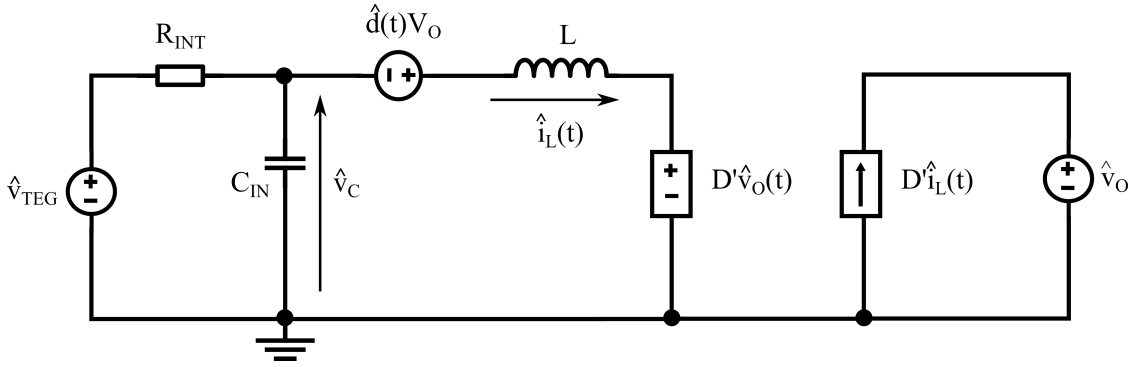

Figure 6–6 – Small-signal model of the input controlled boost converter

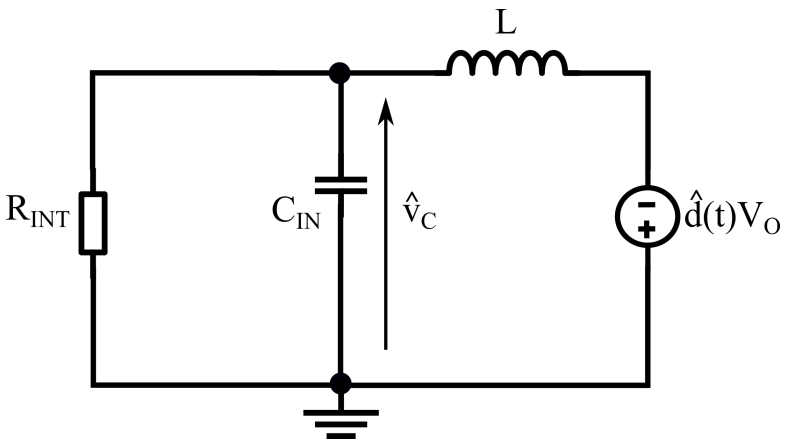

Figure 6–7 – Small-signal circuit used to calculate the $G_{vd}(s)$ transfer function

$$G_{vd}(s) = \frac{\hat{v}_C(s)}{\hat{d}(s)} = -V_O \frac{1}{LCs^2 + \frac{L}{R}s + 1} \tag{6-3}$$

By simple inspection of Equation (**6-3**) the natural frequency ω_n of the system as well as the quality factor Q can be obtained: $\omega_n = 1/\sqrt{LC}$ and $= R\sqrt{C/L}$.

Low values of Q provide lower ringing. The value C_{IN} is calculated to provide a Q-factor lower than 0.5. Using a value of L = 270 μH and R_{INT} = 2.75 Ω, the value of C_{IN} must be lower than 8.92 μF. The value of C_{IN} selected for the boost converter is 4.7 μF. With these values the Q-factor is equal to 0.36.

Figure 6–8 shows the Bode plot of the open-loop $G_{vd}(s)$ transfer function. The values of the boost converter parameters are those shown in Table 5-3, the calculations of which are shown in this section. The transfer function shows a low Q-factor, which implies a low ringing when the duty-cycle is changed. Figure 6–9 shows the simulated input voltage

response of the boost converter, in the time domain, when the duty-cycle is stepped between 50 and 75 %. The value of TEG open-circuit voltage is 20 *V*, and the input voltage waveforms shows a very well damped response. The input voltage changes between 14 and 7 *V*. Figure 6–10 shows the input voltage response of the TEG, in the time domain, of the real hardware for the same duty-cycle changes. It can be seen that the real hardware response is very similar to the simulated one, with the only difference that the simulated model considers an ideal output diode with zero volts drop when the MOSFET turns off, whereas the real hardware uses a real diode with a voltage drop V_D.

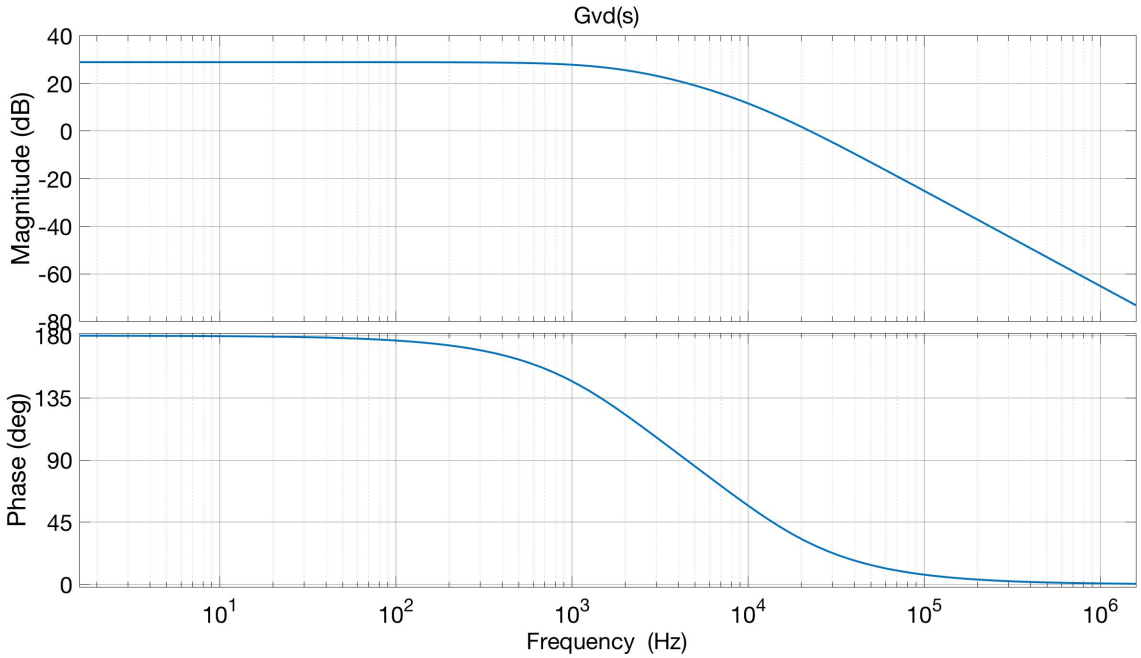

Figure 6–8 - Bode plot of the transfer function $G_{vd}(s)$

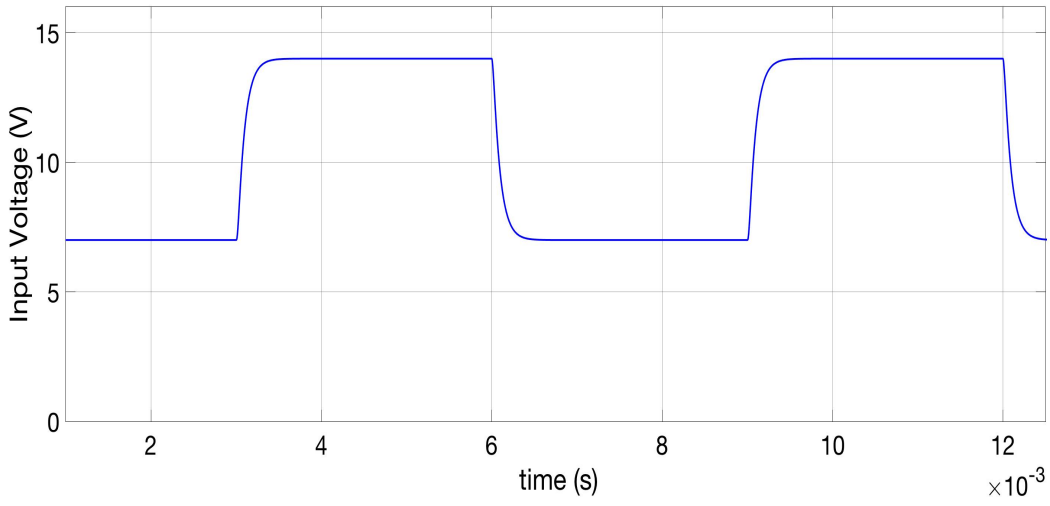

Figure 6–9 - Simulink simulation response of the boost converter for duty-cycle steps between 50 % and 75 %

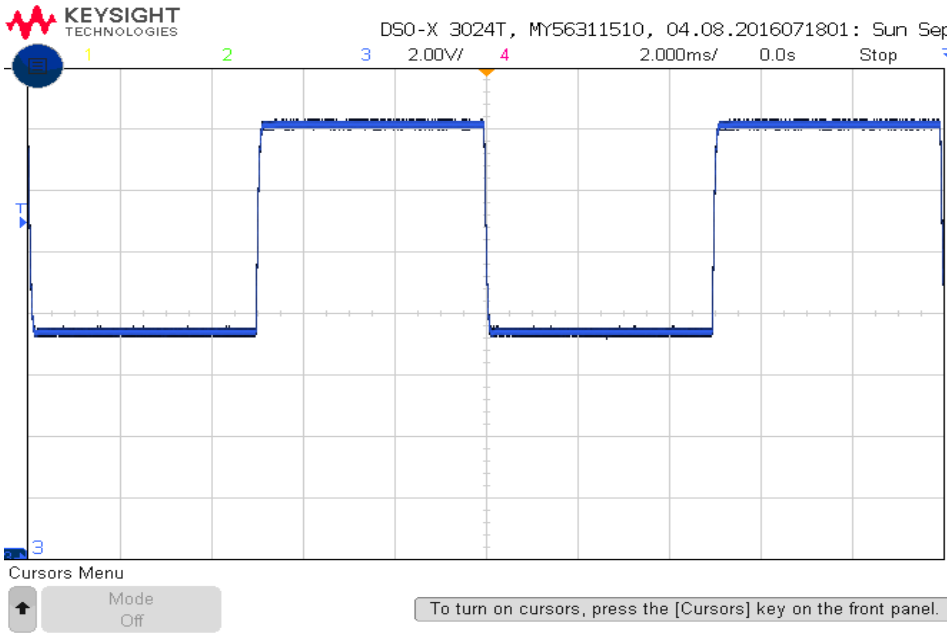

Figure 6–10 - Boost converter response for duty-cycle steps between 50 % and 75 %

6.2.4 MOSFET gate-drive circuit

One of the main advantages of the boost converter is that the source of the power MOSFET is connected to ground; hence the gate drive does not need to implement an isolated output. The only issue is that, with a supply voltage of 3.3 *V*, the microcontroller can only output voltages up to 3.3 *V*; which is not enough to drive the gate-source of the power MOSFET with a voltage that is higher than the gate-source threshold voltage.

The circuit shown in Figure 6–11 uses an open-collector comparator, the LT1011A, and converts the PWM signal from the microcontroller, with levels between 0 to 3.3 *V*, to a PWM signal with levels between 0 to 14 *V*, approximately. The use of an open-collector comparator allows the conversion between the two voltage ranges.

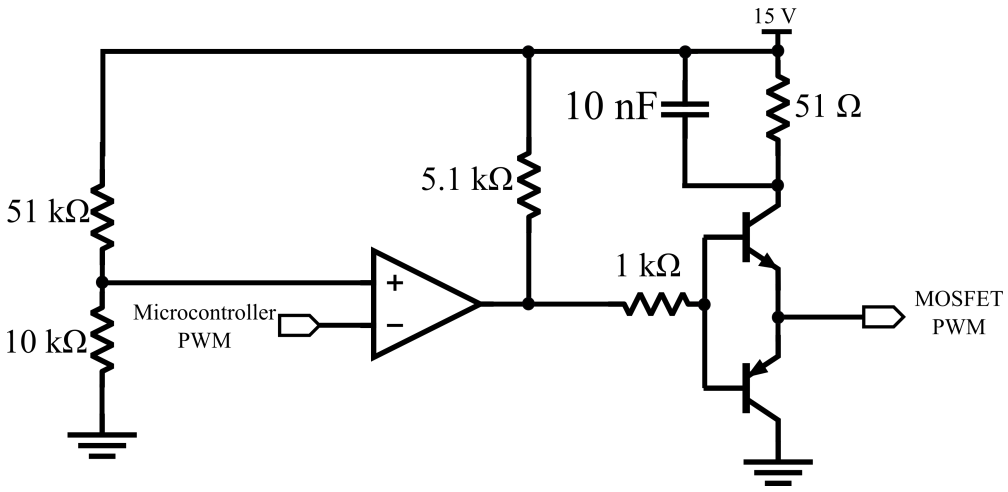

Figure 6–11 - Gate-drive circuit

6.2.5 Isolation switch

The boost converter does not allow the disconnection of the source and the output because, even if the MOSFET is turned off, there is a direct path from the input to the output through the boost inductor and diode. An isolation switch has been added in order to be able to disconnect the battery from the TEG. The isolation switch uses two P-channel MOSFETs connected in a back-to-back configuration; that is, with the sources connected together. The schematic diagram of the isolation switch is shown in Figure 6–12. A BJT is used to control the turn on and turn off of the two MOSFETs M_1 and M_2. The control of the switch is performed by the microcontroller. Before the microcontroller starts applying the PWM signal to the boost converter the microcontroller turns on the isolation switch to connect the battery to the output of the converter.

The component values of the isolation switch circuit are shown in Table 6-2.

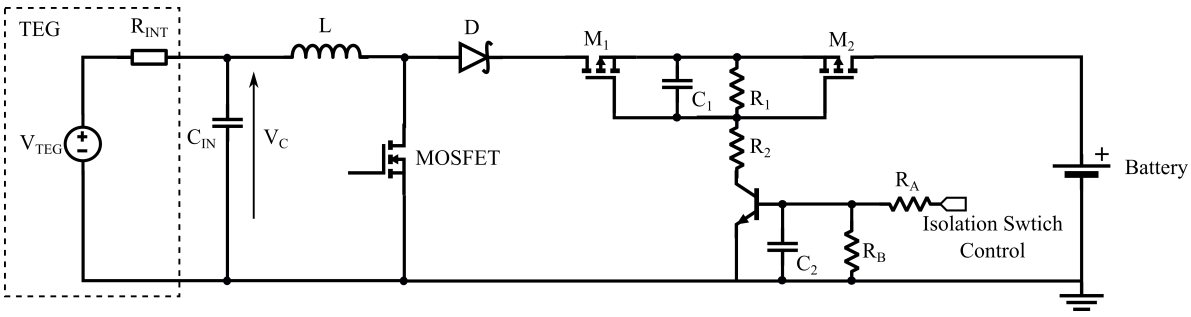

Figure 6–12 - Simplified diagram of the boost converter with the isolation switch connected at the output

Component	Input Voltage
R1	240 $k\Omega$
R2	330 $k\Omega$
RA	100 $k\Omega$
RB	100 $k\Omega$
C1	10 nF
C2	100 nF

Table 6-2- Component values of the isolation switch circuit

6.2.6 Converter telemetries

Telemetries are used for two purposes. The main purpose is to provide readings of voltage and current to the microcontroller in order for it to perform MPPT, but also to provide visual readings of the instantaneous values of TEG and battery voltages and currents on the LCD.

The input voltage of the boost represents the load voltage of the TEG; and the output voltage of the boost represents the battery voltage. The voltage sensors have been designed using potential dividers, from the measuring point to ground, with a decoupling capacitor at the output to avoid noise coupling to the internal ADC. The circuit used for the voltage telemetries is shown in Figure 6–13. The component values used for both input and output voltage telemetry circuits are shown in Table 6-3.

On the other hand, the input current telemetry of the boost represents the output current of the TEG; and the output current telemetry of the boost represents the battery charge current. The current telemetry circuit has been designed using a differential amplifier that measures and amplifies the voltage difference across a sense resistor. Figure 6–14 shows the circuit diagram of the current sensor. Due to the high input resistance of R_2 and the input of the OpAmp, the current sensor circuit does not disturb the operation of the rest of the circuit. The OpAmps of both input and output current sensors are supplied from the 15 V auxiliary power supply, so special attention must be paid to the maximum common-mode input voltage, especially with the output current sensor, which is connected to a voltage that can be as high as 33.6 V. For such reason, the output current sensor is designed using the LT6015 that has an input common-mode range from the negative supply voltage, V^-, to (V^- + 76 V).

The open-circuit voltage of the TEG will be measured by monitoring the open-circuit voltage of the pellets that the monTE™ has available for that purpose. The output voltage however, needs to be amplified since the output voltage of the pellets is very small in magnitude, as shown in Figure 6–16. The voltage sensor for the TEG open-circuit voltage will be designed using a differential amplifier as well. The circuit is shown in Figure 6–15 and the component values in Table 6-5.

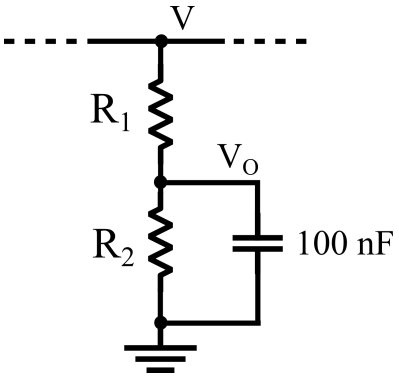

Figure 6–13 - Voltage telemetry circuit

Component	Input Voltage	Output Voltage
R1	180 *kΩ*	330 *kΩ*
R2	20 *kΩ*	20 *kΩ*
Equation	$V_O=0.1 \cdot V$	$V_O=0.0571 \cdot V$

Table 6-3 - Component values of the voltage telemetry circuits

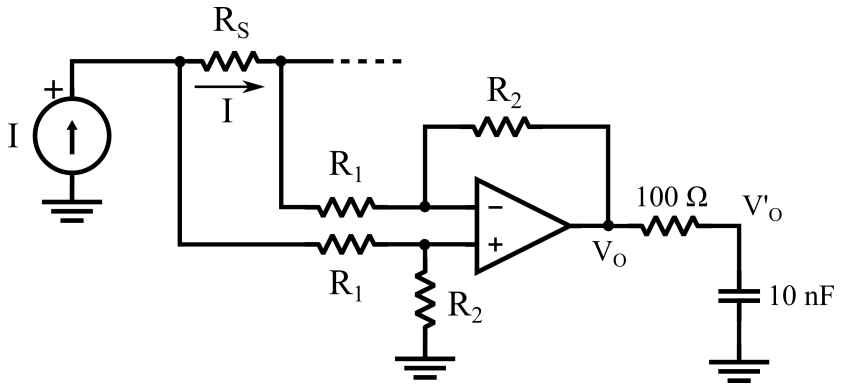

Figure 6–14 - Current telemetry circuit

Component	Input Current	Output Current
R_S	0.1 *Ω*	0.02 *Ω*
R1	100 *kΩ*	1 *kΩ*
R2	750 *kΩ*	100 *kΩ*
Equation	$V_O=0.75 \cdot I$	$V_O=2 \cdot I$
OpAmp	LT1078	LT6015

Table 6-4 - Component values of the current telemetry circuits

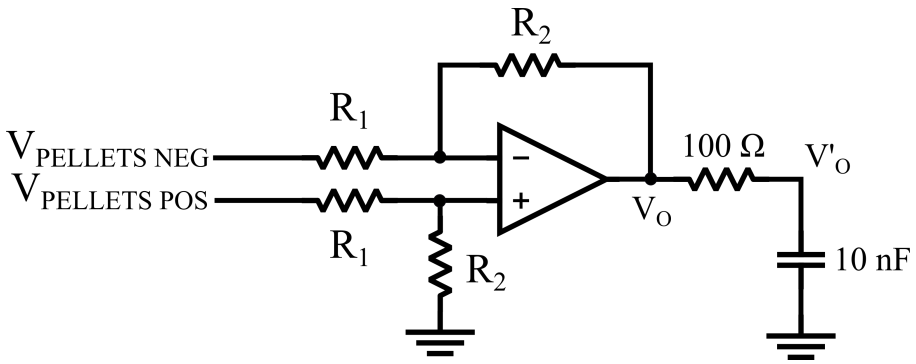

Figure 6–15 – Open-circuit voltage telemetry circuit

Component	Value
R1	100 *kΩ*
R2	620 *kΩ*
Equation	$V_O=6.2 \cdot V_{PELLETS}$
OpAmp	LT1078

Table 6-5 - Component values of the open-circuit voltage telemetry circuits

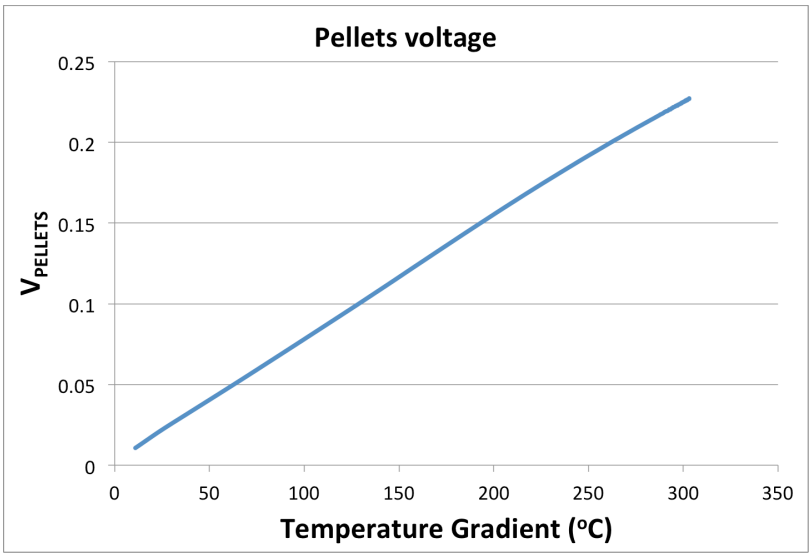

Figure 6–16 - Pellets voltage plotted against temperature difference across the monTE™

6.3 Initial test

The hardware has been tested in a lab bench using a simulated TEG. The schematic diagram of the simulated TEG has already been shown in Figure 4–1, which comprises a voltage supply connected to a resistor in series with it. Even if the simulated TEG does not

represent the real behaviour of a TEG operated under constant heat flux, it allows the test of the hardware implementing the MPPT algorithm described in Section 5.3.

The test setup is shown in Figure 6–17. The simulated TEG, shown on the left hand side of the diagram, comprised a bench-top power supply and a high-power 4.7 Ω resistor. The connection between the power supply and the resistor represents the open-circuit voltage of the TEG. From that point the voltage was fed, using a potential divider, to the input connector that was used to measure the pellets open-circuit voltage. The potential divider was made using standard through-hole resistors, and represents the proportionality factor, equal to 63, between the main voltage of the TEG and that output, as shown in Equation (**4-13**) and Figure 4–14.

The connection between the high-power resistor and the input of the converter represents the output voltage of the TEG. This is the voltage the power converter regulates and the voltage of this node was monitored using a digital oscilloscope.

Finally, the output of the converter was connected to a simulated battery. The simulated battery comprised a bench-top power supply connected in parallel with an electronic load. The output voltage of the bench-top power supply sets the battery voltage; and the electronic load sinks the output current of the power converter.

A single three-channel bench-top power supply was used for both the TEG and the simulated battery. The TEG was simulated using channel number one whereas the simulated battery used channel number two. The diagram of Figure 6–17 shows two power supplies for simplicity. The actual test setup is shown in Figure 6–18. The test equipment used in the test setup shown in Figure 6–17 is listed in Table 6-6 .

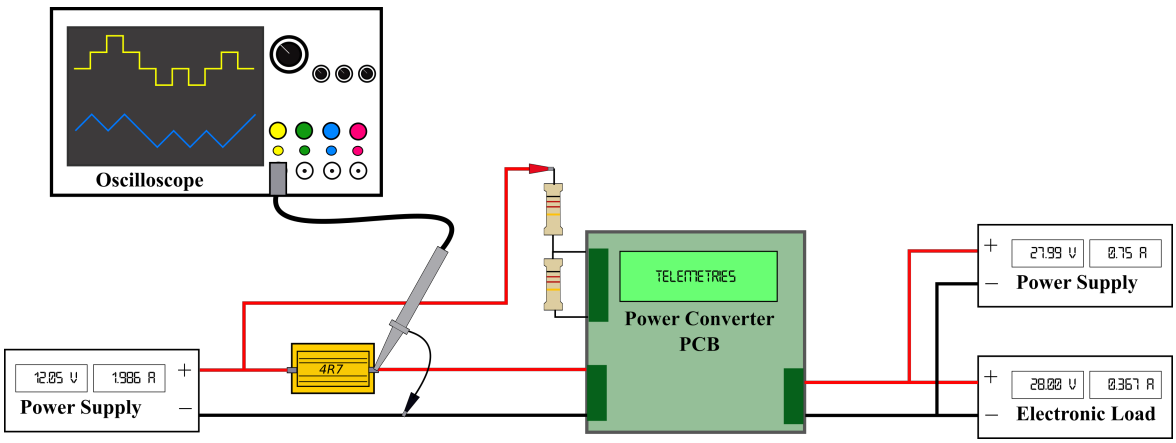

Figure 6–17 - Test setup used to test the MPPT algorithm on the lab bench

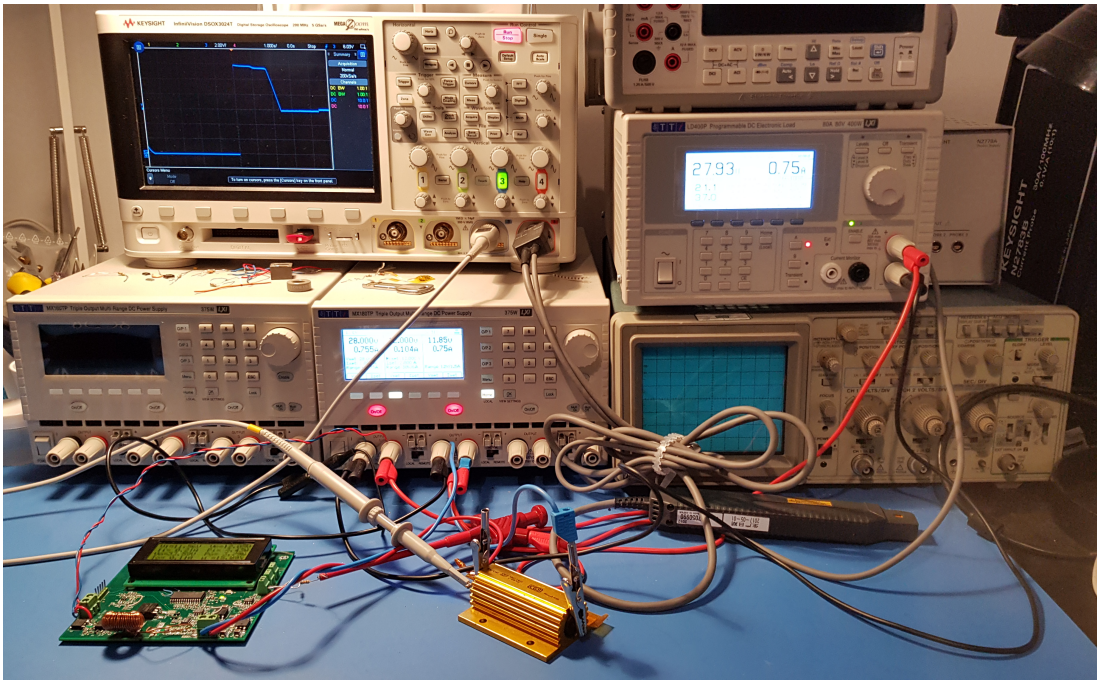

Figure 6–18 - Hardware implementation of the test setup shown in Figure 6–17

Equipment	Functionality	Model	Manufacturer
Power Supply	TEG	MX180TP	TTi
Power Supply	Battery	MX180TP	TTi
Electronic Load	Battery	LD400P	TTi
Oscilloscope	Measurements	DSOX3024T	Keysight

Table 6-6 - Test equipment used in the test setup of Figure 6–17

The MPPT sampling frequency was decreased in order to be able to capture several perturbations, as well as the different transitions between operating points, in a single scope trace. In that sense, the MPPT sampling frequency was decreased by a factor of 100; that is, from 500 *s* to 5 *s*. The time delay to detect changes in the input heat flux was changed by a factor of 100.

Figure 6–19 shows the start-up sequence of the algorithm. First, the open-circuit voltage is measured. The operating point is then set to 50 % of the measured open-circuit voltage and the algorithm starts regulating the input voltage to the voltage set point. The duty-cycle starts to increase up to the point where the input voltage is equal to the voltage set point. As the duty-cycle increases the current through the inductor starts to build up. At the beginning, the inductor current falls to zero before the OFF-time of the PWM signal finishes and the converter operates in Discontinuous Conduction Mode (DCM). As the

current through the inductor keeps increasing, the current does not reach zero anymore before the end of the OFF-time and the converter starts to operate in Continuous Conduction Mode (CCM). The blue trace shows the converter input voltage and the pink trace the inductor current.

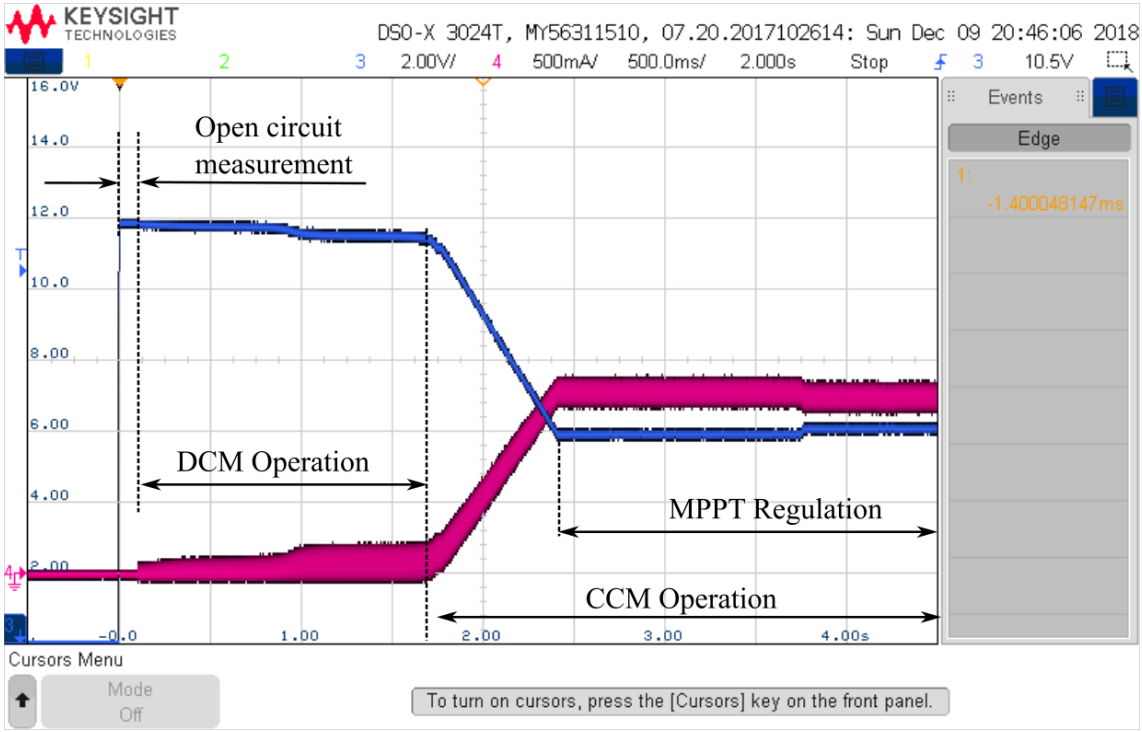

Figure 6–19 - Start-up of the MPPT algorithm. CH3: Input voltage, CH4: inductor current

Figure 6–20 shows the input voltage regulation implemented by the algorithm. The input voltage is monitored every 5 *ms* and compared against the voltage set point. The duty-cycle is then increased or decreased in order to adjust the input voltage to the set point. The blue trace shows the input voltage of the boost converter and the pink trace the boost inductor current. With a fixed value of open-circuit voltage, the inductor, and input, current will decrease as the input voltage increases, and vice versa.

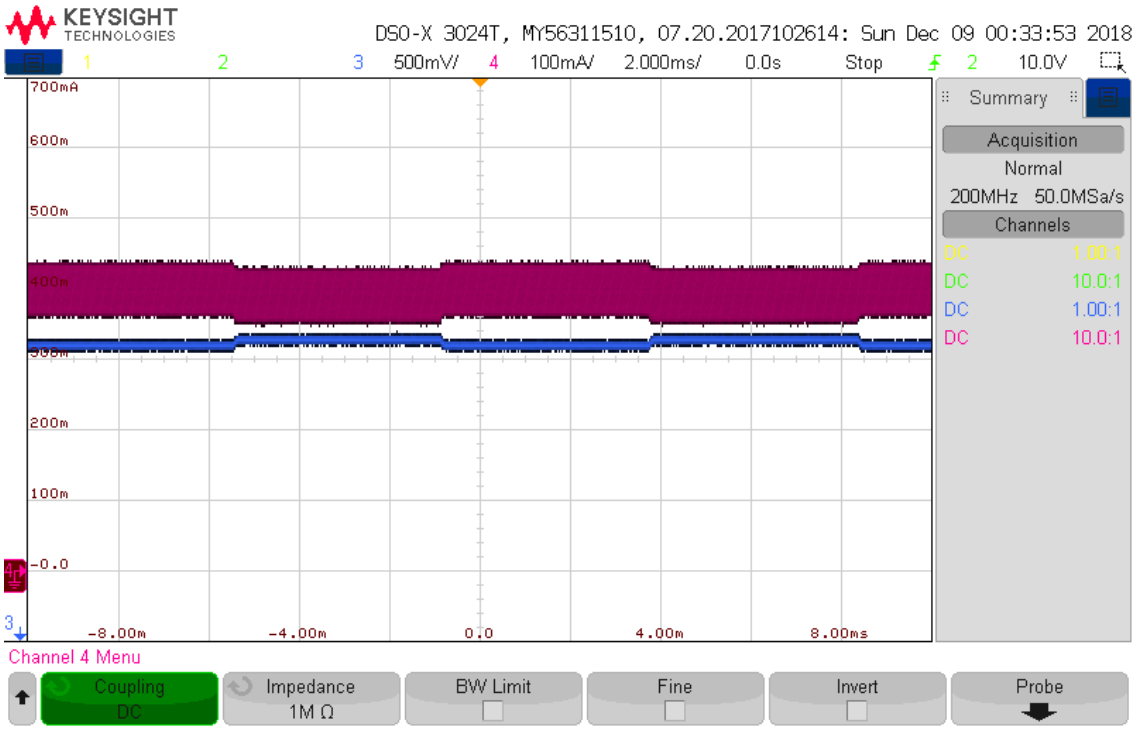

Figure 6–20 - Regulation cycle of the algorithm. CH3: Input voltage, CH4: Inductor current

Figure 6–21 shows a zoomed-in view of the input voltage of the boost converter. The blue trace shows the input voltage of the boost converter and the pink trace the boost inductor current. From the time scale of the oscilloscope, 10 *μs/div*, it can be seen that the waveforms are periodic and the period is 10 *μs*, which corresponds to a switching frequency of 100 *kHz*.

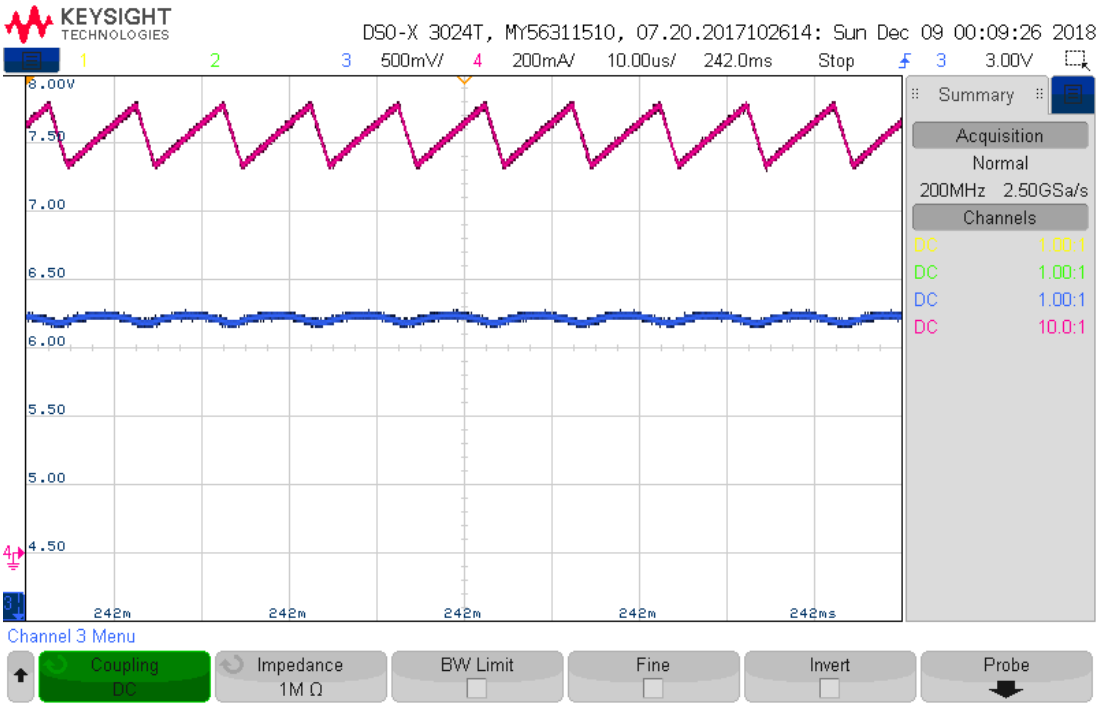

Figure 6–21 - Input voltage and current ripple. CH3: input voltage, CH4: inductor current

Figure 6–22 shows the magnitude of the inductor current ripple with an input voltage equal to 2 *V*. In the figure it can be observed that the inductor current ripple is equal to 67.5 mA, which is the value calculated in Section 6.2.3 for the same value of input voltage.

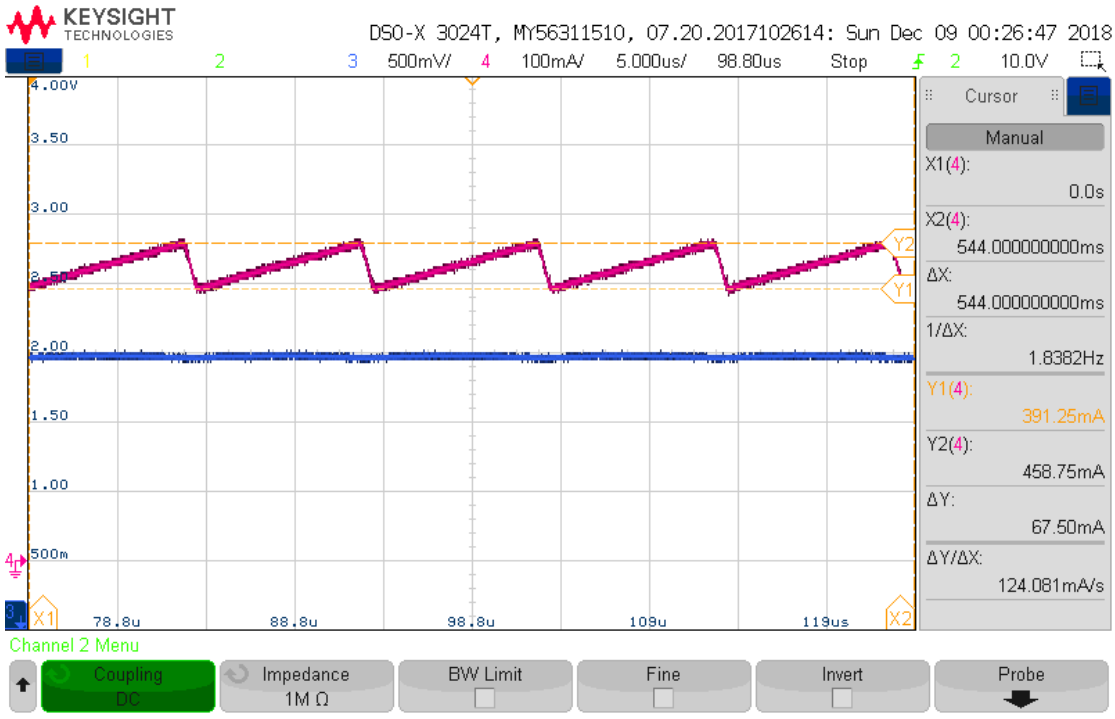

Figure 6–22 - Inductor current ripple with V_{IN} = 2 *V*. CH3: input voltage, CH4: inductor current

The ability to react to step changes in the TEG open-circuit voltage has also been tested. These changes correspond to fast changes in the input heat flux, which, in the extreme case, correspond to a step change in voltage. Figure 6–23 shows the reaction of the MPPT algorithm to an increasing step in the open-circuit voltage. The open-circuit voltage changes from 12 *V* to 14 *V*. The open-circuit voltage changes and, 94 *ms* later the MPPT algorithm detects the change (reaction time). After that, the MPPT algorithm regulates the input voltage to 50 % of the instantaneous open circuit voltage.

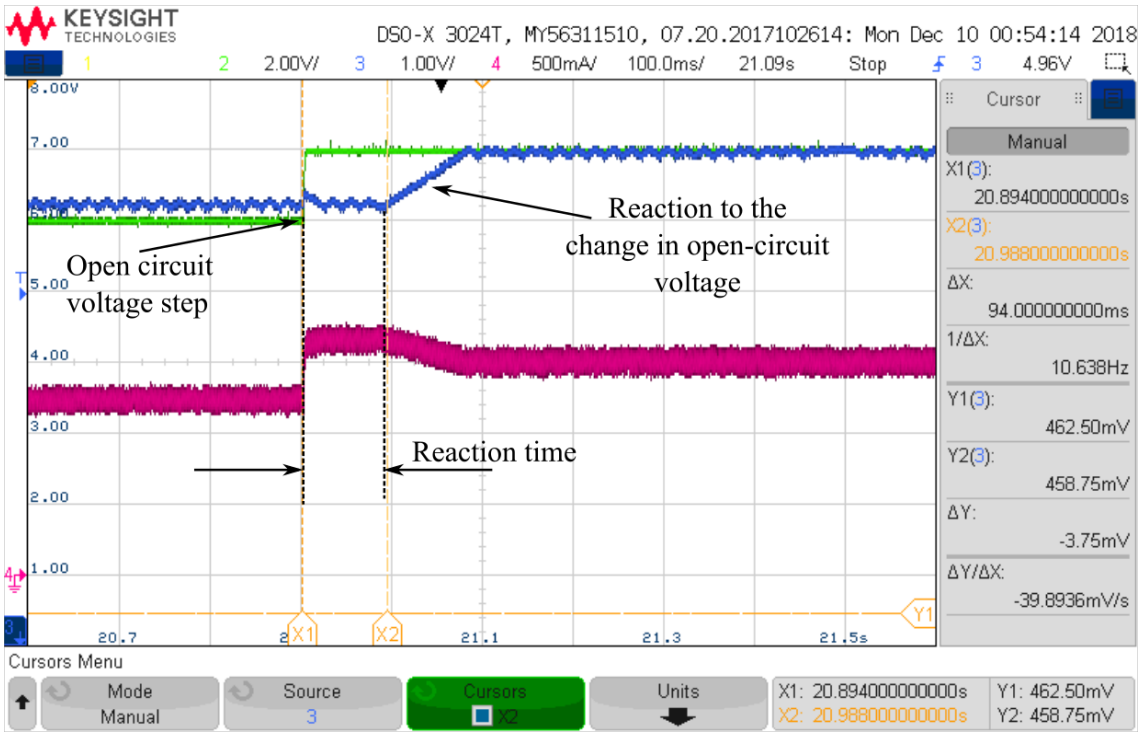

Figure 6–23 - Reaction of the MPPT algorithm to an increasing step in open-circuit voltage. CH2: open-circuit voltage, CH3: input voltage, CH4: inductor current

Figure 6–24, on the other hand, shows the reaction of the MPPT algorithm to a decreasing step in the open-circuit voltage. The open-circuit voltage changes from 14 *V* to 12 *V*. The open-circuit voltage changes and, 384 *ms* later the MPPT algorithm detects the change (reaction time). After that, the MPPT algorithm regulates the input voltage to 50 % of the instantaneous open circuit voltage.

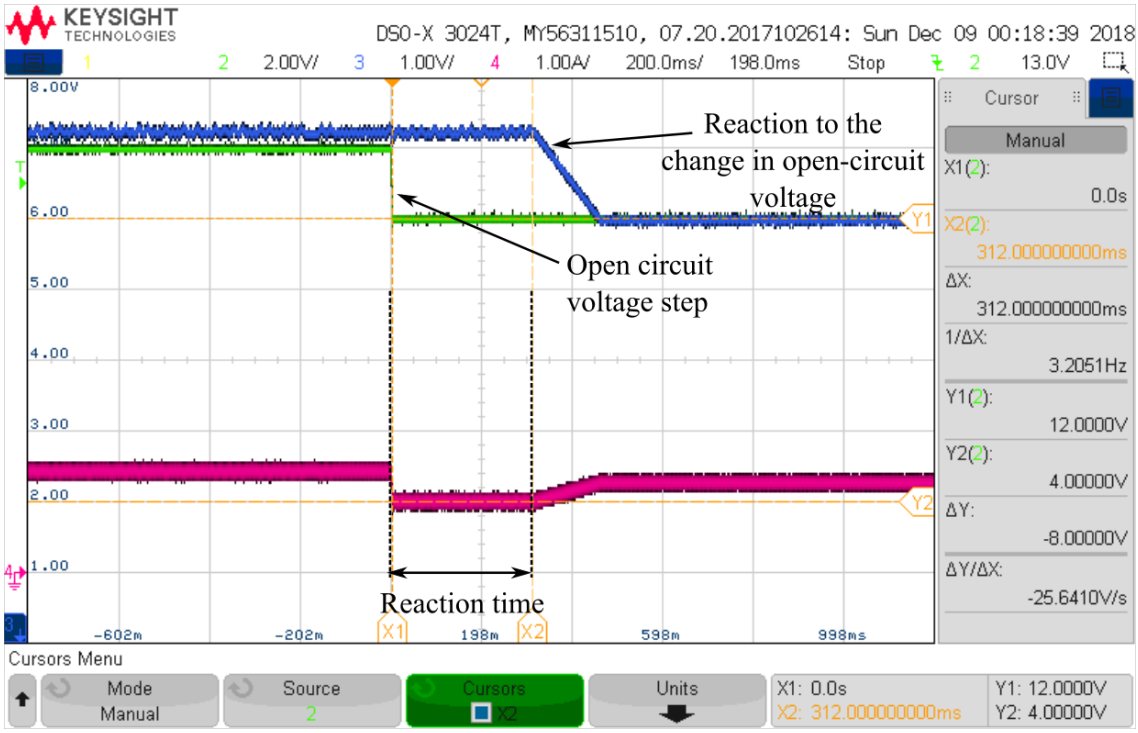

Figure 6–24 - Reaction of the MPPT algorithm to a decreasing step in open-circuit voltage. CH2: open-circuit voltage, CH3: input voltage, CH4: inductor current

Finally, the battery EoC regulation has also been tested. The output voltage has been increased from 30 *V* to 33.6 *V* and both the input voltage and inductor current have been measured. Figure 6–25 shows the transition from MPPT to EoC. The green trace shows the output (battery) voltage, which increases gradually from 30 *V* to 33.6 *V*. Until the battery voltage reaches 33.6 *V*, the converter operates in MPPT mode. When the output voltage reaches 33.6 *V*, the duty-cycle is decreased until the inductor current drops to zero and the input voltage reaches the open-circuit input voltage. This last operation is the EoC mode.

Figure 6–26 shows a zoomed-in view of the EoC control phase. As the battery voltage continues to increase, the duty-cycle is linearly decreased so both the inductor current and input voltage gradually changes as well.

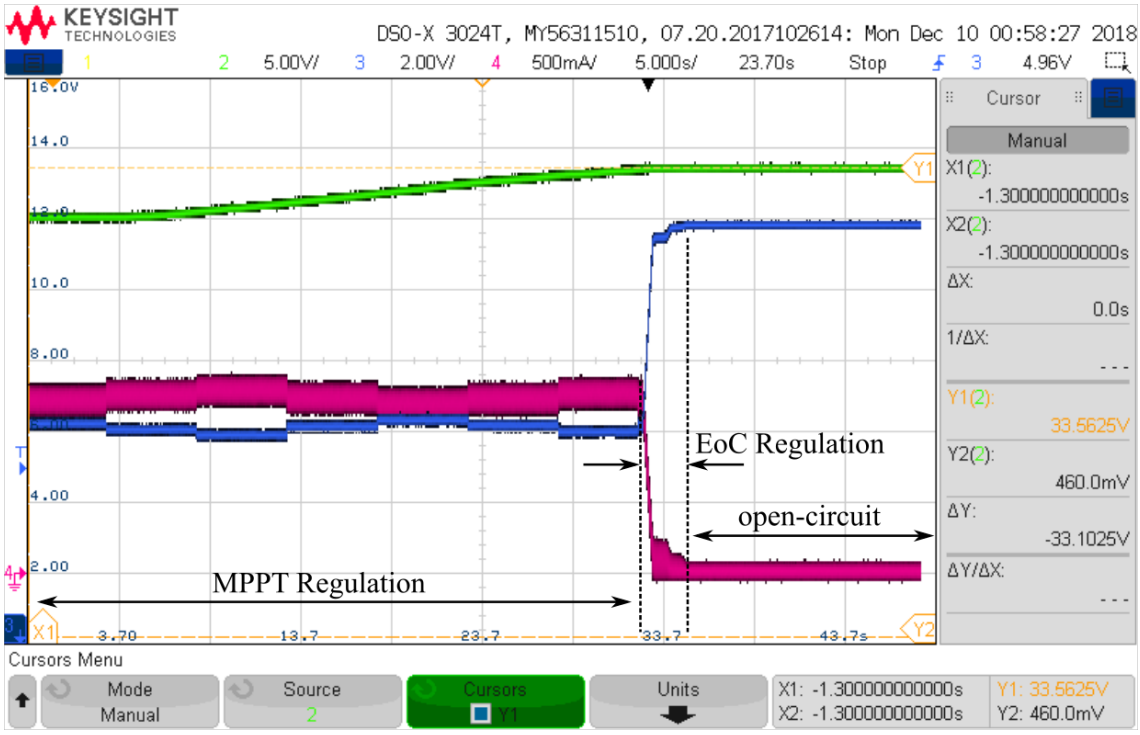

Figure 6–25 - Transition between MPPT and EoC control. CH2: output voltage, CH3: input voltage, CH4: inductor current

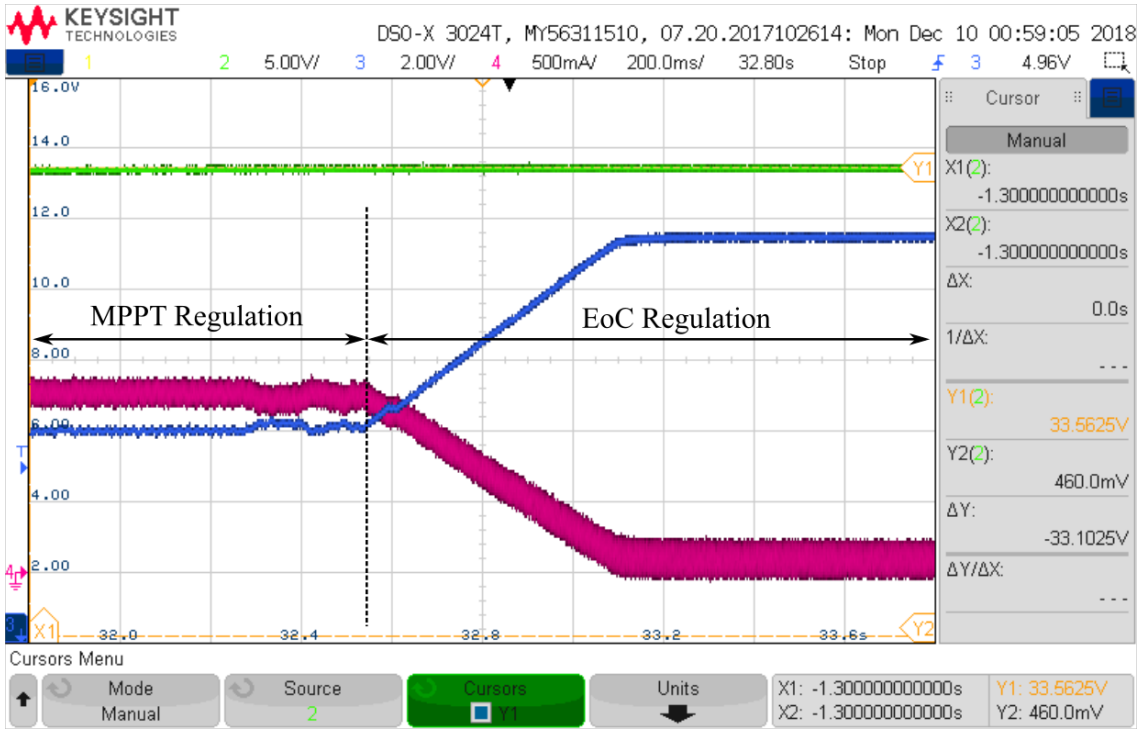

Figure 6–26 – Zoomed-in view of EoC control phase. CH2: output voltage, CH3: input voltage, CH4: inductor current

6.4 Experimental results

The MPPT algorithm has been tested using a monTE™ TEG and the test setup described in Section 4.2.3. The input heat flux profiles are the same that were used in the simulations and described in Section 5.5. First, a test is performed under a steady value of heat flux. The algorithm is tested for three different values of heat flux: 100 W_{th}, 200 W_{th} and 300 W_{th}. Secondly, a test is performed with the test profile shown in Figure 5–27, showing the performance under instantaneous changes (step changes) of the input heat flux. Finally, a ramp test is performed where the TEG operates under the input heat flux profile shown in Figure 5–28. Three different ramps are tested and described in Table 5-5. The profiles of input heat flux that have been tested are the same as those used in the simulations in Section 5.5. For each test not only the proposed algorithm (Figure 5–25) has been tested, but also the "fast" P&O (Figure 5–23) and FOV (Figure 5–22).

The sampling time of the *VEE pro* program is 7 seconds, which sets a main difference with the simulation traces shown in Section 5.5, which have been plotted with a sampling frequency of 100 *kHz*.

Figure 6–27 shows the output power generated by the TEG for an input heat flux of 100 W_{th}. The load voltage is shown in Figure 6–28. The new algorithm generates more power than "fast" P&O and FOV. Also, it can be observed that the most stable algorithm is FOV because the load voltage does not change and remains equal to 50 % of the instantaneous open-circuit voltage. "Fast" P&O presents the highest variations in output power, which is also reflected in the load voltage

A very important graph is shown in Figure 6–29, where the instantaneous value of the beta factor is plotted for all three algorithms. For FOV, as expected, the value of beta remains constant and equal to 0.5. The beta factor for "fast" P&O varies considerably with an average value of 0.516. The new algorithm operates with an average beta factor of 0.564. The most important characteristic is that the new algorithm is capable of operating at a higher value of beta that brings the operating point of the TEG closer to the MPP, when compared to the other two algorithms.

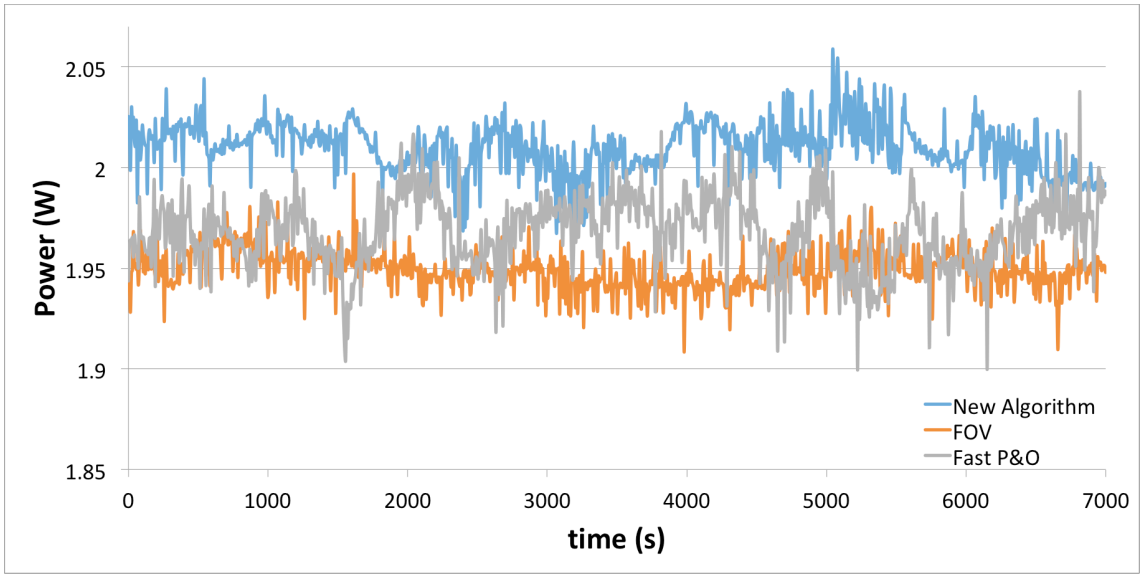

Figure 6–27- TEG output power for an input heat flux of 100 W_{th}

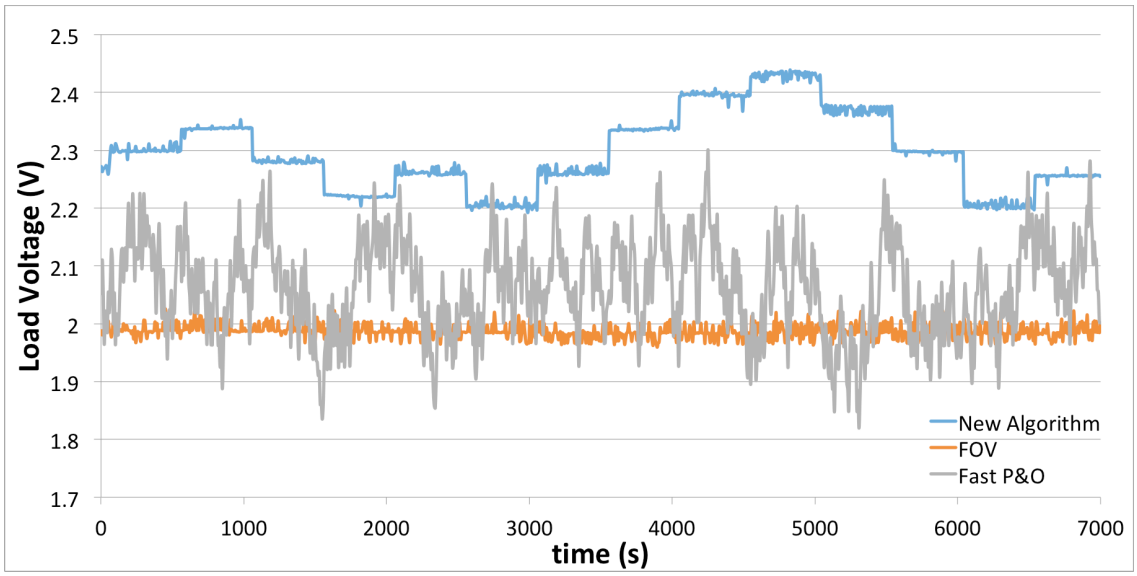

Figure 6–28 - TEG load voltage for an input heat flux of 100 W_{th}

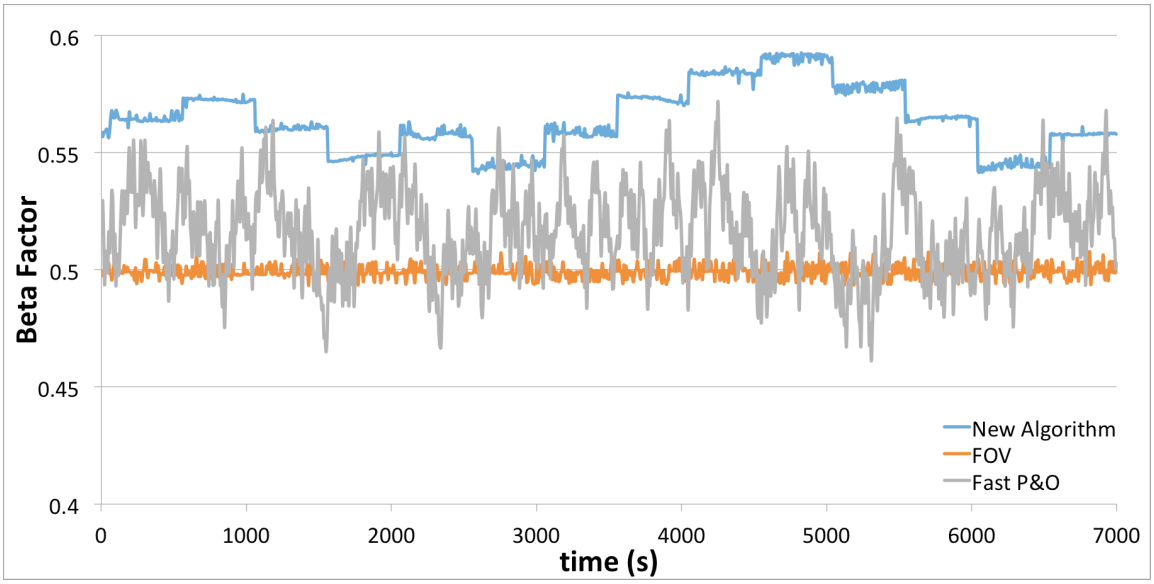

Figure 6–29 - Beta factor for an input heat flux of 100 W_{th}

The average power generated with the new algorithm is equal to 2.01 *W*, with a total energy equal to 14064.12 *J*. The "fast" P&O algorithm generates an average power equal to 1.97 *W* and a total energy of 13770.38 *J*; and with FOV, the average power generated is 1.95 *W* and a total energy of 13639.63 *J*. The new algorithm generates 2.13 % more energy than "fast" P&O and 3.11 % more than FOV.

The results for the tests performed at 200 W_{th} are shown in Figure 6–30 and Figure 6–31. The output power of the TEG is shown in Figure 6–30, which, as previously, is higher for the case of the new algorithm. The beta factor is plotted in Figure 6–31 for all three algorithms.

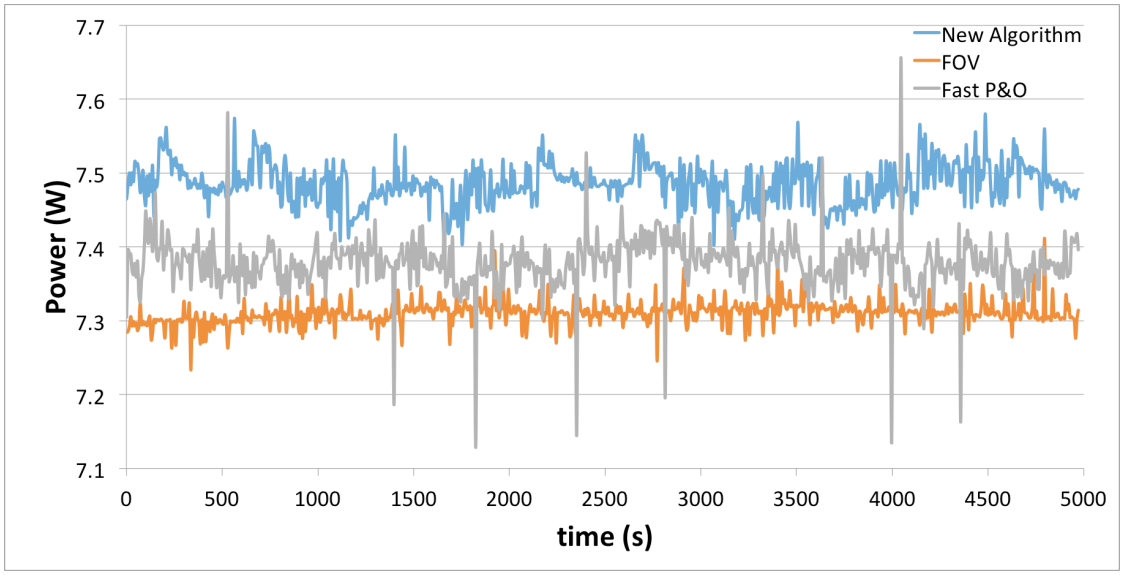

Figure 6–30 - TEG output power for an input heat flux of 200 W_{th}

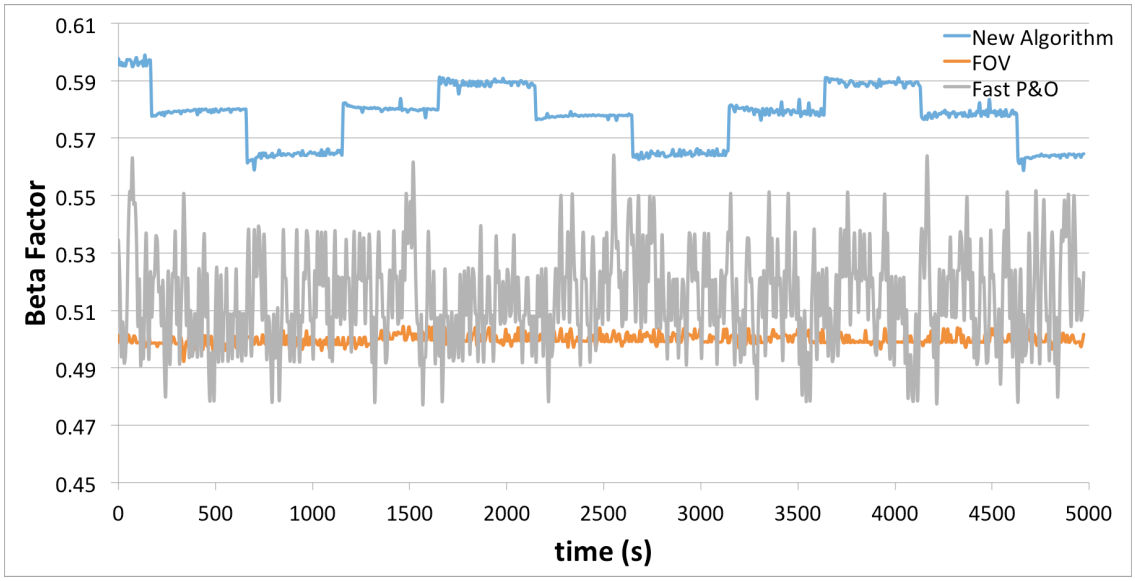

Figure 6–31 - Beta factor for an input heat flux of 200 W_{th}

The average power generated with the new algorithm is equal to 7.49 *W*, with a total energy equal to 37202.77 *J*. The "fast" P&O algorithm generates an average power equal to 7.38 *W* and a total energy of 36672.641 *J*; and with FOV, the average power generated is 7.31 *W* and a total energy of 36333.78 *J*. The new algorithm generates 1.45 % more energy than "fast" P&O and 2.39 % more than FOV.

On the other hand, the average value of beta, when the TEG is controlled using the new algorithm, is 0.577, whereas for "fast" P&O is 0.514 and for FOV is equal to 0.499.

The results for the tests performed at 300 W_{th} are shown in Figure 6–32 and Figure 6–33. The output power of the TEG is shown in Figure 6–32, which is higher for the case of the new algorithm. The beta factor is plotted in Figure 6–33 for all three algorithms.

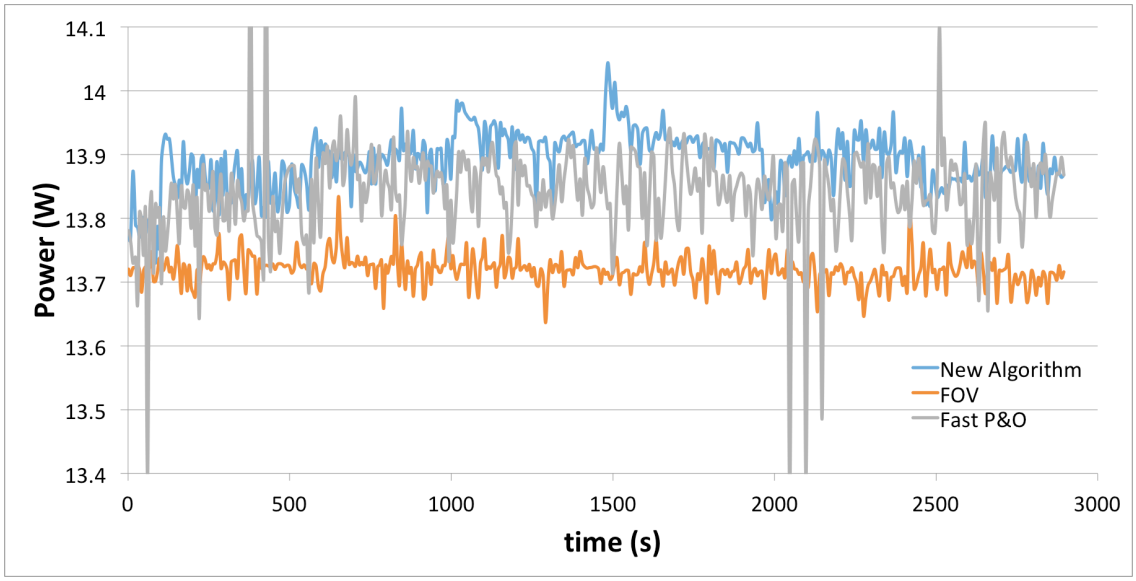

Figure 6–32 - TEG output power for an input heat flux of 300 W_{th}

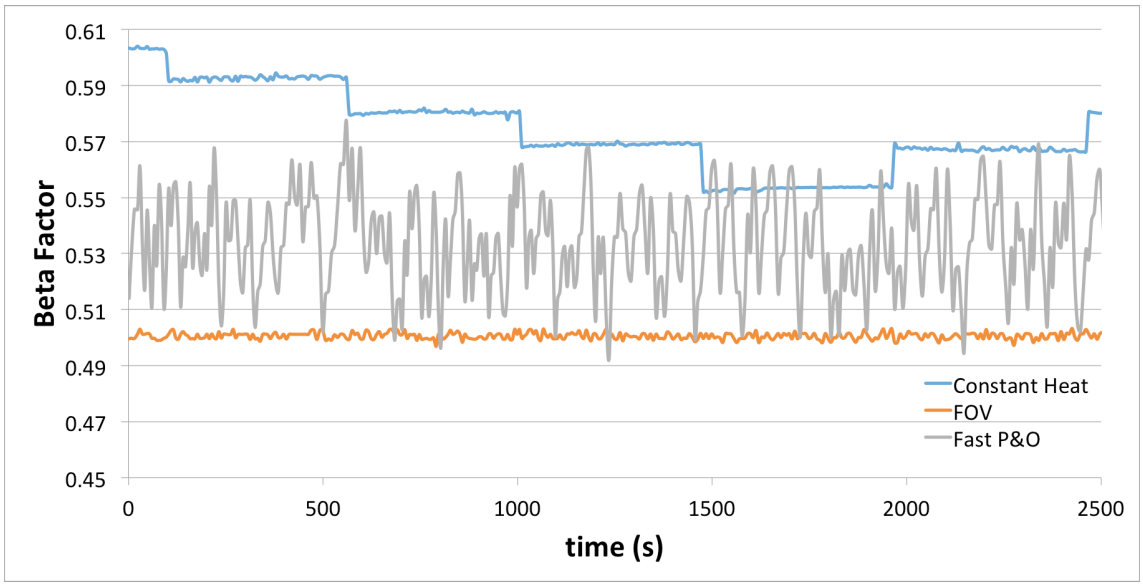

Figure 6–33 - Beta factor for an input heat flux of 300 W_{th}

The average power generated with the new algorithm is equal to 13.89 *W*, with a total energy equal to 40200.15 *J*. The "fast" P&O algorithm generates an average power equal to 13.84 *W* and a total energy of 40054.40 *J*; and with FOV, the average power generated is 13.73 *W* and a total energy of 39701.39 *J*. The new algorithm generates 0.36 % more energy than "fast" P&O and 1.26 % more than FOV.

On the other hand, the average value of beta, when the TEG is controlled using the new algorithm, is 0.574, whereas for "fast" P&O is 0.533 and for FOV is equal to 0.500.

The results for the case where the power is changed as per the profile shown in Figure 5–27 are shown in Figure 6–34. The constant heat flux plateaus used for the case of the new algorithm are longer than for the case of FOV and P&O. For the last two algorithms, the constant heat flux plateaus at 75 W_{th}, 250 W_{th} and 150 W_{th} have durations of 4000 s, approximately. In the case of the new algorithm the duration is around 7500 s. There is no specific reason for the different plateaus times between the algorithms, but the importance of this test lies on the transient response to the input heat flux step changes. Figure 6–35, shows a zoomed-in view of the transients when the edges of Figure 6–34 are aligned. Figure 6–35 a) shows a zoomed-in view of the response of all three algorithms to the step in input heat flux from 75 W_{th} to 250 W_{th}. Figure 6–35 b) shows a zoomed-in view of the response of all three algorithms to the step in input heat flux from 250 W_{th} to 150 W_{th}. The results shown in Figure 6–35 are very similar to those obtained in from the simulation and shown in Figure 5–40. The new algorithm and FOV perform in a very similar manner, whereas the conventional P&O algorithm losses its tracking capability during these transients. The same observations made in Section 5.5 for the case of the input heat flux step transients are applied in here.

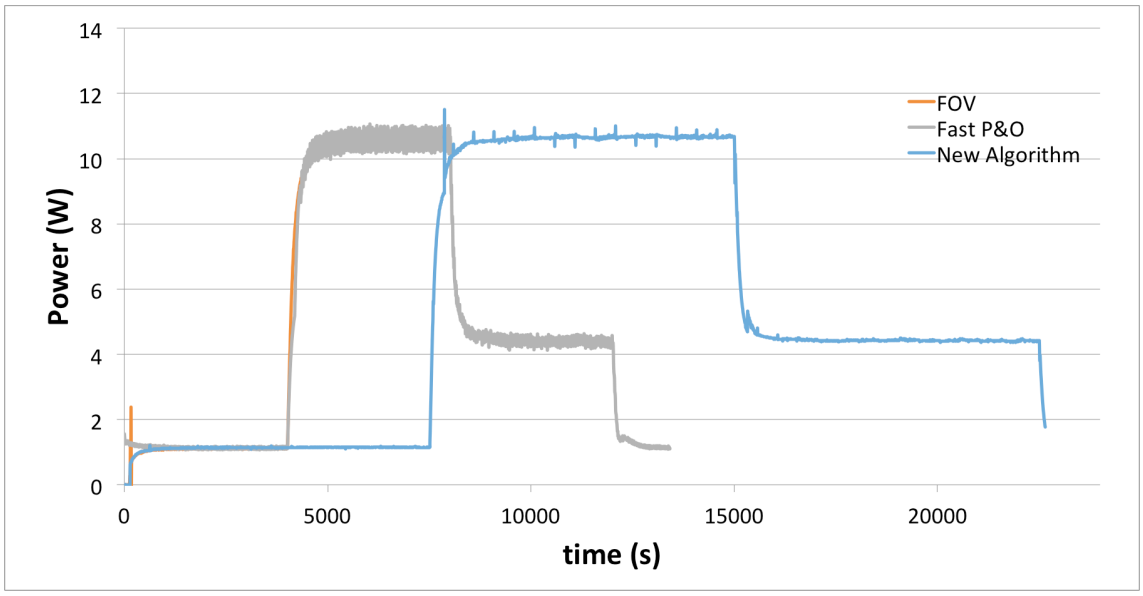

Figure 6–34 - Experimental results for an input heat flux with the profile shown in Figure 5–27

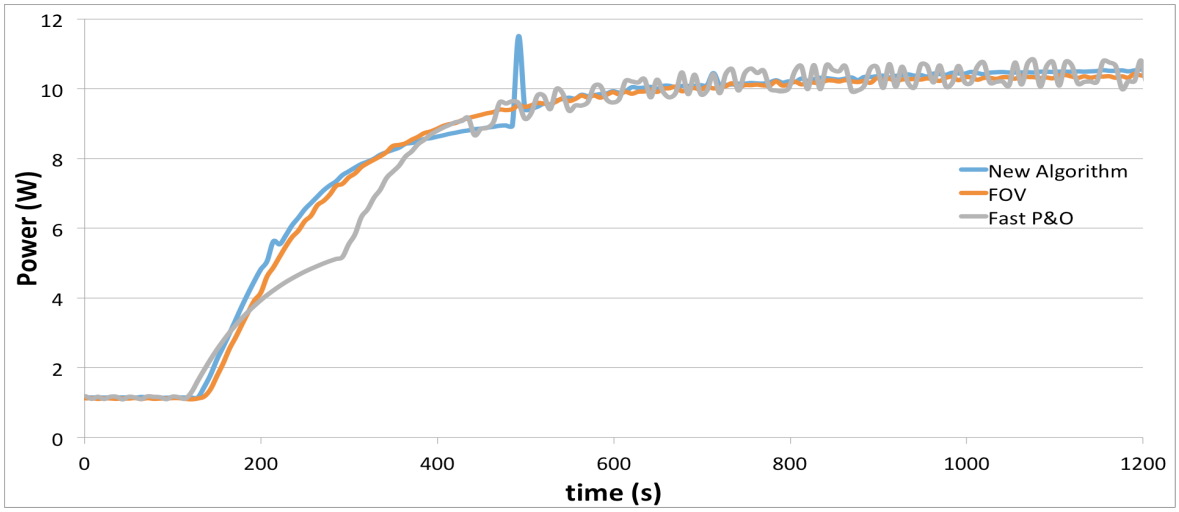

a)

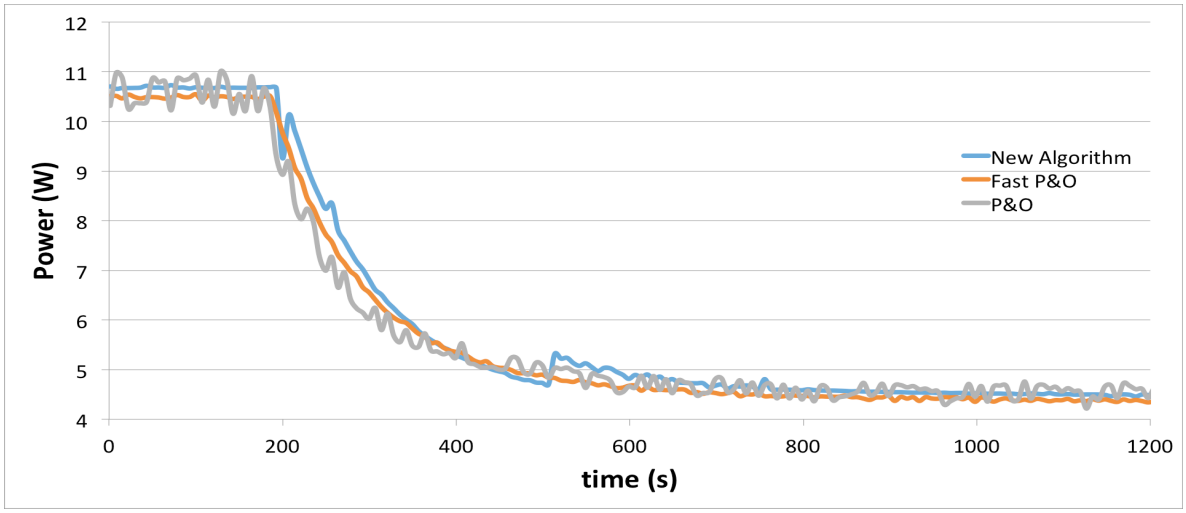

b)

Figure 6–35 – Zoomed-in view of the step transients performed in the test of the TEG a) from 75 W_{th} to 250 W_{th} and b) from 250 W_{th} to 150 W_{th}

The results of the ramp test for an input heat flux that follows the first profile described in Table 5-5 are shown in Figure 6–36. A zoomed-in view of the rising and falling ramps is shown in Figure 6–37 a) and b), respectively. The total energy delivered using the new algorithm is equal to 20536.61 *J*, with FOV it is 20284.86 *J* and 20391.13 *J* with conventional P&O. During the rising ramp, however, the energy delivered with the new algorithm is equal to 4957.40 *J*, 4918.33 *J* with FOV and 4960.88 *J* with P&O. During the rising ramp the conventional P&O algorithm generates 0.07 % more energy than the new algorithm, but the new algorithm generates 0.8 % more energy than FOV. During the falling ramp the energy delivered with the new algorithm is equal to 7089.40 *J*, 6994.12 *J* with FOV and 7004.45 *J* with conventional P&O. During the falling ramp the new

algorithm generates 1.21 % more energy than the conventional P&O and 1.36 % more energy than FOV.

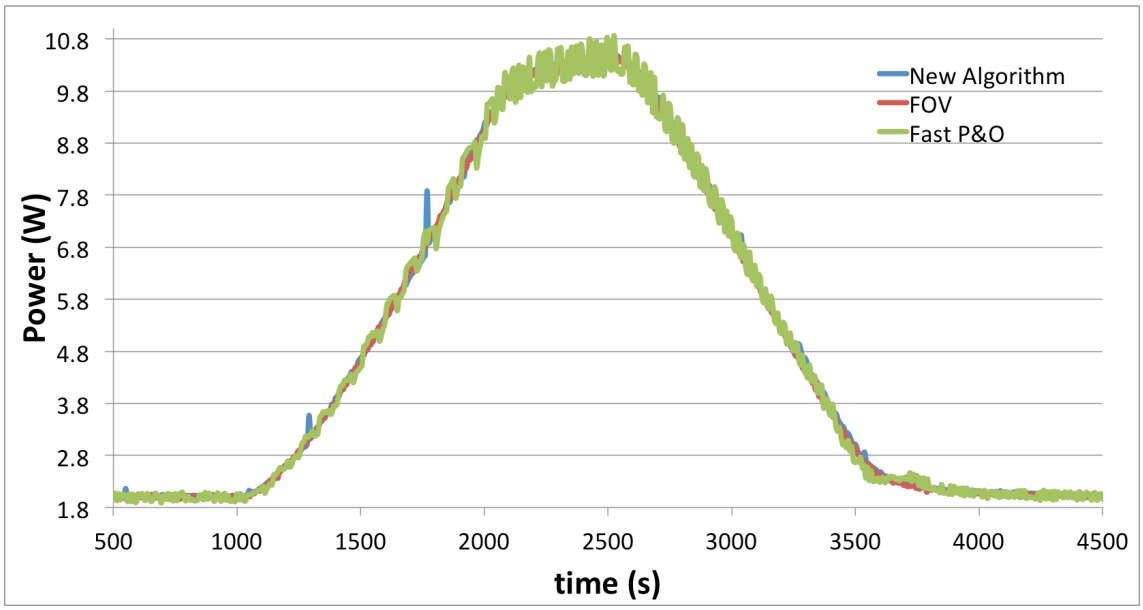

Figure 6–36 - Experimental results of the three algorithms when operated under the first ramp profile shown in Table 5-5

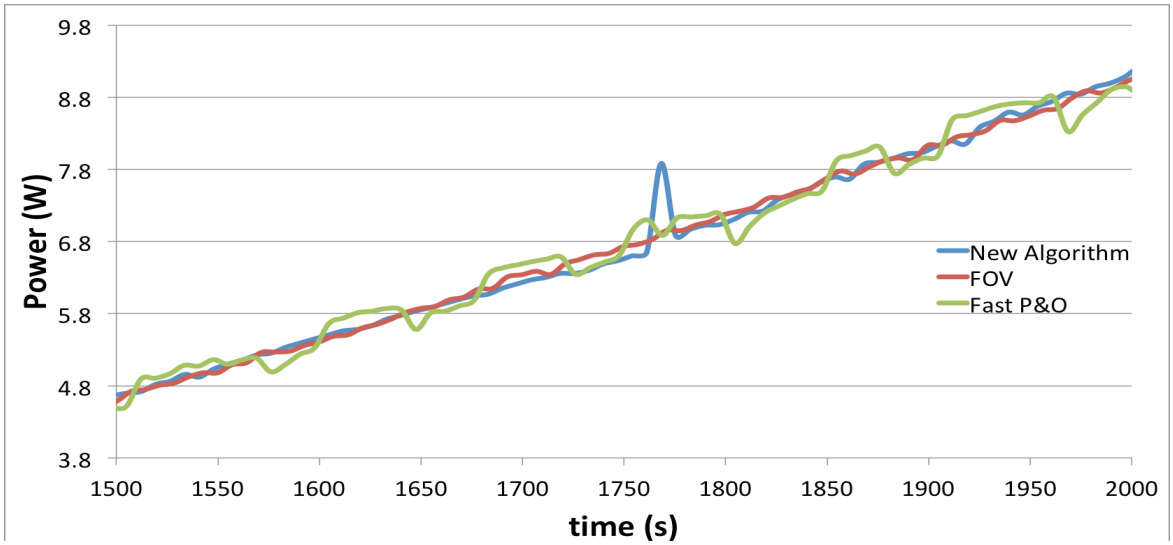

a)

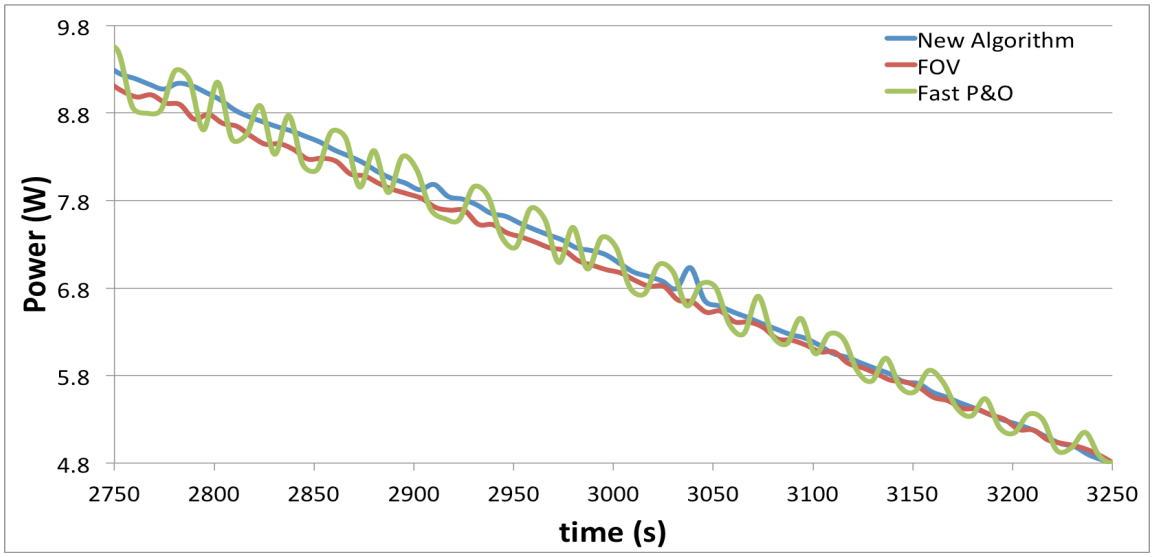

b)

Figure 6–37 - Zoomed-in view of a) the rising slope and b) falling slope of the profiles shown in Figure 6–36

The results with the second profile described in Table 5-5 are shown in Figure 6–38. A zoomed-in view of the rising and falling ramps is shown in Figure 6–39 a) and b), respectively. The total energy delivered using the new algorithm is equal to 50159.49 *J*, with FOV it is 48957.96 *J* and 49575.30 *J* with conventional P&O. During the rising ramp, however, the energy delivered with the new algorithm is equal to 16811.67 *J*, 16516.96 *J* with FOV and 16667.37 *J* with P&O. During the rising ramp the new algorithm generates 0.86 *%* more energy than the P&O and 1.78 *%* more energy than FOV. During the falling ramp the energy delivered with the new algorithm is equal to 19294.24 *J*, 18979.26 *J* with FOV and 19103.44 *J* with P&O. During the falling ramp the new algorithm generates 0.99 *%* more energy than the conventional P&O and 1.66 *%* more energy than FOV.

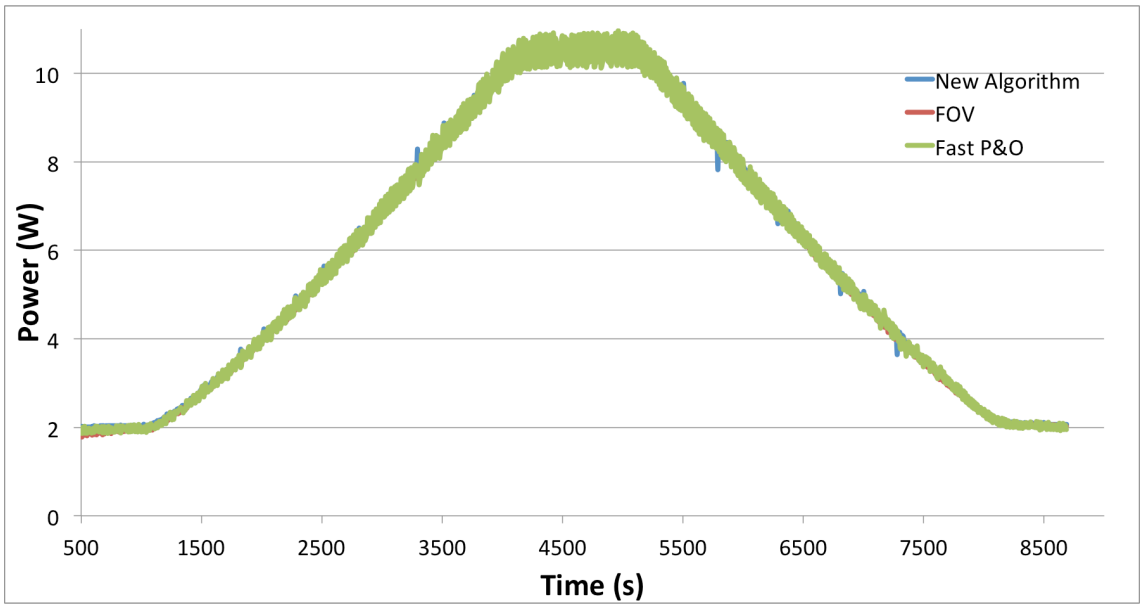

Figure 6–38 - Experimental results of the three algorithms when operated under the second ramp profile shown in Table 5-5

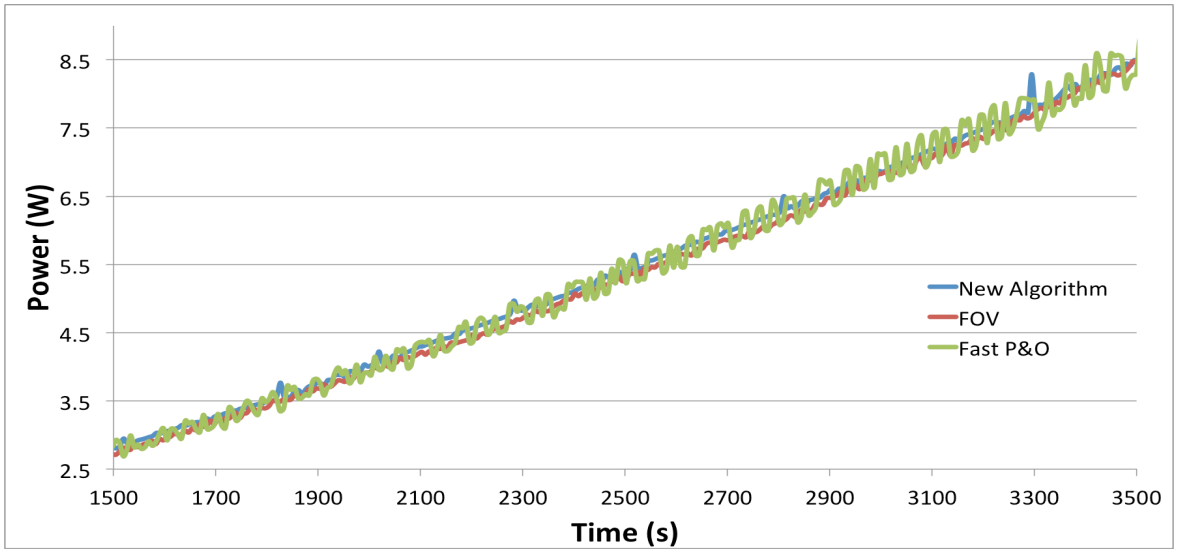

a)

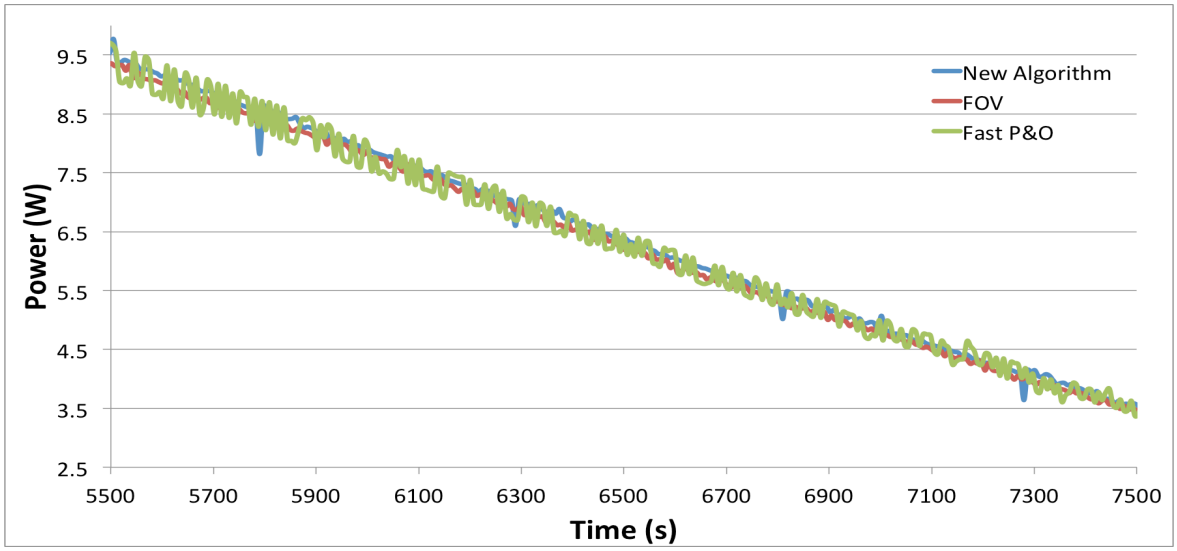

b)

Figure 6–39 - Zoomed-in view of a) the rising slope and b) falling slope of the profiles shown in Figure 6–38

The results with the third profile described in Table 5-5 are shown in Figure 6–40. A zoomed-in view of the rising and falling ramps is shown in Figure 6–41 a) and b), respectively. The total energy delivered using the new algorithm is equal to 32342.04 *J*, with FOV it is 32180.08 *J* and 32272.47 *J* with conventional P&O. During the rising ramp, however, the energy delivered with the new algorithm is equal to 6034.80 *J*, 5984.15 *J* with FOV and 6079.25 *J* with P&O. During the rising ramp the P&O algorithm generates 0.74 % more energy than the new algorithm, but the new algorithm generates 0.85 % more energy than FOV. During the falling ramp the energy delivered with the new algorithm is equal to 9627.11 *J*, 9561.35 *J* with FOV and 9526.78 *J* with P&O. During the falling ramp

the new algorithm generates 1.05 % more energy than the conventional P&O and 0.69 % more energy than FOV.

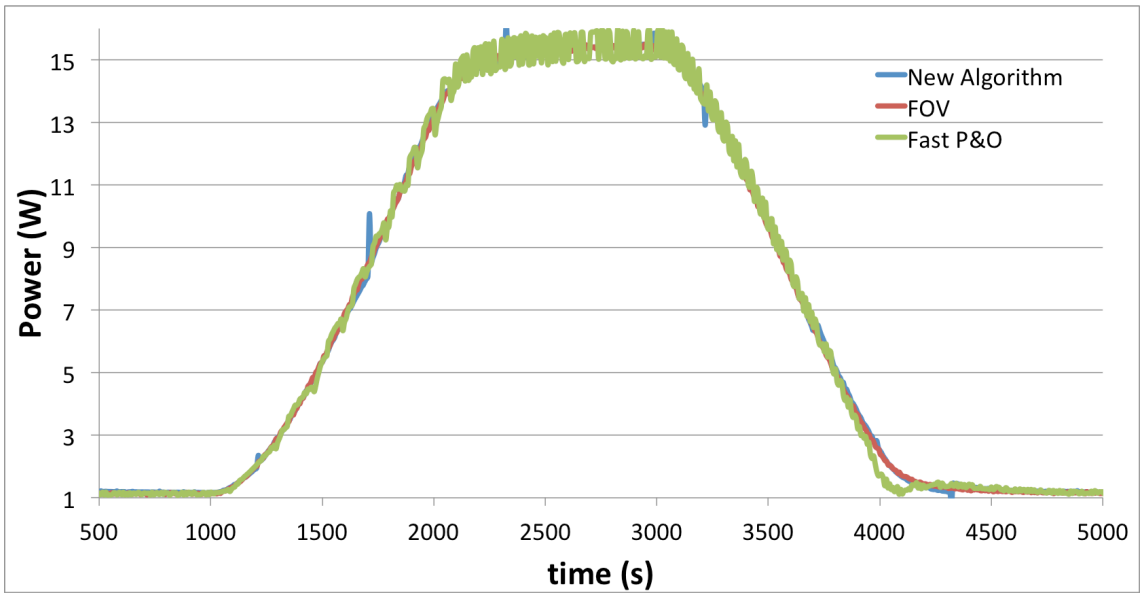

Figure 6–40 - Experimental results of the three algorithms when operated under the second ramp profile shown in Table 5-5

It can be observed in Figure 6–34 to Figure 6–41 the presence of power spikes (positive and negative) every 500 seconds. These spikes correspond to the transient response of the TEG to the change of operating point of the slow P&O performed by the proposed algorithm; and have been explained in Section 4.3.

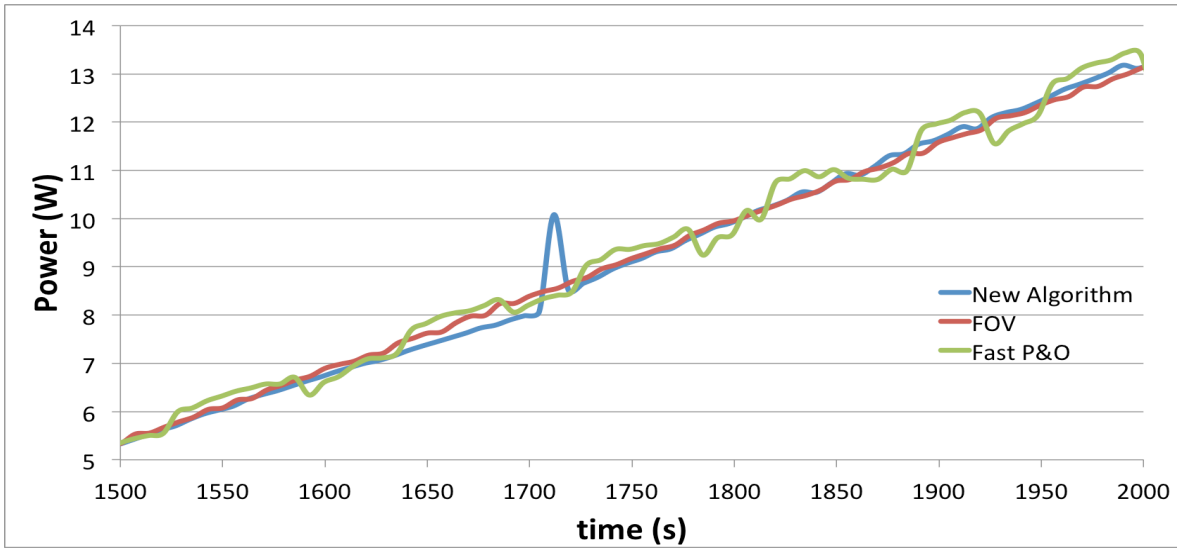

a)

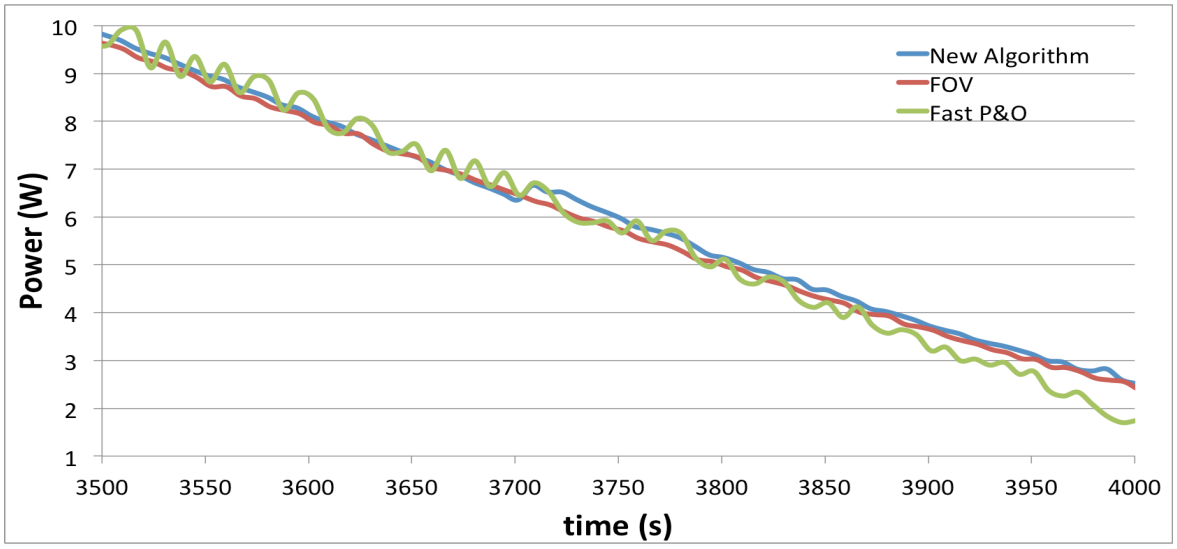

b)

Figure 6–41 - Zoomed-in view of a) the rising slope and b) falling slope of the profiles shown in Figure 6–40

6.5 Summary of experimental results

A summary of the steady-state results for constant input heat flux is presented in Table 6-7. The values for 100 W_{th}, 200 W_{th} and 300 W_{th} are obtained from the results shown in Figure 6–23 to Figure 6–33. The values for 75 W_{th}, 150 W_{th} and 250 W_{th} are obtained from the steady-state values reached during the plateaus of the step response test shown in Figure 6–34. Each experiment has run for a certain length of time, which is different from the others. For this reason, a direct comparison of the energy obtained with each algorithm cannot be established. Instead, a comparison can be established between all three algorithms for each

specific experiment. Table 6-7 shows the length of time over which the data for each algorithm has been obtained.

The new algorithm generates more power in all cases and it works with a value of beta higher than 0.5. The average values of beta at the MPP for different values of input heat flux, from 75 W_{th} to 300 W_{th}, are plotted in Figure 6–42. The average values of beta, in the same input heat flux range, are also plotted in Figure 6–42 for comparison. It can be observed that the MPPT algorithm in the experiments follows very accurately the operating points obtained during the simulation, which highlights the accuracy of the TEG model presented in Chapter 5. The data points at the MPP used to evaluate the accuracy of the MPPT algorithm, compared to the MPPT simulation and the actual MPP operating point obtained from the electrical characterization of the monTE™, which are in agreement with the data presented by Man [112], are shown in Table 6-8 and Table 6-9.

	Q_h = 75 W_{th}			Q_h = 100 W_{th}		
	Time = 3102 *s*			Time = 7000 *s*		
	New	"Fast" P&O	FOV	New	"Fast" P&O	FOV
E_{OUT} (J)	**3524.66**	3507.23	3453.09	**14064.12**	13770.38	13639.63
$V_{LOAD,AVG}$ (V)	**1.66**	1.51	1.48	**2.30**	2.06	1.99
$V_{OC,AVG}$ (V)	**2.97**	2.94	2.92	**4.07**	3.99	3.98
Beta Factor	**0.554**	0.513	0.506	**0.564**	0.517	0.496
	Q_h = 150 W_{th}			Q_h = 200 W_{th}		
	Time = 2996 *s*			Time = 3102 *s*		
	New	"Fast" P&O	FOV	New	"Fast" P&O	FOV
E_{OUT} (J)	**13286.73**	13255.59	13009.74	**37202.77**	36672.64	36333.78
$V_{LOAD,AVG}$ (V)	**3.68**	3.52	3.18	**5.04**	4.39	4.24
$V_{OC,AVG}$ (V)	**6.42**	6.37	6.27	**8.72**	8.53	8.48
Beta Factor	**0.573**	0.552	0.507	**0.577**	0.514	0.499
	Q_h = 250 W_{th}			Q_h = 300 W_{th}		
	Time = 2797 *s*			Time = 3102 *s*		
	New	"Fast" P&O	FOV	New	"Fast" P&O	FOV
E_{OUT} (J)	**29778.02**	29536.13	29252.16	**40200.5**	40054.40	39701.39
$V_{LOAD,AVG}$ (V)	**6.07**	5.64	5.36	**7.36**	6.77	6.29
$V_{OC,AVG}$ (V)	**10.81**	10.68	10.61	**12.80**	13.84	13.72
Beta Factor	**0.562**	0.528	0.505	**0.574**	0.534	0.500

Table 6-7- Summary of experimental results for different values of input heat flux

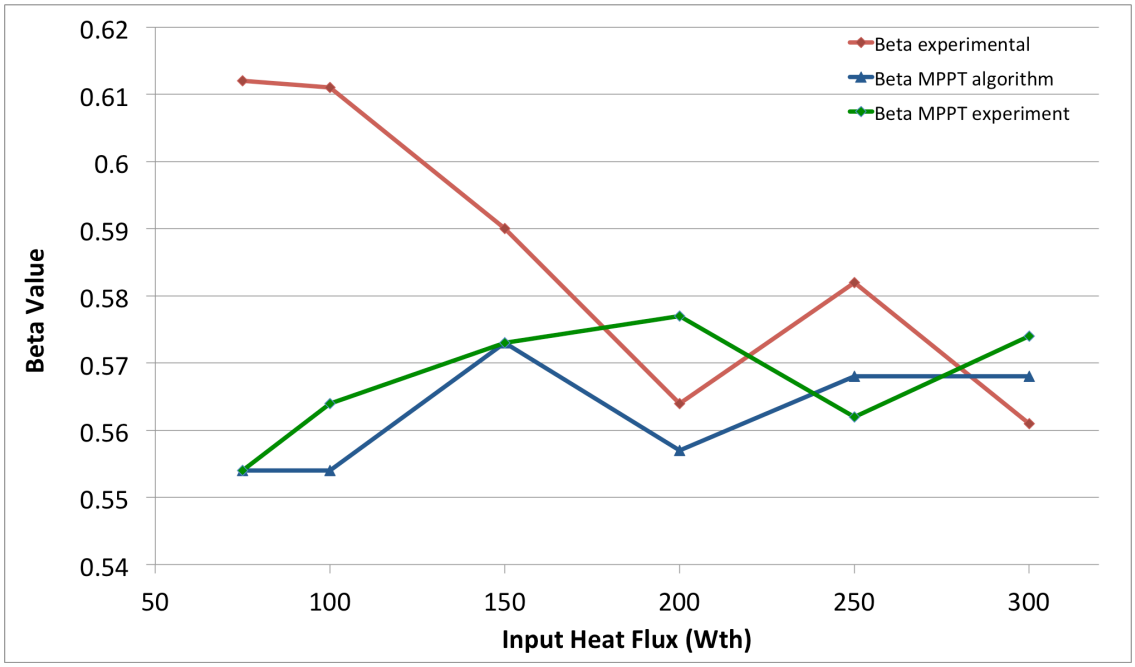

Figure 6–42- Values of beta factor at the MPP, using the new proposed algorithm, for different values of input heat flux (TEG characterization, MPPT simulation and MPPT experimental results)

Table 6-8 shows the error between the operating point set by the MPPT algorithm during steady-state operation compared against the operating point of the TEG at the true MPP, obtained from the electrical characterization of the monTE™. The variables are the TEG output voltage, the TEG open-circuit voltage and the value of the beta factor at the MPP. From the data presented in the table, as well as from the data plotted in Figure 6–42, it can be observed that the error is the highest at the lowest value of input heat flux.

	$Q_h = 75\ W_{th}$			$Q_h = 100\ W_{th}$		
	MPPT Exp.	TEG Charact.	Error	MPPT Exp.	TEG Charact.	Error
$V_{LOAD,AVG}$(V)	**1.66**	1.850	**10.27%**	**2.30**	2.540	**9.45%**
$V_{OC,AVG}$(V)	**2.97**	3.023	**1.75%**	**4.07**	4.157	**2.09%**
Beta Factor	**0.554**	0.612	**9.47%**	**0.564**	0.611	**7.69%**
	$Q_h = 150\ W_{th}$			$Q_h = 200\ W_{th}$		
	MPPT Exp.	TEG Charact.	Error	MPPT Exp.	TEG Charact.	Error
$V_{LOAD,AVG}$(V)	**3.68**	3.785	**2.77%**	**5.04**	4.880	**3.28%**
$V_{OC,AVG}$(V)	**6.42**	6.415	**0.08%**	**8.72**	8.652	**0.79%**
Beta Factor	**0.573**	0.590	**2.88%**	**0.577**	0.564	**2.30%**
	$Q_h = 250\ W_{th}$			$Q_h = 300\ W_{th}$		
	MPPT Exp.	TEG Charact.	Error	MPPT Exp.	TEG Charact.	Error
$V_{LOAD,AVG}$(V)	**6.07**	6.300	**3.65%**	**7.36**	7.125	**3.30%**
$V_{OC,AVG}$(V)	**10.81**	10.825	**0.14%**	**12.80**	12.701	**0.78%**
Beta Factor	**0.562**	0.582	**3.43%**	**0.574**	0.561	**2.32%**

Table 6-8 - Comparison between the operating point of the new algorithm at the MPP against the operating points of the monTE™ at the MPP obtained from the electrical characterization (Exp.: Experimental data, Charact.: Characterisation)

Table 6-9 shows the difference between the operating point set by the MPPT algorithm during steady-state operation compared against the simulation of the MPPT algorithm, obtained using the Matlab/Simulink model. The variables are the TEG output voltage, the TEG open-circuit voltage and the value of the beta factor at the MPP. From the data presented in the table, it can be observed that, even when the value of beta is the same, there is a difference (shift) in the values of the TEG output and open-circuit voltage. The reason could be a difference in the actual heat flux flowing through the TEG (ideal behaviour in the simulation versus real behaviour in the case of the electrical tests).

	Q_h = 75 W_{th}			Q_h = 100 W_{th}		
	MPPT Experiment	MPPT Simulation	Diff.	MPPT Experiment	MPPT Simulation	Diff.
$V_{LOAD,AVG}$ (V)	**1.66**	1.73	**4.04%**	**2.30**	2.31	**0.43%**
$V_{OC,AVG}$ (V)	**2.97**	3.12	**4.80%**	**4.07**	4.17	**2.40%**
Beta Factor	**0.554**	0.554	**0.00%**	**0.564**	0.554	**1.81%**
	Q_h = 150 W_{th}			Q_h = 200 W_{th}		
	MPPT Experiment	MPPT Simulation	Diff.	MPPT Experiment	MPPT Simulation	Diff.
$V_{LOAD,AVG}$ (V)	**3.68**	3.63	**1.38%**	**5.04**	4.68	**7.69%**
$V_{OC,AVG}$ (V)	**6.42**	6.33	**1.42%**	**8.72**	8.40	**3.81%**
Beta Factor	**0.573**	0.573	**0.00%**	**0.577**	0.557	**3.47%**
	Q_h = 250 W_{th}			Q_h = 300 W_{th}		
	MPPT Experiment	MPPT Simulation	Diff.	MPPT Experiment	MPPT Simulation	Diff.
$V_{LOAD,AVG}$ (V)	**6.07**	5.99	**1.34%**	**7.36**	7.18	**2.51%**
$V_{OC,AVG}$ (V)	**10.81**	10.54	**2.56%**	**12.80**	12.63	**1.35%**
Beta Factor	**0.562**	0.568	**1.06%**	**0.574**	0.568	**1.06%**

Table 6-9 - Comparison between the operating point of the new algorithm at the MPP against the operating point at the MPP of the simulation.

Table 6-10 and Figure 6–43 show the performance of the new algorithm compared to "fast" P&O and FOV. The performance is shown in terms of the percentage of extra energy that the new algorithm generates compared to the other two (third and fourth column). The maximum energy, obtained using the new algorithm, is presented in the second column. The power gains are calculated using Equation (5-12) and (5-13).

Input Heat Flux	New algorithm	"Fast" P&O	FOV
75 W_{th}	3524.66 J	0.50 %	2.07 %
100 W_{th}	14064.12 J	2.13 %	3.12 %
150 W_{th}	13286.73 J	0.23 %	2.13 %
200 W_{th}	37202.77 J	1.45 %	2.39 %
250 W_{th}	29778.02 J	0.82 %	1.80 %
300 W_{th}	40200.50 J	0.36 %	1.26 %

Table 6-10 - Performance of the new algorithm compared to "fast" P&O and FOV (simulation results)

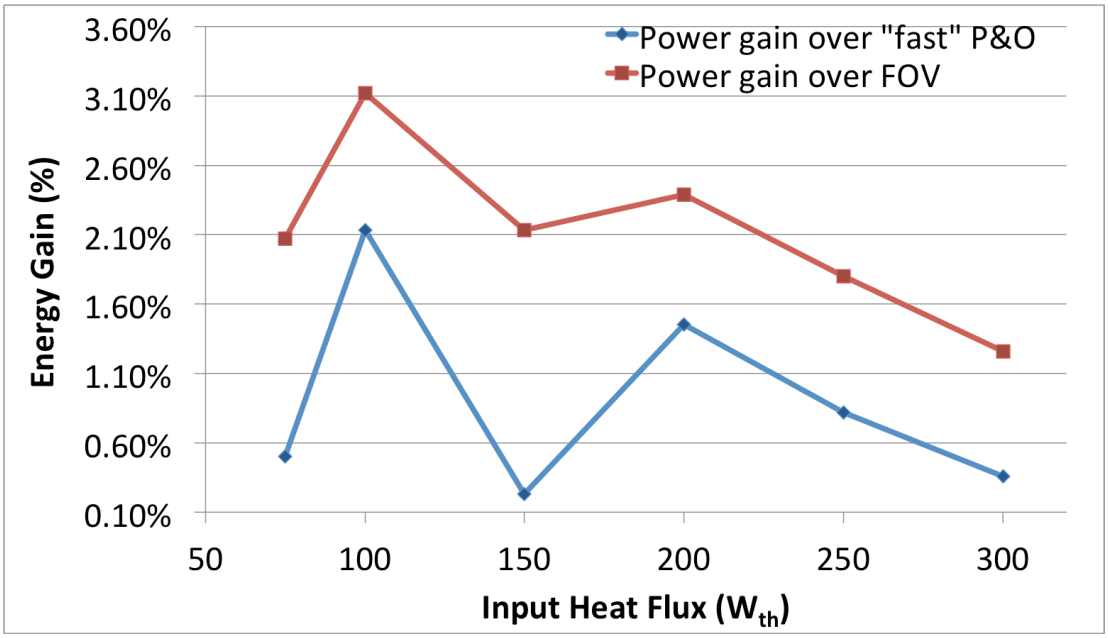

Figure 6–43 - Power gain of the new algorithm over "fast" P&O and FOV for different values of constant input heat flux (experimental results)

For the case of a step change in the input heat flux, Figure 6–35 shows that the performance of the new algorithm is as good as the performance of FOV, which provides the fastest response of all three algorithms. Indeed, the performance during step changes in the input heat flux is exactly the same as the performance observed in the simulation model (Figure 5–40), so the same observations and conclusions, drawn from the simulation results, apply to the experimental results. The new algorithm is capable of detecting the change in the input heat flux and react in a fast manner to the changes. The main limitation of the new algorithm is that it will only detect the transient at $t = 2\tau_{TEG}$ after the previous perturbation of the operating point, otherwise it could interpret a normal perturbation as a change in the input heat flux.

The experimental results obtained from the ramp changes in input heat flux are the same as those obtained with the simulation model. The results show that the for the case of the fastest ramp, 225 *mW/s*, the "fast" P&O algorithm is capable of producing more energy, during the rising ramp, than the other three algorithms. For the slowest ramp, 50 *mW/s*, the low MPPT frequency of the new algorithm has less effect on the MPP tracking capability hence producing more energy than the other two algorithms. For the 150 mW_{th}/s ramp, "fast" P&O generates more energy than the new algorithm but only during the rising ramp. In both cases where the "fast" P&O algorithm generates more energy than the new proposed one, the extra energy is less than 1 %. The energy generated by each algorithm during the ramps is shown in Table 6-11.

The percentage of extra energy generated by the new algorithm with respect to the "fast" P&O and FOV, is shown in Table 6-12. In this table, the positive values represent the extra energy produced by the new algorithm, whereas a negative value represents the loss of energy of the new algorithm, with respect to one of the other two. The results presented in Table 6-12 are visually presented in the graphs of Figure 6–44. These graphs represent the gain (positive percentages) and loss (negative percentages) plotted against the different ramp rates (mW_{th}/s). The trend shows that as the rate of change of input heat flux decreases, the new algorithm tends to increase the power generated. For an increasing ramp, "fast" P&O tracks better the MPP only with fast ramps. For a decreasing ramp, the new algorithm is capable of tracking better the MPP even at fast ramps.

	1st Ramp – 150 mW_{th}/s		
	New	"Fast" P&O	FOV
Rising ramp E_{OUT} (J)	4957.40	**4960.88**	4918.33
Falling ramp E_{OUT} (J)	**7089.40**	7004.45	6994.12
	2nd Ramp – 50 mW_{th}/s		
	New	"Fast" P&O	FOV
Rising ramp E_{OUT} (J)	**16811.67**	16667.37	16516.96
Falling ramp E_{OUT} (J)	**19294.24**	19103.44	18979.26
	3rd Ramp – 225 mW_{th}/s		
	New	"Fast" P&O	FOV
Rising ramp E_{OUT} (J)	6034.80	**6079.25**	5984.15
Falling ramp E_{OUT} (J)	**9627.11**	9626.78	9561.35

Table 6-11 - Energy generated by all three algorithms during increasing and decreasing ramp changes in input heat flux (simulation results)

	1st Ramp – 150 mW_{th}/s		
	New	"Fast" P&O	FOV
Rising ramp E_{OUT} (J)	4957.40	-0.07 %	0.79 %
Falling ramp E_{OUT} (J)	7089.40	1.21 %	1.36 %
	2nd Ramp – 50 mW_{th}/s		
	New	"Fast" P&O	FOV
Rising ramp E_{OUT} (J)	16811.67	0.87 %	1.78 %
Falling ramp E_{OUT} (J)	19294.24	1.00 %	1.66 %
	3rd Ramp – 225 mW_{th}/s		
	New	"Fast" P&O	FOV
Rising ramp E_{OUT} (J)	6034.80	-0.73 %	0.85 %
Falling ramp E_{OUT} (J)	9627.11	0.003 %	0.69 %

Table 6-12 - Percentages of energy gain generated by the new algorithm with respect to "fast" P&O and FOV (simulation results)

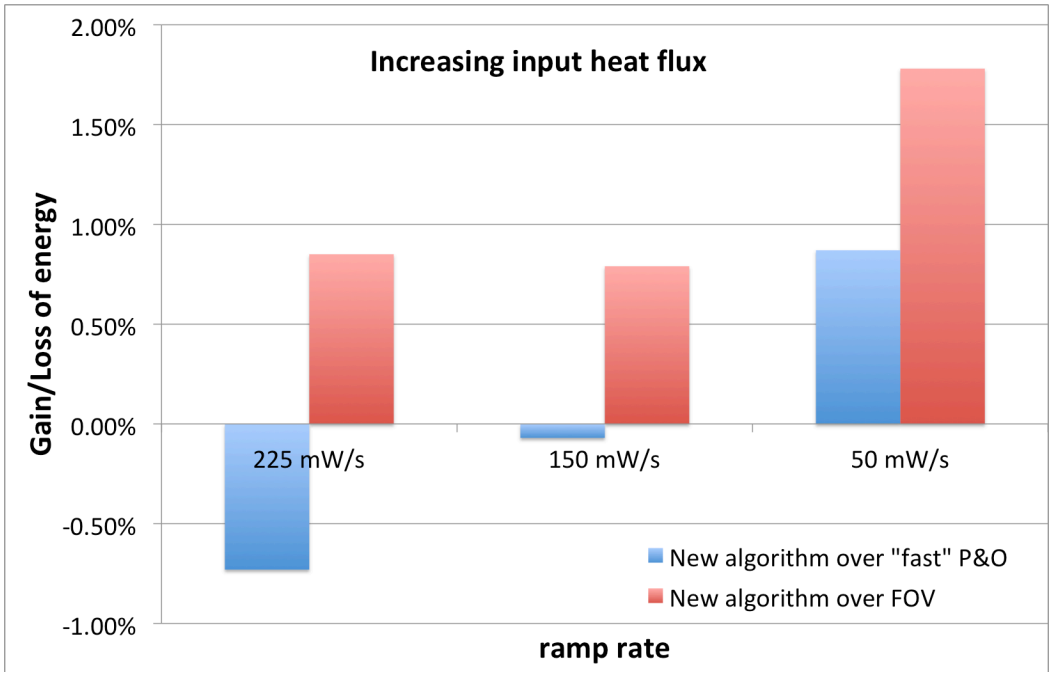

a)

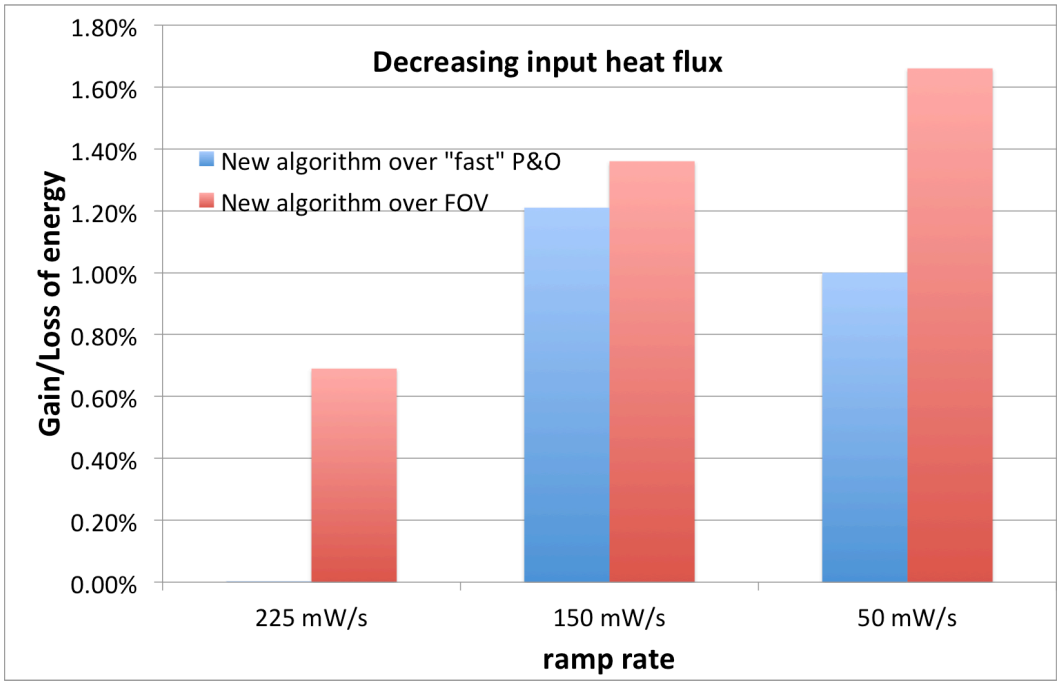

b)

Figure 6–44 - Gain/Loss of energy of the new algorithm with respect to "fast" P&O and FOV (MPPT experimental results) a) Rising ramp b) Falling ramp

6.6 Conclusions

The hardware implementation of the power converter used to operate the TEG at the MPP is presented in this section. The converter topology is a boost, or step-up converter, and the calculations of the different component values are shown in Section 6.2.3. The MPPT algorithm is embedded in a microcontroller PIC16F1788, the resources of which are described in Section 6.2.1. The additional circuitry used on the PCB is also described in this chapter.

An initial test of the MPPT algorithm has been performed in the lab bench, using a bench top power supply and a power resistor in series with it. Although it is not an accurate model of a TEG operated under constant heat flux, it is a valid circuit to test the performance of the MPPT algorithm. Results of the test of the MPPT algorithm are presented in Section 6.3 in the form of oscilloscope measurements.

Using a monTE™ and the test jig described in Section 4.2.3 the new MPPT algorithm has been tested and compared against the conventional P&O and FOV MPPT algorithms. The results are presented in this section, showing that the proposed algorithm generates more power under constant values of input heat flux. During step transients, the new algorithm responds as quickly as FOV and quicker than conventional P&O, whenever the step change in input heat flux occurs a time equal to $2\tau_{TEG}$ after the previous perturbation of the operating point.

The algorithms have also been tested against ramp changes in the input heat flux. From Table 6-12 and Figure 6–44 it can be observed that the new algorithm performs better than the other two with slow changes in input heat flux. As the rate of change of input heat flux increases, the conventional P&O algorithm performs better than the other two, although the proposed algorithm performs always better than FOV. It is important to note that the algorithm's performance gain is greatest at relatively low heat flux levels. This would suggest that the algorithm would be particularly well suited to energy harvesting applications where low thermal power levels are available for the TEG. This is something to be explored in the future for IoT-type sensors using thermoelectric devices.

The accuracy of the TEG system model presented in Chapter 5 has been also analyzed in this section, showing that the hardware experimental results are very close to the results obtained from the simulated model, see Table 6-9.

Chapter 7 Conclusions

This thesis presented the main differences between the operation under constant temperature gradient and constant heat flux. A new TEG model was presented; its operation verified and compared against experimental results, and integrated in an overall TEG system model comprising the TEG itself, the power converter and an MPPT algorithm. A new MPPT algorithm was proposed and showed to have superior performance to two state-of-the-art most used algorithms, P&O and FOV.

This thesis, therefore, provides novel ideas, modeling techniques and observations, supported by simulation and experimental results, to the field of thermoelectric power generation systems.

Chapter 2 provided a wide-ranging review of past literature and industrial research relevant to the main elements of this thesis. Five main areas were covered:

- Thermoelectric materials and the figure of merit.
- Thermoelectric applications: space, automotive, stove and low-power applications.
- Optimization of thermoelectric modules.
- Maximum power generation and maximum power point tracking techniques in TEG and PV applications.
- Thermoelectric generator models.

Chapter 3 summarised the important physical phenomena that collectively describe the electrical and thermal behaviour of the class of semiconductor materials, which have useful thermoelectric properties. These properties are broadly applicable to many different types of TEGs – *BiTe*, *SiGe*, oxides, skutterdites, and so on.

Chapter 4 presented the main difference between the operation under constant temperature gradient and constant heat flux, introducing the concepts of limited and unlimited heat flux. When operating under constant temperature gradient the influence of the Peltier

effect, considered as parasitic in power generation applications, limits the maximum efficiency of the TEG and the MPP does not correspond to the point of maximum TEG efficiency. However, in constant heat flux applications the MPP corresponds to the point of maximum TEG efficiency. The equivalent circuits under each operation, as well as the characteristic curves, obtained through theoretical calculations and experimental data, were presented. The TEG system, used to obtain the experimental characteristic curves, as well as to test the MPPT algorithms, was described in this chapter. The theoretical and experimental results showed that the MPP, under constant heat flux conditions, corresponds to an operation at a value of beta factor higher than 0.5. The theoretical calculations to find the MPP were also presented in this chapter, which led to the solution of a third order equation. Finally, this chapter presented a study on the transient response of the TEG to current steps, which is a consequence of the thermal time constant of the overall TEG system. It was shown that the transient response corresponds to transitions between constant ΔT characteristic curves and an experimental characterisation of the behaviour of the TEG, to current steps, for different values of input heat flux was presented.

Chapter 5 presented a new Matlab/Simulink model of the TEG system. The TEG was modeled based on the TEG equations presented in chapter 4 and the thermal time constant of the system. The result was a new model than does not require large computational resources to accurately mimic the behaviour of a real TEG. The methodology used to calculate the overall TEG thermal time constant, based on the temperature response after applying a current step, was presented. A boost converter was used to charge a battery with a nominal voltage of 28 V. The average model of the boost, also implemented in Matlab/Simulink, was used in the model, and it was built based on the equations obtained from the average model of the boost. A new MPPT algorithm was presented which is based on a combination between FOV and P&O. Traditional P&O algorithms found in the literature use MPPT sampling frequencies in the order of few seconds, or less, which are optimized for operation under constant temperature gradient, but not for operation under constant heat flux. On the other hand, the optimum value of beta that leads to operation at the true MPP is not fixed and changes with input heat flux and the type of TEG. The FOV algorithm, which sets the operating point to a fix value equal to 50 % of the instantaneous open-circuit voltage, will not operate the TEG at the true MPP. In the new algorithm, the P&O MPPT sampling frequency was adjusted to the thermal time constant of the system. A new adaptive step, based on the open-circuit voltage, was used in the proposed algorithm. The slowness introduced by an MPPT sampling frequency adjusted to the

thermal time constant of the system was compensated by a new mechanism for detecting changes in the input heat flux, which set the next operating point at 50 % of the instantaneous open-circuit voltage (FOV). The performance of the new algorithm was checked with different profiles of input heat flux and showed a superior performance over FOV and conventional P&O ("fast" P&O), with a better performance at lower values of input heat flux. For varying input heat flux profiles, like a ramp change, the proposed algorithm performed better with low variations of input heat flux. As the input heat flux changing-speed increased, the conventional P&O algorithm performed better. Also, the proposed algorithm performed better with continuously decreasing input heat flux than with continuously increasing profiles.

Chapter 6 showed the experimental results using a real TEG and a power converter. The calculations used to obtain the values of the component of the boost converter were presented and the different circuits used to gather telemetries, generate the auxiliary voltages to power the microcontroller and other components, drive the MOSFET and isolate the power converter to the battery were shown in this chapter. The performance of the algorithm and the boost converter was tested using a simulated TEG, which comprised a bench-top power supply and a resistor connected in series at the output. The response of the boost converter to changes in the operating point, dictated by the resonant peak in the $G_{vd}(s)$ transfer function, was well damped; and it was tested applying a step change in the duty-cycle between 50 % and 75 %. The experimental results showed a very good correlation with the simulated results. The value of beta at the MPP was found in the range between 0.55 – 0.57 for an input heat flux range between 75 – 300 W_{th}. The difference between the operating point at the MPP and the simulation model was between 0 – 3.47 % for the same input heat flux range. This difference increased to 0.08 – 9.47 % when the operating point at the MPP was compared against the experimental characterization of the monTE™; and the difference increased with decreasing input heat flux. The experimental results showed that the new algorithm responded as quick as it responded with FOV when the change in input heat flux occurred at a time $t = 2\tau_{TEG}$ after the previous MPPT perturbation. When the new algorithm was tested against ramp changes in the input heat flux; it was observed that the new algorithm performed better than the other two with slow changes in input heat flux. As the rate of change of input heat flux increased, the conventional P&O algorithm performed better than the other two, although the proposed algorithm performed always better than FOV.

The better performance of the proposed algorithm, over the other two most common state-of-the-art algorithms, is attributed to the *tracking speed* of the new algorithm, which was adjusted to be around 4 times the thermal time constant of the TEG. Conventional algorithms use a tracking speed in the order of few milliseconds to few seconds, which is between two or three orders of magnitude lower than the thermal time constant of the TEG system. In conventional algorithms, when the operating point is changed quickly after the previous perturbation (fast tracking speed) the algorithm sets the next operating point towards the MPP that corresponds to the power curve at that instantaneous value of temperature gradient. However, when the operating point of the TEG is changed, there is also a gradual change in the temperature gradient of the TEG, drifting the operating point of the TEG to another one with a different value of temperature gradient in steady-state conditions. For this reason, when the conventional algorithms changed the operating point at a faster rate than the thermal time constant of the system, they did not measure the power generated at steady state conditions and they were not able to calculate correctly the next operating point.

7.1 Future work

The algorithm presented in this work has been designed to prove the effect of the MPPT tracking speed on the performance of the algorithm, more specifically in its ability to operate at the true MPP when the TEG operates under a constant value of input heat flux. The response to fast, or step, changes in the input heat flux has not been optimized, and there are cases where the proposed algorithm does not perform better than P&O and FOV. This is the case when the step change occurs within a time equal to $2\tau_{TEG}$ after the previous MPPT perturbation, or for fast input heat flux ramps. Future work could focus on how to overcome these issues by anticipating the next operating point under these circumstances.

The analysis, simulations and experiments presented in this work have considered a fixed temperature on the cold side. This has been done to remove the influence of the Seebeck coefficient with the average temperature across the TEG. Future work could also study the performance of the proposed algorithm in a system where the cold side temperature is not controlled and set to a fixed value. This can be done performing the tests on a hot gas rig, or any similar system, without thermal control on the cold side of the TEG.

For small power applications, or applications with a small number of TEGs, the superiority of the proposed algorithm is translated into the gain of few hundred *milliwatts*, or less, depending on the level of input heat flux. However, in applications with a large number of TEGs the proposed algorithm could generate several tens of watts more than the current state of the art algorithms, and this is a considerable amount of power considering that the hardware required to implement all three algorithms is the same. For instance, a single 40*x*40 *mm BiTe* TEG operated at 100 W_{th}, the proposed algorithm will generate around 40 mW_{el} more than conventional P&O and around 60 mW_{el} more than FOV. An array of a hundred TEGs, taking only a surface of 400*x*400 *mm*, will generate 4 W_{el} more than conventional P&O and 6 W_{el} more than FOV, which is a considerable power gain over the other two algorithms.

The proposed algorithm can be used in energy harvesting applications because the power gain has shown to be higher at low values of input heat flux. In these applications, the number of TEGs, and therefore the amount of generated power, has to be traded-off against the power consumption of the proposed algorithm. The reason being that there might be instances were the power gain of the new algorithm might be comparable to the power consumption of the extra circuitry required to perform the calculations required to implement the new algorithm. In these cases, for instance, a simple FOV algorithm implemented with discrete analogue components could be a better solution. It is therefore important to look at the overall system efficiency.

Appendix A.

Table A-1 shows steady-state values of for different operating points, from open-circuit to short-circuit, of the TEG with an input heat flux of 100 W_{th}. Figure A-1 shows the characteristic curves of output power and ΔT, Figure A-2 shows the characteristic curves of output power and load voltage, and Figure A-3 shows the characteristic curve of output power and β; all for Q_h = 100 W_{th}.

Q_h = 100 W_{th}				
Power (W)	**V_{TEG} (V)**	**I_{TEG} (A)**	**V_{OC} (V)**	**β**
0.000	5.325	0.000	5.325	1.000
0.933	4.666	0.200	5.109	0.913
1.610	4.025	0.400	4.903	0.821
2.041	3.401	0.600	4.705	0.723
2.235	2.794	0.800	4.515	0.619
2.202	2.202	1.000	4.333	0.508
1.950	1.625	1.200	4.159	0.391
1.487	1.062	1.400	3.991	0.266
0.820	0.512	1.600	3.831	0.134

Table A-1 - Steady-state parameters for Q_h = 100 W_{th}

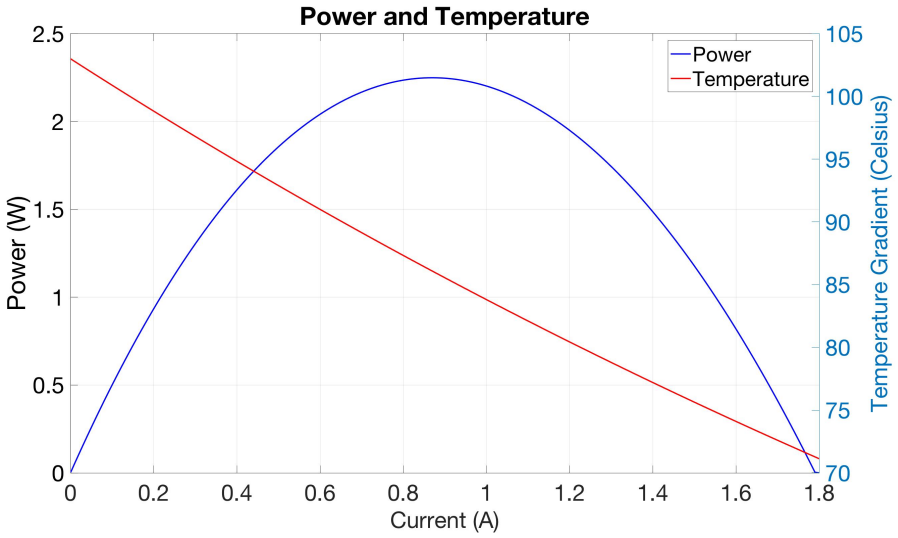

Figure A-1 - Power and ΔT against TEG current for Q_h = 100 W_{th}

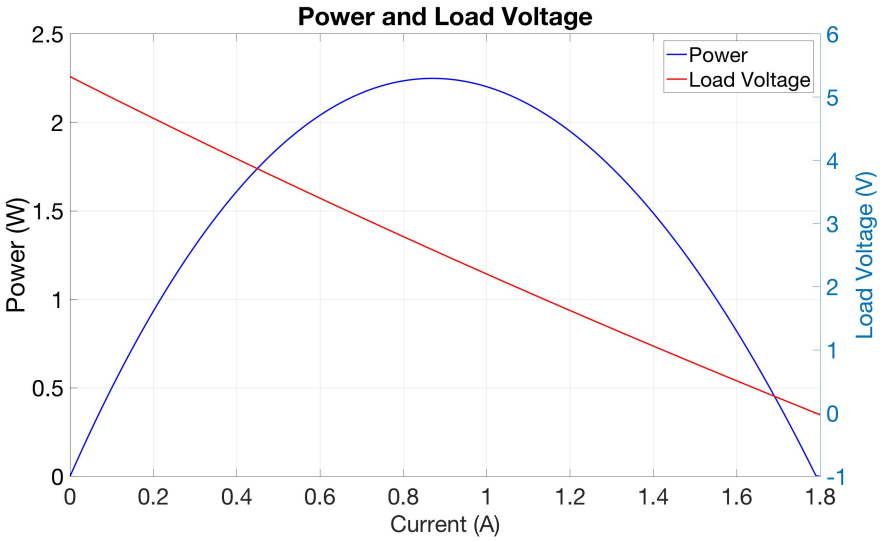

Figure A-2 - Power and load voltage against TEG current for Q_h = 100 W_{th}

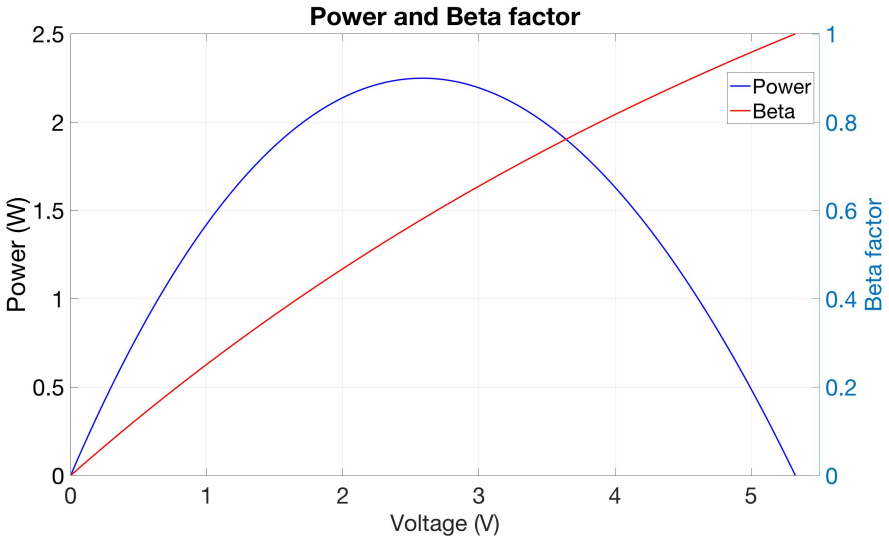

Figure A-3 - Power and beta factor against load voltage for Q_h = 100 W_{th}

Table A-2 shows steady-state values of for different operating points, from open-circuit to short-circuit, of the TEG with an input heat flux of 150 W_{th}. Figure A-4shows the characteristic curves of output power and ΔT, Figure A-5shows the characteristic curves of output power and load voltage, and Figure A-6 shows the characteristic curve of output power and β; all for Q_h = 150 W_{th}.

Q_h = 150 W_{th}				
Power (W)	**V_{TEG} (V)**	**I_{TEG} (A)**	**V_{OC} (V)**	**β**
0.000	7.988	0.000	7.988	1.000
2.065	6.884	0.300	7.626	0.903
3.493	5.822	0.600	7.287	0.799
4.320	4.800	0.900	6.969	0.689
4.577	3.814	1.200	6.671	0.572
4.294	2.863	1.500	6.391	0.448
3.498	1.943	1.800	6.128	0.317
2.212	1.053	2.100	5.882	0.179
0.459	0.191	2.400	5.651	0.034

Table A-2 - Steady-state parameters for Q_h = 150 W_{th}

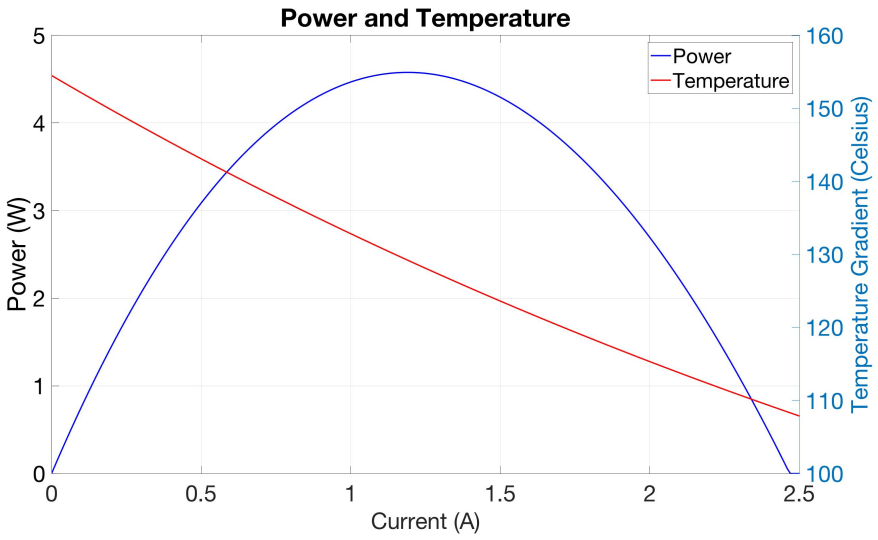

Figure A-4 - Power and ΔT against TEG current for Q_h = 150 W_{th}

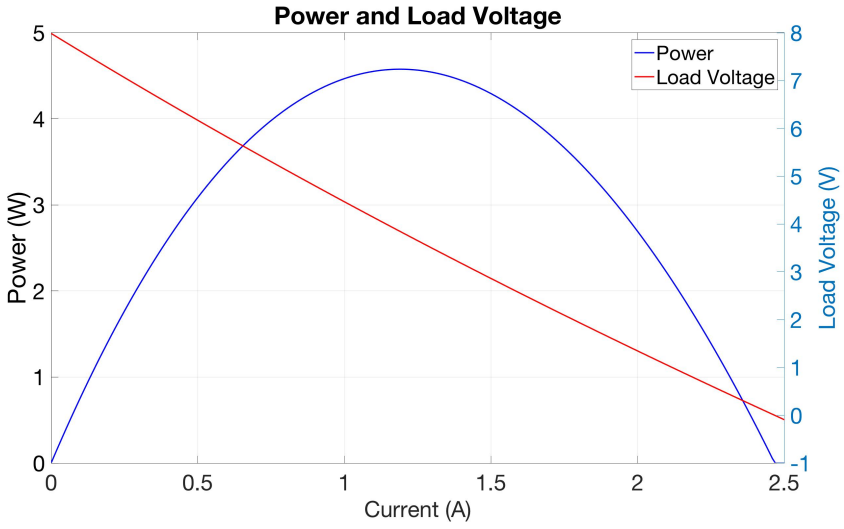

Figure A-5 - Power and load voltage against TEG current for Q_h = 150 W_{th}

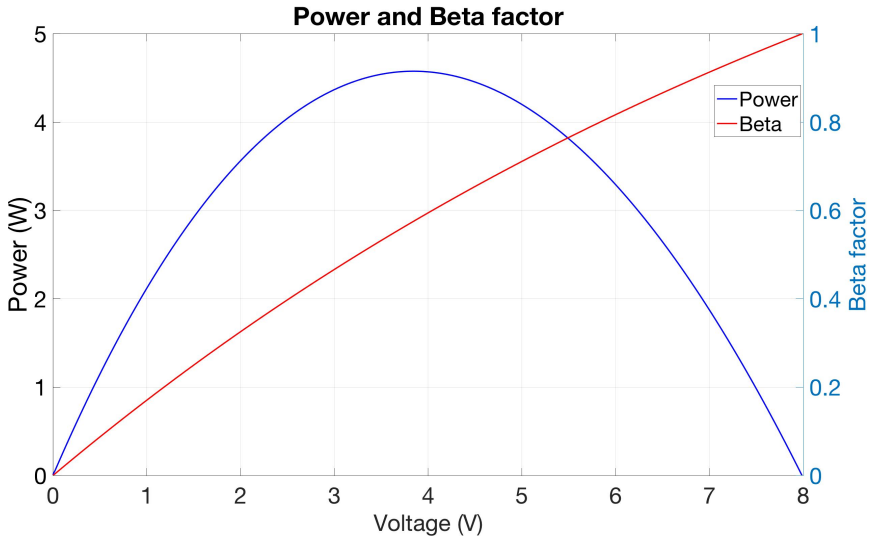

Figure A-6 - Power and beta factor against load voltage for Q_h = 150 W_{th}

Table A-3 shows steady-state values of for different operating points, from open-circuit to short-circuit, of the TEG with an input heat flux of 200 W_{th}. Figure A-7 shows the characteristic curves of output power and ΔT, Figure A-8 shows the characteristic curves of output power and load voltage, and Figure A-9 shows the characteristic curve of output power and β; all for Q_h = 200 W_{th}.

Q_h = 200 W_{th}				
Power (W)	**V_{TEG} (V)**	**I_{TEG} (A)**	**V_{OC} (V)**	**β**
0.000	10.650	0.000	10.650	1.000
2.830	9.433	0.300	10.248	0.921
4.956	8.260	0.600	9.870	0.837
6.416	7.129	0.900	9.515	0.749
7.243	6.036	1.200	9.182	0.657
7.470	4.980	1.500	8.870	0.561
7.124	3.958	1.800	8.577	0.461
6.231	2.967	2.100	8.302	0.357
4.814	2.006	2.400	8.045	0.249
2.895	1.072	2.700	7.803	0.137
0.493	0.164	3.000	7.578	0.022

Table A-3 - Steady-state parameters for Q_h = 200 W_{th}

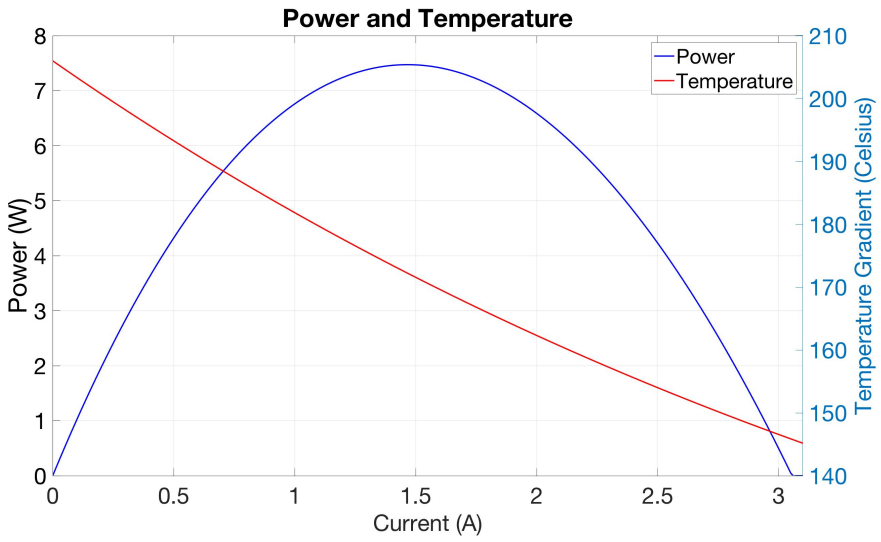

Figure A-7 - Power and ΔT against TEG current for Q_h = 200 W_{th}

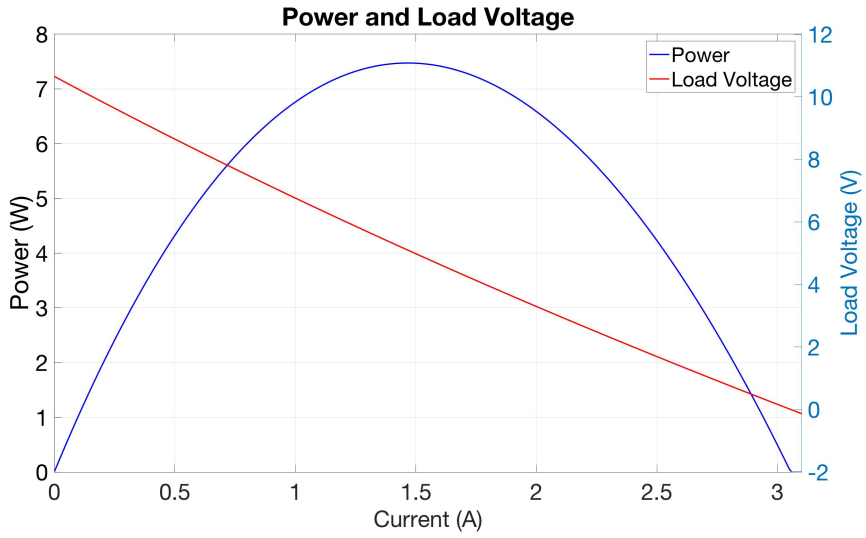

Figure A-8 - Power and load voltage against TEG current for Q_h = 200 W_{th}

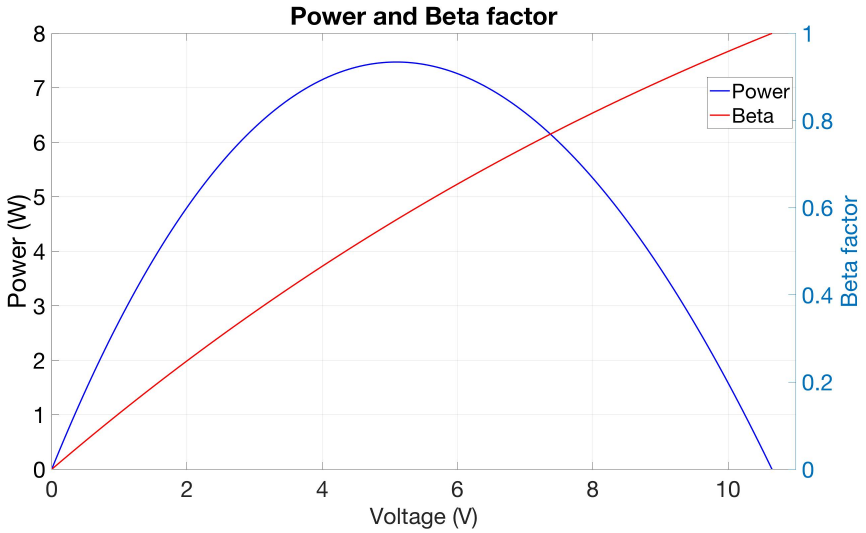

Figure A-9 - Power and beta factor against load voltage for Q_h = 200 W_{th}

Table A-4 shows steady-state values of for different operating points, from open-circuit to short-circuit, of the TEG with an input heat flux of 250 W_{th}. Figure A-10 shows the characteristic curves of output power and ΔT, Figure A-11 shows the characteristic curves of output power and load voltage, and Figure A-12 shows the characteristic curve of output power and β; all for Q_h = 250 W_{th}.

Q_h = 250 W_{th}				
Power (W)	**V_{TEG} (V)**	**I_{TEG} (A)**	**V_{OC} (V)**	**β**
0.000	13.313	0.000	13.313	1.000
4.625	11.561	0.400	12.727	0.908
7.912	9.890	0.800	12.188	0.811
9.950	8.291	1.200	11.693	0.709
10.817	6.761	1.600	11.237	0.602
10.583	5.292	2 000	10.819	0.489
9.311	3.879	2.400	10.435	0.372
7.054	2.519	2.800	10.083	0.250
3.860	1.206	3.200	9.761	0.124

Table A-4 - Steady-state parameters for Q_h = 250 W_{th}

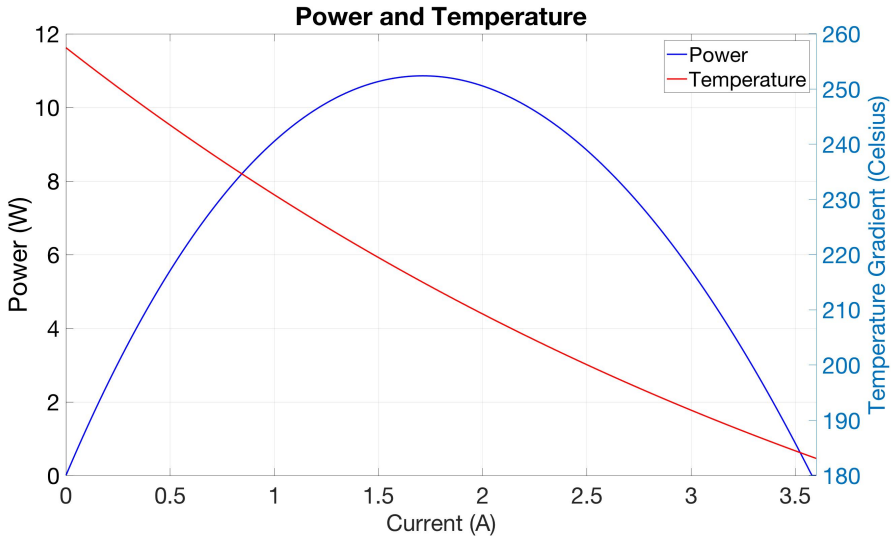

Figure A-10 - Power and ΔT against TEG current for Q_h = 250 W_{th}

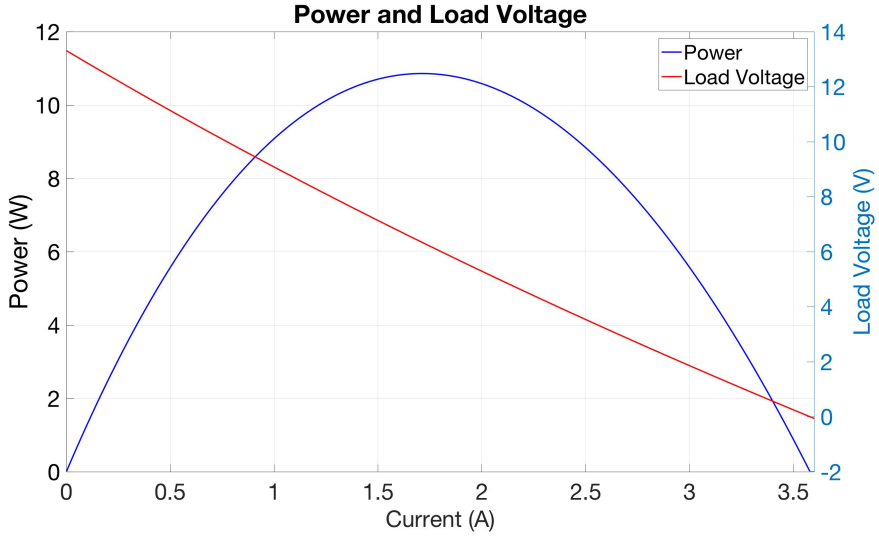

Figure A-11 - Power and load voltage against TEG current for Q_h = 250 W_{th}

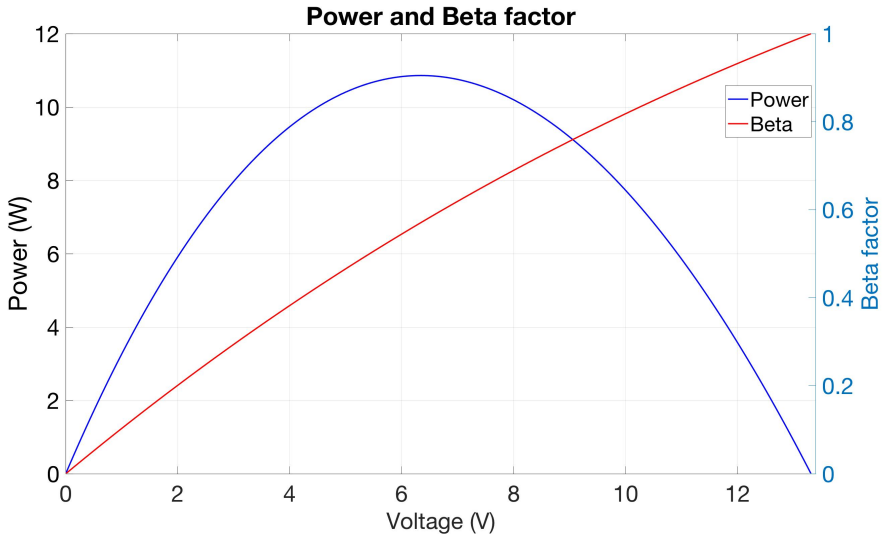

Figure A-12 - Power and beta factor against load voltage for Q_h = 250 W_{th}

Table A-5 shows steady-state values of for different operating points, from open-circuit to short-circuit, of the TEG with an input heat flux of 300 W_{th}. Figure A-13 shows the characteristic curves of output power and ΔT, Figure A-14 shows the characteristic curves of output power and load voltage, and Figure A-15 shows the characteristic curve of output power and β; all for Q_h = 300 W_{th}.

Q_h = 300 W_{th}				
Power (W)	**V_{TEG} (V)**	**I_{TEG} (A)**	**V_{OC} (V)**	**β**
0.000	15.975	0.000	15.975	1.000
6.821	13.641	0.500	15.183	0.898
11.431	11.431	1.000	14.468	0.790
14.002	9.335	1.500	13.823	0.675
14.680	7.340	2.000	13.243	0.554
13.596	5.43	2.500	12.721	0.427
10.858	3.619	3.000	12.253	0.295
6.563	1.875	3.500	11.834	0.158
0.791	0.198	4.000	11.461	0.017

Table A-5 - Steady-state parameters for Q_h = 300 W_{th}

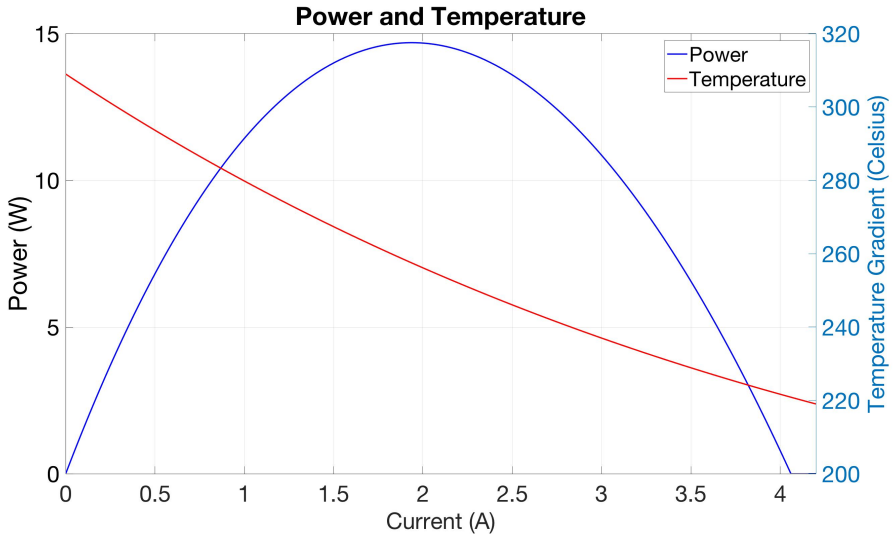

Figure A-13 - Power and ΔT against TEG current for $Q_h = 300\ W_{th}$

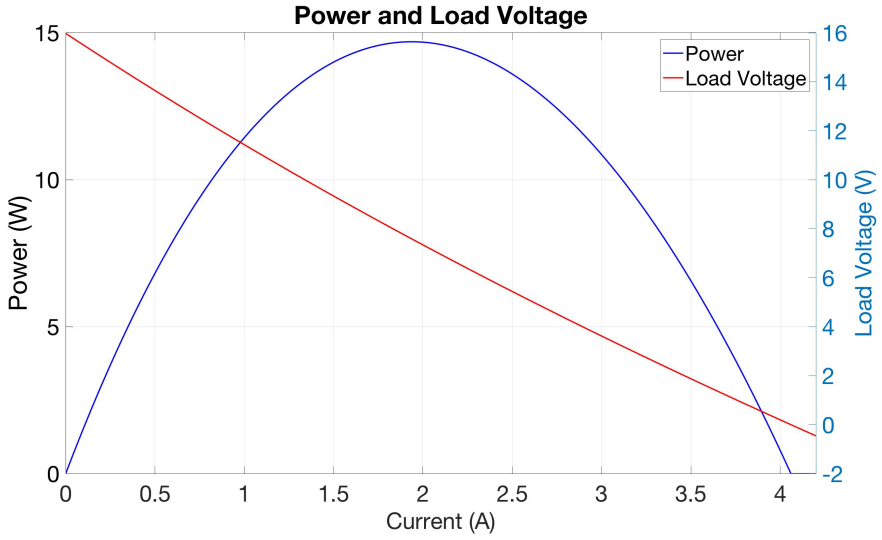

Figure A-14 - Power and load voltage against TEG current for $Q_h = 300\ W_{th}$

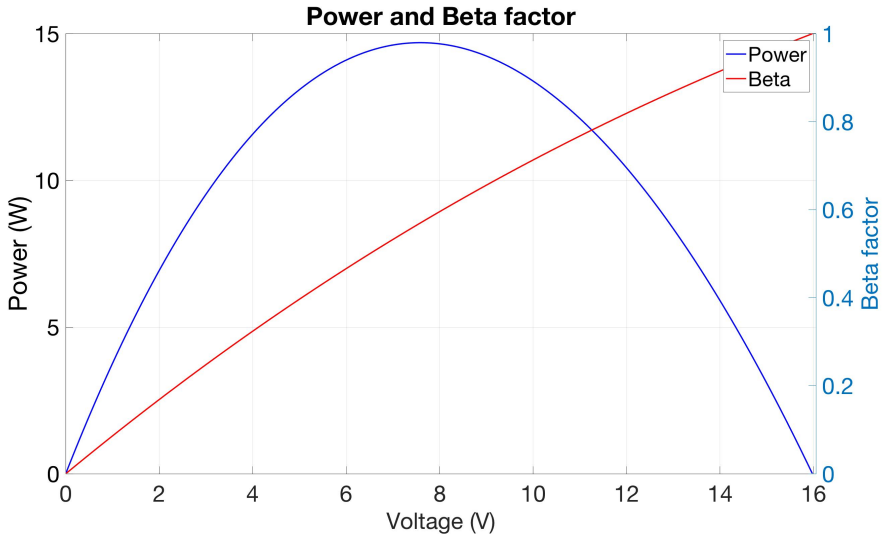

Figure A-15 - Power and beta factor against load voltage for $Q_h = 300\ W_{th}$

Appendix B.

Table B-1 shows the steady-state values of different TEG parameters at different operating points for an input heat power equal to 100 W_{th}. The operating points have been changed in steps of 200 *mA*, approximately. TEG power and ΔT curves are plotted against load current in Figure B-1. TEG power and load voltage curves, plotted against load current, are shown in Figure B-2. TEG power and beta factor have been plotted against load voltage in Figure B-3. All these curves have been obtained with the values in Table B-1.

T_H (°C)	T_C (°C)	ΔT (°C)	P_{HEATER} (W)	I_{LOAD} (A)	V_{TEG} (V)	$V_{PELLETS}$ (V)	Power (W)	V_{OC} (V)	β
130.379	23.659	106.720	104.087	0.001	5.050	0.079	0.006	4.956	1.019
125.868	23.580	102.288	103.901	0.204	4.394	0.075	0.897	4.738	0.927
121.763	23.517	98.246	103.760	0.404	3.775	0.072	1.525	4.538	0.832
117.857	23.476	94.381	103.602	0.604	3.174	0.069	1.919	4.348	0.730
114.197	23.553	90.644	103.474	0.807	2.583	0.066	2.085	4.166	0.620
110.700	23.574	87.126	103.361	1.008	2.016	0.063	2.033	3.996	0.505
107.395	23.605	83.790	103.227	1.208	1.464	0.061	1.769	3.834	0.382
104.249	23.630	80.619	103.113	1.407	0.926	0.058	1.303	3.681	0.252
100.911	23.657	77.254	102.973	1.629	0.338	0.056	0.550	3.519	0.096

Table B-1 - Steady-state values of the TEG parameters used to plot the characteristic curves at Q_h = 100 W_{th}

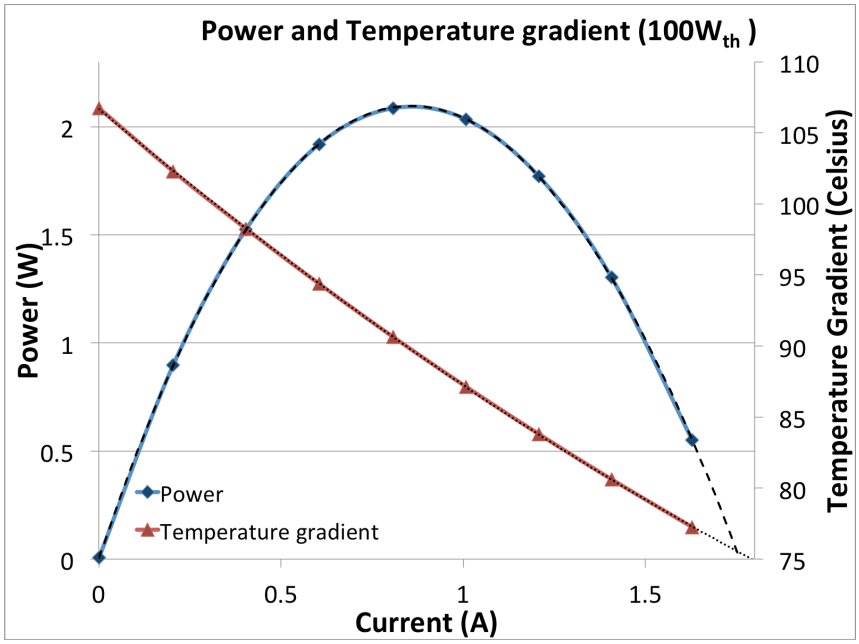

Figure B-1 - Power and temperature gradient against TEG current for Q_h = 100 W_{th}

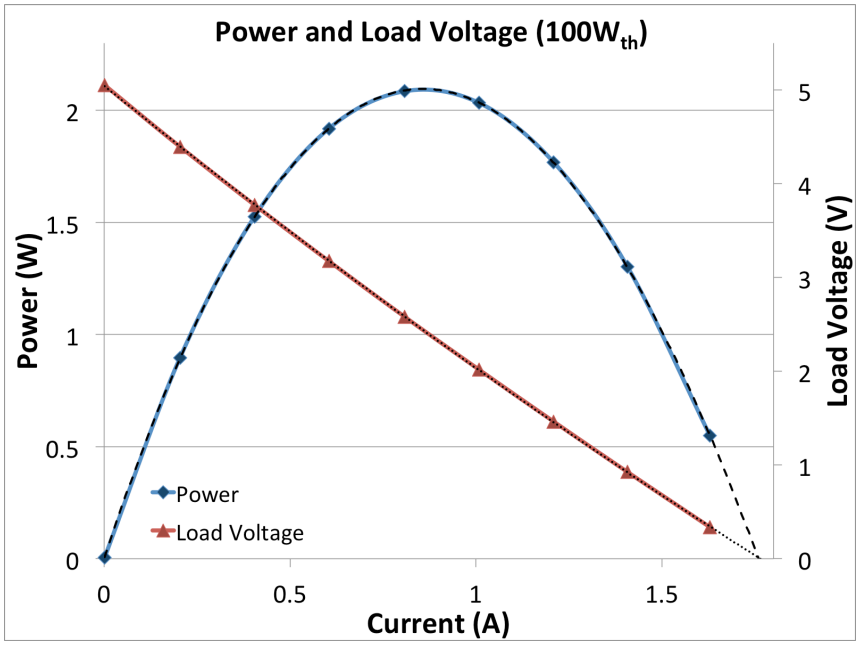

Figure B-2 - Power and output voltage against TEG current for Q_h = 100 W_{th}

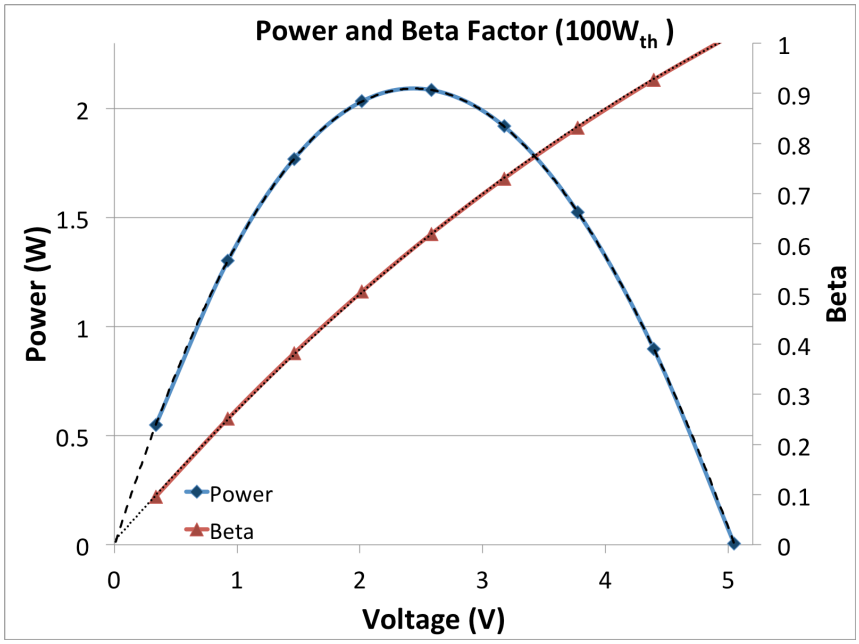

Figure B-3 - Power and beta factor against output voltage for Q_h = 100 W_{th}

Table B-2 shows the steady-state values of different TEG parameters at different operating points for an input heat power equal to 150 W_{th}. The operating points have been changed in steps of 300 mA, approximately. TEG power and ΔT curves are plotted against load current in Figure B-4. TEG power and load voltage curves, plotted against load current, are shown in Figure B-5. TEG power and beta factor have been plotted against load voltage in Figure B-6. All these curves have been obtained with the values in Table B-2.

T_H (°C)	T_C (°C)	ΔT (°C)	P_{HEATER} (W)	I_{LOAD} (A)	V_{TEG} (V)	$V_{PELLETS}$ (V)	Power (W)	V_{OC} (V)	β
190.008	26.656	163.352	156.687	0.000	7.942	0.123	0.002	7.780	1.021
182.333	26.415	155.918	156.331	0.303	6.815	0.117	2.067	7.398	0.921
175.339	26.371	148.968	155.945	0.603	5.755	0.112	3.473	7.048	0.817
168.820	26.265	142.555	155.693	0.903	4.743	0.107	4.285	6.723	0.706
162.581	26.155	136.426	155.431	1.204	3.766	0.102	4.535	6.412	0.587
156.466	26.046	130.420	155.155	1.508	2.811	0.097	4.238	6.105	0.460
151.171	25.997	125.174	154.928	1.808	1.910	0.093	3.452	5.833	0.327
146.405	26.208	120.197	154.724	2.107	1.042	0.089	2.195	5.595	0.186
143.595	26.657	116.938	154.644	2.306	0.457	0.086	1.053	5.432	0.084

Table B-2 - Steady-state values of the TEG parameters used to plot the characteristic curves at Q_h = 150 W_{th}

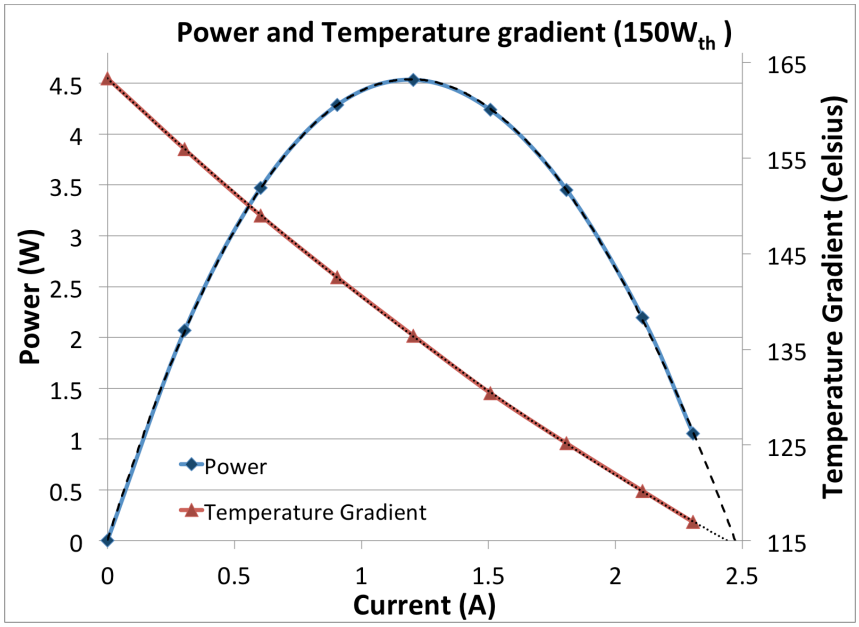

Figure B-4 - Power and temperature gradient against TEG current for Q_h = 150 W_{th}

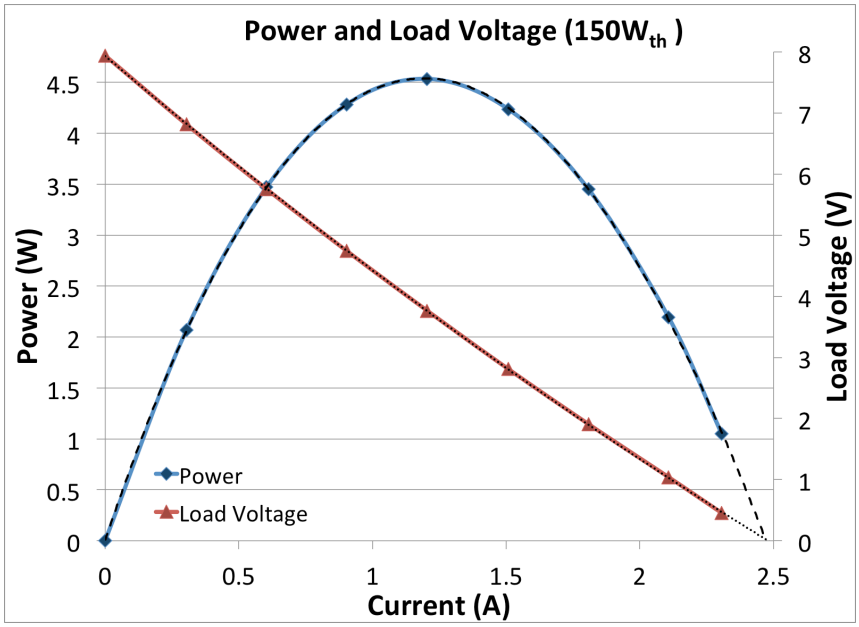

Figure B-5 - Power and output voltage against TEG current for Q_h = 150 W_{th}

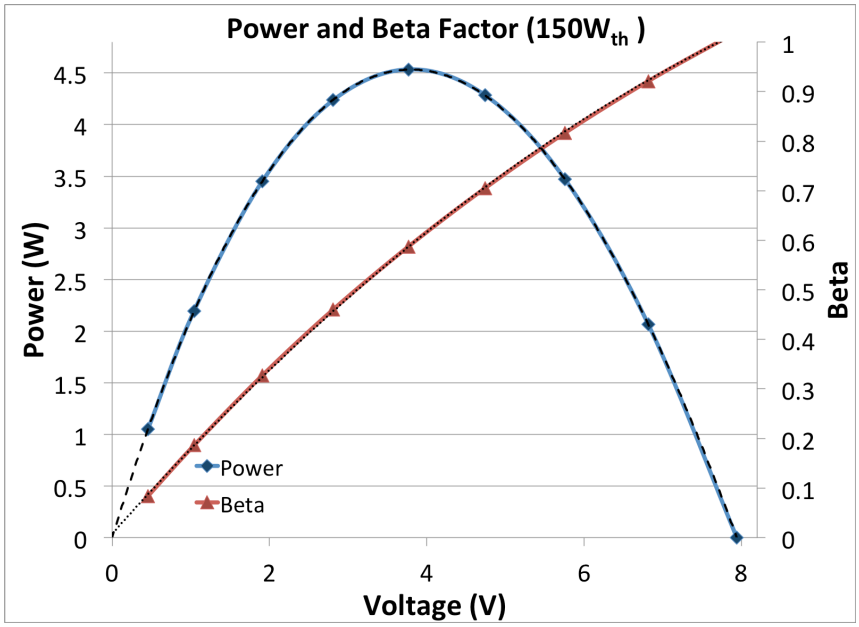

Figure B-6 - Power and beta factor against output voltage for Q_h = 150 W_{th}

Table B-3 shows the steady-state values of different TEG parameters at different operating points for an input heat power equal to 200 W_{th}. The operating points have been changed in steps of 400 mA, approximately. TEG power and ΔT curves are plotted against load current in Figure B-7. TEG power and load voltage curves, plotted against load current, are shown in Figure B-8. TEG power and beta factor have been plotted against load voltage in Figure B-9. All these curves have been obtained with the values in Table B-3.

T_H (°C)	T_C (°C)	ΔT (°C)	P_{HEATER} (W)	I_{LOAD} (A)	V_{TEG} (V)	$V_{PELLETS}$ (V)	Power (W)	V_{OC} (V)	β
246.488	29.656	216.832	209.505	0.000	10.686	0.165	0.004	10.408	1.027
236.031	29.475	206.556	208.963	0.404	9.074	0.157	3.667	9.909	0.916
226.484	29.314	197.170	208.460	0.804	7.560	0.150	6.078	9.446	0.800
217.586	29.240	188.346	208.017	1.204	6.112	0.143	7.357	9.010	0.678
209.504	29.196	180.308	207.618	1.604	4.735	0.137	7.593	8.608	0.550
202.218	29.463	172.755	207.263	2.004	3.412	0.131	6.837	8.232	0.415
195.557	29.809	165.748	206.949	2.406	2.127	0.125	5.117	7.883	0.270
189.185	31.518	157.667	206.689	2.907	0.544	0.119	1.582	7.486	0.073

Table B-3 - Steady-state values of the TEG parameters used to plot the characteristic curves at Q_h = 200 W_{th}

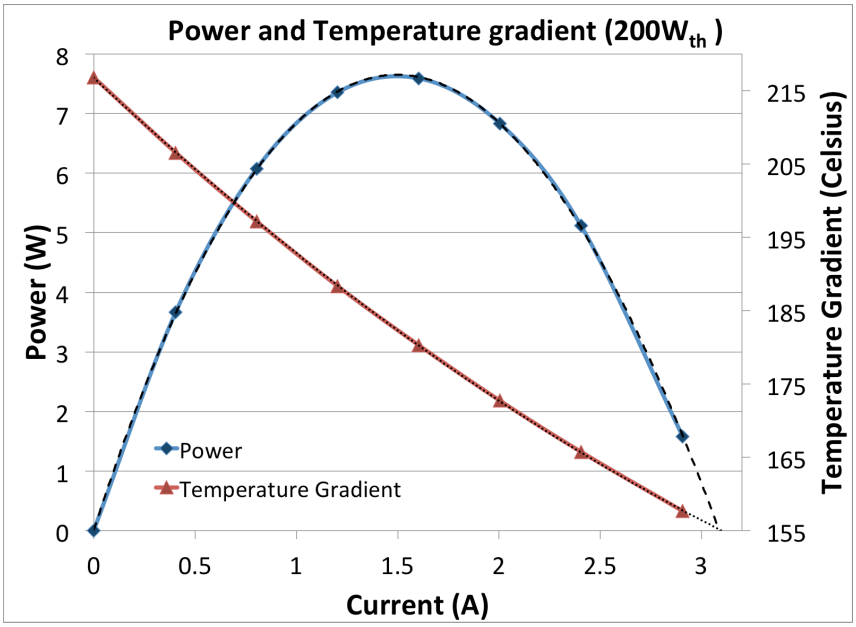

Figure B-7 - Power and temperature gradient against TEG current for Q_h = 200 W_{th}

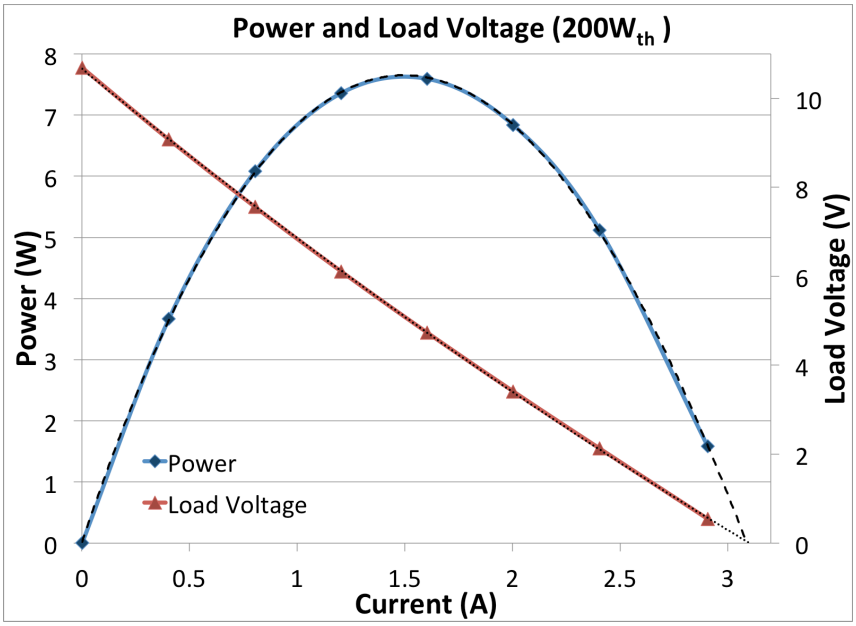

Figure B-8 - Power and output voltage against TEG current for Q_h = 200 W_{th}

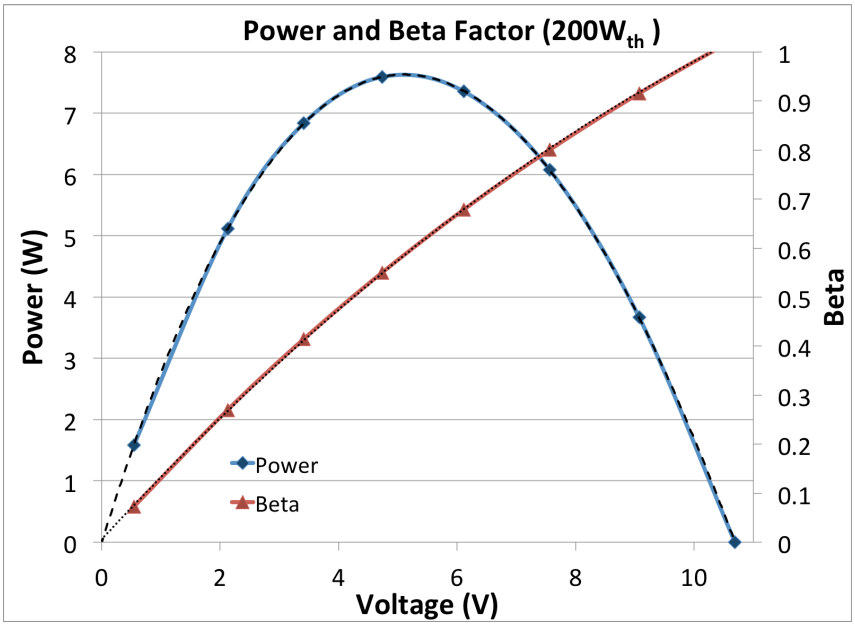

Figure B-9 - Power and beta factor against output voltage for Q_h = 200 W_{th}

Table B-4 shows the steady-state values of different TEG parameters at different operating points for an input heat power equal to 250 W_{th}. The operating points have been changed in steps of 400 mA, approximately. TEG power and ΔT curves are plotted against load current in Figure B-10. TEG power and load voltage curves, plotted against load current, are shown in Figure B-11. TEG power and beta factor have been plotted against load voltage in Figure B-12. All these curves have been obtained with the values in Table B-4.

T_H (°C)	T_C (°C)	ΔT (°C)	P_{HEATER} (W)	I_{LOAD} (A)	V_{TEG} (V)	$V_{PELLETS}$ (V)	Power (W)	V_{OC} (V)	β
296.439	32.744	263.695	262.325	-0.002	12.929	0.199	-0.019	12.527	1.032
287.520	32.495	255.025	261.851	0.403	11.349	0.193	4.572	12.164	0.933
278.255	32.266	245.989	261.264	0.804	9.786	0.187	7.863	11.764	0.832
269.444	32.145	237.299	260.788	1.204	8.264	0.180	9.946	11.368	0.727
261.263	32.102	229.161	260.367	1.603	6.796	0.174	10.896	10.987	0.619
253.636	32.194	221.442	259.987	2.005	5.375	0.169	10.776	10.622	0.506
246.618	32.312	214.306	259.608	2.404	3.999	0.163	9.613	10.278	0.389
240.133	32.480	207.653	259.243	2.807	2.657	0.158	7.458	9.955	0.267
234.146	32.530	201.616	258.947	3.207	1.366	0.153	4.381	9.658	0.141
231.000	32.634	198.366	258.797	3.429	0.636	0.151	2.181	9.498	0.067

Table B-4 - Steady-state values of the TEG parameters used to plot the characteristic curves at Q_h = 250 W_{th}

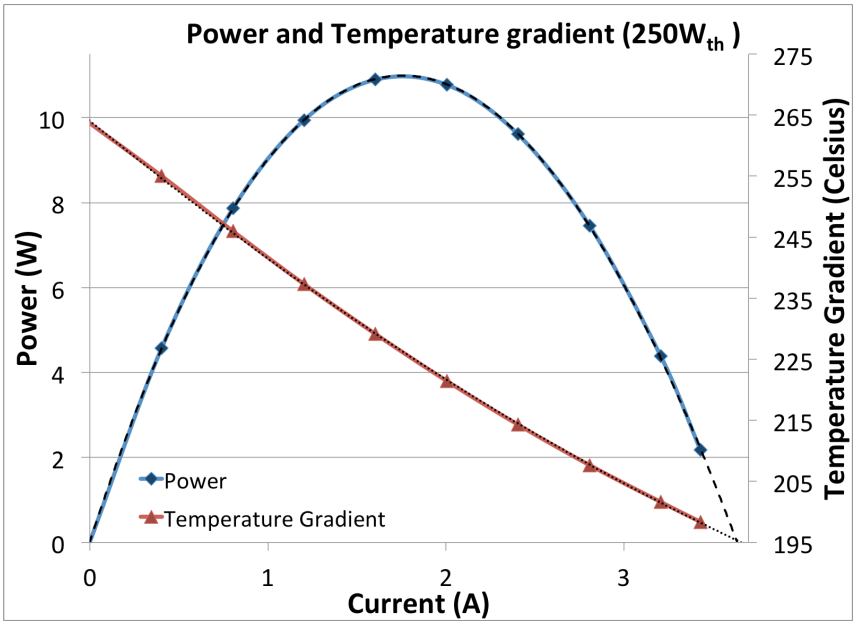

Figure B-10 - Power and temperature gradient against TEG current for Q_h = 250 W_{th}

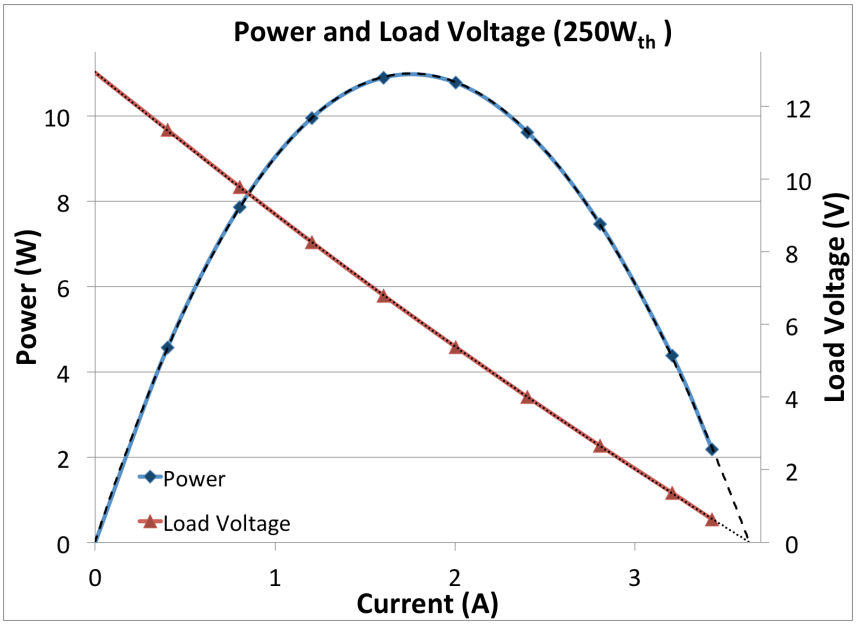

Figure B-11 - Power and output voltage against TEG current for Q_h = 250 W_{th}

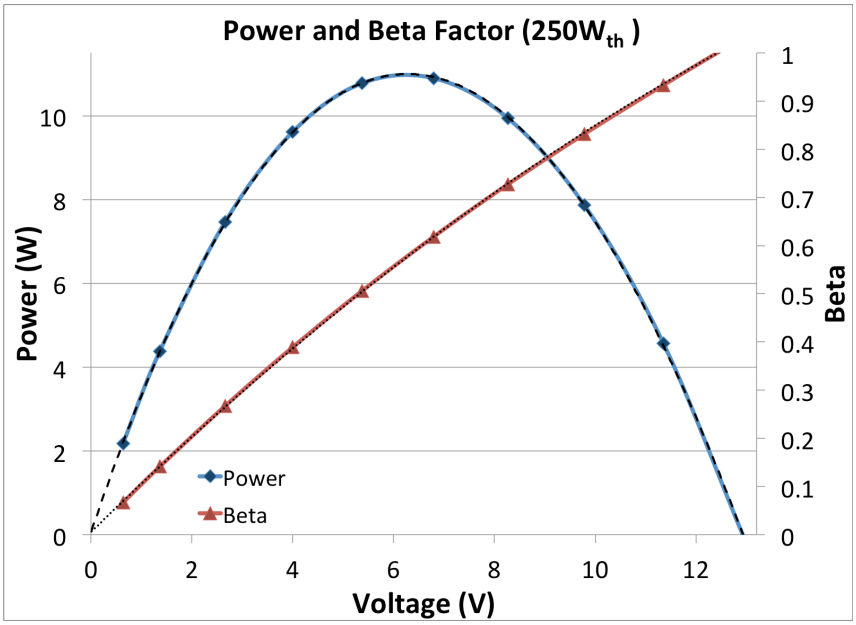

Figure B-12 - Power and beta factor against output voltage for Q_h = 250 W_{th}

Table B-5 shows the steady-state values of different TEG parameters at different operating points for an input heat power equal to 300 W_{th}. The operating points have been changed in steps of 500 mA, approximately. TEG power and ΔT curves are plotted against load current in Figure B-13. TEG power and load voltage curves, plotted against load current, are shown in Figure B-14. TEG power and beta factor have been plotted against load voltage in Figure B-15. All these curves have been obtained with the values in Table B-5.

T_H (°C)	T_C (°C)	ΔT (°C)	P_{HEATER} (W)	I_{LOAD} (A)	V_{TEG} (V)	$V_{PELLETS}$ (V)	Power (W)	V_{OC} (V)	β
345.131	36.325	308.806	315.342	-0.001	14.883	0.228	-0.021	14.380	1.035
333.151	35.650	297.501	314.634	0.503	12.841	0.222	6.463	13.963	0.920
321.780	35.209	286.571	313.868	1.003	10.852	0.215	10.887	13.529	0.802
311.482	35.224	276.258	313.287	1.504	8.920	0.208	13.411	13.100	0.681
301.785	35.255	266.530	312.684	2.004	7.051	0.201	14.132	12.686	0.556
292.918	35.238	257.680	312.192	2.504	5.249	0.195	13.146	12.294	0.427
284.943	35.410	249.533	311.687	3.005	3.500	0.189	10.517	11.928	0.293
277.773	35.700	242.073	311.322	3.507	1.791	0.184	6.281	11.586	0.155
273.697	35.872	237.825	311.105	3.810	0.739	0.181	2.815	11.390	0.065

Table B-5 - Steady-state values of the TEG parameters used to plot the characteristic curves at Q_h = 300 W_{th}

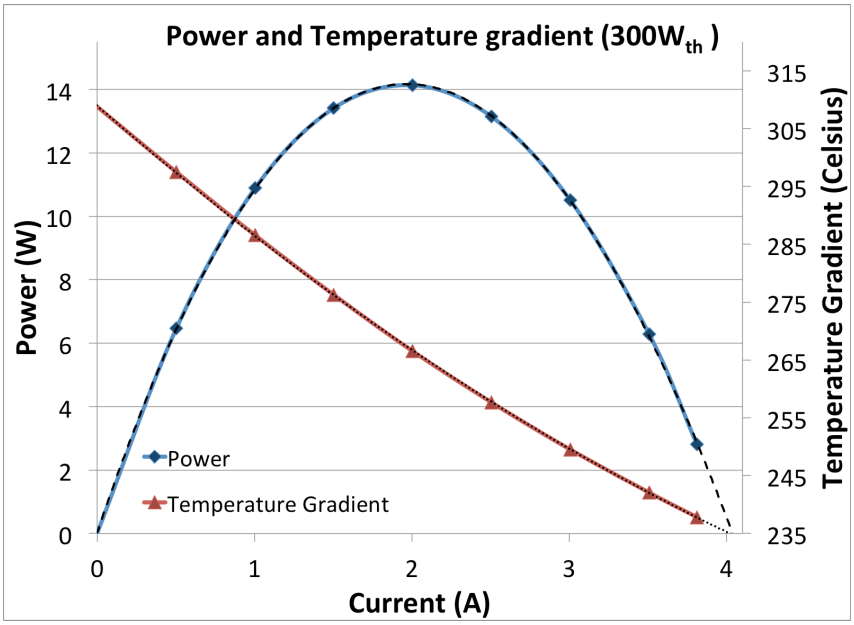

Figure B-13 - Power and temperature gradient against TEG current for Q_h = 300 W_{th}

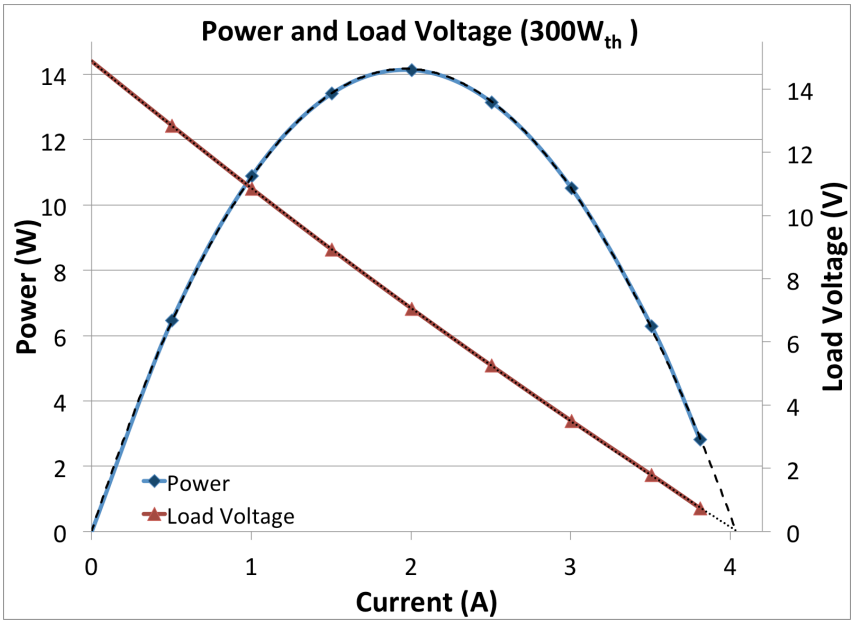

Figure B-14 - Power and output voltage against TEG current for Q_h = 300 W_{th}

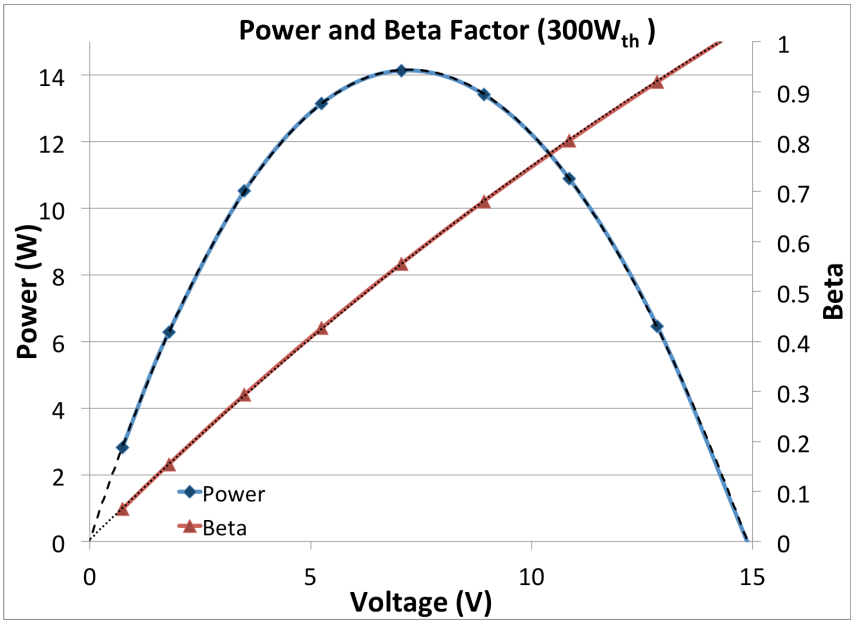

Figure B-15 - Power and beta factor against output voltage for Q_h = 300 W_{th}

Appendix C.

Figure C-1 to Figure C-4 show the transient behaviour of the TEG when the input power is 100 W_{th} and the load current is changed with steps of 200 mA. In Figure C-1 and Figure C-2the current is stepped from zero to the short-circuit current, whereas in Figure C-3 and Figure C-4 the current is stepped from the short-circuit current down to zero.

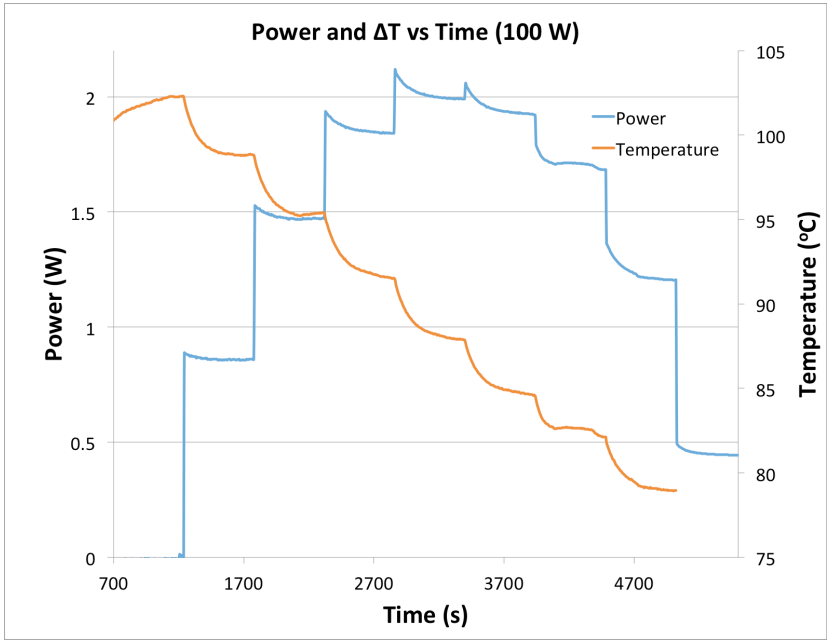

Figure C-1 - Transient behaviour of the output power and ΔT for increasing steps of output current with 100 W_{th} input heat flux

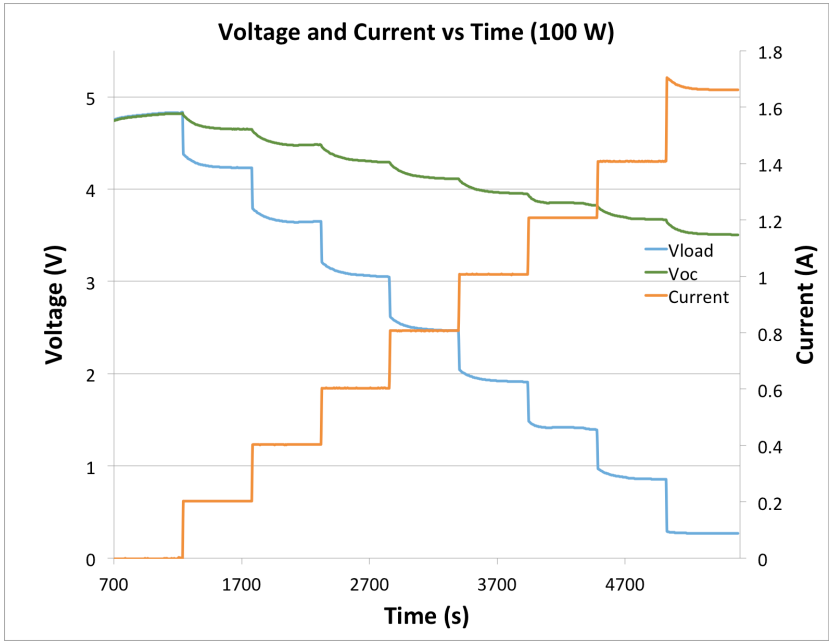

Figure C-2 - Transient behaviour of the load and open-circuit voltages and load current increasing steps of output current with 100 W_{th} input heat flux

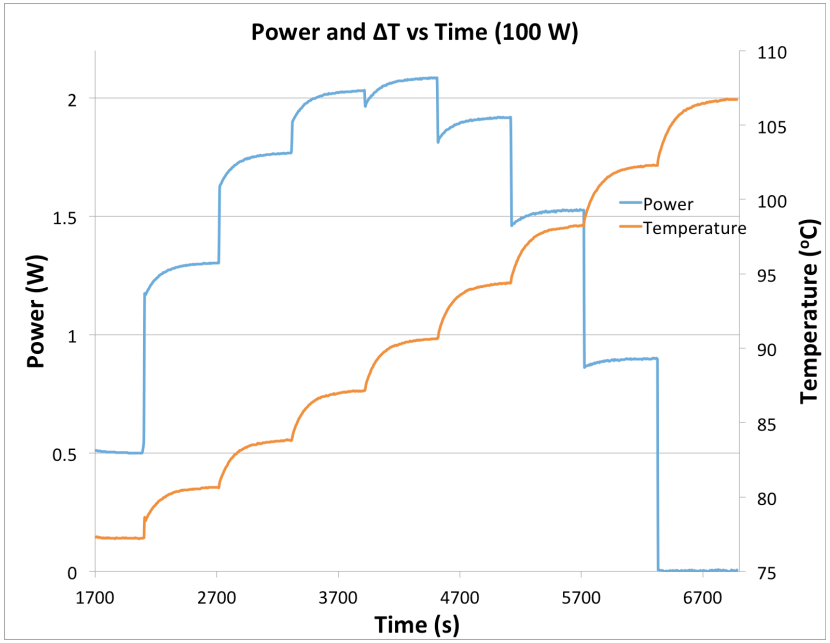

Figure C-3 - Transient behaviour of the output power and ΔT for decreasing steps of output current with 100 W_{th} input heat flux

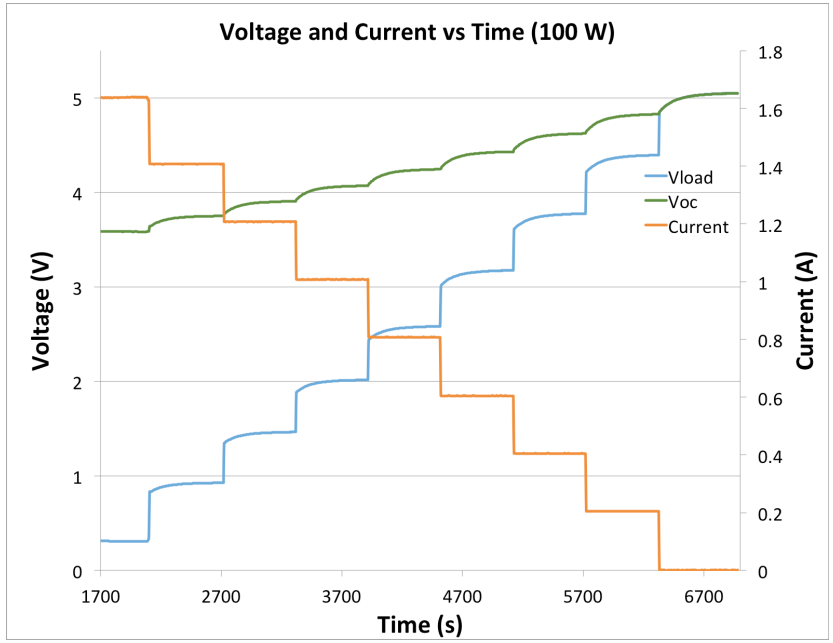

Figure C-4 - Transient behaviour of the load and open-circuit voltages and load current decreasing steps of output current with 100 W_{th} input heat flux

Figure C-5 to Figure C-8 show the transient behaviour of the TEG when the input power is 150 W_{th} and the load current is changed with steps of 300 *mA*. In Figure C-5 and Figure C-6 the current is stepped from zero to the short-circuit current, whereas in Figure C-7 and Figure C-8 the current is stepped from the short-circuit current down to zero.

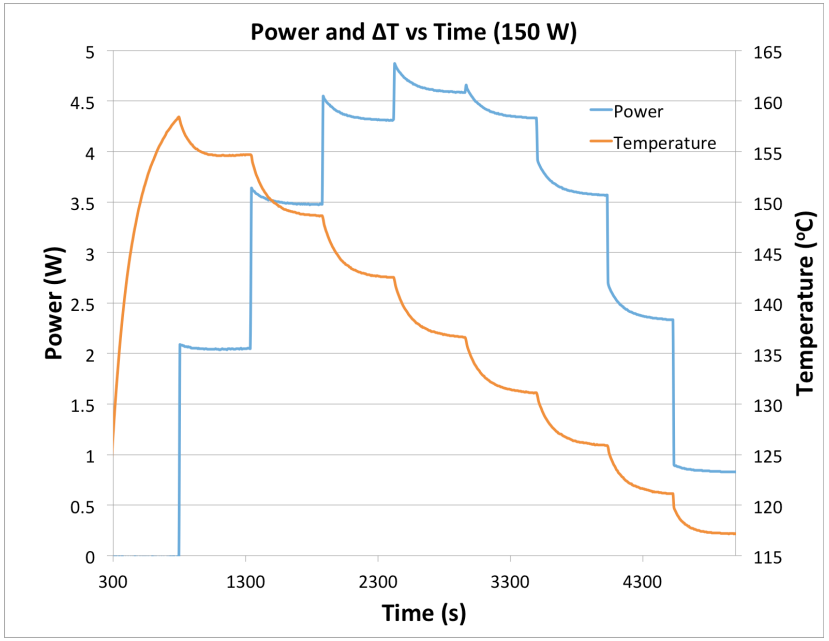

Figure C-5 - Transient behaviour of the output power and ΔT for increasing steps of output current with 150 W_{th} input heat flux

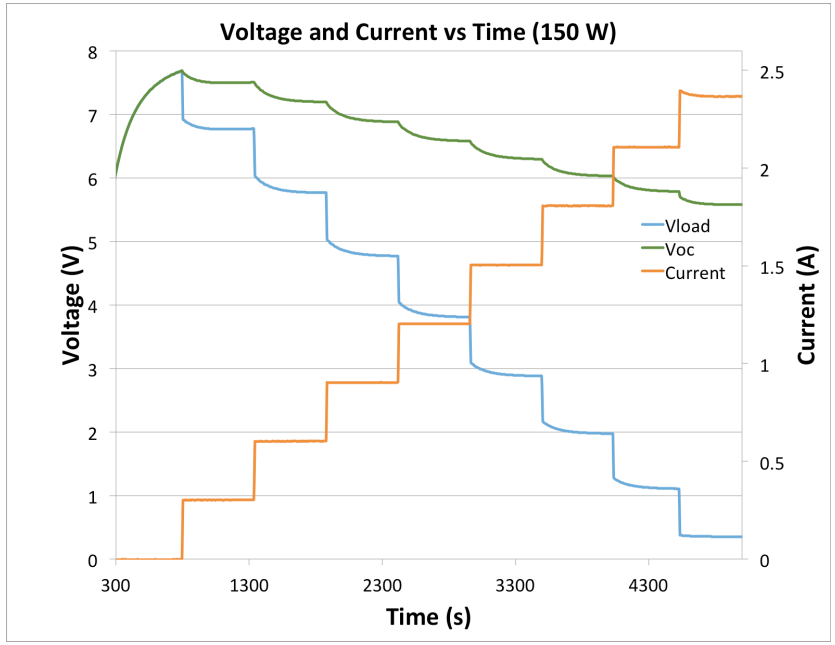

Figure C-6 - Transient behaviour of the load and open-circuit voltages and load current increasing steps of output current with 150 W_{th} input heat flux

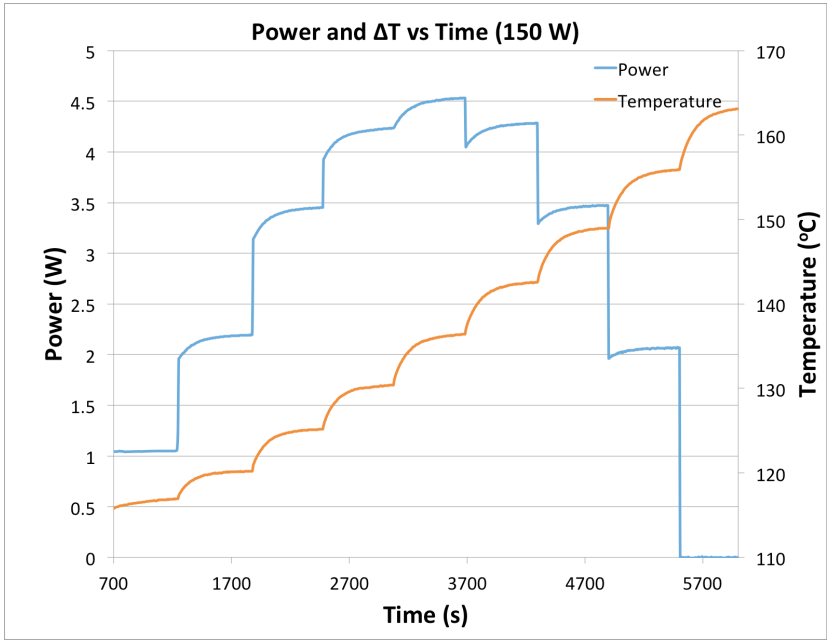

Figure C-7 - Transient behaviour of the output power and ΔT for decreasing steps of output current with 150 W_{th} input heat flux

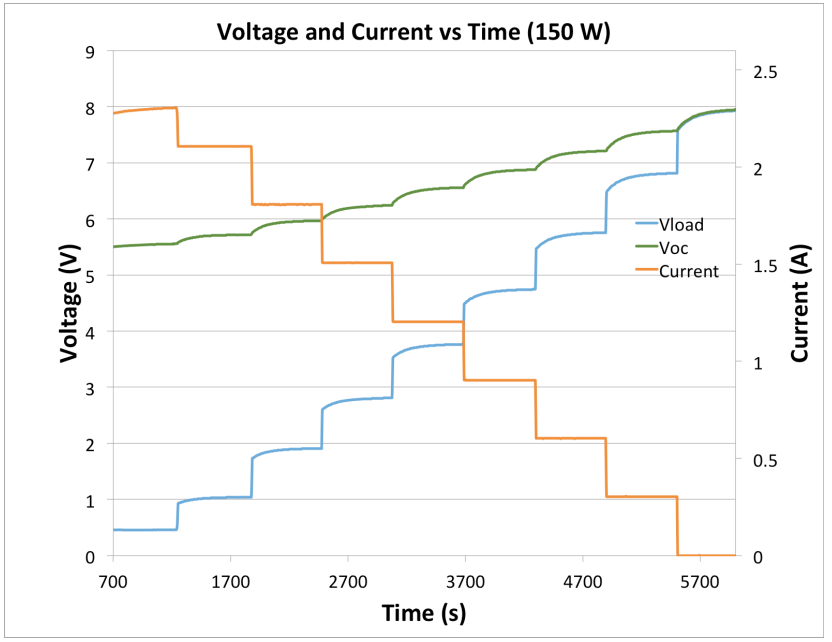

Figure C-8 - Transient behaviour of the load and open-circuit voltages and load current decreasing steps of output current with 150 W_{th} input heat flux

Figure C-9 to Figure C-12 show the transient behaviour of the TEG when the input power is 200 W_{th} and the load current is changed with steps of 400 *mA*. In Figure C-9 and Figure C-10 the current is stepped from zero to the short-circuit current, whereas in Figure C-11 and Figure C-12 the current is stepped from the short-circuit current down to zero.

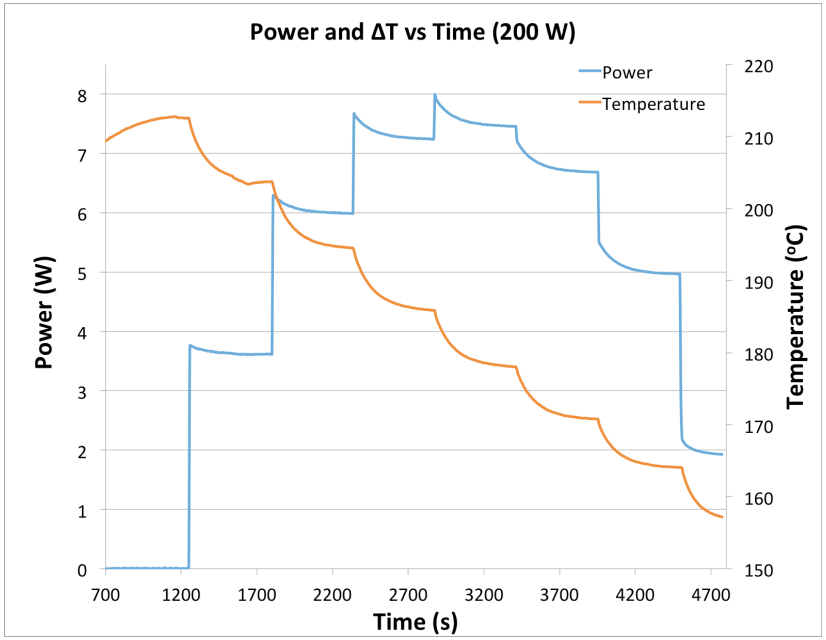

Figure C-9 - Transient behaviour of the output power and ΔT for increasing steps of output current with 200 W_{th} input heat flux

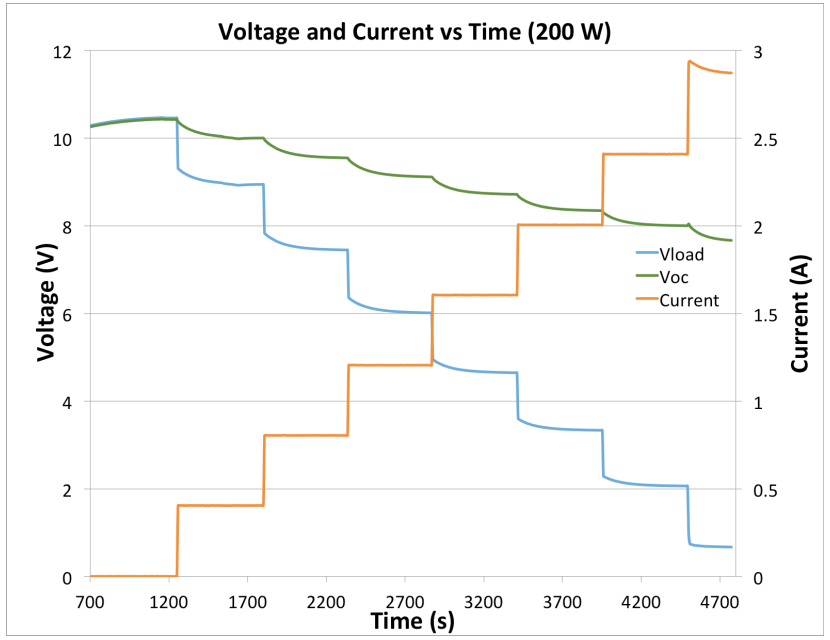

Figure C-10 - Transient behaviour of the load and open-circuit voltages and load current increasing steps of output current with 200 W_{th} input heat flux

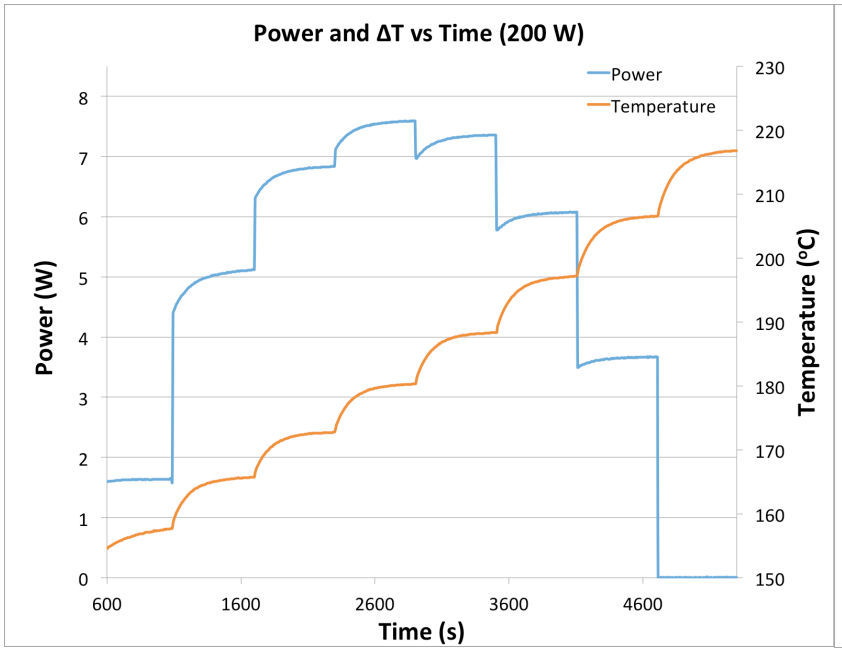

Figure C-11 - Transient behaviour of the output power and ΔT for decreasing steps of output current with 200 W_{th} input heat flux

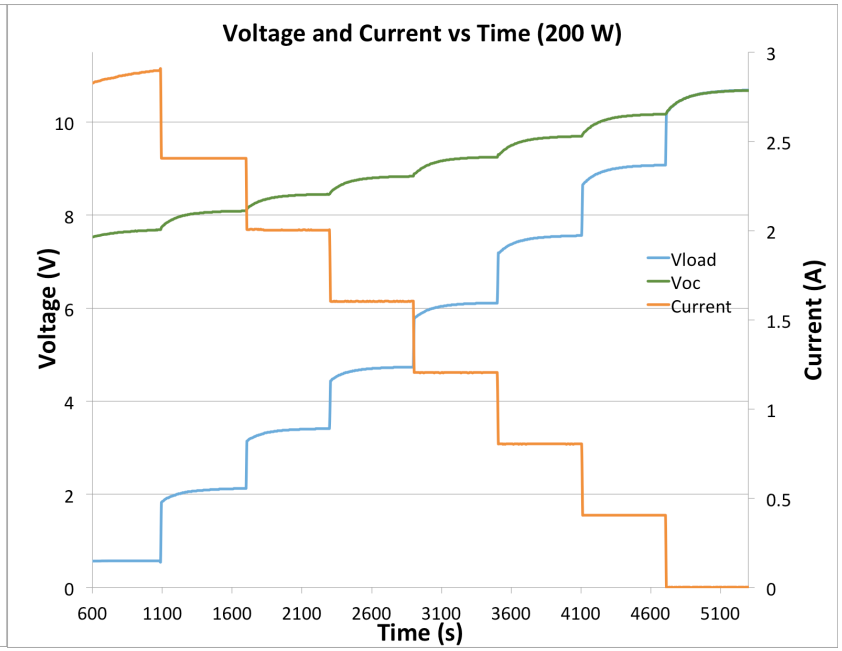

Figure C-12 - Transient behaviour of the load and open-circuit voltages and load current decreasing steps of output current with 200 W_{th} input heat flux

Figure C-13 to Figure C-16 show the transient behaviour of the TEG when the input power is 250 W_{th} and the load current is changed with steps of 400 *mA*. In Figure C-13 and Figure C-14 the current is stepped from zero to the short-circuit current, whereas in Figure C-15 and Figure C-16 the current is stepped from the short-circuit current down to zero.

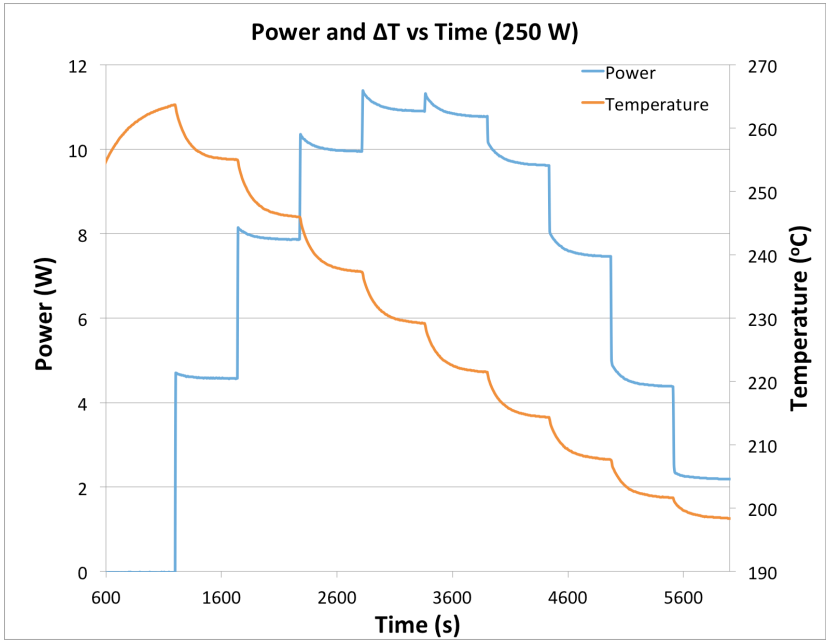

Figure C-13 - Transient behaviour of the output power and ΔT for increasing steps of output current with 250 W_{th} input heat flux

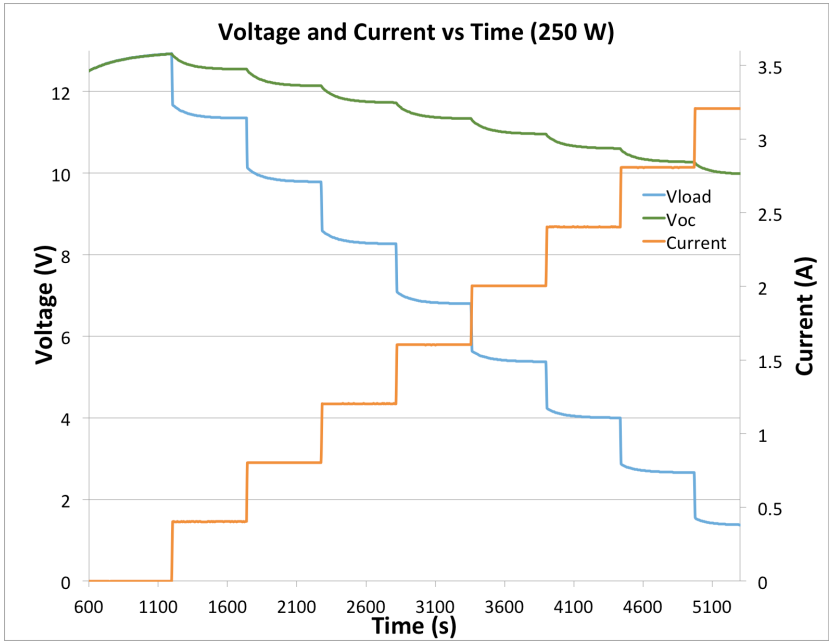

Figure C-14 - Transient behaviour of the load and open-circuit voltages and load current increasing steps of output current with 250 W_{th} input heat flux

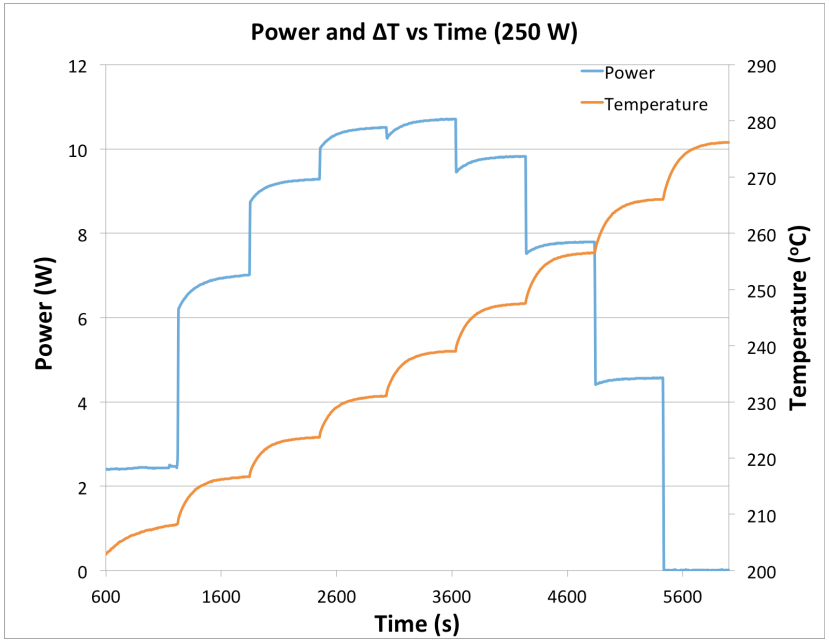

Figure C-15 - Transient behaviour of the output power and ΔT for decreasing steps of output current with 250 W_{th} input heat flux

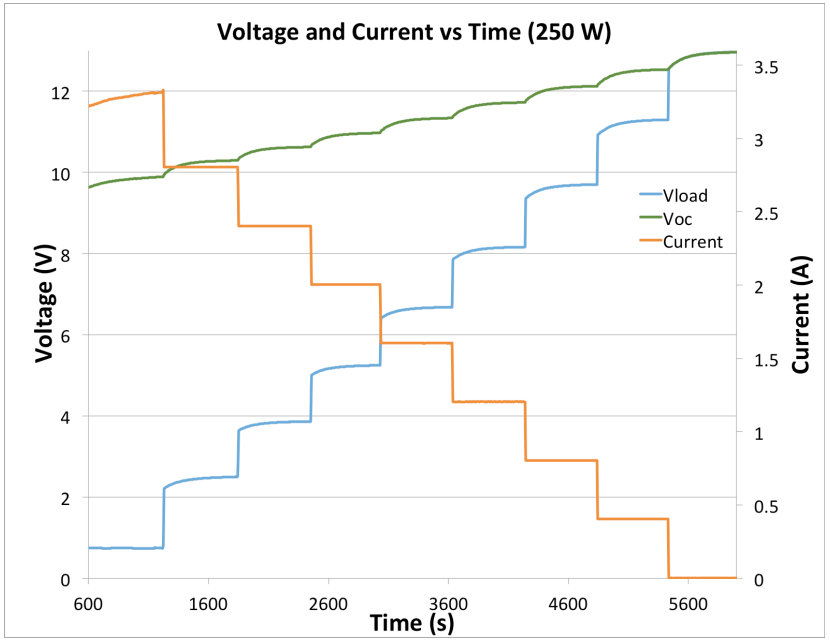

Figure C-16 - Transient behaviour of the load and open-circuit voltages and load current decreasing steps of output current with 250 W_{th} input heat flux

Figure C-17 to Figure C-20 show the transient behaviour of the TEG when the input power is 300 W_{th} and the load current is changed with steps of 500 *mA*. In Figure C-17 and Figure C-18 the current is stepped from zero to the short-circuit current, whereas in Figure C-19 and Figure C-20 the current is stepped from the short-circuit current down to zero.

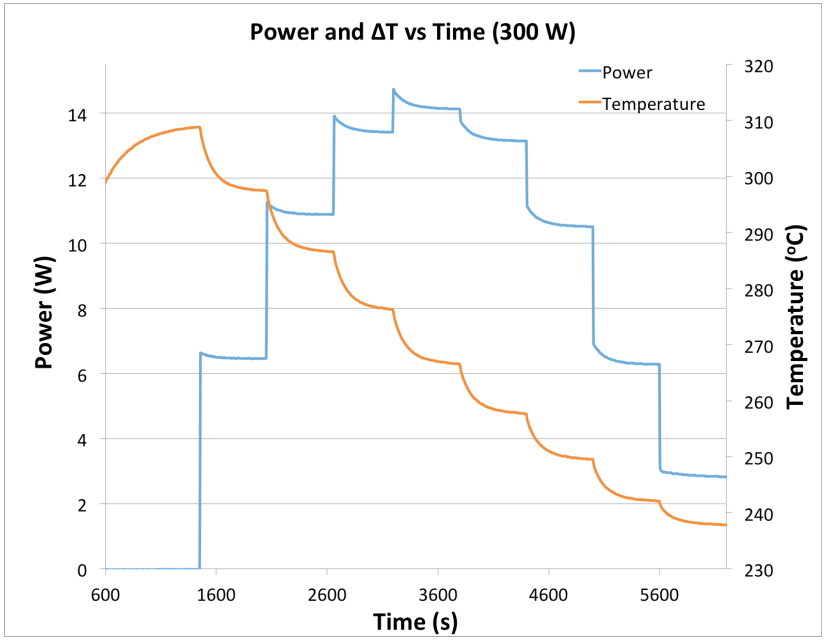

Figure C-17 - Transient behaviour of the output power and ΔT for increasing steps of output current with 300 W_{th} input heat flux

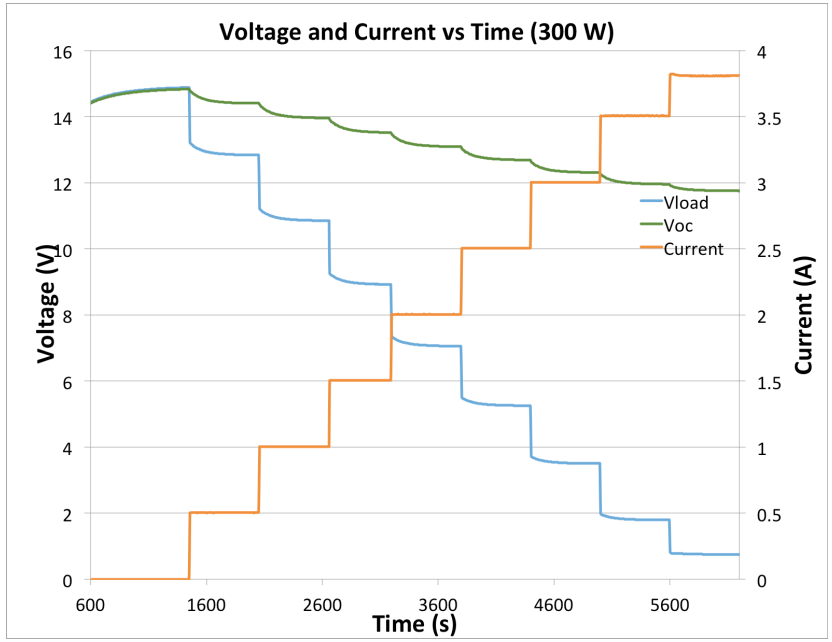

Figure C-18 - Transient behaviour of the load and open-circuit voltages and load current increasing steps of output current with 300 W_{th} input heat flux

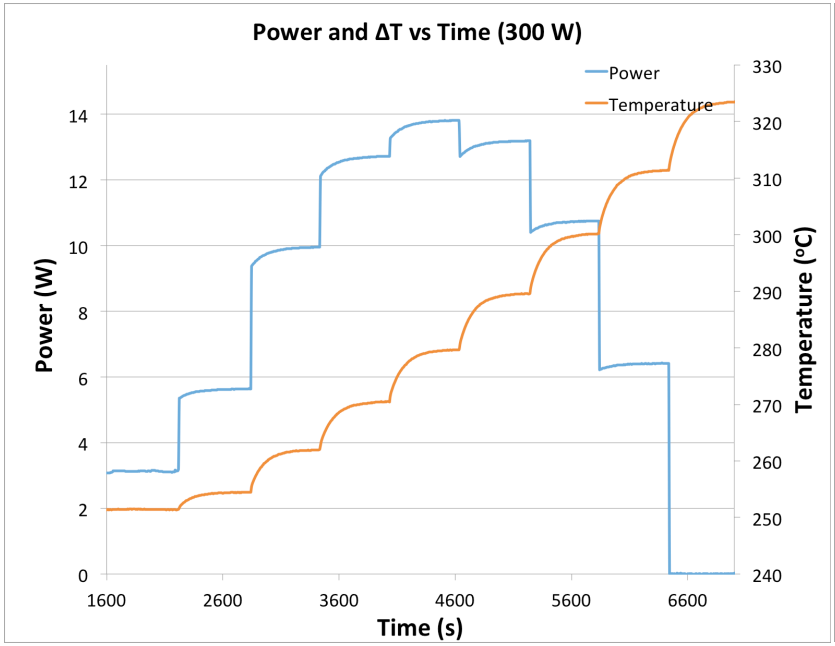

Figure C-19 - Transient behaviour of the output power and ΔT for decreasing steps of output current with 300 W_{th} input heat flux

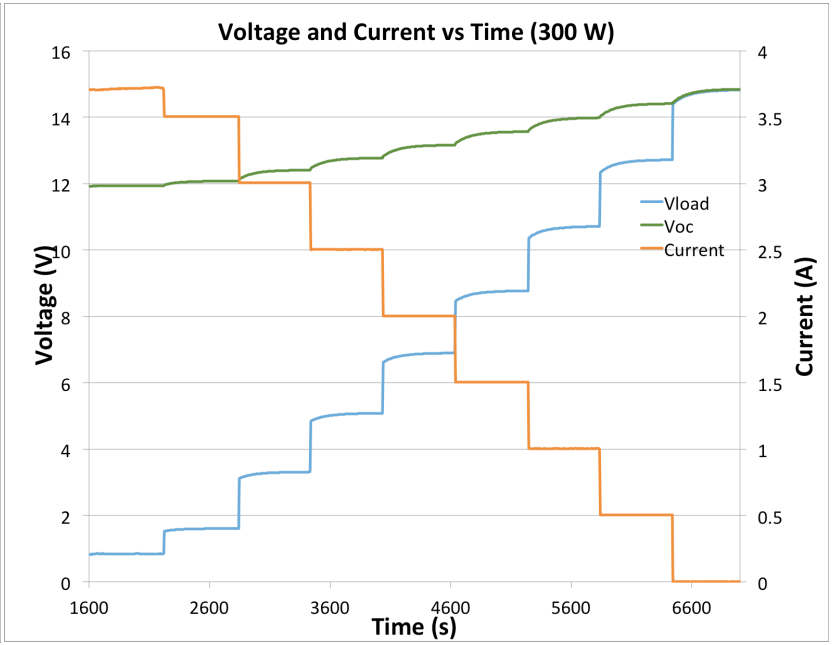

Figure C-20 - Transient behaviour of the load and open-circuit voltages and load current decreasing steps of output current with 300 W_{th} input heat flux

Bibliography

[1] P. J. Taroni, I. Hoces, N. Stingelin, M. Heeney, and E. Bilotti, "Thermoelectric materials: A brief historical survey from metal junctions and inorganic semiconductors to organic polymers," *Isr. J. Chem.*, vol. 54, no. 5–6, pp. 534–552, 2014.

[2] C. Gayner and K. K. Kar, "Recent advances in thermoelectric materials," *Prog. Mater. Sci.*, vol. 83, pp. 330–382, 2016.

[3] A. Polozine, S. Sirotinskaya, and L. Schaeffer, "History of development of thermoelectric materials for electric power generation and criteria of their quality," *Mater. Res.*, vol. 17, no. 5, pp. 1260–1267, 2014.

[4] L. D. Hicks and M. S. Dresselhaus, "Effect of quantum-well structures on the thermomagnetic figure of merit," *Phys. Rev. B*, vol. 47, no. 19, pp. 727–731, 1993.

[5] Enn Velmre, "Thomas Johann Seebeck (1770–1831)," *Est. J. Eng.*, vol. 13, no. 4, pp. 276–282, 2007.

[6] C. Wood, "Materials for thermoelectric energy conversion," *Inst. Phys.*, vol. 51, pp. 459–539, 1988.

[7] N. S. Bennett, "Thermoelectric performance in n-type bulk silicon: The influence of dopant concentration and dopant species," *Phys. Status Solidi Appl. Mater. Sci.*, vol. 214, no. 7, 2017.

[8] Z. Tian, S. Lee, and G. Chen, "A Comprehensive Review of Heat Transfer in Thermoelectric Materials and Devices," *Annu. Rev. Heat Transf.*, pp. 1–64, 2014.

[9] S. Twaha, J. Zhu, Y. Yan, and B. Li, "A comprehensive review of thermoelectric technology : Materials , applications , modelling and performance improvement," vol. 65, pp. 698–726, 2016.

[10] L. Yang, Z. Chen, M. S. Dargusch, and J. Zou, "High Performance Thermoelectric Materials : Progress and Their Applications," vol. 1701797, pp. 1–28, 2018.

[11] U. Department of Energy, "Chapter 6: Innovating Clean Energy Technologies in Advanced Manufacturing | Direct Thermal Energy Conversion Materials, Devices, and Systems Technology Assessment," *Quadrenn. Technol. Rev.*, 2015.

[12] T. M. He, Jian; Tritt, "Advances in thermoelectric materials research: Looking back and moving forward," *Science (80-.).*, vol. 9997, no. 357, pp. 1379–1378, 2017.

[13] D. K. Aswal, R. Basu, and A. Singh, "Key issues in development of thermoelectric power generators: High figure-of-merit materials and their highly conducting interfaces with metallic interconnects," *Energy Convers. Manag.*, vol. 114, pp. 50–67, 2016.

[14] D. Champier, "Thermoelectric generators : A review of applications," *Energy Convers. Manag.*, vol. 140, pp. 167–181, 2017.

[15] J. L. Webb and G. H. Kramer, "An evaluation of germanium detectors employed for the measurement of radionuclides deposited in lungs using an experimental and Monte Carlo approach," *Health Phys.*, vol. 81, no. 6, pp. 711–719, 2001.

[16] D. M. Rowe, "Applications of nuclear-powered thermoelectric generators in space," *Appl. Energy*, vol. 40, no. 4, pp. 241–271, 1991.

[17] T. C. Holgate, R. Bennett, T. Hammel, T. Caillat, S. Keyser, and B. Sievers, "Increasing the Efficiency of the Multi-mission Radioisotope Thermoelectric Generator," *J. Electron. Mater.*, vol. 44, no. 6, pp. 1814–1821, 2015.

[18] G. Bennett, "Space Nuclear Power: Opening the Final Frontier," *4th Int. Energy Convers. Eng. Conf. Exhib.*, no. June, pp. 26–29, 2006.

[19] R. R. Furlong and E. J. Wahlquist, "US space missions using radioisotope power systems," *Nucl. News*, vol. 42, no. April, pp. 26–35, 1999.

[20] C. Yu and K. T. Chau, "Thermoelectric automotive waste heat energy recovery using maximum power point tracking," *Energy Convers. Manag.*, vol. 50, no. 6, pp.

1506–1512, 2009.

[21] M. Brignone and A. Ziggiotti, “Impact of novel thermoelectric materials on automotive applications,” *AIP Conf. Proc.*, vol. 1449, no. 2012, pp. 493–496, 2012.

[22] D. Tatarinov, M. Koppers, G. Bastian, and D. Schramm, “Modeling of a thermoelectric generator for thermal energy regeneration in automobiles,” *J. Electron. Mater.*, vol. 42, no. 7, pp. 2274–2281, 2013.

[23] S. Kumar, S. D. Heister, X. Xu, J. R. Salvador, and G. P. Meisner, “Thermoelectric generators for automotive waste heat recovery systems part I: Numerical modeling and baseline model analysis,” *J. Electron. Mater.*, vol. 42, no. 4, pp. 665–674, 2013.

[24] S. Kumar, S. D. Heister, X. Xu, J. R. Salvador, and G. P. Meisner, “Thermoelectric generators for automotive waste heat recovery systems part II: Parametric evaluation and topological studies,” *J. Electron. Mater.*, vol. 42, no. 6, pp. 944–955, 2013.

[25] X. Liu, Y. D. Deng, W. S. Wang, and C. Q. Su, “Experimental Investigation of Exhaust Thermoelectric System and Application for Vehicle,” vol. 44, no. 6, pp. 2203–2210, 2015.

[26] L. Kutt and M. Lehtonen, “Automotive waste heat harvesting for electricity generation using thermoelectric systems ; An overview,” *2015 IEEE 5th Int. Conf. Power Eng. Energy Electr. Drives*, vol. 5, pp. 55–62, 2015.

[27] F. P. Brito, J. Martins, and E. Hanc, “Thermoelectric Exhaust Heat Recovery with Heat Pipe-Based Thermal Control,” 2015.

[28] K. Huang, Y. Yan, B. Li, Y. Li, K. Li, and J. Li, “A Novel Design of Thermoelectric Generator for Automotive Waste Heat Recovery,” pp. 54–61, 2018.

[29] Y. Wang, C. Dai, and S. Wang, “Theoretical analysis of a thermoelectric generator using exhaust gas of vehicles as heat source,” *Appl. Energy*, vol. 112, pp. 1171–1180, 2013.

[30] F. Frobenius, G. Gaiser, and U. Rusche, “Thermoelectric Generators for the

Integration into Automotive Exhaust Systems for Passenger Cars and Commercial Vehicles," vol. 45, no. 3, pp. 1433–1440, 2016.

[31] R. J. Stevens, S. J. Weinstein, and K. S. Koppula, "Theoretical limits of thermoelectric power generation from exhaust gases," *Appl. Energy*, vol. 133, pp. 80–88, 2014.

[32] J. I. Ghojel and J. G. Haidar, "WASTE HEAT RECOVERY FROM THE EXaAUST OF LOW-POWER DIESEL ENGINE USING THERMOELECTRIC GENETATORS," *20th Int. Conf. Thermoelectr.*, pp. 413–417, 2001.

[33] S. Risse and H. Zellbeck, "Close-Coupled Exhaust Gas Energy Recovery in a Gasoline Engine," *Res. Therm. Manag.*, vol. 74, pp. 54–61, 2013.

[34] A. Killander and J. C. Bass, "A stove-top generator for cold areas," *Fifteenth Int. Conf. Thermoelectr. Proc. ICT '96, 26-29 March 1996*, no. March, pp. 390–393, 1996.

[35] G. Min and D. M. Rowe, "'Symbiotic' application of thermoelectric conversion for fluid preheating/power generation," *Energy Convers. Manag.*, vol. 43, no. 2, pp. 221–228, 2002.

[36] R. Y. Nuwayhid, A. Shihadeh, and N. Ghaddar, "Development and testing of a domestic woodstove thermoelectric generator with natural convection cooling," vol. 46, pp. 1631–1643, 2005.

[37] C. Favarel, D. Champier, J. Rozis, T. Kousksou, and P. Bédécarrats, "Thermoelectricity - A Promising Complementarity with Efficient Stoves in Off-grid-areas," vol. 3, no. 3, pp. 256–268, 2015.

[38] G. F. Rinalde, L. E. Juanicó, E. Taglialavore, S. Gortari, and M. G. Molina, "Development of thermoelectric generators for electrification of isolated rural homes," *Int. J. Hydrogen Energy*, vol. 35, no. 11, pp. 5818–5822, 2010.

[39] D. Champier, J. P. Bédécarrats, T. Kousksou, M. Rivaletto, F. Strub, and P. Pignolet, "Study of a TE (thermoelectric) generator incorporated in a multifunction wood stove," vol. 36, pp. 1518–1526, 2011.

[40] A. Montecucco, J. Siviter, and A. R. Knox, "A combined heat and power system for solid-fuel stoves using thermoelectric generators," *Energy Procedia*, vol. 75, pp. 597–602, 2015.

[41] A. Montecucco, J. Siviter, and A. R. Knox, "Combined heat and power system for stoves with thermoelectric generators," *Appl. Energy*, vol. 185, pp. 1336–1342, 2017.

[42] M. P. Codecasa, C. Fanciulli, R. Gaddi, F. Gomez-paz, and F. Passaretti, "Design and Development of a TEG Cogenerator Device Integrated into a Self-Standing Natural Combustion Gas Stove," 2014.

[43] S. M. O. Shaughnessy, M. J. Deasy, J. V Doyle, and A. J. Robinson, "Performance analysis of a prototype small scale electricity-producing biomass cooking stove," *Appl. Energy*, vol. 156, pp. 566–576, 2015.

[44] J. M. Damaschke, "Design of a low input voltage converter for thermoelectric generator," *Ieee Trans. Ind. Appl.*, vol. 33, no. 5, pp. 1203–1207, 1997.

[45] E. Carlson, K. Strunz, and B. Otis, "A 20mV Input Boost ConverterWith Efficient Digital Control for Thermoelectric Energy Harvesting," *IEEE J. Solid-State Circuits*, vol. 4, no. 4, pp. 741–750, 2010.

[46] Y. K. Ramadass and A. P. Chandrakasan, "A battery-less thermoelectric energy harvesting interface circuit with 35 mV startup voltage," *IEEE J. Solid-State Circuits*, vol. 46, no. 1, pp. 333–341, 2011.

[47] J. P. Im *et al.*, "A 40mV transformer-reuse self-startup boost converter with MPPT control for thermoelectric energy harvesting," *Dig. Tech. Pap. - IEEE Int. Solid-State Circuits Conf.*, vol. 55, no. November 2010, pp. 104–105, 2012.

[48] K. Simpson and R. Shuttleworth, "Discrete, matched-load, step-up converter for 60–400 mV thermoelectric energy harvesting source," *Electron. Lett.*, vol. 49, no. 11, pp. 719–720, 2013.

[49] J. R. Buckle, A. Knox, J. Siviter, and A. Montecucco, "Autonomous underwater vehicle thermoelectric power generation," *J. Electron. Mater.*, vol. 42, no. 7, pp.

2214–2220, 2013.

[50] D. G. Ebling *et al.*, "Development of a System for Thermoelectric Heat Recovery from Stationary Industrial Processes," *J. Electron. Mater.*, vol. 45, no. 7, pp. 3433–3439, 2016.

[51] P. Aranguren, D. Astrain, A. Rodríguez, and A. Martínez, "Experimental investigation of the applicability of a thermoelectric generator to recover waste heat from a combustion chamber," *Appl. Energy*, vol. 152, pp. 121–130, 2015.

[52] L. Merotto, C. Fanciulli, R. Dondè, and S. De Iuliis, "Study of a thermoelectric generator based on a catalytic premixed meso-scale combustor," *Appl. Energy*, vol. 162, pp. 346–353, 2016.

[53] G. Min and N. M. Yatim, "Variable thermal resistor based on self-powered Peltier effect," *J. Phys. D. Appl. Phys.*, vol. 41, no. 22, p. 222001, 2008.

[54] A. Rezania, L. A. Rosendahl, and H. Yin, "Parametric optimization of thermoelectric elements footprint for maximum power generation," *J. Power Sources*, vol. 255, pp. 151–156, 2014.

[55] A. Montecucco, J. Siviter, and A. R. Knox, "Constant heat characterisation and geometrical optimisation of thermoelectric generators," *Appl. Energy*, vol. 149, pp. 248–258, 2015.

[56] D. M. Rowe and G. Min, "Evaluation of thermoelectric modules for power generation," *J. Power Sources*, vol. 73, no. 2, pp. 193–198, 1998.

[57] D. M. Rowe, *Thermoelectrics Handbook - Macro to Nano*. CRC Taylor & Francis, 2006.

[58] R. Decher, *Direct energy conversion: fundamentals of electric power production*. New York: Oxfor University Press Inc., 1997.

[59] D. Nemir and J. Beck, "On the significance of the thermoelectric figure of merit Z," *J. Electron. Mater.*, vol. 39, no. 9, pp. 1897–1901, 2010.

[60] K. Yazawa and A. Shakouri, "Cost-efficiency trade-off and the design of thermoelectric power generators," *Environ. Sci. Technol.*, vol. 45, no. 17, pp. 7548–7553, 2011.

[61] J. W. Stevens, "Optimized Thermal Design of Small ΔT Thermoelectric Generators," no. 724, 1999.

[62] P. M. Mayer and R. J. Ram, "Optimization of Heat Sink–Limited Thermoelectric Generators," *Nanoscale Microscale Thermophys. Eng.*, vol. 10, no. 2, pp. 143–155, 2006.

[63] B. Hauke, "Basic Calculation of a Buck Converter's Power Stage," *Texas Instruments, Appl. Rep. Novemb.*, no. November 2011, pp. 1–8, 2011.

[64] B. Hauke, "Basic Calculation of a Boost Converter's Power Stage," *Texas Instruments, Appl. Rep. Novemb.*, no. November 2009, pp. 1–9, 2009.

[65] J. Falin, "Designing DC / DC converters based on SEPIC topology," *Texas Instruments, Analog Appl. J.*, pp. 18–23, 2008.

[66] M. Green, "Design Calculations for Buck-Boost Converters," *Texas Instruments, Appl. Rep. August*, no. August, pp. 1–12, 2012.

[67] H. N. Zainudin and S. Mekhilef, "Comparison Study of Maximum Power Point Tracker Techniques for PV Systems," *Proc. 14th Int. Middle East Power Syst. Conf. (MEPCON'10), Cairo Univ. Egypt*, no. 1, pp. 750–755, 2010.

[68] R. Faranda and S. Leva, "Energy comparison of MPPT techniques for PV Systems," *Trans. Power Syst.*, vol. 03, no. 06, pp. 446–455, 2008.

[69] A. Garrigós, D. Marroquí, J. M. Blanes, R. Gutiérrez, M. Compadre, and C. Clark, "An analog global maximum power point tracking for photovoltaic systems: Application to nanospacecrafts," *2017 19th Eur. Conf. Power Electron. Appl. EPE 2017 ECCE Eur.*, vol. 2017-Janua, pp. 1–9, 2017.

[70] B. J. Huang, P. C. Hsu, R. J. Tsai, and M. M. Hussain, "A thermoelectric generator using loop heat pipe and design match for maximum-power generation," *Appl.*

Therm. Eng., vol. 91, pp. 1082–1091, 2015.

[71] C. E. Kinsella, S. M. O'Shaughnessy, M. J. Deasy, M. Duffy, and A. J. Robinson, "Battery charging considerations in small scale electricity generation from a thermoelectric module," *Appl. Energy*, vol. 114, pp. 80–90, 2014.

[72] S. Kim, S. Cho, N. Kim, N. Baatar, and J. Kwon, "A Digital Coreless Maximum Power Point Tracking Circuit for Thermoelectric Generators.pdf," *J. Electron. Mater.*, vol. 40, no. 5, pp. 867–872, 2011.

[73] S. Maniktala, "Voltage-Mode, Current-Mode (and Hysteretic Control)," *Microsemi Tech. Note TN-203*, pp. 1–19, 2012.

[74] D. E. Schwartz, "A maximum-power-point-tracking control system for thermoelectric generators," *Proc. - 2012 3rd IEEE Int. Symp. Power Electron. Distrib. Gener. Syst. PEDG 2012*, pp. 78–81, 2012.

[75] R. Y. Kim and J. S. Lai, "A seamless mode transfer maximum power point tracking controller for thermoelectric generator applications," *IEEE Trans. Power Electron.*, vol. 23, no. 5, pp. 2310–2318, 2008.

[76] T. Suntio, *Dynamic Profile of Switched-Mode Converter*. WILEY-VCH Verlag GmbH & Co. KGaA, 2009.

[77] K. Sun, H. Wu, Y. Cai, and Y. Xing, "A power conditioning stage based on analog-circuit MPPT control and a superbuck converter for thermoelectric generators in spacecraft power systems," *J. Electron. Mater.*, vol. 43, no. 6, pp. 2287–2292, 2014.

[78] W. Denzinger, "Electrical power subsystem of Globalstar," in *4th European Space Power Conference, Poitiers, France*, 1995.

[79] J. Gao *et al.*, "A thermoelectric generation system and its power electronics stage," *J. Electron. Mater.*, vol. 41, no. 6, pp. 1043–1050, 2012.

[80] Y. H. Liu, Y. H. Chiu, J. W. Huang, and S. C. Wang, "A novel maximum power point tracker for thermoelectric generation system," *Renew. Energy*, vol. 97, pp. 306–318, 2016.

[81] C. G. Jan Hendrik Carstens, “Control concept for the electrical integration of thermoelectric generators into a vehicle power supply,” in *Proceedings 14. Internationales Stuttgarter Symposium*, 2014, pp. 911–921.

[82] M. Bond and J. Do Park, “Current-sensorless power estimation and MPPT implementation for thermoelectric generators,” *IEEE Trans. Ind. Electron.*, vol. 62, no. 9, pp. 5539–5548, 2015.

[83] S. Nakayama and H. Koizumi, “A design of boost chopper circuit with thermoelectric generator for rechargeable battery and development of MPPT algorithm,” *2013 Brazilian Power Electron. Conf. COBEP 2013 - Proc.*, vol. 20, pp. 630–635, 2013.

[84] K. K. Win, S. Dasgupta, and S. K. Panda, “An optimized MPPT circuit for thermoelectric energy harvester for low power applications,” *8th Int. Conf. Power Electron. - ECCE Asia "Green World with Power Electron. ICPE 2011-ECCE Asia*, pp. 1579–1584, 2011.

[85] A. Paraskevas and E. Koutroulis, “A simple maximum power point tracker for thermoelectric generators,” *Energy Convers. Manag.*, vol. 108, pp. 355–365, 2016.

[86] H. Yamada, K. Kimura, T. Hanamoto, T. Ishiyama, T. Sakaguchi, and T. Takahashi, “A Novel MPPT Control Method of Thermoelectric Power Generation with Single Sensor,” *Appl. Sci.*, vol. 3, no. 2, pp. 545–558, 2013.

[87] K. Z. Ahmed and S. Mukhopadhyay, “A wide conversion ratio, extended input 3.5-μA boost regulator with 82% efficiency for low-voltage energy harvesting,” *IEEE Trans. Power Electron.*, vol. 29, no. 9, pp. 4776–4786, 2014.

[88] A. Hidaka, T. Tsuji, and S. Matsumoto, “A Thermoelectric Power Generation System with Ultra low Input Voltage Boost Converter with Maximum power Point Tracking,” *Renew. Energy Res. Appl. (ICRERA), 2012 Int. Conf.*, pp. 1–5, 2012.

[89] J. Kim and C. Kim, “A DC-DC boost converter with variation-tolerant MPPT technique and efficient ZCS circuit for thermoelectric energy harvesting applications,” *IEEE Trans. Power Electron.*, vol. 28, no. 8, pp. 3827–3833, 2013.

[90] S. Carreon-Bautista, A. Eladawy, A. Nader Mohieldin, and E. Sanchez-Sinencio, "Boost converter with dynamic input impedance matching for energy harvesting with multi-array thermoelectric generators," *IEEE Trans. Ind. Electron.*, vol. 61, no. 10, pp. 5345–5353, 2014.

[91] Z. Qiu, K. Sun, H. Wu, J. Huang, and Y. Xing, "A high efficiency cascaded thermoelectric generation system with power balancing mechanism," *Conf. Proc. - IEEE Appl. Power Electron. Conf. Expo. - APEC*, vol. 2015-May, no. May, pp. 647–653, 2015.

[92] A. Petucco, S. Saggini, L. Corradini, and P. Mattavelli, "Analysis of Power Processing Architectures for Thermoelectric Energy Harvesting," *IEEE J. Emerg. Sel. Top. Power Electron.*, vol. 4, no. 3, pp. 1036–1049, 2016.

[93] A. Montecucco, J. Siviter, and A. R. Knox, "The effect of temperature mismatch on thermoelectric generators electrically connected in series and parallel," *Appl. Energy*, vol. 123, pp. 47–54, 2014.

[94] H. Wu, K. A. I. Sun, M. I. N. Chen, and Y. A. N. Xing, "Evaluation of Power Conditioning Architectures for Energy Production Enhancement in Thermoelectric Generator Systems," 2013.

[95] L. Piegari, R. Rizzo, I. Spina, and P. Tricoli, "Optimized adaptive perturb and observe maximum power point tracking control for photovoltaic generation," *Energies*, vol. 8, no. 5, pp. 3418–3436, 2015.

[96] J. Ahmed and Z. Salam, "An improved perturb and observe (P&O) maximum power point tracking (MPPT) algorithm for higher efficiency," *Appl. Energy*, vol. 150, pp. 97–108, 2015.

[97] S. Chun and A. Kwasinski, "Analysis of classical root-finding methods applied to digital maximum power point tracking for sustainable photovoltaic energy generation," *IEEE Trans. Power Electron.*, vol. 26, no. 12, pp. 3730–3743, 2011.

[98] N. Femia, G. Petrone, G. Spagnuolo, and M. Vitelli, "Perturb and observe MPPT technique robustness improved," *IEEE Int. Symp. Ind. Electron.*, vol. 2, no. 2, pp. 845–850, 2004.

[99] N. Femia, G. Petrone, G. Spagnuolo, and M. Vitelli, "Increasing the Efficiency of P&O MPPT by Converter Dynamic Matching," *Ieee*, no. 1, pp. 1017–1021, 2004.

[100] L. Chen, D. Cao, Y. Huang, and F. Z. Peng, "Modeling and power conditioning for thermoelectric generation," *PESC Rec. - IEEE Annu. Power Electron. Spec. Conf.*, pp. 1098–1103, 2008.

[101] S. Lineykin and S. Ben-Yaakov, "Modeling and analysis of thermoelectric modules," *IEEE Trans. Ind. Appl.*, vol. 43, no. 2, pp. 505–512, 2007.

[102] P. Dziurdzia, "Modeling and Simulation of Thermoelectric Energy Harvesting Processes," in *Sustainable Energy Harvesting Technologies - Past, Present and Future*, Dr. Yen Kheng Tan, Ed. InTech, 2011, pp. 109–128.

[103] A. Montecucco and A. R. Knox, "Accurate simulation of thermoelectric power generating systems," *Appl. Energy*, vol. 118, pp. 166–172, 2014.

[104] A. Montecucco, "Efficiently Maximising Power Generation from Thermoelectric Generators," University of Glasgow, 2014.

[105] M. Von Lukowicz, E. Abbe, T. Schmiel, and M. Tajmar, "Thermoelectric Generators on Satellites — An Approach for Waste Heat Recovery in Space," 2016.

[106] G. Min, "Thermoelectric energy harvesting," *Energy Harvest. Technol.*, pp. 325–336, 2009.

[107] R. J. B. Balaguru, "Lattice Vibrations , Phonons , Specific Heat Capacity , Thermal Conductivity." NPTEL -National Programe onTechnology Enhance Le, pp. 1–24.

[108] P. Horowitz and W. Hill, *The Art of Electronics*, Third. Cambridge University Press, 2015.

[109] F. P. Incropera and D. P. DeWitt, *Introduction to Heat Transfer*, Fourth. John Wiley & Sons.

[110] A. Montecucco, J. R. Buckle, and A. R. Knox, "Solution to the 1-D unsteady heat conduction equation with internal Joule heat generation for thermoelectric devices,"

Appl. Therm. Eng., vol. 35, no. 1, pp. 177–184, 2012.

[111] M. C. Torrecilla, A. Montecucco, J. Siviter, A. Strain, and A. R. Knox, "Transient response of a thermoelectric generator to load steps under constant heat flux," *Appl. Energy*, vol. 212, no. June 2017, pp. 293–303, 2018.

[112] E. A. Man, "Design Considerations for Thermoelectric Power Generation," Aalborg University, 2016.

[113] L. Chen, D. Cao, H. Yi, and F. Z. Peng, "Modeling and power conditioning for thermoelectric generation," in *IEEE Power Electronics Specialists Conference*, 2008, pp. 1098–1103.

[114] C. Batard, F. Poitiers, C. Millet, and N. Ginot, "Simulation of Power Converters Using Matlab-Simulink," *MATLAB - A Fundam. Tool Sci. Comput. Engeneering Apl.*, pp. 43–68, 2012.

[115] A. Khajezadeh, A. Ahmadipour, and M. S. Motlagh, "DC-DC CONVERTERS VIA MATLAB / SIMULINK," vol. 5, no. 10, pp. 906–914, 2014.

[116] E. Hosseini, "MODELING AND SIMULATION OF CHOPPERS SWITCHING VIA MATLAB / SIMULINK," vol. 12, no. 1, pp. 10–17, 2015.

[117] M. G. N. M, Y. Kiran, and S. S. Parthasarthy, "Modelling of Buck DC-DC Converter Using Simulink," vol. 3, no. 7, pp. 14965–14975, 2014.

[118] J. Su, C. Chien, J. Chen, and C. Wang, "Simulink Behavior Models for DC ± DC Switching Converter Circuits using PWM Control ICs *," vol. 22, no. 2, pp. 315–322, 2006.

[119] A. A. Elbaset and A. A. Elbaset, "Small-Signal MATLAB / Simulink Model of DC-DC Buck Converter using State-Space Averaging Method Small-Signal MATLAB / Simulink Model of DC-DC Buck Converter using State-Space Averaging Method," 2015.

[120] R. W. Erickson and D. Maksimovic., *Fundamentals of Power Electronics*. Chapman and Hall, 1997.